

N O T I C E

THIS DOCUMENT HAS BEEN REPRODUCED FROM
MICROFICHE. ALTHOUGH IT IS RECOGNIZED THAT
CERTAIN PORTIONS ARE ILLEGIBLE, IT IS BEING RELEASED
IN THE INTEREST OF MAKING AVAILABLE AS MUCH
INFORMATION AS POSSIBLE



PSU/TURBO 82-2

**THREE DIMENSIONAL MEAN VELOCITY AND TURBULENCE
CHARACTERISTICS IN THE ANNULUS WALL REGION OF
AN AXIAL FLOW COMPRESSOR ROTOR PASSAGE**

R. DAVINO AND B. LAKSHMINARAYANA



NASA GRANT Nsg 3212

NATIONAL AERONAUTICS & SPACE ADMINISTRATION

LEWIS RESEARCH CENTER

(NASA-CR-169003) THREE DIMENSIONAL MEAN
VELOCITY AND TURBULENCE CHARACTERISTICS IN
THE ANNULUS WALL REGION OF AN AXIAL FLOW
COMPRESSOR ROTOR PASSAGE (Pennsylvania State
Univ.) 262 p HC A12/MF A01

N82-25252

Unclas
22704

CSCI 21E G3/07

**TURBOMACHINERY LABORATORY
DEPARTMENT OF AEROSPACE ENGINEERING
THE PENNSYLVANIA STATE UNIVERSITY
UNIVERSITY PARK, PA 16802**

MAY 1982

**THREE DIMENSIONAL MEAN VELOCITY AND TURBULENCE
CHARACTERISTICS IN THE ANNULUS WALL REGION OF
AN AXIAL FLOW COMPRESSOR ROTOR PASSAGE**

R. Davino and B. Lakshminarayana

NASA Grant NSG 3212

National Aeronautics & Space Administration

Lewis Research Center

**Turbomachinery Laboratory
Department of Aerospace Engineering
The Pennsylvania State University
University Park, PA 16802**

May 1982

PRECEDING PAGE BLANK NOT FILMED

ABSTRACT

Three-dimensional characteristics of the mean velocity and turbulence structure in the annulus-wall region of a moderately loaded compressor rotor is reported in this thesis. The experimental investigation was performed using the rotating hot-wire technique within the rotor blade passage and the stationary hot-wire technique for the exit-flow of the rotor blade passage. These measurements revealed the effect of rotation and subsequent flow interactions upon the rotor blade flow-field and wake development in the annulus-wall region.

The flow near the rotor blade tips was found to be highly complex due to the interaction of the annulus-wall boundary layer, the blade boundary layers, the tip leakage flow, and the secondary flow. Within the blade passage, this interaction resulted in an appreciable radial inward flow as well as a defect in the mainstream velocity near the mid-passage. Turbulence levels within this region were very high. This indicated a considerable extent of flow mixing due to the viscous flow interactions. The size and strength of this loss core was found to grow with axial distance from the blade trailing edge. The nature of the rotor blade exit-flow was dominated by the wake development. Steep gradients in the wake velocity profile were found to exist at radial locations below the interference region. Large radially outward flows in the wake indicated the effect of rotation on the rotor blade boundary layers. The wake near the annulus-wall reflected the viscous interaction of the annulus-wall layer and the tip leakage flow. Large wake

widths and substantial reductions in the mean velocity profiles were measured, as well as increased turbulence intensities and stresses in this region.

A preliminary consideration to the above investigation was the response of the three-sensor hot-wire probe under flow conditions similar to those in the rotor blade passage. The response of the probe was found to be invariant to the effect of rotation; however, the response was found to be dependent upon the incident flow direction. This dependence was determined to be a function of the hot-wire sensor configuration and the deviation angle of its flow from the direction normal to the sensor. The response of the probe was corrected by employing a sensitivity function.

TABLE OF CONTENTS

	<u>Page</u>
ABSTRACT	111
LIST OF TABLES	viii
LIST OF FIGURES	ix
NOMENCLATURE	xvi
ACKNOWLEDGEMENTS	xxi
 I. INTRODUCTION	 1
1.1 Problem Relevance and Objectives	1
1.2 Previous Investigations	3
1.2.1 Secondary Flow	3
1.2.2 Annulus-Wall Boundary Layer	6
1.2.3 Blade Boundary Layer	6
1.2.4 Tip Leakage Flow	7
 II. TEST FACILITY, DATA ACQUISITION, AND PROCEDURES	 10
2.1 Axial-Flow Compressor Facility	10
2.2 The Compressor Rotor	14
2.3 Probe Traverse Mechanisms	18
2.3.1 Rotating Probe Traverse Gear	18
2.3.2 Stationary Probe Traverse Unit	20
2.4 Data Transmission System	20
2.4.1 Brush Slip-Ring Unit	20
2.4.2 Mercury Slip-Ring Unit	21
2.5 Rotor Passage-Flow Probe and Instrumentation	21
2.5.1 Three-Sensor Hot-Wire Probe	21
2.5.2 Signal Processing Equipment	24
2.6 Rotor Exit-Flow Probe and Instrumentation	26
2.6.1 Three-Sensor Hot-Wire Probe	26
2.6.2 Signal Processing Equipment	28
 III. THREE-SENSOR HOT-WIRE PROBE ACCURACY AND LIMITATIONS.	 30
3.1 Background	30
3.2 Data Transmission System Response	33
3.3 Effect of Rotation on a Three-Sensor Hot-Wire Probe	33

	<u>Page</u>
3.4 Sensitivity of Single- and Three-Sensor Hot-Wire Probes to Yaw and Pitch Angles	43
3.4.1 Experimental Set-Up and Procedure	45
3.4.2 Sensitivity of the Single-Sensor Hot-Wire Probe.	47
3.4.3 Sensitivity of the Three-Sensor Hot-Wire Probe	51
3.5 Error in Three-Sensor Hot-Wire Probe Measurements Subjected to a Fluctuating (Unsteady) Velocity Vector	79
3.5.1 Effect of Probe Angle in the Stationary Frame of Reference with Respect to the Average Absolute Flow Direction	80
3.5.2 Effect of Ensemble-Average Sample Size. . .	86
IV. EXPERIMENTAL RESULTS AND INTERPRETATION OF THE FLOWFIELD IN THE ANNULUS-WALL REGION	92
4.1 Rotor In-Flow Conditions	92
4.1.1 Surveys Upstream of the Inlet Guide Vanes .	92
4.1.2 Surveys Downstream of the Inlet Guide Vanes	93
4.2 Mean Velocity Profiles in the Annulus-Wall Region	97
4.2.1 Streamwise Mean Velocity	102
4.2.2 Normal Mean Velocity	113
4.2.3 Radial Mean Velocity	126
4.2.4 Total Relative Velocity Inside the Blade Passage	134
4.3 Turbulence Intensity Profiles in the Annulus-Wall Region.	138
4.3.1 Streamwise Turbulence Intensity	157
4.3.2 Normal Turbulence Intensity	160
4.3.3 Radial Turbulence Intensity	161
4.3.4 Total Turbulent Energy Inside the Blade Passage	163
4.4 Annulus-Wall Flow Turbulence Shear Stress Profiles	166
4.5 Passage-Averaged Flow Angle Variation	181
4.6 Passage-Averaged Velocities and Annulus-Wall Mean Boundary Layer Properties	185
4.6.1 Passage-Average Total Velocity.	185
4.6.2 Momentum Thickness and Shape Factor of the Annulus-Wall Boundary Layer	187
4.7 Variation of Rotor Wake Decay in the Radial and Streamwise Directions	188
4.7.1 Maximum Defect in Mean Velocities	191
4.7.2 Maximum Turbulence Intensity in the Wake. .	196
4.7.3 Free-Stream Turbulence Intensity	200
4.7.4 Semi-Wake Width	204

	<u>Page</u>
4.8 Structure of Blade Passage Turbulence	206
V. SUMMARY AND CONCLUSIONS	215
5.1 Sensitivity of Three-Sensor Hot-Wire Probes. . . .	215
5.2 Annulus-Wall Flow Characteristics.	217
REFERENCES	223
APPENDIX A: SCALES OF THE FLOW	228
APPENDIX B: ESTIMATION OF THREE-SENSOR HOT-WIRE MEASUREMENT ERRORS	232
B.1 Three-Sensor Hot-Wire Probe Error	232
B.2 Instrumentation Error	237
B.3 Mechanical Error	238

LIST OF TABLES

<u>Table</u>		<u>Page</u>
1	Axial-Flow Compressor Facility Specifications and Operating Conditions	13
2	Blade Element Details	17
3	Single-Sensor Probe Specifications	46
4	Direction Cosines Between Wire Directions and the Reference Coordinates	63
5	Rotor Blade Annulus-Wall Flow Axial and Radial Measurement Stations	99
6	Maximum Streamwise Velocity for the Reported Measurement Stations	101

LIST OF FIGURES

<u>Figure</u>		<u>Page</u>
1	Nature of Annulus-Wall Flow and Coordinate System	4
2	PSU Axial-Flow Compressor Facility and Data Transmission Systems	11
3	Performance Curve of the PSU Axial-Flow Compressor	15
4	PSU Axial-Flow Compressor Rotor-Blade Geometry . .	16
5	Rotating Probe Traverse Gear	19
6	Mercury Slip-Ring Unit of Data Transmission System	22
7	Three-Sensor Hot-Wire Probe for Axial-Flow Compressor Annulus-Wall Passage-Flow Measurements.	23
8	Schematic of Instrumentation for Hot-Wire Measurements	25
9	Three-Sensor Hot-Wire Probe for Axial-Flow Compressor Annulus-Wall Exit-Flow Measurements . .	27
10	Spectra of Mercury Slip-Ring Test Signal	36
11	Three-Sensor Hot-Wire Probe for Rotation Effect Investigation	39
12	Three-Sensor Hot-Wire Probe Static and Dynamic Calibration.	40
13	Comparison of Measured Velocities of Static and Dynamic Calibration.	42
14	Single-Sensor Probe Response to Yaw Angle Variation	48
15	Response of Three-Sensor Hot-Wire to Varying Angles of Yaw and Pitch	54
16	Error of Uncorrected Three-Sensor Hot-Wire Probe Response with Yaw and Pitch Angle Variation . . .	57

<u>Figure</u>		<u>Page</u>
17	Response of Sensor-One of Three-Sensor Hot-Wire Probe with Flow Deviation Angle Variation	59
18	Response of Sensor-Two of Three-Sensor Hot-Wire Probe with Flow Deviation Angle Variation	60
19	Response of Sensor-Three of Three-Sensor Hot-Wire Probe with Flow Deviation Angle Variation . .	61
20	Flow Deviation Angle of Sensor-One with Three-Sensor Probe Yaw and Pitch Angle Variation	64
21	Flow Deviation Angle of Sensor-Two with Three-Sensor Probe Yaw and Pitch Angle Variation	65
22	Flow Deviation Angle of Sensor-Three with Three-Sensor Probe Yaw and Pitch Angle Variation	66
23	Behavior of Deviation Angle Sensitivity Function (Eqn. 11) with Deviation Angle Variation	69
24	Behavior of Deviation Angle Sensitivity Function (Eqn. 12) with Deviation Angle Variation	70
25	Behavior of Deviation Angle Sensitivity Function (Eqn. 13) with Deviation Angle Variation	71
26	Comparison of Sensor-One Response and Deviation Angle Sensitivity Function (Eqn. 14) with Deviation Angle Variation	73
27	Comparison of Sensor-Two Response and Deviation Angle Sensitivity Function (Eqn. 14) with Deviation Angle Variation	74
28	Comparison of Sensor-Three Response and Deviation Angle Sensitivity Function (Eqn. 14) with Deviation Angle Variation	75
29	Error of Corrected Three-Sensor Hot-Wire Response and Yaw and Pitch Angle Variation	77
30	Streamwise Mean Velocity Profile Variation with Three-Sensor Probe Yaw Angle	82
31	Normal Mean Velocity Profile Variation with Three-Sensor Probe Yaw Angle	83
32	Radial Mean Velocity Profile Variation with Three-Sensor Probe Yaw Angle	84

<u>Figure</u>		<u>Page</u>
33	Streamwise Mean Velocity Profile Variation with Sample Size	87
34	Normal Mean Velocity Profile Variation with Sample Size	88
35	Radial Mean Velocity Profile Variation with Sample Size	89
36	Velocity Across the Annulus Upstream of the Inlet Guide Vanes	94
37	Tangential Variation of Axial Velocity Behind the Inlet Guide Vanes, $Z = 1.042$, $\phi = 0.56$	95
38	Tangential Variation of Axial Velocity Behind the the Inlet Guide Vanes, $Z = 2.000$, $\phi = 0.56$	96
39	Definition of Streamwise Coordinate System	98
40	Streamwise Mean Velocity Profiles, $Z = 0.750$. . .	103
41	Streamwise Mean Velocity Profiles, $Z = 0.979$. . .	104
42	Streamwise Mean Velocity Profiles, $Z' = 0.021$. . .	105
43	Streamwise Mean Velocity Profiles, $Z' = 0.042$. . .	106
44	Streamwise Mean Velocity Profiles, $Z' = 0.125$. . .	107
45	Streamwise Mean Velocity Profiles, $Z' = 0.456$. . .	108
46	Normal Mean Velocity Profiles, $Z = 0.750$	114
47	Normal Mean Velocity Profiles, $Z = 0.979$	115
48	Variation of the Blade Passage-Flow Angle in the s-n Plane	116
49	Normal Mean Velocity Profiles, $Z' = 0.021$	120
50	Normal Mean Velocity Profiles, $Z' = 0.042$	121
51	Normal Mean Velocity Profiles, $Z' = 0.125$	122
52	Normal Mean Velocity Profiles, $Z' = 0.458$	123
53	Variation of the Blade Exit-Flow Angle in the s-n Plane	124

<u>Figure</u>		<u>Page</u>
54	Radial Mean Velocity Profiles, $Z = 0.750$	127
55	Radial Mean Velocity Profiles, $Z = 0.979$	128
56	Radial Mean Velocity Profiles, $Z' = 0.021$	129
57	Radial Mean Velocity Profiles, $Z' = 0.042$	130
58	Radial Mean Velocity Profiles, $Z' = 0.125$	131
59	Radial Mean Velocity Profiles, $Z' = 0.458$	132
60	Total Relative Velocity at $Z = 0.750$	135
61	Total Relative Velocity at $Z = 0.979$	136
62	Streamwise Turbulence Intensity Profiles, $Z = 0.750$	139
63	Streamwise Turbulence Intensity Profiles, $Z = 0.979$	140
64	Streamwise Turbulence Intensity Profiles, $Z = 1.021$	141
65	Streamwise Turbulence Intensity Profiles, $Z = 1.042$	142
66	Streamwise Turbulence Intensity Profiles, $Z = 1.125$	143
67	Streamwise Turbulence Intensity Profiles, $Z = 1.458$	144
68	Normal Turbulence Intensity Profiles, $Z = 0.750$. .	145
69	Normal Turbulence Intensity Profiles, $Z = 0.979$. .	146
70	Normal Turbulence Intensity Profiles, $Z' = 0.021$. .	147
71	Normal Turbulence Intensity Profiles, $Z' = 0.042$. .	148
72	Normal Turbulence Intensity Profiles, $Z' = 0.125$. .	149
73	Normal Turbulence Intensity Profiles, $Z' = 0.458$. .	150
74	Radial Turbulence Intensity Profiles, $Z = 0.750$. .	151
75	Radial Turbulence Intensity Profiles, $Z = 0.979$. .	152

<u>Figure</u>		<u>Page</u>
76	Radial Turbulence Intensity Profiles, $Z' = 0.021$. .	153
77	Radial Turbulence Intensity Profiles, $Z' = 0.042$. .	154
78	Radial Turbulence Intensity Profiles, $Z' = 0.125$. .	155
79	Radial Turbulence Intensity Profiles, $Z' = 0.458$. .	155
80	Total Turbulence Energy at $Z = 0.750$	164
81	Total Turbulence Energy at $Z = 0.979$	165
82	Stress Correlation τ_{sn} , $Z = 0.750$	167
83	Stress Correlation τ_{sn} , $Z = 0.979$	168
84	Stress Correlation τ_{sn} , $Z' = 0.021, 0.042$	169
85	Stress Correlation τ_{sn} , $Z' = 0.125, 0.458$	170
86	Stress Correlation τ_{rn} , $Z = 0.750$	171
87	Stress Correlation τ_{rn} , $Z = 0.979$	172
88	Stress Correlation τ_{rn} , $Z' = 0.021, 0.042$	173
89	Stress Correlation τ_{rn} , $Z' = 0.125, 0.458$	174
90	Stress Correlation τ_{rs} , $Z = 0.750$	175
91	Stress Correlation τ_{rs} , $Z = 0.979$	176
92	Stress Correlation τ_{rs} , $Z' = 0.021, 0.042$	177
93	Stress Correlation τ_{rs} , $Z' = 0.125, 0.458$	178
94	Radial Variation of Passage-Average Flow Angle at Various Axial Locations	182
95	Radial Variation of Passage-Average Meridional Angle at Various Axial Locations	183
96	Radial and Axial Distribution of the Passage- Average Total Relative Velocity	186
97	Annulus-Wall Flow Momentum Thickness Variation with Axial Distance	189
98	Annulus-Wall Flow Shape Factor Variation with Axial Distance	190

<u>Figure</u>		<u>Page</u>
99	Radial and Axial Variation of the Streamwise Mean Velocity Defect	192
100	Radial and Axial Variation of the Normal Mean Velocity Defect	193
101	Radial and Axial Variation of the Radial Mean Velocity Defect	194
102	Radial and Axial Variation of the Maximum Streamwise Turbulence Intensity	197
103	Radial and Axial Variation of the Maximum Normal Turbulence Intensity	198
104	Radial and Axial Variation of the Maximum Radial Turbulence Intensity	199
105	Radial and Axial Variation of the Free-Stream Streamwise Turbulence Intensity	201
106	Radial and Axial Variation of the Free-Stream Normal Turbulence Intensity	202
107	Radial and Axial Variation of the Free-Stream Radial Turbulence Intensity	203
108	Variation of the Semi-Wake Width with Axial Distance	205
109	Turbulence Energy Spectra in the Relative Frame of Reference Inside the Blade Passage at $Z = 0.750$, $R = 0.891$	207
110	Turbulence Energy Spectra in the Relative Frame of Reference Inside the Blade Passage at $Z = 0.750$, $R = 0.946$	208
111	Turbulence Energy Spectra in the Relative Frame of Reference Inside the Blade Passage at $Z = 0.750$, $R = 0.980$	209
112	Turbulence Energy Spectra in the Relative Frame of Reference Inside the Blade Passage at $Z = 0.979$, $R = 0.891$	210
113	Turbulence Energy Spectra in the Relative Frame of Reference Inside the Blade Passage at $Z = 0.979$, $R = 0.946$	211

<u>Figure</u>		<u>Page</u>
114	Turbulence Energy Spectra in the Relative Frame of Reference Inside the Blade Passage at Z = 0.979, R = 0.980	212
115	Qualitative Nature of Annulus-Wall Flow Due to Flowfield Interactions	222

NOMENCLATURE

Symbol

A	Constant of King's heat transfer law
a	Constant
B	Intercept of hot-wire calibration curve
b	Small parameter of yaw sensitivity function
b_1, b_2	Constants of deviation angle sensitivity function
C	Correction factor
C_{L_0}	Camber expressed as design lift coefficient of an isolated airfoil
C_W	Specific heat of hot-wire sensor material
c	Blade chord length
d_p	Diameter of hot-wire sensor support prong
d_s	Diameter of hot-wire probe stem
d_w	Diameter of hot-wire tungsten sensor
E	Anemometer mean voltage output, elastic modulus
E_0	Anemometer mean voltage at zero flow velocity
e	Anemometer fluctuating voltage output, blade passage exit condition
e_c	Conversion constant between heat and electrical units
$f(\alpha)$	Yaw angle sensitivity function
$g(\lambda)$	Deviation angle sensitivity function
H	Boundary layer shape factor
I	Amperage in anemometer circuit, moment of area

Symbol

i	Blade passage inlet condition
k	Small parameter of yaw sensitivity function
k_1, k_2, k_3	Constants of the deviation angle sensitivity function
L	Blade span, sum of the characteristic lengths on the pressure and suction surfaces of the blade normalized by the semi-blade spacing
L.E.	Blade leading-edge
ℓ	Large eddy length scale
ℓ_e	Etched length of hot-wire sensor
ℓ_p	Length of hot-wire sensor support prong
(ℓ_1, ℓ_2, ℓ_3)	Three-sensor hot-wire probe coordinate system (Figure 7)
M	Time constant, mass of the probe
m	Constant of yaw sensitivity function, mass per unit length of the probe
N	Ensemble-average sample size
n	Slope of hot-wire calibration curve
PS	Pressure side of rotor blade passage
q	Total energy of turbulence
R	Radius ratio (r/r_{tip}), resistance of hot-wire sensor
R_f	Resistance of hot-wire sensor at fluid temperature
R_w	Resistance of hot-wire sensor at working fluid temperature
r	Local radius, radial direction, radial location of the probe
S	Blade spacing
SS	Suction side of the rotor blade passage

Symbol

s	Sensitivity of the hot-wire
(s, n, r)	End-wall flow coordinate system (streamwise, normal, and radial coordinate directions)
T.E.	Blade trailing-edge
t	Blade thickness
U	Flow velocity
\bar{U}	Mean flow velocity
U_{eff}	Effective cooling velocity
U_1	Incident flow velocity
U_N	Normalized cooling velocity
U_{ref}	Reference flow velocity
U_t	Total flow velocity
U_{tip}	Peripheral speed of the rotor blade
u'	Flow turbulence
W	Flow relative velocity
w	Defect or maximum value of relative velocity
w'	Fluctuating component of relative velocity
Y_p, Y_e	Tangential distance inside and at the exit of the blade passage respectively
Z	Chordwise distance from leading edge normalized by the local blade chord
Z'	Axial distance from trailing edge normalized by the local blade chord
z	Axial coordinate direction corresponding to the axis of the compressor
α	Hot-wire probe angle, annulus-wall flow angle measured from axial direction
β	Hot-wire probe pitch angle, meridional angle of annulus-wall flow

Symbol

γ	Absolute probe angle
δ	Boundary layer thickness
ϵ	Turbulence dissipation rate, flow turning angle (eqn. 15)
ϵ_T	Total three-sensor probe error
ζ	Vorticity in radial direction
η	Vorticity in normal direction, Kolmogorov scale
$\bar{\eta}$	Rotor efficiency (Euler) = $\bar{\psi}/\bar{\psi}_{\text{Euler}}$
θ_f	Working fluid temperature
θ_w	Heated hot-wire temperature
θ^*	Momentum thickness of a boundary layer
κ	Wave number
λ	Deviation angle of incident flow
λ_g	Taylor's microscale
μ	Fluid viscosity
ν	Kinematic viscosity
ξ	Vorticity in streamwise direction
ρ	Fluid density
τ_s, τ_n, τ_r	Normalized turbulence intensities in the streamwise, normal, and radial directions, respectively $((\bar{w}_s^{-2})^{1/2}/W_s, (\bar{w}_n^{-2})^{1/2}/W_s, (\bar{w}_r^{-2})^{1/2}/W_s)$
$\tau_{sn}, \tau_{rn}, \tau_{rs}$	Stress correlations given by $\overline{w_s' w_n'}/W_s^2, \overline{w_n' w_r'}/W_s^2, \overline{w_r' w_s'}/W_s^2$, respectively
$\bar{\phi}$	Mass averaged flow coefficient (\bar{W}/U_{tip})
$\bar{\psi}$	Mass averaged stagnation pressure rise coefficient incident normalized by $1/2 \rho U_{\text{tip}}^2$

Symbol

Ω	Rotational speed of the rotor blade
ω	Frequency
ω_n	Natural frequency, in bending mode, of the hot-wire support

Subscripts

A	Average value
c	Center of blade wake
comb	Due to combined three-sensor probe calibration
d	Defect (difference between free-stream and wake)
indv.	Due to individual three-sensor probe calibration
measured	An experimentally measured parameter
o	Free-stream value
(s, n, r)	Values in the streamwise, normal, and radial coordinate directions, respectively
T	Total
tip	Blade tip location
w	Hot-wire at operating conditions
(z, θ , r)	Values in the axial, tangential, and radial coordinate directions, respectively
∞	At surrounding conditions

Superscript

—	Average value
'	Fluctuating quantity

ACKNOWLEDGMENT

The authors wish to thank G. Kane and J. Fetterolf for their aid in the experimental setup and instrumentation. This work was supported by the National Aeronautics and Space Administration through Grant NSG 3212 with Dr. P. M. Sockol as the Technical Monitor.

CHAPTER I

INTRODUCTION

1.1 Problem Relevance and Objectives

The level of performance obtained in turbomachinery is a direct reflection of the degree of understanding of the flow mechanisms occurring in the blade rows. Stationary cascades have been of great value in studying many of these mechanisms. The cascade, however, is unsuitable for the study of a variety of mechanisms which are present in turbomachinery. The effect of rotation, curvature, the relative motion between the rotor and the end-wall, and other three-dimensional effects in the end-wall region are most suitably studied in an actual turbo-machine environment. The relative motion between the rotating rotor blade row and the stationary wall casing generates a region of complex flow interaction in the flow; this annulus-wall region is greatly influenced by the effects of rotation, the tip leakage flow, the annulus-wall boundary layer, the cascade secondary flow, and the blade boundary layer. This results in large frictional losses and introduces considerable three-dimensionality to the flow, thus making the prediction of the flow behavior extremely difficult.

The primary objective of the current study reported in this thesis has been to gather additional understanding of the complex inviscid and viscous effects of the annulus-wall flowfield, including the three components of mean velocity, turbulence intensity, and turbulence stress

inside the rotor blade passage. It is hoped that the knowledge gained from this investigation will help serve in establishing a theoretical model for the eventual analysis of the three-dimensional flow in the annulus-wall region. Certain types of information about the flow in the rotating frame of reference may be obtained by high response measurements in the stationary frame of reference. However, there is a distinct advantage in obtaining measurements in the rotating frame of reference. The accuracy of measurements obtained from the end-wall flowfield employing these two methods of measurement was a secondary concern of this thesis.

The subjects addressed in this thesis are:

1. To determine the accuracy of measurements obtained using a three-sensor hot-wire probe in the rotating and stationary frames of reference.
2. To develop a measuring technique using a three-sensor hot-wire probe to measure the three components of velocity, turbulence intensity, and stress within the rotating blade passage.
3. To perform a complete flow survey inside the rotor blade passage of the annulus-wall flowfield using a rotating three-sensor hot-wire probe
4. To perform a complete flow survey at several axial locations behind the rotor blade passage of the annulus-wall flowfield using a stationary three-sensor hot-wire probe.

1.2 Previous Investigations

The annulus-wall flowfield present in axial-flow compressor blading is a result of complex flow interactions. The flowfield in the annulus-wall region is a result of the combined effects of the annulus-wall boundary layer, the rotor blade boundary layer, the tip leakage flow, and the secondary flow as shown in Figure 1. These various flow phenomena have been investigated separately or with limited interaction by many investigators.

1.2.1 Secondary Flow

The three-dimensional viscous flows near the annulus wall of an axial compressor are known to strongly influence the annulus-wall flow development and play a major role in determining the performance of the machine. Early work on this problem was based upon inviscid secondary flow calculations which assumed no growth in boundary layer thickness across a blade row.

Within a blade passage in a cascade, a balance between the pressure gradients and the centrifugal forces in the principal normal direction is maintained. However, the deflexion of the low momentum fluid in the boundary layer is not equal to the deflexion of the mainstream flow. To compensate, the low momentum flow is turned more than the mainstream flow. This deviation from a uniformly deflected stream is the secondary flow. A streamwise component of vorticity is developed near the cascade wall due to the secondary flow. This cascade secondary vorticity is located in the channel between the blades. Neglecting viscosity and compressibility, Squire and Winter (1951) have shown that this vorticity

ORIGINAL PAGE IS
OF POOR QUALITY

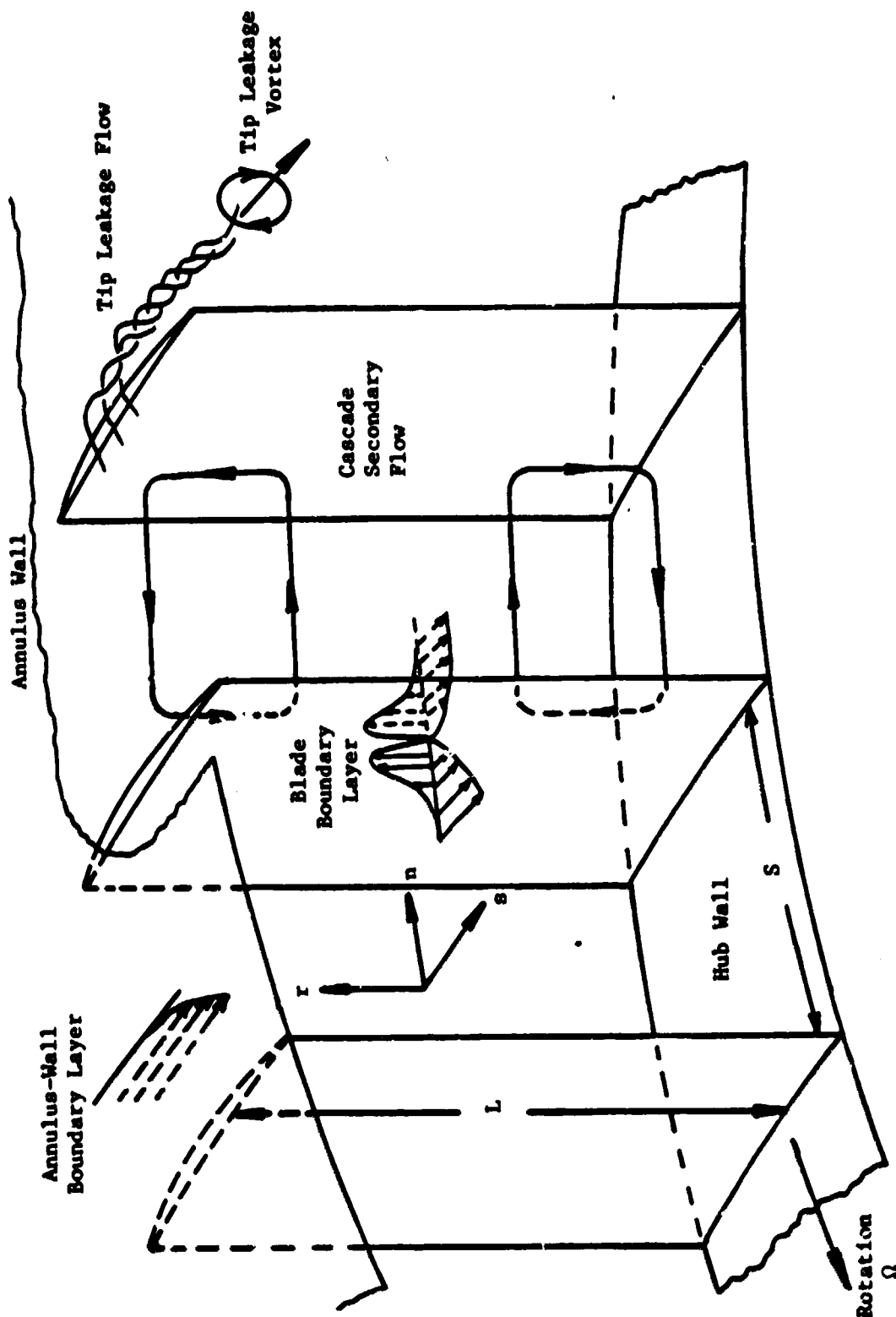


Figure 1. Nature of Annulus-Wall Flow and Coordinate System

is a function of the turning angle of the cascade and the mainstream velocity gradient. Hawthorne (1951) later developed a general theory for the secondary flow of an inviscid incompressible fluid and included the effect of the gradient in stagnation pressure. The validity of these theories has been confirmed by several experimental workers. A visualization study of secondary flows in cascades is reported by Herzig, et al. (1953).

Investigations of changes in deflexion due to the secondary flow in cascades have pursued several directions. One approach, followed by Carter (1948) employs the trailing vortex sheets which are shed from the blades. The values of the induced deflexion are derived from the induced velocities which are calculated from the strength of the vortex sheets. Another approach, pursued by Hawthorne (1951) and Smith (1955), is to consider the secondary motions to be induced by the distributed vortices in the flow between the blades. By solving Poisson's equations for the secondary vorticity, the stream function of the secondary flow is obtained.

Work in this area has been reviewed by Lakshminarayana and Horlock (1963), Horlock and Lakshminarayana (1973), and more recently by Horlock (1977). The basic difficulty with methods based on inviscid flow is that the calculated boundary layer does not change across a diffusing blade row due to the neglect of viscous terms. Various investigations have recently been conducted on the cascade and the rotor blade secondary flow. A comprehensive review of these investigations and of the application of their theories to a compressor rotor blade is discussed by Billet (1978).

1.2.2 Annulus-wall Boundary Layer

A prediction scheme for the annulus-wall boundary layer which employs integral boundary layer techniques has been developed by Mellor and Wood (1971) and Horlock and Perkins (1974). The three-dimensional equations of motion are averaged across the blade pitch and then integrated across the shear layer normal to the annulus wall. In principle these equations can predict the blockage and loss in the annulus-wall region. However, many approximations are required to evaluate important terms in the equations. One promising approach, pursued by Horlock (1973), is to use secondary flow theory to model some of the terms arising from three-dimensional effects. Sockol (1978) has recently employed secondary flow theory in this manner.

1.2.3 Blade Boundary Layer

Calculations of the boundary layer development on the surface of compressor blades suggest that there is some laminar flow on both the suction and the pressure surfaces. Calculations of the boundary layer development using the method of Thwaites (1949) support this and even show laminar flow at high values of chordwise Reynolds number and high levels of free-stream turbulence. If laminar separation occurs before transition, then information on the length of the separation bubble is required before any calculation can proceed into the turbulent region. Seyb (1965) has undertaken comprehensive calculations of the full boundary layer growth using laminar boundary layer transition data. Seyb found that at a small positive incidence laminar separation occurred quickly on the suction surface. A short bubble of reattachment then occurred which

resulted in turbulent flow over most of the blade suction surface. The flow on the pressure surface was found to be entirely laminar. Seyb's calculations were checked by experiments employing cascades.

An attempt to calculate the three-dimensional laminar flow on turbomachinery blading has been made by Horlock and Wordsworth (1965). They have considered the boundary layer on a helical plate rotating at zero incidence in a swirling flow. A differential equation for the radial velocity distribution through the boundary layer was employed and solved numerically. This transverse flow was found to be dependent upon the centrifugal pressure gradient and the Coriolis force.

A similar analysis for the turbulent flow on a rotating helical plate has since been carried out by Lakshminarayana et al. (1972), Horlock (1973), and Anand and Lakshminarayana (1975). Lakshminarayana et al. (1972) performed a momentum integral analysis of the turbulent boundary layer on a rotating blade and confirmed the analysis experimentally. For all these analyses, the mainstream flow was assumed to be in radial equilibrium. Also, the streamwise and radial momentum equations were integrated across the blade boundary layer with suitable assumptions for the velocity profile in the streamwise direction. The radial or cross-flow velocity profile was modeled using Mager's velocity profile. Anand and Lakshminarayana's analysis has been verified with measurements inside a rotating channel.

1.2.4 Tip Leakage Flow

The tip leakage flow in turbomachines is mainly due to two factors. One factor is the direct flow through the clearance space

which is undeflected by the blading. This flow is not available for doing work. Its magnitude depends upon the thickness and profile of the annulus-wall boundary layer and the size of the clearance space. Another factor is the indirect flow due to the pressure differences between the suction and pressure surfaces of the blade.

Early investigators, Rains (1954) and Vavra (1960), have assumed that the leakage flow results from the pressure difference across the blade tips and that the leakage flow occurs in an annulus of height equal to the clearance height. This flow, perpendicular to the blade chord, then rolls up into a vortex whose energy cannot be recovered. This analysis does not take into account the effect of the clearance gap-to-chord ratio and perturbations in the flow at various spanwise conditions. Betz (1925) has considered the velocities induced at the lifting line by the bound vortices shed all along the blade span. A procedure of this nature overestimates the losses since the viscous effects due to the gap and the presence of the annulus wall are neglected. Wu and Wu (1954) have performed an order-of-magnitude analysis which reduced the governing equations to a set of simplified equations for both high and low Reynolds number. Expressions were determined for the distributions of pressure and velocity in the clearance space. This procedure, however, overestimates the losses since viscous effects are neglected. Investigators such as Sugiyama (1975) investigated the effect of the annulus-wall boundary layer upon the tip leakage flow.

Based upon the theory of Betz, Lakshminarayana (1969) proposed a modified lifting line approach. This model assumed that the lift is uniform all along the span of the blade and only part of the bound vortex

at the tip is shed off. The blade distributions and the induced drag predicted from this model agree with his measurements. A more realistic flow model was presented by Lakshminarayana (1969) where the effect of solid body rotation in the viscous core of the leakage vortex is considered. Employing this model, the outlet angles were predicted accurately and the loss distributions were predicted qualitatively.

The combined effects of the radial clearance at the blade tip and the relative movement of the casing wall have been investigated by Dean (1954), Herzig et al. (1953), and Gearhart (1966) in the case of linear cascades. In addition, the investigation of Klein (1966) was similar in nature for the annular cascade.

The annulus-wall flowfield present in an axial-flow compressor is a result of an interaction of the above mentioned flow phenomena. A schematic of such phenomena, presented by Lakshminarayana and Horlock (1963), is shown in Figure 1. This illustration of the various annulus-wall flow phenomena is based upon a "separatist" view of the basic flows. No flow interaction is proposed by any of the above theories. The unique measurement capabilities of the axial-flow compressor facility employed for this investigation allows a comprehensive view of the interaction of these flows in the annulus-wall region.

CHAPTER II

TEST FACILITY, DATA ACQUISITION, AND PROCEDURE

The measurements reported in this investigation were performed using the axial-flow compressor facility located in the Turbomachinery Laboratory of The Pennsylvania State University. The measurements were acquired employing a rotating three-sensor hot-wire probe in the rotor blade passage and a stationary three-sensor hot-wire probe behind the rotor blade row. These measurements yielded information on the three components of mean velocity, turbulence intensity, and Reynolds stress, and various characteristics of the flow in the rotor annulus-wall region. This experimental information is required not only for the understanding of the rotor annulus-wall flow, but it is also essential for predicting the aerodynamic and acoustic properties of turbomachines.

2.1 The Axial-Flow Compressor Facility

The axial-flow research compressor facility built at The Pennsylvania State University and used for the measurements reported in this investigation is shown in Figure 2. The compressor facility consists of a rotor which is located between an inlet-guide-vane assembly and a stator assembly. The design features of this single-stage compressor are given by Smith (1956). An additional feature of this facility is a 3 m x 1.5 m x 3 m enclosure at the inlet (not shown). This enclosure consists of a wire mesh coated with 0.318 cm thick foam which enables dust free and smooth entry flow to the inlet.

ORIGINAL PAGE IS
OF POOR QUALITY

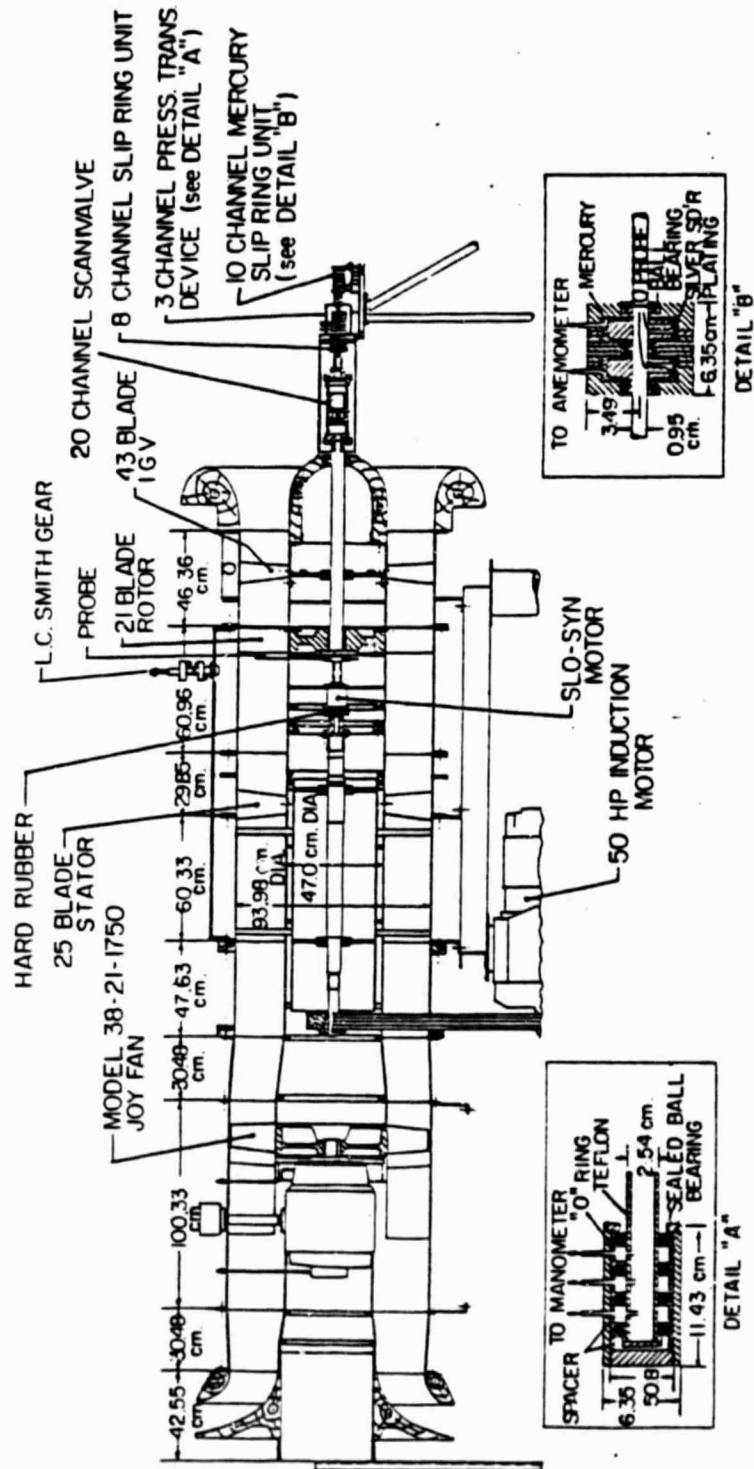


Figure 2. PSU Axial-Flow Compressor Facility and Data Transmission Systems.

The data transmission system for rotating probe measurements is upstream of the nose cone and is mounted on a tripod stand with vibration dampers. This is followed by an aerodynamically designed inlet. The hub/annulus wall diameter ratio is 0.5, with the diameter of the annulus-wall equal to 0.932 m. The inlet guide vane which consists of 45 blades is followed by the rotor. The rotor which consists of 21 blades is driven by a 37.29 kW variable speed motor through a belt and pulley system. The motor is driven by an eddy current drive and "Dynamatic Adjusts Speed" control system. The speed of the motor can be continuously varied from 175 to 1695 rpm with accurate and precise control. The speed of the rotor can be held constant to ± 1 rpm even with normal fluctuations in line voltages. The shaft reaching from the rotor to the data transmission system is hollow to accommodate the electrical and pneumatic lines from the probes as well as the traversing mechanism system which is described later. Downstream of the rotor and inside the rotating hub is located the probe traversing mechanism. The rotating hub is followed by a stator with 25 blades. The stator is followed by a Joy axial-flow fan with variable blade setting for the variation of pressure rise and mass flow. This enables the operation of the compressor at various flow coefficients. The facility is terminated downstream by an aerodynamically designed throttle which provides an additional control of the stage operating characteristics. The throttle is lined with perforated metal with fiberglass backing to attenuate the noise from the auxiliary fan.

Table 1 lists some of the relevant data of the compressor stage. A detailed discussion of the axial flow research compressor facility is given by Lakshminarayana (1980). Good peak efficiencies are exhibited

Table 1. Axial-Flow Compressor Facility Specifications and Operating Conditions

Particular	Facility Specifications
Number of Blades	43-IGV, 21-Rotor, 25-Stator
Outer Diameter of Rotor	0.929 m
Hub/Tip Ratio	0.5
Blade Element	Modified NACA 65 Series (See Table 2)
Tip Clearance (Average)	0.254 cm at $Z = 0.750$ 0.2870 cm at $Z = 0.979$
Rotor Drive Power	37.29 kw
Auxiliary Fan	Series 1,000 Joy Airvane Fan #0 to #16 Blade Setting, Fan Diameter = 0.9652 m
Fan Drive Power	37.29 kw
Particular	Operating Conditions
Inlet Static Pressure	-5.321 cm of H_2O
Inlet Velocity	29.04 m/s
Flow Coefficient	0.56
Rotor Speed	1066 RPM
Average Pressure Rise Coefficient	0.486
Rotor Lift Coefficient	0.524

by the rotor and the performance curve of the compressor is given in Figure 3. Design details of the inlet guide vane, rotor, and stator blade row can be found in Smith (1956).

2.2 The Compressor Rotor

The rotor used for the reported measurements has 21 cambered and twisted blades. It was designed by Smith (1956) using the cascade data of Herrig et al. (1957). The rotor has a tip diameter of 0.929 m and a hub/annulus wall diameter ratio of 0.5. The blades have a varying stagger angle and blade chords along the radius. The rotor blade geometry at various locations is shown in Figure 4 and relevant details are given in Table 2. The blades are cast from aluminum with tee-shaped roots and are attached to the hub at the design pitch angle.

To evaluate the blade element properties and to determine the blade static pressure distribution, one of the blades is instrumented by static pressure taps. The pressure leads from the rotating blade are taken to a stationary data acquisition system through a 20-channel scanivalve and a three-channel pressure transfer device. This system is illustrated in Figure 2.

All measurements reported have been conducted at a rotor speed of approximately 1060 rpm. Slight variation of this speed was necessary to maintain the operating flow coefficient (ϕ) of 0.56. The speed of the rotor was monitored by a photocell circuit which used a 60 slot calibrated disk mounted on the rotor shaft. The output of the photocell circuit was displayed on an electronic counter.

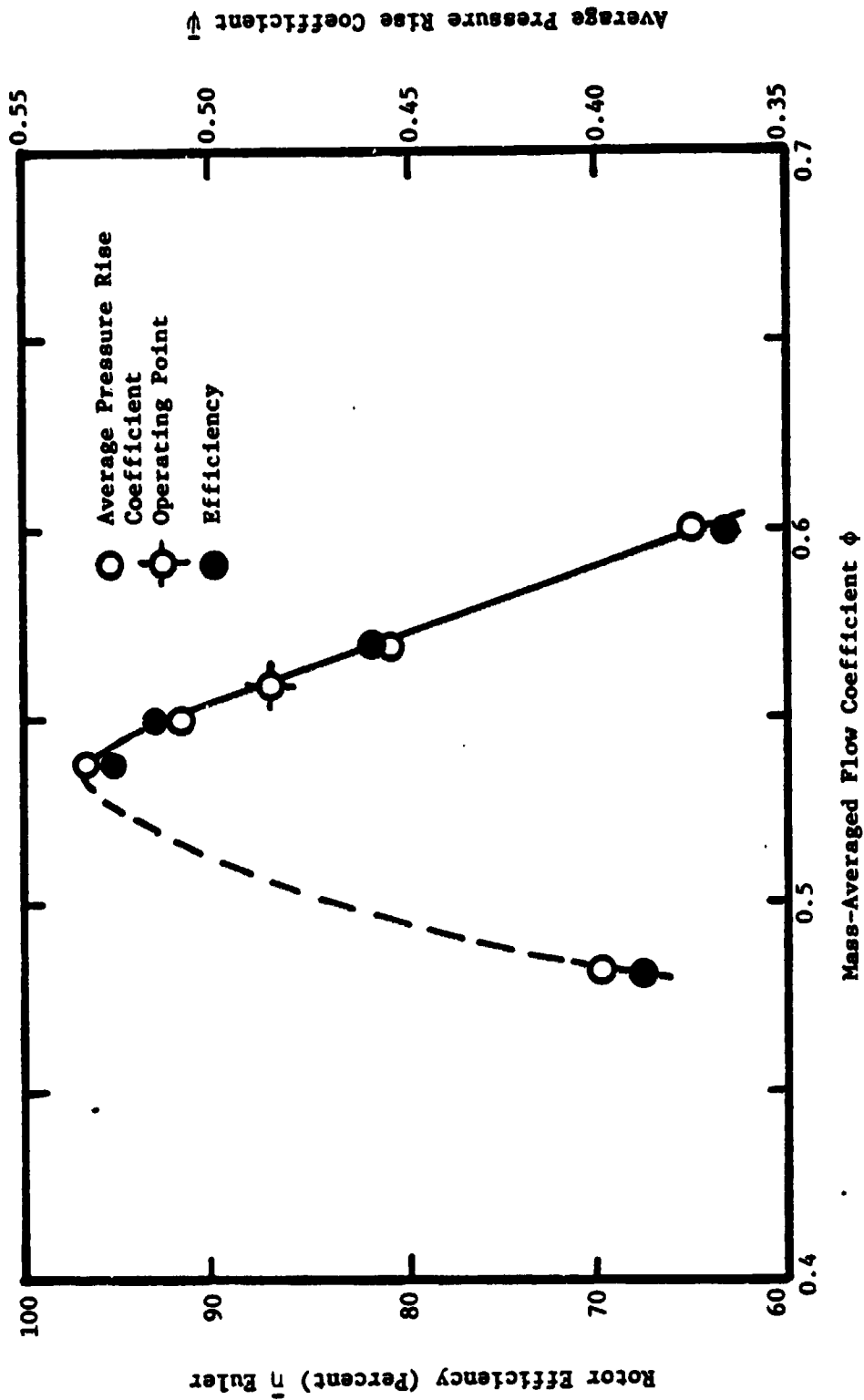


Figure 3. Performance Curve of the PSU Axial-Flow Compressor

ORIGINAL PAGE IS
OF POOR QUALITY

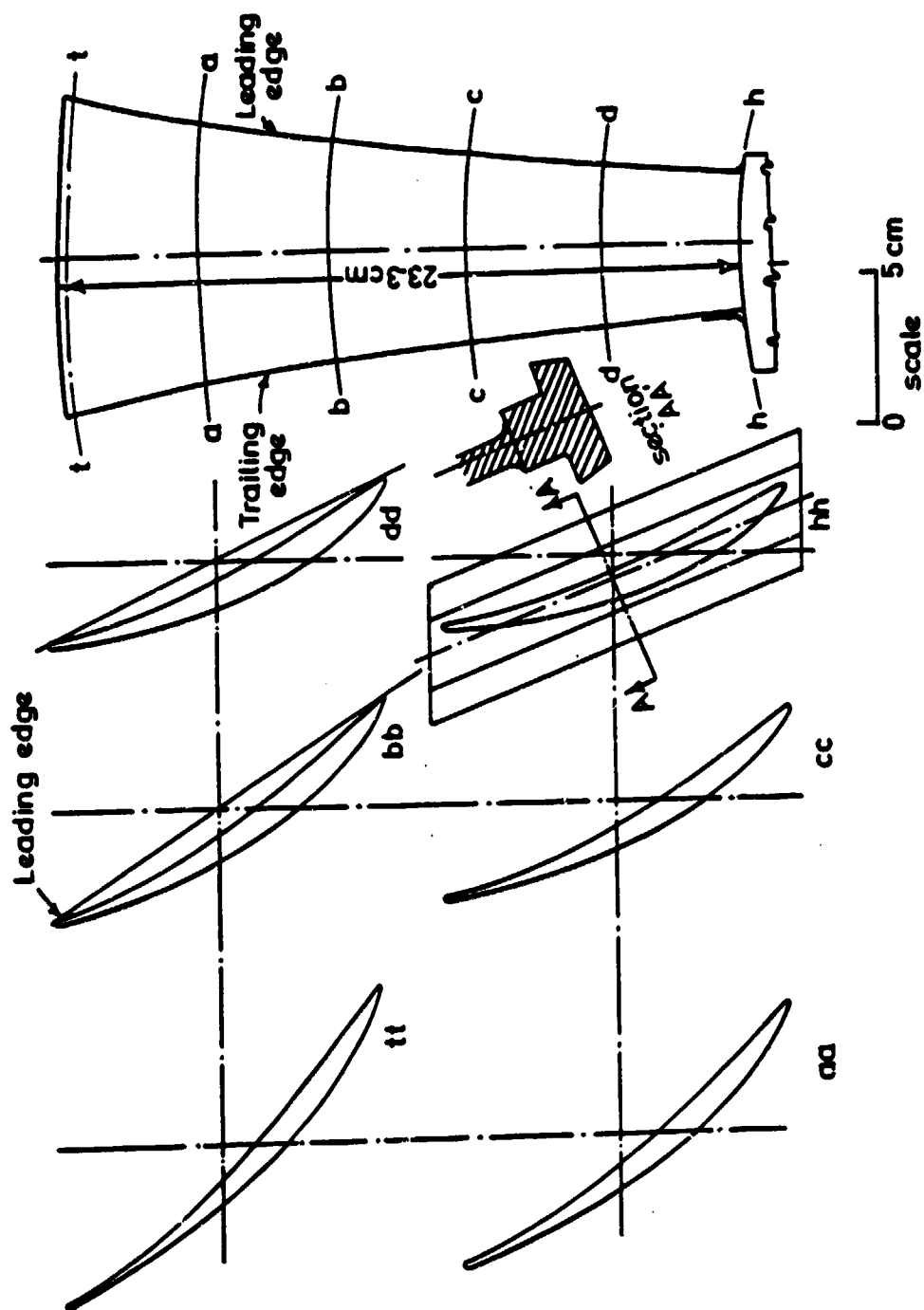


Figure 4. PSU Axial-Flow Compressor Rotor-Blade Geometry.

Table 2. Blade Element Details

Particulars	RADIUS RATIO																	
	Inlet-Guide-Vane						Rotor						Stator					
	0.5	0.6	0.7	0.8	0.9	1.0	0.5	0.6	0.7	0.8	0.9	1.0	0.5	0.6	0.7	0.8	0.9	1.0
Chord, C (cm)	5.19	6.63	7.64	8.64	9.80	10.95	12.39	13.25	13.68	14.41	15.41		8.83	10.37	12.09			
Spacing, S (cm)	3.46	4.61	4.90	5.47	6.05	6.91	6.91	8.35	9.80	11.24	12.68	14.12	5.76	6.91	8.35	10.66		
Camber Y (deg) (C_{10} for Rotor & Stator)	5.0	6.0	16.0	24.0	32.0	45.0	1.35	1.45	1.50	1.50	1.48	1.32	1.70	1.40	1.05	0.80	0.50	0.40
Thickness ($t/c \times 100$)	13.0	12.0	10.5	9.50	8.50	8.00	9.50	9.10	7.60	6.50	5.90	5.10	9.35	8.75	8.30	7.70	6.80	6.50
Stagger Angle, λ (deg)	----	----	----	----	----	----	22.5	26.0	28.5	34.0	39.0	45.0	16.5	24.0	31.0	37.0	42.0	50.0

2.3 Probe Traverse Mechanisms

2.3.1 Rotating Probe Traverse Gear

One unique feature of the research facility is the traverse gear unit for the rotating probe measurements which was developed by Ravindranath (1979). This unit enables a tangential traverse of the three-sensor hot-wire during rotation of the rotor blade row. This mechanism was employed for the data acquisition in the rotor blade passage.

The probe traversing mechanism, shown in Figure 5, consists of a Slo-Syn motor of 1.59 Nm torque driving a 3.81 cm diameter shaft through a 20:1 planetary gear train. The gear train steps down the circumferential travel 1.80 degrees/step to 0.09 degrees/step. The radial and axial movement of the probe was accomplished manually. The shaft and motor of the traverse mechanism are along the axis of the compressor which minimized the balancing problem. The shaft carries a rider upon which the probe and counterbalance weight are mounted. The mounting block provides two degrees of freedom. Alignment of the probe in any desired yaw position was accomplished by rotating the probe about its own axis. The movement of the probe in the radial and axial direction was locked during the rotation of the rotor. This traverse assembly is inside the hub and does not interfere with the flow in the compressor annulus. The probe support traverses across slots in the hub which are lined with an adhesive foam to prevent substantial flow disturbances from occurring due to the slots. The electrical cables from the probe are brought through the rider into the hollow shaft along the axis of the machine and connected to data transmission system shown in Figure 2.

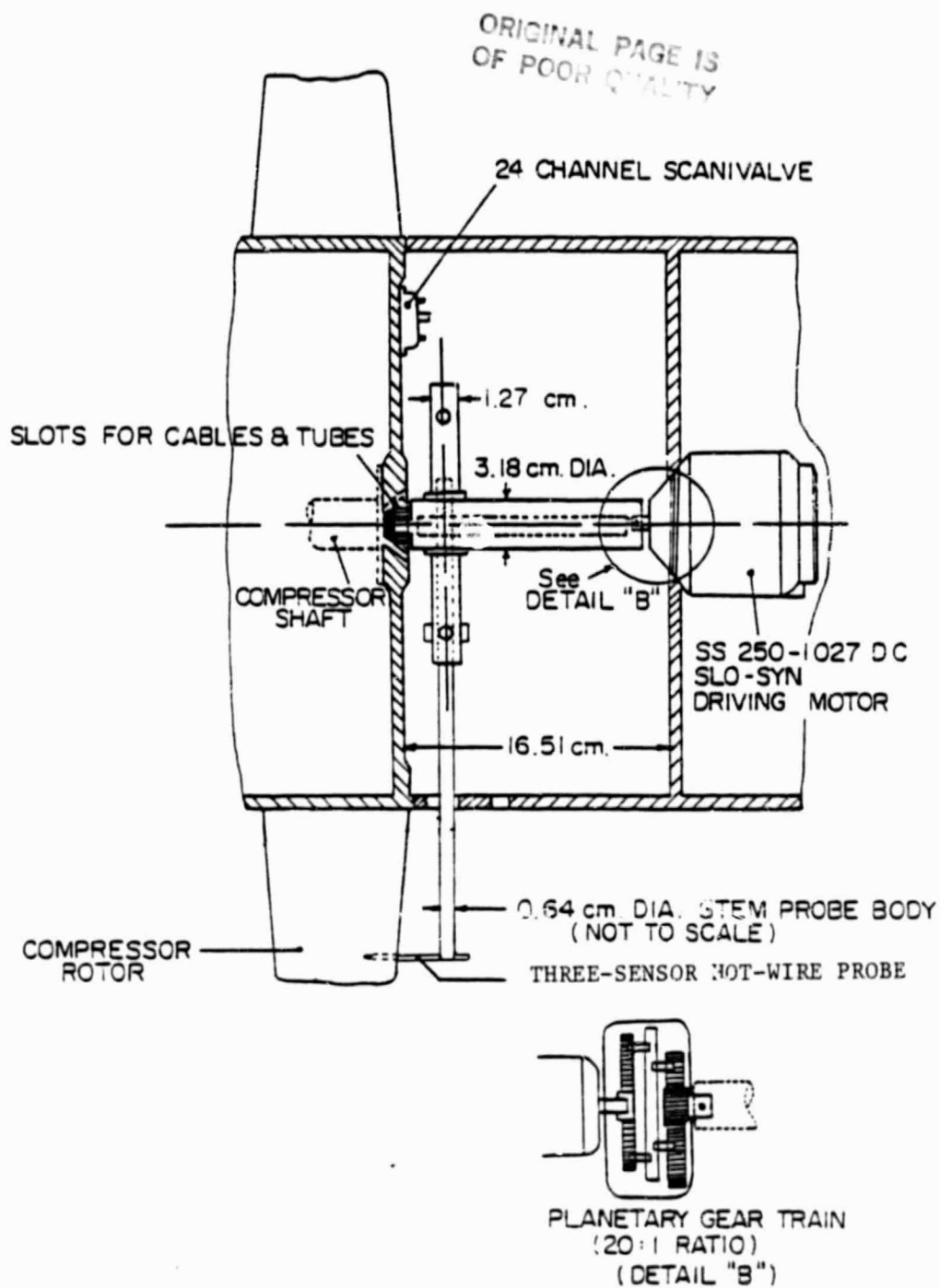


Figure 5. Rotating Probe Traverse Gear.

2.3.2 Stationary Probe Traverse Unit

The traverse mechanism used for the rotor annulus-wall exit flow survey is shown in Figure 2. This mechanism is mounted on a traverse assembly which allows accurate movement of the entire assembly in the axial and tangential directions. The probe traverse mechanism provides an angular and radial movement of the probe. The radial movement is precise with an accuracy of ± 0.0025 cm and the angular movement is precise with an accuracy of $\pm 0.1^\circ$. This entire assembly provided an accurate movement of the probe for the exit-flow in the stationary frame of reference.

2.4 Data Transmission System

Hot-wire signal transmission was accomplished by a conventional co-axial cable in the stationary frame of reference. However, during the rotation of the probe a more complicated situation existed. The probe actuating mechanism electrical signal and the hot-wire signal had to be transferred from the rotating frame of reference to the stationary frame of reference. Described below are the mechanisms used to accomplish the signal transferring.

2.4.1 Brush Slip-ring Unit

A commercial eight-channel slip-ring unit was used to transmit the electrical signals from the stationary indexing unit to the rotating traverse gear motor. The electrical continuity from the stationary frame to the rotating frame of reference was provided by carbon brushes in contact with a rotating commutator. The brush

slip-ring unit was mounted next to the pressure transfer device. The conduit in the rotor shaft which carried the hot-wire co-axial cables also carried the electrical cables for the brush slip-ring unit.

2.4.2 Mercury Slip-Ring Unit

A ten-channel mercury slip-ring unit made by the Meridian Laboratory, Inc. was used to transmit the hot-wire signals from the rotating, tri-axial hot-wire probe to the stationary hot-wire anemometer and the data acquisition system. This unit is shown in Figure 6. Each channel consists of a thin disk rotating in a small housing which is partially filled with triple distilled mercury. The shear pumping effect of the rotating disk carries the mercury to the gap between the housing and the disk where it acts as a conductor. The signals from the tri-axial hot-wire probe are transferred from the inner shaft through the rotating disk and the mercury pool to the stationary conductors on the casing of the slip-ring unit. This unit provided an extremely low noise-to-signal ratio. It also provided a negligibly small distortion of the amplitude and frequency characteristics of the hot-wire signal. This is reported in more detail in Chapter 3. In addition, the system was calibrated both statically and dynamically to ensure accuracy.

2.5 Rotor Passage-Flow Probe and Instrumentation

2.5.1 Three-Sensor Hot-Wire Probe

The rotor passage-flow measurement technique described below was developed by Poncet and Lakshminarayana (1973). Figure 7 shows the three-sensor hot-wire probe used for all the rotating hot-wire measurements. In this figure the orientation of each sensor to the probe

ORIGINAL PAGE IS
OF POOR QUALITY

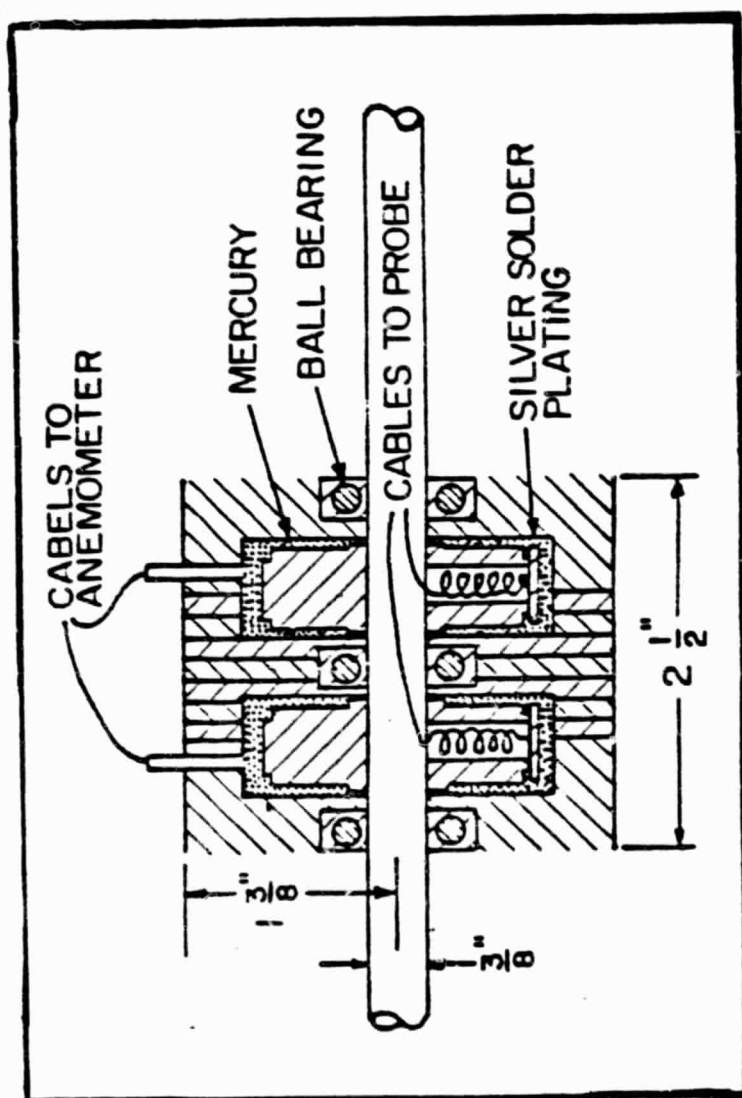
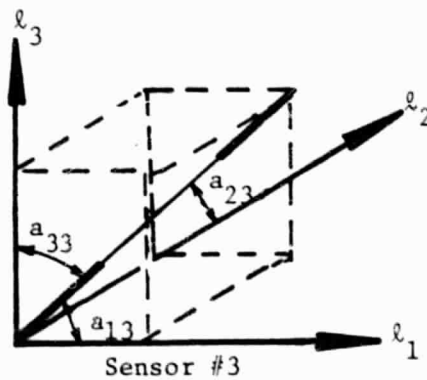
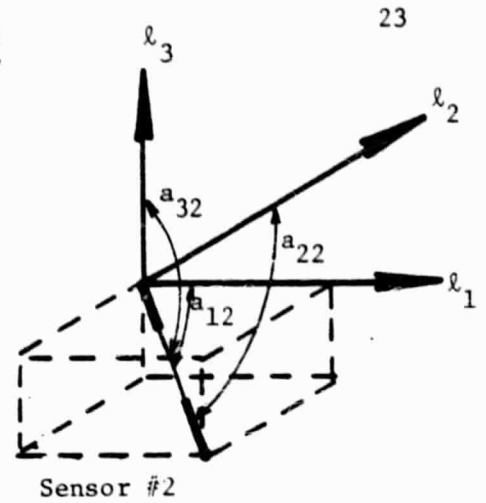
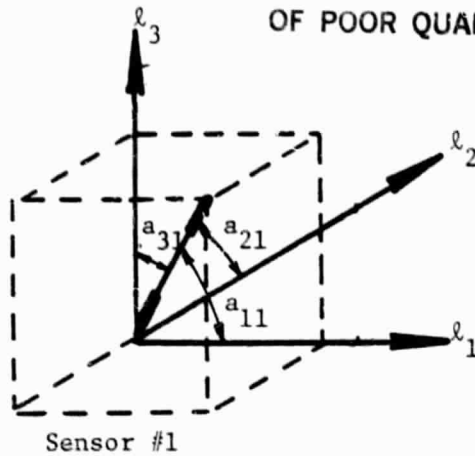


Figure 6. Mercury Slip-Ring Unit of Data Transmission System.

ORIGINAL PAGE IS
OF POOR QUALITY

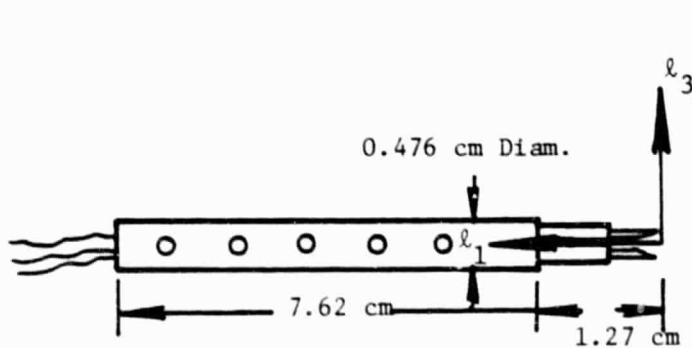


Direction Cosine, a_{ij} , where

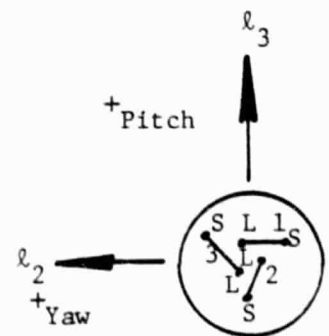
i = Coordinate

j = Wire Direction

(see Table 4)



(l_1, l_2, l_3) - Probe Coordinate System



L = Long Prong

S = Short Prong

Figure 7. Three-Sensor Hot-Wire Probe for Axial-Flow Compressor Annulus-Wall Passage-Flow Measurements.

coordinate axis is given as well as the dimensions of the probe. The probe sensors were constructed out of tungsten wire which was copper coated to allow easy handling of the sensor. The middle third of the each wire was etched to expose the tungsten sensor which yielded a length-to-diameter ratio of 135. Only having the middle third of the wire etched reduced the error introduced in measurement due to prong interference. Each sensor also had a resistance of approximately 4.50 ohms. A simultaneous calibration of the three sensors was performed employing a low turbulence open-jet calibration facility. These calibrations were corrected for the variation of temperature and aging of the wire. A detailed investigation of the response of this probe in the rotating measurement environment is reported in Chapter 3.

2.5.2 Signal Processing Equipment

The rotating hot-wire probe system illustrated at the left-hand side of Figure 8 shows the instrumentation used for the rotating tri-axial hot-wire probe. This system provided three mean voltages and nine RMS values of fluctuating voltages. These were processed using the method of Gorton and Lakshminarayana (1976) to derive the three components of mean velocity, turbulence intensity, and shear stress in any coordinate system.

The output of the three DISA Model 55M01 anemometer consisted of three d.c. signals and three a.c. signals. The d.c. signals were a measure of the mean velocity and the a.c. signals were a measure of the turbulence sensed by each wire. The d.c. signals were measured by a HP Model 5327B timer counter digital voltmeter with an accuracy of 1

ORIGINAL PAGE IS
OF POOR QUALITY

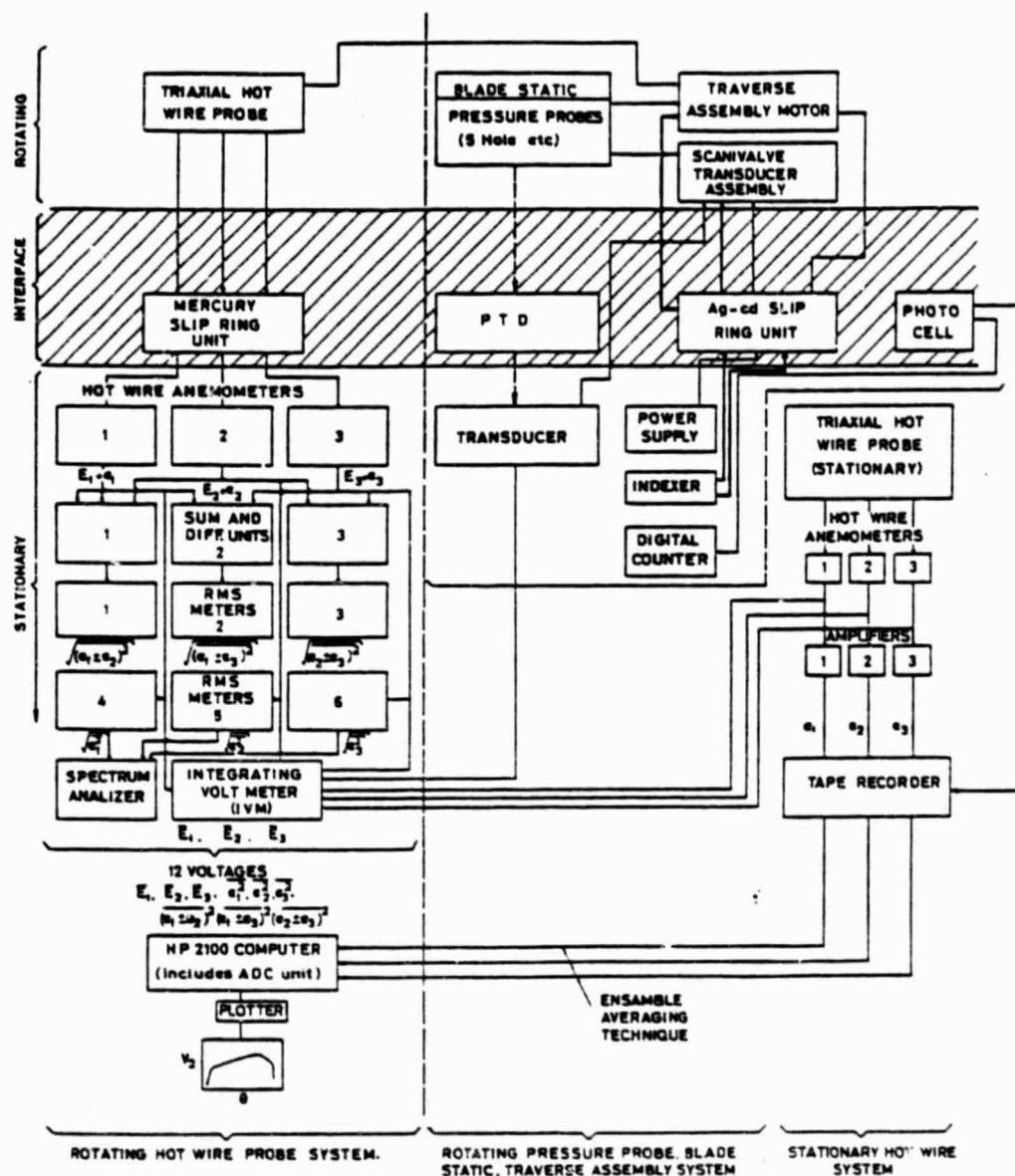


Figure 8. Schematic of Instrumentation for Hot-Wire Measurements.

millivolt. The a.c. signals were measured by a DISA type 55D35 RMS meter using a 30 second integration time. To evaluate the Reynolds stress component in the flow, a model AD 530 analog sum and difference unit was used. The three sum and difference signals were channeled through a selector switch to a DISA type 55D35 RMS meter for measurement using a 30 second integration time.

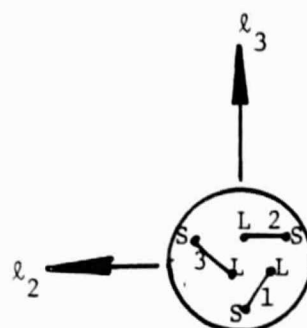
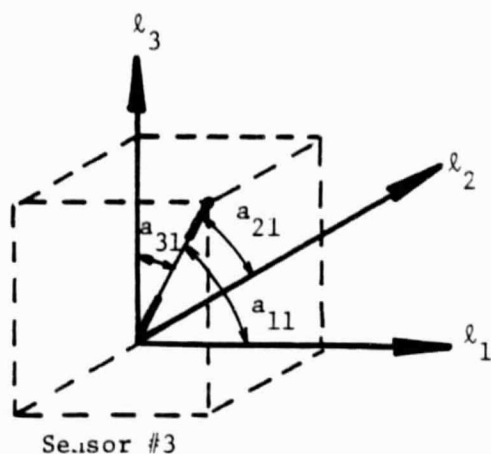
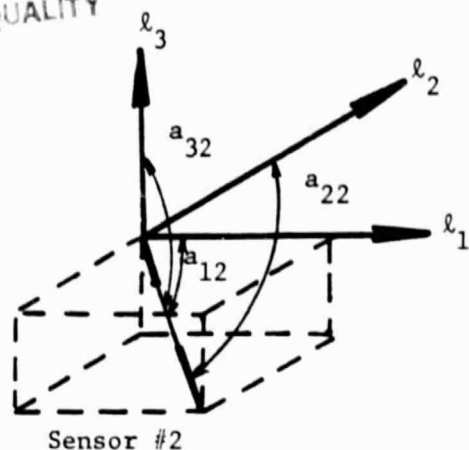
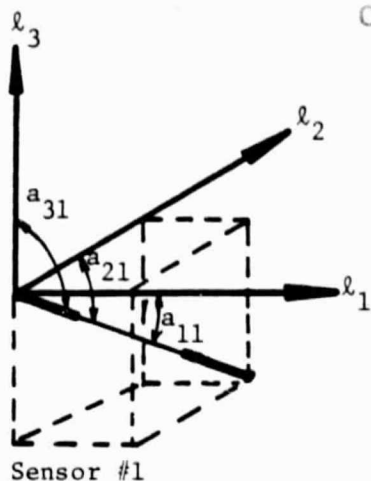
A four-channel Tektronix type RM561A storage oscilloscope was employed to display all three instantaneous output of the anemometers and the tachometer pulse. Turbulence spectral measurements were performed utilizing a Ubiquitous Spectrum Analyzer-Averager model UA-500-1 in conjunction with a Tektronix type 531 oscilloscope and a HP 7044A x-y recorder. All spectra were taken at 10 KHZ on a 0db scale.

The hot-wire measurements were found to be very sensitive to ambient conditions as well as to the physical constraints imposed on the probe. The DISA type 55M01 anemometer compensates for instabilities in the sensing circuit through a cable compensation unit. This unit was adjusted to compensate for the bridge unbalance caused by the differences in cable parameters (BNC connections and mercury-slip-ring unit).

2.6 Rotor Exit-Flow Probe and Instrumentation

2.6.1 Three-Sensor Hot-Wire Probe

The three-sensor hot-wire probe employed for the rotor exit annulus-wall flow measurements is shown in Figure 9. This miniaturized tri-axial hot-wire probe was manufactured by DISA. It had tungsten sensors which were etched in the center to minimize prong interference



(see Table 4 for values of a_{ij})

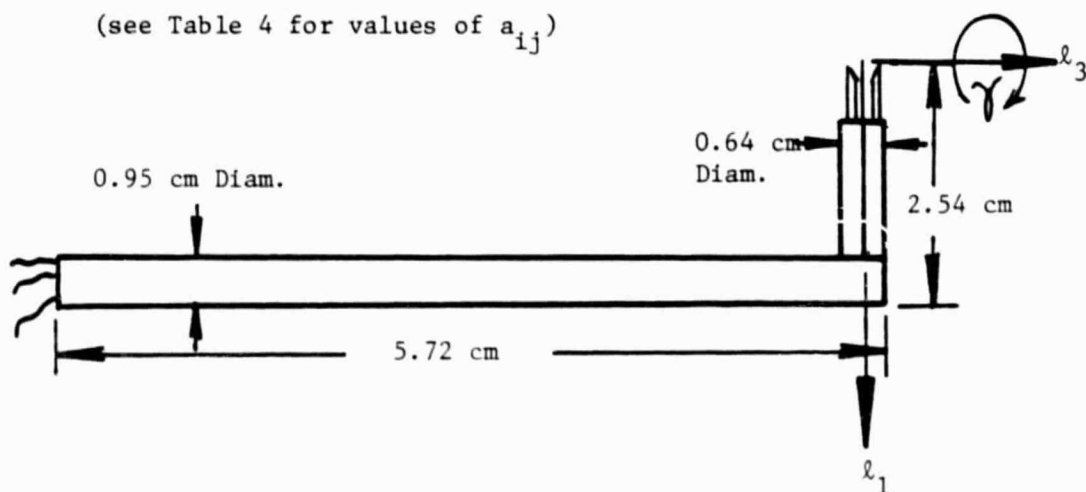


Figure 9. Three-Sensor Hot-Wire Probe for Axial-Flow Compressor Annulus-Wall Exit - Flow Measurements.

effects. The length-to-diameter ratios of the sensors were 300 and each sensor had a resistance of approximately 4.10 ohms. The probe calibration was performed employing a low turbulence open-jet calibration facility. The resulting calibration was corrected for temperature variation and aging of the sensor.

2.6.2 Signal Processing Equipment

The stationary probe measurement technique described below was developed by Poncet and Lakshminarayana (1973). The stationary hot-wire probe system illustrated at the right-hand side of Figure 8 shows the instrumentation used for the stationary tri-axial hot-wire probe measurements. The sensors were connected to three DISA 55M10 constant-temperature anemometer units. The signals of these anemometers were channeled to an integral digital voltmeter to obtain the overall mean voltage of the anemometer output. The fluctuating a.c. signals were amplified and recorded with a SAVRE IV FM signal recorder/reproducer at a tape speed of 15 i.p.s. The center frequency of recording was 43 KHZ and the frequency of the signals could vary from 0 to 10 KHZ. A specific position behind the rotor was identified by referring to a pulse generator which was installed on the compressor axis. This pulse generator provided one sharp pulse for each revolution of the rotor row. Each of the rotor passage-flows could be identified with the pulse signal. An ensemble average was obtained for the specific passage-flow of interest. All three instantaneous anemometer output signals and the pulse signal were displayed on a Tektronix type RM 561A storage oscilloscope.

Due to the high rotational speed of the rotor (1060 rpm) and number of rotor blades (21), one survey of a blade passage requires very little time (0.0027 second). This gives an impractically high sampling speed; therefore, the analog signal was digitized at 1/16 real time. The H.P. 7900 A.D.C. unit was used for this analog-to-digital conversion. The digitizing was performed at a tape reproduction speed of 1/16 i.p.s. This was based on the number of points required to represent adequately the passage-flow. The digitized hot-wire signal was converted to a corresponding instantaneous cooling velocity. The instantaneous flow velocity was obtained from the cooling velocities of the three sensors using hot-wire equations. The various mean and turbulent flow characteristics were obtained statistically with these instantaneous velocities. A detailed discussion of the data processing procedure is given by Reynolds and Lakshminarayana (1979).

CHAPTER III

THREE-SENSOR HOT-WIRE PROBE ACCURACY AND LIMITATIONS

3.1 Background

The hot-wire is one of the most commonly used probes in experimental fluid mechanics. Since its introduction as a measuring instrument, many investigations have been made into the principles and applications of the instrument. Despite the great quantity of this work, Kovaszny's (1959) remark that, "The method has more the caprice of an art than the complete reliability of a convenient routine laboratory procedure" has not yet lost its validity. However, with proper care in calibration procedures and applications, precise and accurate data can be obtained.

The hot-wire sensor in conjunction with a constant temperature anemometer unit provides unique capabilities which to date are only rivaled by the laser doppler velocimeter (LDV). Because of various limitations of the LDV such as very high cost, ambiguities related to the scattering particles, and errors introduced by continuous tracking signal processing units, the hot-wire anemometer will most likely remain a primary instrument for velocity measurements. The hot-wire does, however, have many of its own limitations, some of which cannot be eliminated, e.g., the need for the sensor and its support to be located in the flowfield and the nonlinearity of the anemometer output. An investigation of the consequences of these two aspects as applied

to the measurement environment of the reported experimentation is presented in the following sections.

The Penn State group has successfully developed methods of measuring the mean and turbulence properties of the flowfield in the passage and at the exit of a rotating blade. These methods utilize a rotating hot-wire probe and are presented by Lakshminarayana and Poncet (1974) and Gorton and Lakshminarayana (1976). The flow properties in a turbomachinery passage are usually steady when they are viewed in the relative frame of reference. The measurement of the properties of the annulus-wall flow and of the rotor wake was conducted using hot-wire probes with multiple sensors that were rotating with the blade passage. The accuracy of the hot-wire system and the response of the sensors rotating with the blade passage have been a concern of the Penn State group. Various sources of error in hot-wire measurements with the three-sensor probe have been discussed by Lakshminarayana and Poncet (1974) and Anand (1976). These discussions give an excellent overview of the errors associated with various aspects of flow measurement. In the following sections the major sources of error associated with a rotating probe environment and a directionally varying flowfield are discussed.

The investigation of the annulus-wall flowfield reported in this thesis was conducted experimentally employing a three-sensor hot-wire probe and three constant-temperature anemometer units. This measurement system was employed in a rotating scheme where the probe was rotated inside the rotor blade passage. The three-sensor probe was fixed in an angular position relative to the blade row and traversed tangentially

across the blade passage. Due to the nature of this set-up and the presence of the annulus-wall flow phenomena, such as the tip leakage vortex and secondary flow, the probe experienced a varying flow incidence angle during the experiment. The variation of the incident flow was not known "a priori." Thus, it was necessary to determine the response of the three-sensor hot-wire probe when exposed to a directionally varying flowfield.

To facilitate measurement of the annulus-wall flowfield behind the rotor blade passage, an ensemble-average technique was employed to separate the periodic signal embedded in a random signal from the three-sensor hot-wire probe. The position of the probe with respect to the absolute velocity vector in this region was a factor in determining proper system response. The effect of varying the incident direction of the absolute velocity vector with respect to the probe was also investigated.

The rotation of a three-sensor hot-wire probe in a turbomachinery passage has additional complications not encountered in stationary usage. The hot-wire sensors are exposed to centrifugal forces which may modify the response of the sensors. This could occur through a deformation or straining of the sensors under centrifugal acceleration. Also, the transmission of the sensor signal from the rotating frame of reference to the stationary or laboratory frame of reference requires an additional handling of the signal. In the experiments conducted, a mercury slip-ring unit was employed to transfer the hot-wire signal from a rotating to a stationary frame of reference. These additional aspects of employing a three-sensor hot-wire probe in a rotating turbomachine passage were investigated.

3.2 Data Transmission System Response

An initial investigation into the use of the hot-wire probe in the rotating flow passage had been conducted in the three-bladed Penn State inducer by Gorton and Lakshminarayana (1976). One problem experienced had been the inability of the slip-ring unit to maintain the continuity of the hot-wire circuitry. This did not permit suitable operation of the hot-wire probe for the duration of the experiment. This arrangement was improved upon by Gorton (1974) by employing a mercury slip-ring unit. Through the usage of this unit, it was found that hot-wire probes were suitable for the measurement of the mean and fluctuating relative velocities. The present study was an investigation of the accuracy of the data transmission system when a mercury slip-ring unit was employed for the annulus-wall flow measurement.

A ten-channel mercury slip-ring unit was used for the experimental investigation reported in this thesis. This unit acted as an interface for the three-sensor hot-wire probe signal between the rotating and the stationary frame of reference. It was of extreme importance that the signal be transmitted without attenuation or discontinuity since such phenomena will modify the anemometer output to give erroneous results. One problem encountered had been a varying resistance dependent upon the rotation of the slip-ring core. This was highly undesirable and was found to be due to contaminated mercury. With the possibility of errors of this type, it was decided that a dynamic determination of the system response was necessary. The present study was an investigation of the data transmission system response in the rotating mode of operation.

The ten-channel mercury slip-ring unit is shown in Figure 6. Contact between the rotating wires and the stationary contact screws is made through a round contact disc to which the rotating wire is connected which is immersed in mercury. Triple-distilled mercury was used to provide the greatest conductivity and the lowest possible noise level distortion.

A test signal for the dynamic system response was generated from a wide range oscillator and a d.c. offset unit. The resulting test signal consisted of a sinusoidally varying signal with an a.c. and d.c. component. The a.c. and d.c. components of the signal could be varied in magnitude as well as in frequency. The test signal was generated with the following characteristics:

a.c. component = 0.049 volts (RMS)

d.c. component = 2.466 volts

frequency = 1,000 cycles/second

The test signal was analyzed before and during rotation by a storage oscilloscope, a d.c. digital voltmeter, a true r.m.s. voltmeter, and a spectrum analyzer.

The characteristics of the test signal given above were found to remain invariant during the dynamic testing of the slip-ring unit. This indicated that the test signal was transmitted by the slip-ring without modification. To determine a more precise response of the system, the signal was processed by a spectrum analyzer before and during rotation. A peculiarity in the system's response would appear on the spectrum at its characteristic frequency which would be related to the rotational speed of the slip-ring core. The test signal spectra

before and during rotation are shown in Figure 10. There was no change in the test signal spectra during the dynamic test. The small perturbations upon the baseline were due to the signal generator. The dynamic testing was conducted for all channels of the slip-ring and similar results were obtained.

The suitability of employing a mercury slip-ring unit as an interface between the hot-wire's rotating frame of reference and the laboratory's stationary frame of reference was thus found to be excellent. Proper precautions must be observed in employing the mercury slip-ring unit, however, such as using triple-distilled mercury and conducting a dynamic test of the system's response.

3.3 Effect of Rotation on a Three-Sensor Hot-Wire Probe

The mechanical and aerodynamic effects of rotation upon the response of a three-sensor hot-wire probe were determined to investigate the accuracy of the rotating probe measurements. The hot-wire output voltage depends on the characteristics of the measuring environment and on the properties of the wire. The heat transfer equation for the hot-wire relates the Nusselt, Prandtl, and Reynolds number. The Prandtl number is nearly constant for the measurement environment of air. The Reynolds number depends upon the fluid flow velocity, the wire diameter, and the viscosity of the fluid. In the stationary frame of reference, the output of the hot-wire anemometer is mainly dependent upon the Reynolds number through the fluid flow velocity. The heat transfer between the wire and the flow is related to the Nusselt number.

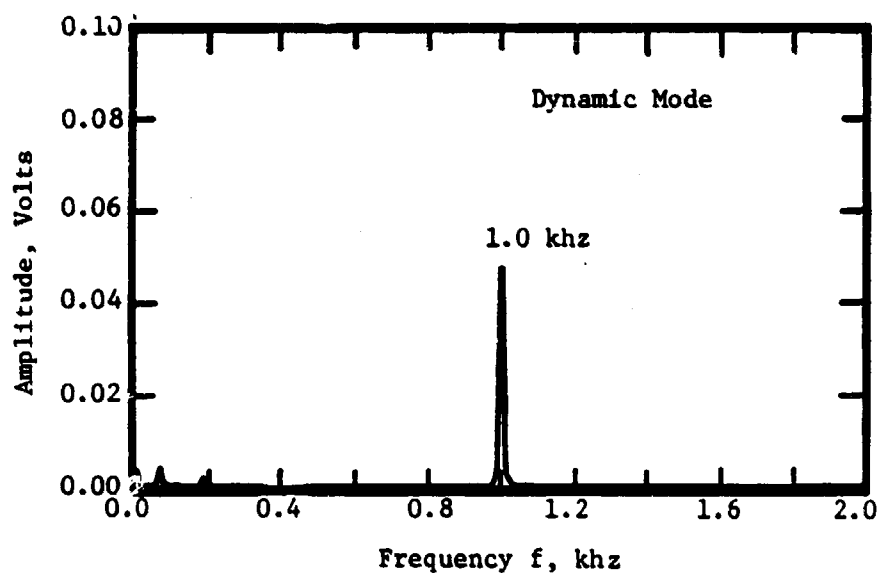
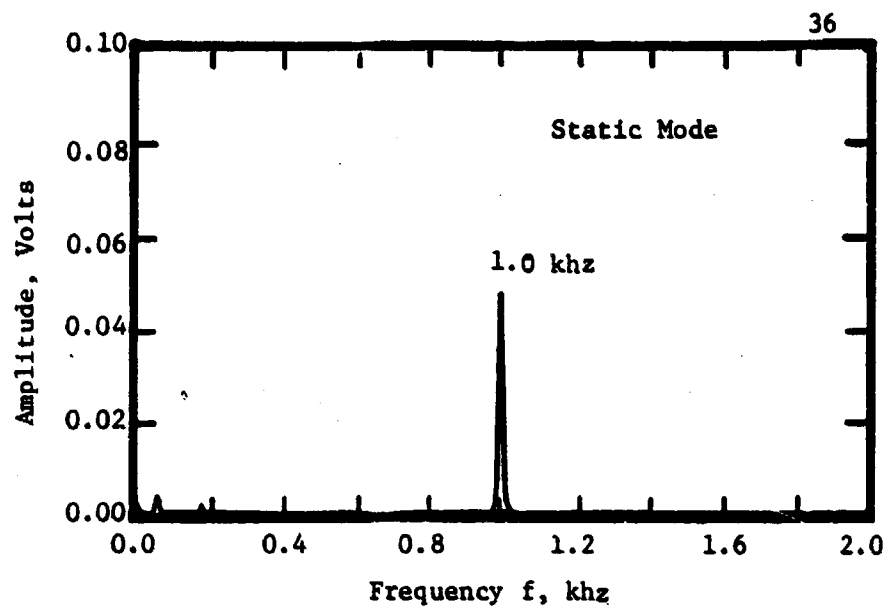


Figure 10. Spectra of Mercury Slip-Ring Test Signal.

For the rotating hot-wire, it has been suggested that additional parameters relating to rotationally induced forces be included. Such parameters are the Rossby number which is the ratio of the inertia to Coriolis forces. In addition, the Coriolis and centrifugal forces could affect the wire response through elongation of the wire, probe vibration, and viscid effects on the flow properties. A primary investigation of the effect of rotation on a rotating single-sensor hot-wire probe was performed by Hah and Lakshminarayana (1978). This investigation reported a negligible effect on the fluid mechanics, heat transfer, and material characteristics of the single-sensor hot-wire probe. However, the investigation by Hah and Lakshminarayana (1978) considered a sensor placed in only one orientation with respect to the centrifugal acceleration vector and was carried out over a limited range of velocities and relative speeds. The annulus-wall flow measurements were performed using a three-sensor hot-wire probe at a considerably higher rotational speed. Thus it was necessary to determine the effect of a higher rotational speed on multiple sensors at varying orientations to the centrifugal acceleration vector.

The experimental set-up used in this investigation was similar to that employed by Hah and Lakshminarayana (1978). A thick-walled hollow shaft was attached to a rigid horizontal base by means of pillow blocks. To one end of the shaft was attached a mercury slip-ring unit which transferred the electrical signal of the hot-wire. The noise-to-signal ratio of the mercury slip-ring was nearly zero. On the other end of the shaft was attached the probe holder which could allow for a radial variation of the probe location and a balancing counterweight.

The shaft was driven by a V-belt between the pillow blocks by a 0.56 kw variable-speed motor mounted underneath the base plate. A photo-cell/disc system was used to measure the angular velocity of the probe accurately. The photocell output, which was approximately a 2 volt d.c. pulse, was directed to an electronic counter. Three DISA constant-temperature anemometers were used in this experiment in conjunction with a switching circuit and digital voltmeter. The three-sensor hot-wire probe employed is shown in Figure 11. The length-to-diameter ratios of the three sensors were all approximately 300.

A reference calibration was conducted using a conventional open-jet wind tunnel in the stationary frame of reference. To determine the effects of rotation, a dynamic calibration was performed in the rotating frame of reference, the resistance of the sensors was monitored throughout the velocity range, and a comparison between the velocity vector sensed by the probe in both reference frames was determined. To obtain the information, the probe was rotated in a position aligned with the direction of motion. The rotational speed of the probe was varied from 700 to 1500 r.p.m., at a fixed radial location of the probe. This corresponded to a centrifugal acceleration ranging from 250 to 1100 g.

For the stationary reference calibration and the rotational tests, the ambient fluid properties remained constant. A comparison between the probe calibrations for the stationary and rotating frames of reference is presented in Figure 12. For the calibration, the following equation was used to relate the anemometer voltages to the sensor cooling velocities:

$$E^2 = E_o^2 + B U_{eff}^n \quad (1)$$

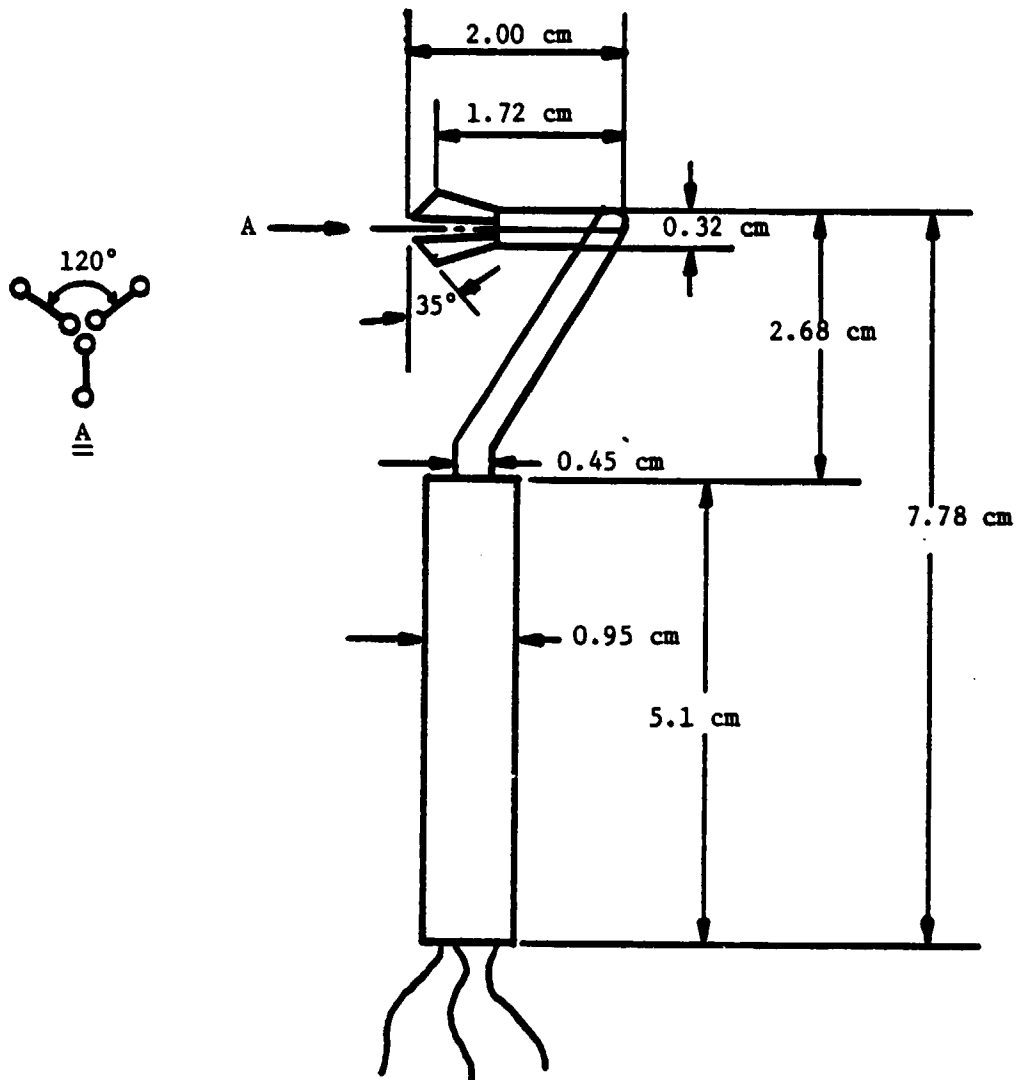


Figure 11. Three-Sensor Hot-Wire Probe for Rotation Effect Investigation.

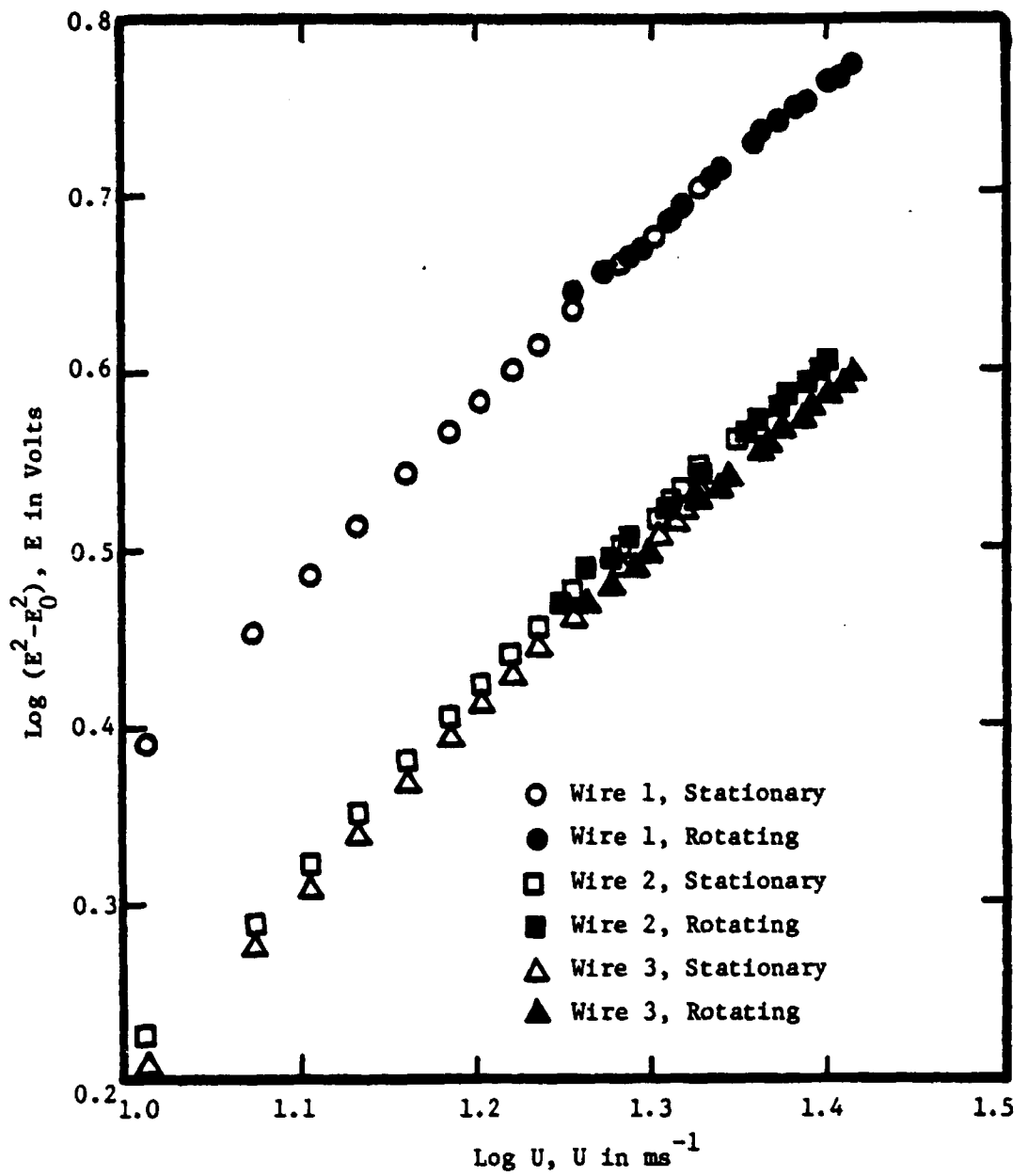


Figure 12. Three-Sensor Hot-Wire Probe Static and Dynamic Calibration.

where E is the voltage corresponding to the effective cooling velocity U_{eff} and E_0 is the voltage corresponding to zero velocity. The constants B and n are characteristic of the calibration. It is evident from Figure 12 that the stationary and dynamic calibrations are identical and no apparent influence due to rotation is observed. To determine further the accuracy of employing a stationary calibration curve to rotating probe data, a comparison of measured velocities is given in Figure 13. Here the total velocity sensed by the rotating three-sensor hot-wire probe based on the wind tunnel calibration curve ($\bar{U}_{\text{measured}}$) is compared with that directly calculated from the known rotational speed Ωr , where Ω is the angular velocity and r is the radial location of the probe. There is a very good correspondence between these velocities. This indicates that there is a negligible error associated with employing a stationary calibration to rotating three-sensor data. An anticipated phenomenon of sensor elongation was not observed through the monitoring of the sensor resistances. All three sensors were found to maintain their initial stationary values of resistance. If elongation had occurred due to the centrifugal force, a rise in sensor resistance would have been observed. The extremely small mass of the sensor probably made this effect negligible. All three sensors of the probe were found to respond with accuracy in the rotating frame of reference. The orientation of the sensors to the centrifugal acceleration vector was found to be of no consequence for this particular probe configuration.

In summary, the effect of rotation on a three-sensor hot-wire probe was found to be negligible. However, caution should be exercised in

ORIGINAL PAGE IS
OF POOR QUALITY

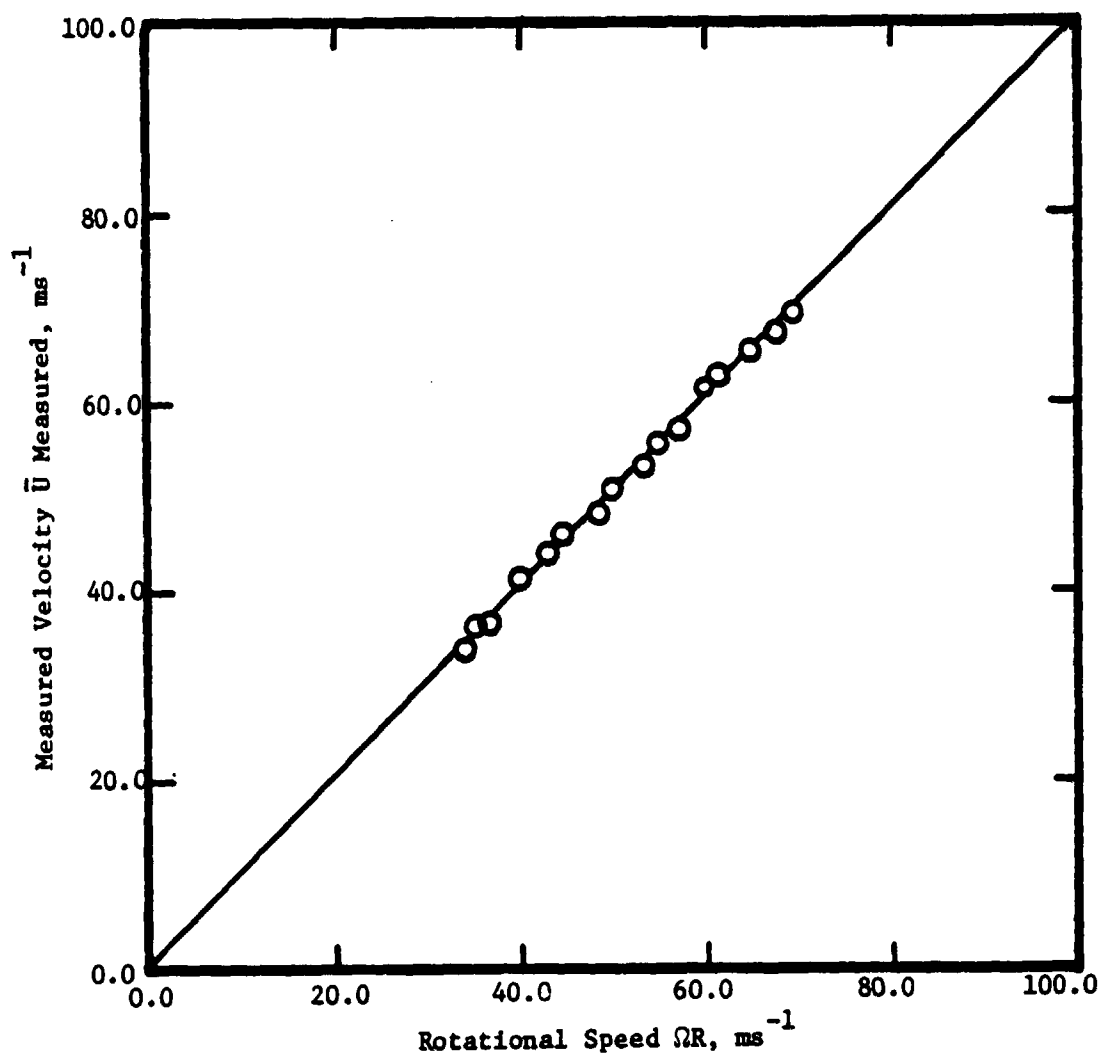


Figure 13. Comparison of Measured Velocities of Static and Dynamic Calibration.

extrapolating these results to higher rotational speeds and/or larger sensor length-to-diameter ratios where a higher centrifugal force exists or the mass of the sensor.

3.4 Sensitivity of Single- and Three-Sensor Hot-Wire Probes to Yaw and Pitch Angles

For highly turbulent flows, flows of a swirling nature, and situations where a hot-wire probe is placed in a flowfield with appreciable fluctuations in the flow angle, the response of the probe cannot be assumed to be the same as that during its calibration. In these situations or when the direction of the incident flowfield is not known "a priori" it is necessary to determine the accuracy of the probe when the incidence angle varies or when the probe is yawed and pitched with respect to the calibration flow. It has been the experience of the Penn State group that when the incident flowfield deviates from the axis of symmetry of the sensitivity cone formed by the three sensors, an error is introduced. An additional error due to the yaw and pitch angle of the probe is the interference effect. This effect is due to the complex geometry of the sensors and the resultant wakes of the prongs, sensors, and stems when the axis of the probe deviates from the incident flowfield direction.

The prongs and the probe body affect the hot-wire measurement in two ways. First, a change in the flow velocity vector near the wire occurs due to an obstruction of the flow. Second, the heat transfer rate of the sensor is altered. The obstruction of the flow due to the probe stem can be eliminated by choosing a probe configuration where

the sensors are located many stem diameters upstream from the probe stem. The effect of the flow disturbance due to the prongs and the sensors cannot be eliminated; however, their effect can be minimized to an acceptable degree. The major parameters which influence this error are the prong-to-wire diameter, ratio the prong length-to-diameter ratio, and the spacing between the prongs. Vagt (1979) has determined that a probe which employs tapered prongs considerably reduces this interference effect. A careful consideration of the above parameters with respect to the flowfield under investigation yields a probe configuration which poses a minimal disturbance to the flowfield. This results in a minimal loss of accuracy in the sensor's response.

The heat transfer rate of the sensors cannot be assumed to be independent of the probe configuration. The interference effect of the three-sensors and a variable flow direction during measurement leads to a situation where the accuracy of the probe diminishes at specific angles of yaw and pitch. This inaccuracy may be generated by the shed wakes of the prongs and the thermal wakes of the sensors which impinge upon the other sensors and their prongs. These thermal wakes result in a change of the heat-transfer characteristics of the sensors which were assumed during calibration. The nature of this interference is characteristic to each geometrically different probe. However, for each probe, the response of the probe was observed to be a function of its yaw and pitch angle relative to the flowfield. The investigation reported here is an attempt to define the specific behavior of the sensor response and to formulate a correlation for relating the sensor response to the yaw and pitch angle of the probe. This investigation

was a necessary prelude to meaningful data acquisition of the annulus-wall flowfield employing a three-sensor hot-wire probe. The flowfield in the annulus-wall region is highly complicated and is the result of the interaction of the tip-leakage flow, annulus-wall boundary layer, secondary flow, and scraping vortices.

3.4.1 Experimental Set-Up and Procedure

The investigation of the probe's response was performed in the potential core of a 30.5 centimeter-diameter circular jet of low turbulence intensity. A constant velocity of 32.3 meters per second was maintained to an accuracy of $\pm 0.1\%$. The temperature variation of the air was limited to ± 0.2 deg. C. The hot-wire probes were operated at a constant temperature employing three DISA Model 55M10 anemometer units. Overheat ratios $((R_w - R_\infty)/R_\infty)$ of 0.5 were used and the bridge output voltage was recorded using a digital voltmeter and true r.m.s. meter. The probes were of the copper-coated tungsten type where the center section of the wire was etched to expose the sensing tungsten wire. An initial investigation concerning the response of single-sensor probes of varying configuration to yaw angle sensitivity was also performed. These probes were of similar construction. The values of the sensor diameter d_s , the length-to-diameter ratio of the etched portion of the sensor l_e/d_w , and the ratio of the support needle diameter to the probe stem diameter d_p/d_s , are given for the various probe types in Table 3.

The experimental apparatus was similar to that employed by Friehe and Schwarz (1968). With this set-up the three-sensor probe was yawed

Table 3. Single-Sensor Probe Specifications

Particulars	Probe		
	A	B	C
Type	single-sensor	single-sensor	slant single-sensor, wire angle = 54.7 deg.
etched length of sensor-to-sensor diameter ratio (l_e/d_s); $d_s = 0.003048$ mm	150.0	116.7	158.3
prong length-to-probe stem diameter ratio (l_p/d_s)	4.00	2.00	4.00
prong diameter-to-probe stem diameter ratio (d_p/d_s)	0.128	0.250	0.128
prong diameter	tapered 0.1016 mm tip 0.6096 mm base	127 mm	tapered 0.1016 mm tip 0.6096 mm base

± 40 degrees and pitched ± 30 degrees with an accuracy of ± 0.5 degrees. At each position the anemometer output was recorded. The single-sensor experiments were performed with the pitch angle set at 0 degrees and a yaw angle variation of ± 90 degrees. Prior to this test, all the probes were calibrated in a 2.54 square centimeter calibration tunnel for a velocity range from 11.0 to 51.8 meter per second employing the same instrumentation. During the calibration and experiment, the output of the anemometer at zero flow velocity incident to the sensor was checked to detect any drift due to ambient resistance changes of the sensor.

3.4.2 Sensitivity of the Single-Sensor Hot-Wire Probe

It is illustrative to first show the effect of varying yaw angle upon the response of several single sensor probes. Figure 14 shows the response of probes A, B, and C of the configurations indicated in Table 3. The probes were rotated through a yaw angle of ± 90 degrees at 5 degree increments. This yaw angle corresponds to the deviation angle or the angle between the incident flow direction and the normal to the hot-wire sensor. At each deviation angle the normalized cooling velocity U_N was calculated. U_N is the ratio of the effective cooling velocity at yaw angle α , $U_{eff}(\alpha)$, to the effective cooling velocity at zero yaw angle, $U_{eff}(0)$. As is shown in Figure 14, the sensor configuration has a significant effect upon the response of the sensor even for the simple configuration of a single-sensor probe. In this case, the interference effects due to the prongs of other sensors and the thermal wakes of the other sensors, as with the three-sensor probe, are nonexistent. However, substantial deviations from the cosine law (solid line) are observed.

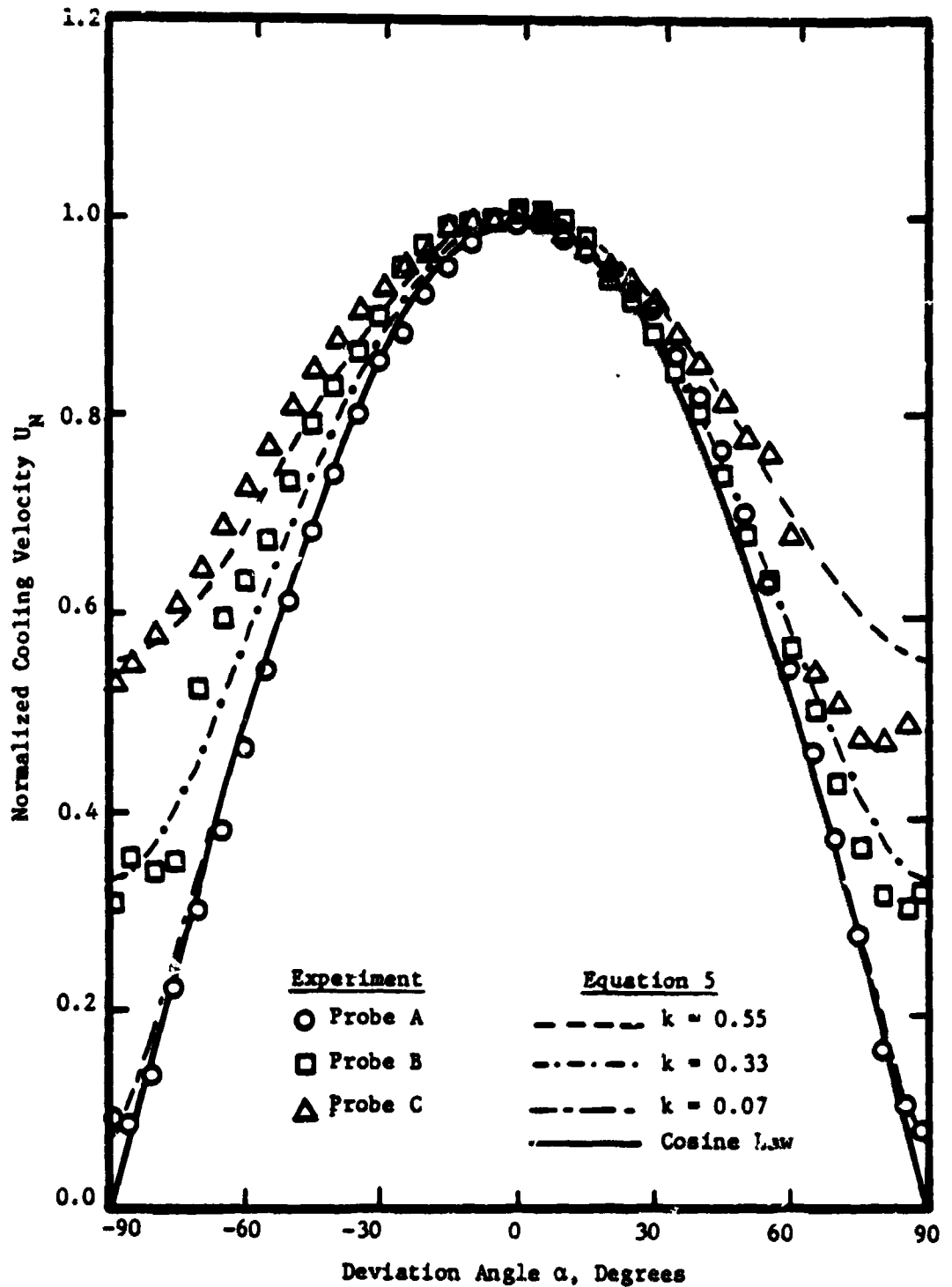


Figure 14. Single-Sensor Probe Response to Yaw Angle Variation.

The effective cooling velocity sensed by the sensor was derived according to the heat-transfer law formulated by King (1914). The output of the anemometer E is related to the velocity, U_{eff} , normal to the wire, by:

$$E^2 = A + B U_{eff}^n \quad (2)$$

where the exponent n and the constant B are determined during calibration. The constant A was taken to be equal to square of the anemometer output with no incident flow (ambient conditions), E_0^2 . In regard to the yaw dependence, Prandtl (1946), and Jones (1947) determined that for an infinite heated cylinder only the velocity component normal to the cylinder was effective in the cooling. This is the component used during calibration. During exposure to a yawed incident flow the effective cooling velocity, U_{eff} , is related to the incident velocity U_1 , by a yaw sensitivity function, $f(\alpha)$. For the case of an infinite cylinder this sensitivity function is given by:

$$f(\alpha) = \cos \alpha \quad (3)$$

where α is the angle between the incident velocity and the normal to the wire. The effective cooling velocity U_{eff} is therefore related to the incident velocity U_1 by:

$$U_{eff} = U_1 f(\alpha) \quad (4)$$

If no deviation from the cosine law, equation (3), occurred the data presented in Figure 14 would lie on the solid line.

Hinze (1959), Webster (1962), and Champagne et al. (1967) realized that for finite wires a correction to the cosine law must be employed in the yaw sensitivity function to account for deviations from the cosine law. They suggested the following yaw sensitivity function:

$$f(\alpha) = (\cos^2 \alpha + k^2 \sin^2 \alpha)^{1/2} \quad (5)$$

where k is a small parameter accounting for the component of velocity parallel to the wire. This velocity component would contribute to the cooling of the sensor with a sinusoidal function dependence of a small amount, thus the correction was derived. The small parameter k was found to vary with the sensor length-to-diameter ratio l_e/d_w as would be expected since the component of velocity parallel to the wire cools the sensor an amount related to the available surface area which is proportional to the length and diameter of the wire.

Friehe and Schwarz (1968) have proposed a yaw sensitivity function of the form:

$$f(\alpha) = [1 - b(1 - \cos^{0.5} \alpha)]^2 \quad (6)$$

where b is a function of the length-to-diameter ratio of the wire and the deviation angle α . In an attempt to explain these trends, and to examine the sensor response in water, Roberts et al. (1975) generalized this expression to:

$$f(\alpha) = [1 - b(1 - \cos^m \alpha)]^2 \quad (7)$$

This generalization was based on observed trends in their data which indicated that a combination of behaviors existed.

The data presented in Figure 14 best fit the expression due to Hize (1959), Webster (1962), and Champagne (1967). This yaw sensitivity function is shown plotted against the experimental data with values of the small parameter k varying between the probes as indicated. The variation of k and the shape of the deviation of the data is a consequence of the geometry of the sensor. As reported by other investigators, the value of k was seen to increase with decreasing l_e/d_w . This can be seen by comparing probes A and B. Also, the value of k was seen to increase as the sensor prongs were shortened and thickened thus increasing the aerodynamic disturbance due to these prongs at higher values of yaw angle. This can be seen by comparing probes A and B.

The shape of the yaw sensitivity function is dependent upon the geometry of the sensor. Even with the simple configuration of the single-sensor, considerable deviations were observed to occur. The investigation reported above is fundamental to the evaluation of the sensitivity of the three-sensor hot-wire where complex geometries and aerodynamic and heat-transfer phenomena exist.

3.4.3 Sensitivity of the Three-Sensor Hot-Wire Probe

The sensitivity of a three-sensor hot-wire probe to varying angles of yaw α and pitch β angle was investigated to determine the nature and magnitude of errors involved. The configuration of the three-sensor hot-wire probe used for this investigation is shown in Figure 7. Also, the direction of positive yaw and pitch angle is indicated. The mechanism described previously was employed to yaw and pitch the probe in 5-degree increments. In this way, a mapping of the individual sensor

response was obtained for a range of ± 40 degrees of yaw angle and ± 30 degrees of pitch angle. From the data the total incident velocity U_T sensed by the probe was derived. This velocity was then compared to the reference velocity U_{ref} of the calibration jet at its potential core which had a value of 30.5 m/s. Initially, each sensor of the probe had been individually calibrated with the calibration jet normal to the sensor. The resultant calibrations were fit to equation (2). The total incident velocity U_T sensed by the probe at various positions of yaw and pitch angle was derived using these calibrations.

Figure 15 shows the response of the three-sensor hot-wire probe at various positions of yaw α and pitch β angle. Each curve represents the response of the probe for various values of β at one value of α . The probe response is given as the ratio of U_T -to- U_{ref} . The left hand scale is the value of U_T/U_{ref} based upon the individual sensor calibration described above and the right hand scale is the value of U_T/U_{ref} based upon a combined sensor calibration which is described below. The difference in sensor response, based upon either calibration, is illustrated by reviewing the datum point of 0 deg. yaw and 0 deg. pitch. At this point the ratio of U_T/U_{ref} should equal 1.0. However, the individual sensor calibration yields a value of 0.885, which is approximately 11 percent in error. This error associated with an individual sensor calibration has been a recurrent phenomenon experienced by the Penn State group. It is believed to be due to a slight inaccuracy in the measured values of the direction cosines of the sensors. A small deviation in one of the nine direction cosines describing the configuration of the three sensors was found to be reflected in the derived

value of U_T . A cumulative error associated with the nine direction cosines was found to result in an error of the order given above. The methods used for measuring the direction cosines of the sensors were accurate to within 3 percent. These methods were the most precise which could be obtained and are described in Appendix B.

A combined sensor calibration was found to yield more correct values of U_T , given the same direction cosines of the sensors. In this procedure, the probe was placed so that the calibration jet was aligned with the x_1 axis of the probe (Figure 7). The response of each sensor, at this probe position, was fit using equation (2) to the calibration jet velocity which was varied in magnitude. Using this method, all three sensors were simultaneously calibrated at one probe position. This calibration procedure was found to determine accurately the incident velocity sensed by the probe, as indicated by Figure 15.

Figure 15, using the combined calibration scale for U_T/U_{ref} , shows the response of the probe at varying angles of yaw and pitch. The value of U_T was derived from the response of the three sensors, using a cosine law dependence only. This assumes that each sensor senses only the magnitude of the vector component of the incident flow normal to the axis of the wire. The probe response is shown to be accurate at small values of yaw and pitch angle. However, at larger values of yaw and pitch angle, deviations as large as 12 percent of the reference velocity were measured. This type of deviation was observed for the response of the single-sensor hot-wire probe. The response of the three-sensor probe is seen to be slightly asymmetric about the pitch angle β . The deviation from the cosine law, as assumed in deriving

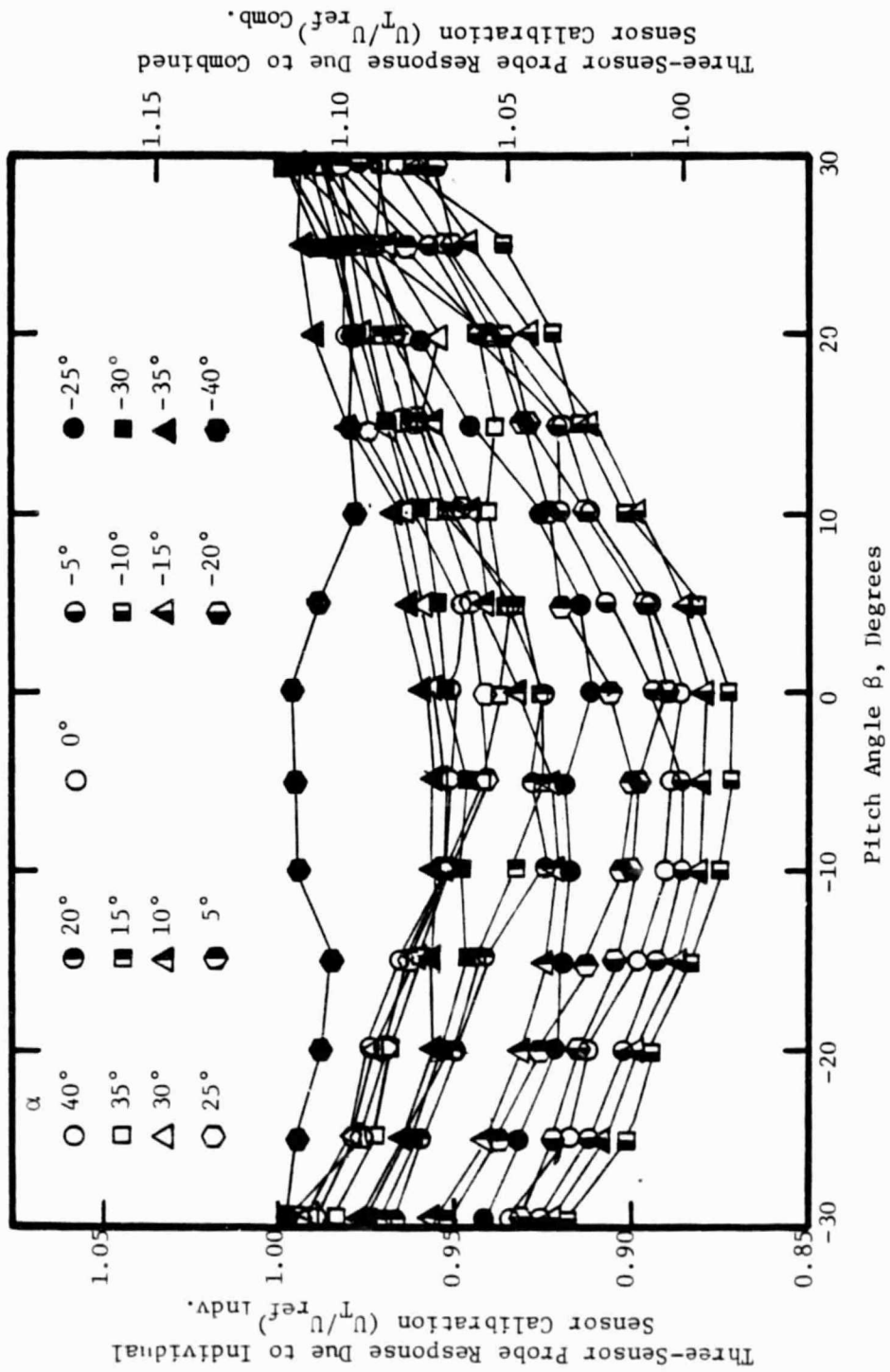


Figure 15. Response of Three-Sensor Hot-Wire to Varying Angles of Yaw and Pitch.

U_T , is seen to increase with increasing values of α and β . This increase in sensor response is partially due to the component of velocity parallel to the sensor. The asymmetric nature of this increase of the measured velocity may be due to the geometry of the probe and the orientation of the three sensors with respect to each other and the incident flow direction. The orientation of the sensor may produce aerodynamic interference effects which contribute to this asymmetric response.

The error ϵ_T between the total velocity (based on combined sensor calibration) sensed by the three-sensor hot-wire probe and the reference velocity is defined by:

$$\epsilon_T = \frac{U_T - U_{ref}}{U_T} \times 100 \quad (8)$$

This error was plotted as function of yaw and pitch angle and is shown in Figure 16. The contours of error indicate that substantial asymmetric deviations from the cosine law occur as the probe is exposed to a directionally varying incident flow. In addition, the probe configuration results in a greater yaw angle sensitivity which is probably due to the orientation of the three sensors. The increase in error at non-zero values of yaw and pitch is due mainly to the component of velocity parallel to the axis of the sensors. The maximum error is 12 percent over the yaw angle range of ± 40 degrees. The error is seen to increase above a level of 4 percent at values of yaw and pitch angle above 10 degrees. This rapid increase in error is due to the small l_e -to- d_w ratio (135) of the sensors. The asymmetric nature of the probe error is

probably due to a complex interaction of the response of all three sensors. This interaction is due to prong interference and the shed thermal wakes of each sensor.

To gain an insight into the complex interaction giving rise to Figures 15 and 16, an investigation of the individual sensor responses was performed. As can be seen by Figure 7, the overall probe configuration is a function of each sensor's position relative to the probe coordinate system (l_1, l_2, l_3). For the orthogonal type configuration of the probe, each sensor should be at an angle of 54.7 degrees relative to the l_1 -axis. This configuration generates a cone of sensitivity for the three sensors. If the flowfield under investigation has a resultant velocity vector which lies in the cone, the sensor will yield correct velocity measurements plus an associated error. If the resultant velocity lies outside this cone, special data reduction schemes must be incorporated. For this investigation, the resultant velocity of the calibration jet always remained within this cone of sensitivity formed by the three sensors. Each sensor was properly located with respect to the incident velocity field.

It is clear from Figure 7, that even at a position of zero yaw and zero pitch angle the sensors are not aligned perpendicularly to the flowfield which is parallel to the l_1 -axis. Each sensor is positioned at an angle which deviates from the l_1 -axis. Sensors 1, 2, and 3 have a deviation angle of 35.99 deg., 31.22 deg., and 44.13 deg., respectively. At the various positions of yaw and pitch, the deviation angles of the three sensors and the associated errors are continually varying. The result of this variation is seen in Figures 15 and 16.

ORIGINAL PAGE IS
OF POOR QUALITY

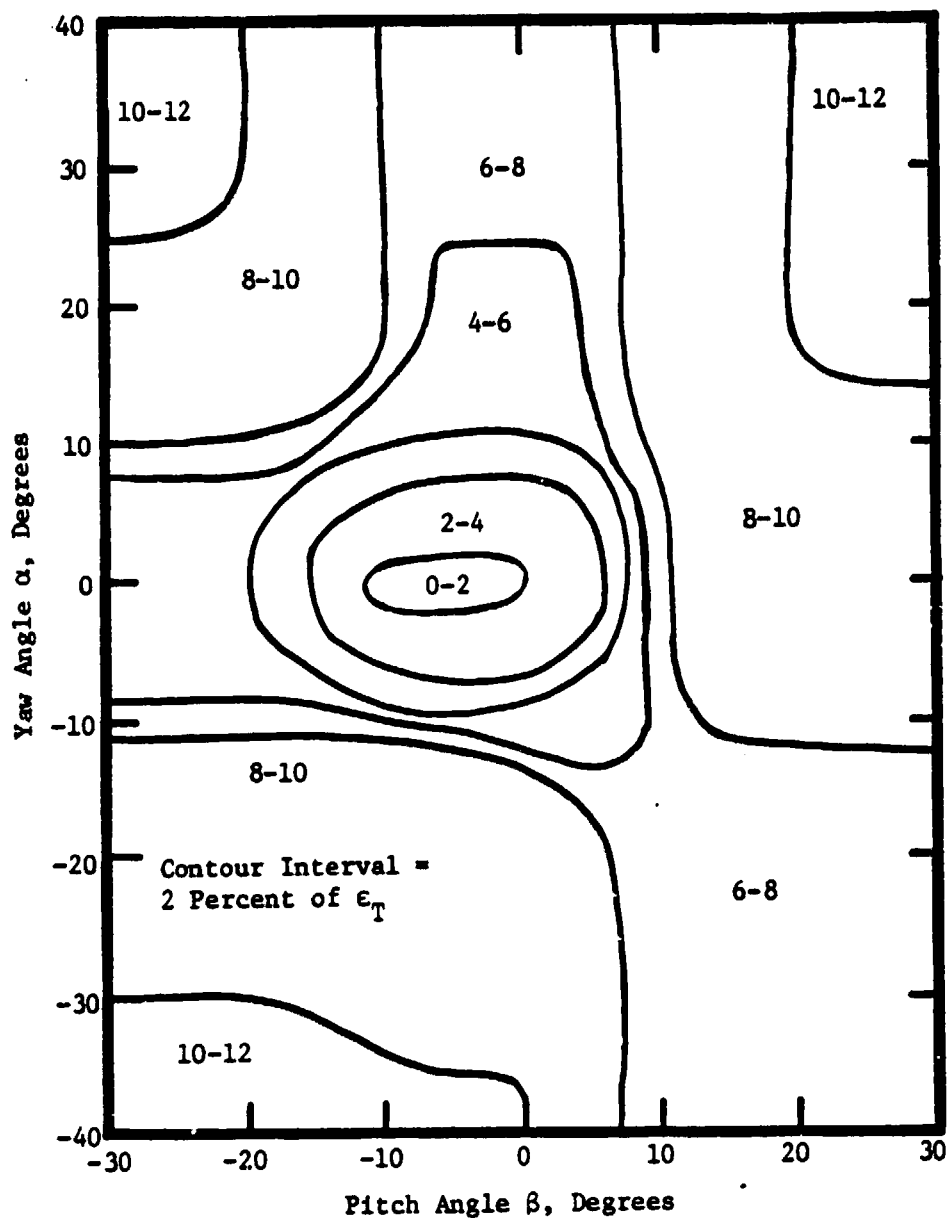


Figure 16. Error of Uncorrected Three-Sensor Hot-Wire Probe Response with Yaw and Pitch Angle Variation.

The response of each sensor was investigated in an attempt for a more precise determination of the nature of the variation in the probe response. The normalized cooling velocity of each sensor $(U_N)_i$, given by:

$$(U_N)_i = \frac{(U_{eff})_i}{(U_{ref})_i} ; i = 1, 2, 3 \quad (9)$$

where i refers to an individual wire, was plotted as a function of the deviation angle λ for each sensor. The deviation angle λ was calculated from our knowledge of knowing the sensor position relative to the probe axis and the yaw and pitch angle. The normalized cooling velocity U_N was calculated from the response of the individual sensor (effective cooling velocity U_{eff}) and the normal component U_{ref} of the calibration velocity vector which was a function of the yaw and pitch angle. The resultant plots are given for sensors 1, 2, and 3 in Figures 17, 18, and 19, respectively. These data are plotted against the cosine law (solid line) for reference. Considerable deviations from the cosine law exist for each sensor and these deviations do not necessarily occur at only high deviation angles. The deviation from the cosine law is also different in character for each sensor.

The deviation in the response of a sensor is a function of the yaw and pitch angle of the probe. This can be seen by observing the trends in the data shown for the sensors. For each sensor the data lie in a band whose width is determined by the yaw and pitch angle. The character of these data bands of the deviation from the cosine law indicates that it is necessary to consider the orientation of each sensor relative to the incident velocity field and the other sensors.

ORIGINAL PAGE IS
OF POOR QUALITY

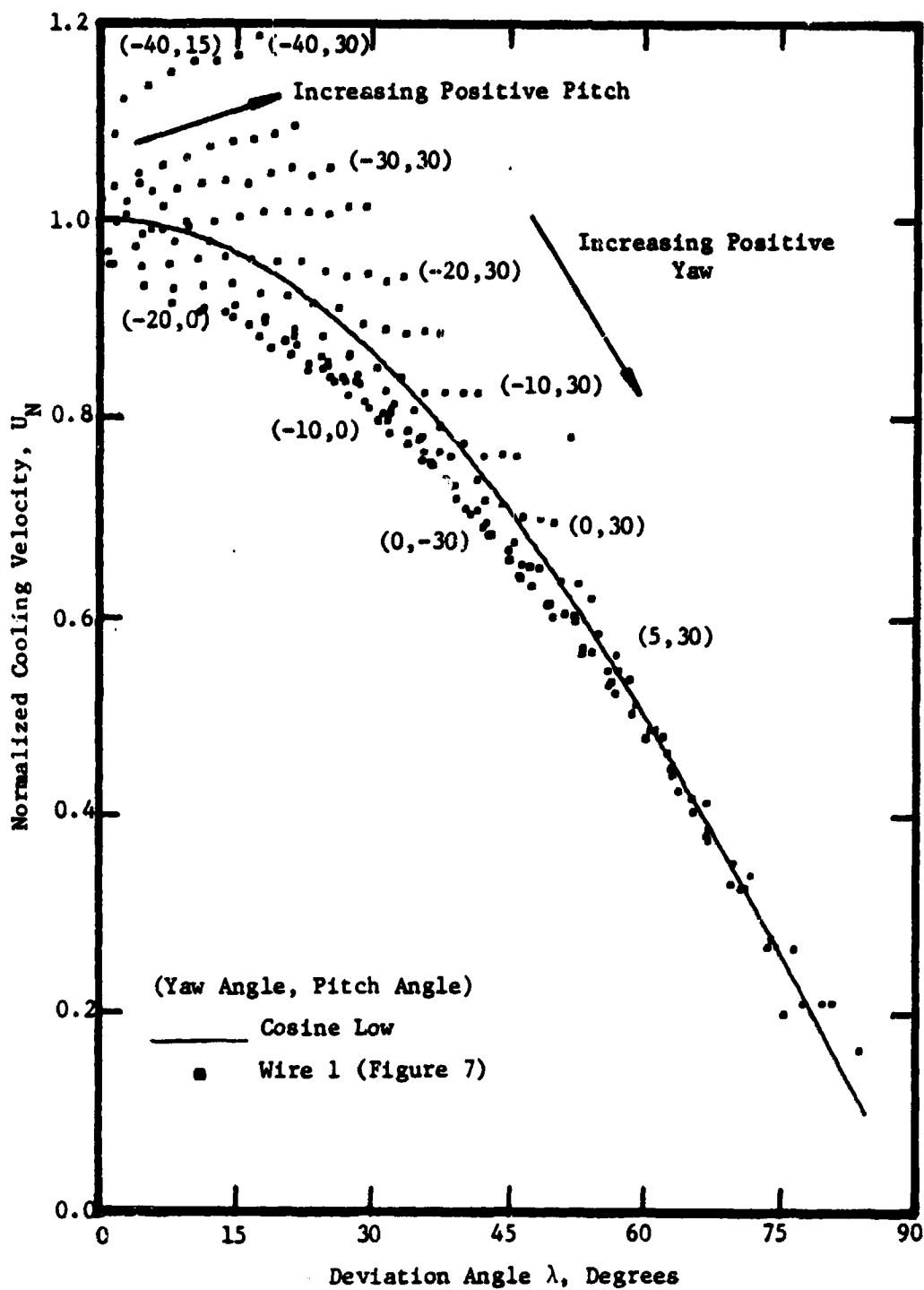


Figure 17. Response of Sensor-One of Three-Sensor Hot-Wire Probe with Flow Deviation Angle Variation.

ORIGINAL PAGE IS
OF POOR QUALITY

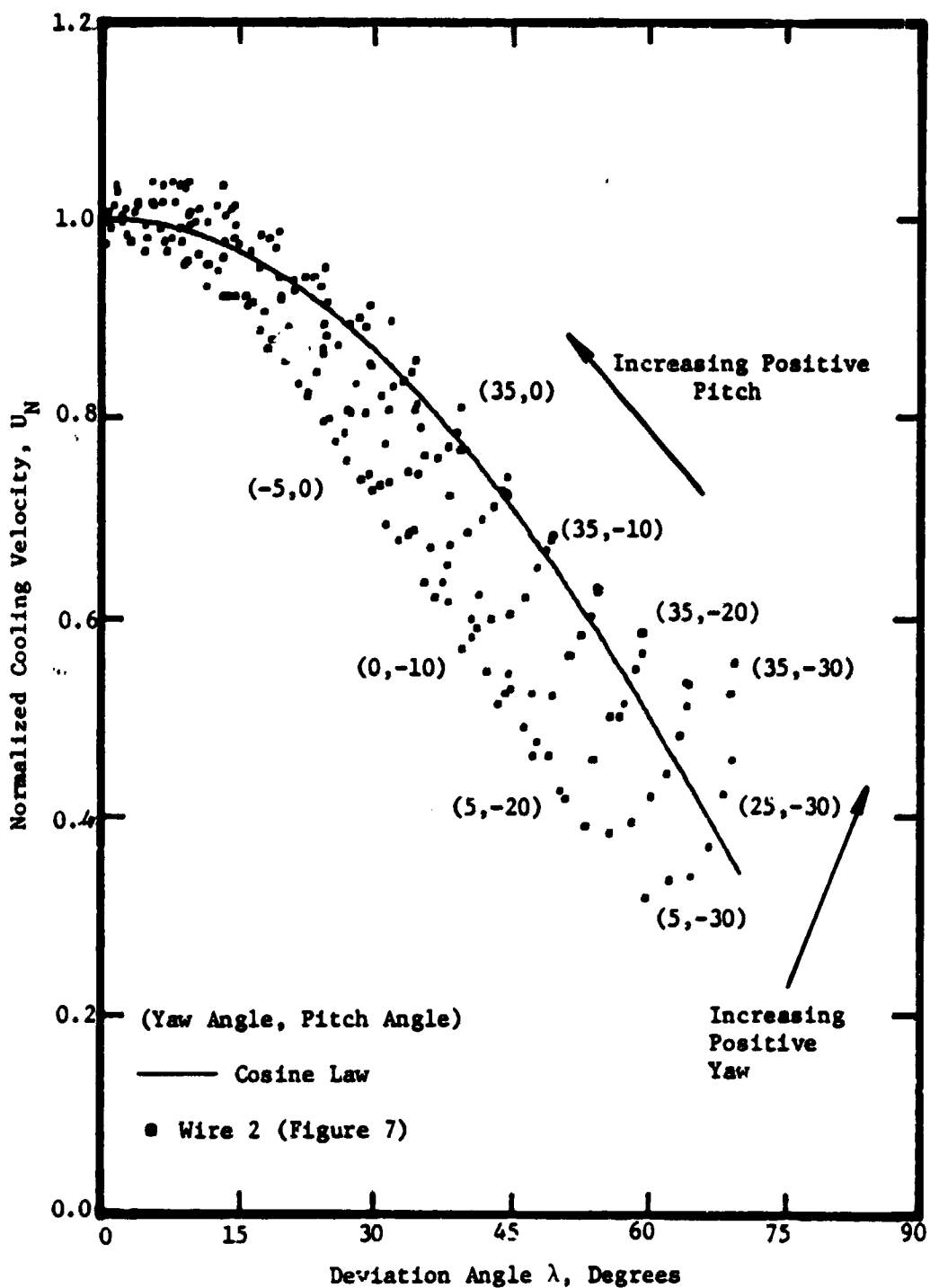


Figure 18. Response of Sensor-Two of Three-Sensor Hot-Wire Probe with Flow Deviation Angle Variation.

ORIGINAL PAGE IS
OF POOR QUALITY

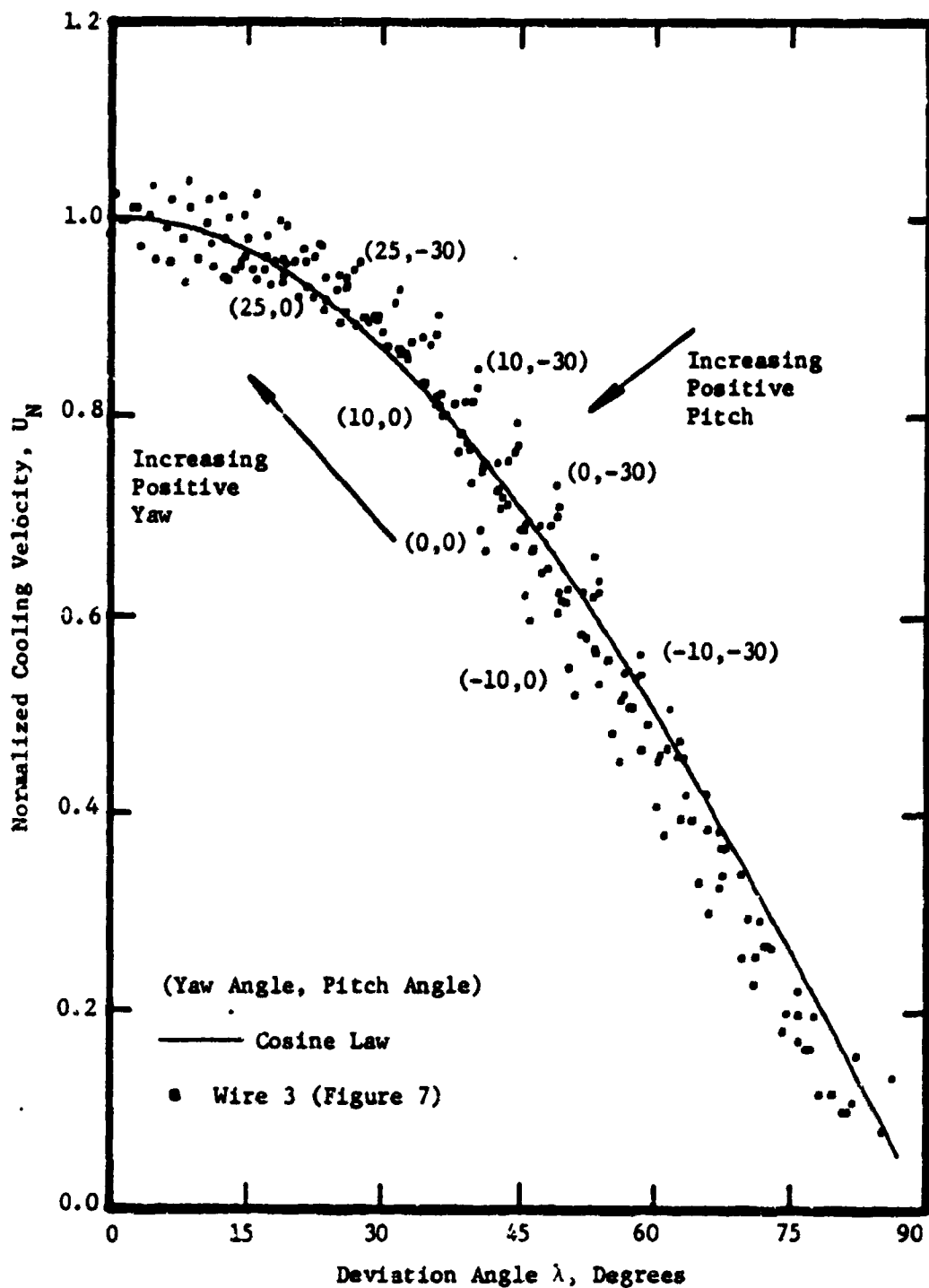


Figure 19. Response of Sensor-Three of Three-Sensor Hot-Wire Probe with Flow Deviation Angle Variation.

Figure 7 shows the orientation of each sensor with respect to the probe's coordinate system and the positive sense of the yaw and pitch angle with respect to these sensors. The direction cosines for these sensors are given in Table 4. The projection of the three sensors in the probe's $\ell_2 - \ell_3$ plane with the long and short prongs indicated is given in Figure 7. The sense of positive yaw and pitch is also indicated. The ratio of the sensor length to the difference in length between the long and short prongs is 1.71. By properly considering Figure 7 an accurate orientation of the sensors can be inferred.

As a consequence of yawing and pitching the probe, each sensor was at a different deviation angle to the incident flow. Figures 20, 21, and 22 show contours of these deviation angles for sensors 1, 2, and 3, respectively as a function of the yaw and pitch angle. These trends are evident when the orientation of each sensor, λ , is considered relative to the resulting velocity vector due to the yaw α and pitch β angle. At 0 deg yaw and 0 deg pitch the resultant velocity vector coincides with the ℓ_1 -axis of the probe. At other values of yaw and pitch the sensor is appropriately reoriented with respect to the flow direction.

With increasing values of positive yaw and pitch angle, the deviation angle λ of sensor 1 increased. This is indicated by Figure 20. However, as Figure 17 shows, the deviation of the normalized cooling velocity from the cosine law is small at high deviation angles. This results in little error from sensor 1 at these values of yaw and pitch. Sensor 2 indicates that large deviation angles occur with increasing values of positive yaw and negative pitch. Figure 17 shows that at

ORIGINAL PAGE IS
OF POOR QUALITY

Table 4. Direction Cosines (a_{ij}) Between the Wire Directions and the Reference Coordinates.

Rotating Probe (Figure 7)

		Wire Direction		
		1	2	3
Coordinate	l_1	0.5876	0.5168	0.6963
	l_2	-0.6152	-0.3636	0.6452
	l_3	0.5256	-0.7670	0.3143

Stationary Probe (Figure 9)

		Wire Direction		
		1	2	3
Coordinate	l_1	0.4699	0.4880	0.3984
	l_2	0.8187	-0.7508	-0.2065
	l_3	-0.3300	-0.4464	0.8936

ORIGINAL PAGE IS
OF POOR QUALITY

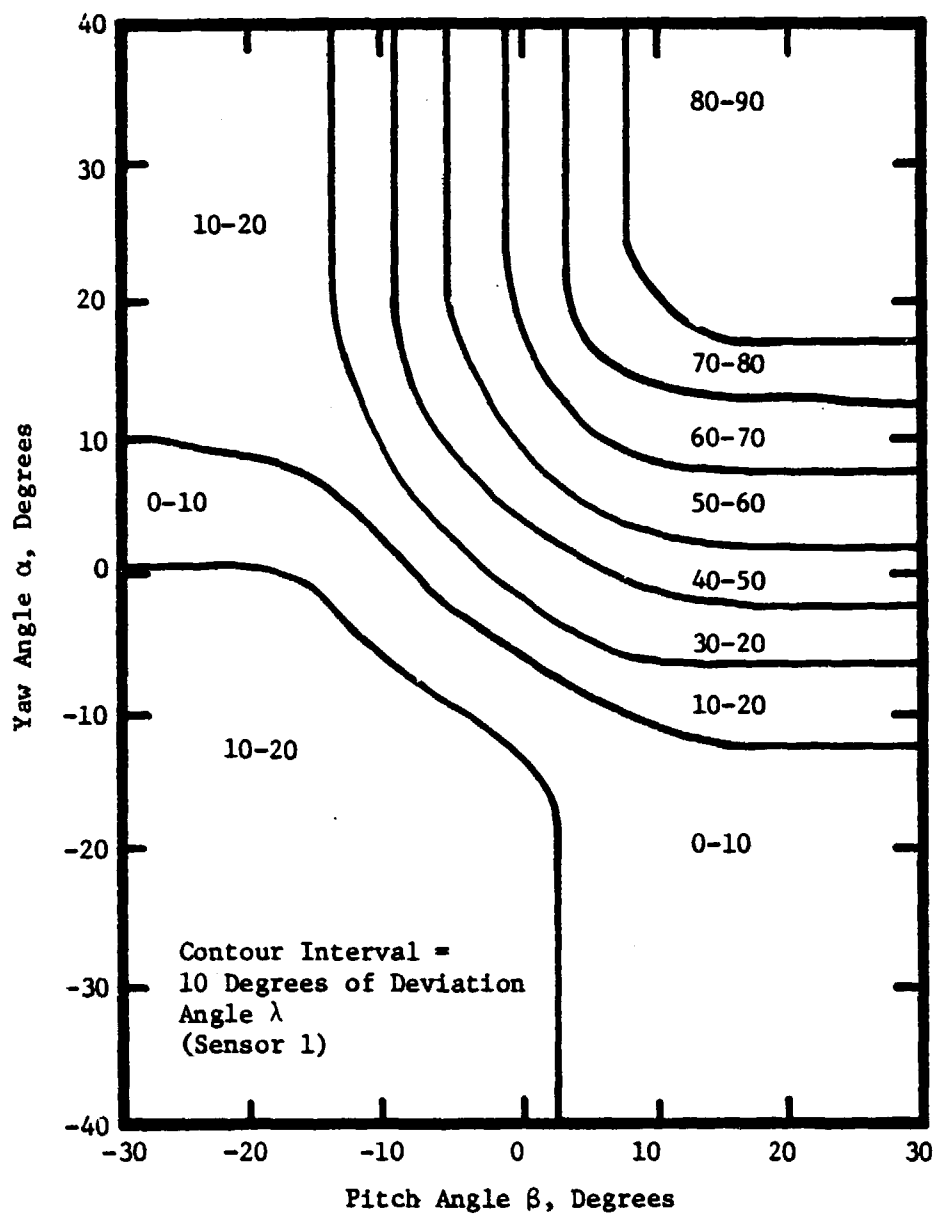


Figure 20. Flow Deviation Angle of Sensor-One with Three-Sensor Probe Yaw and Pitch Angle Variation.

ORIGINAL PAGE IS
OF POOR QUALITY

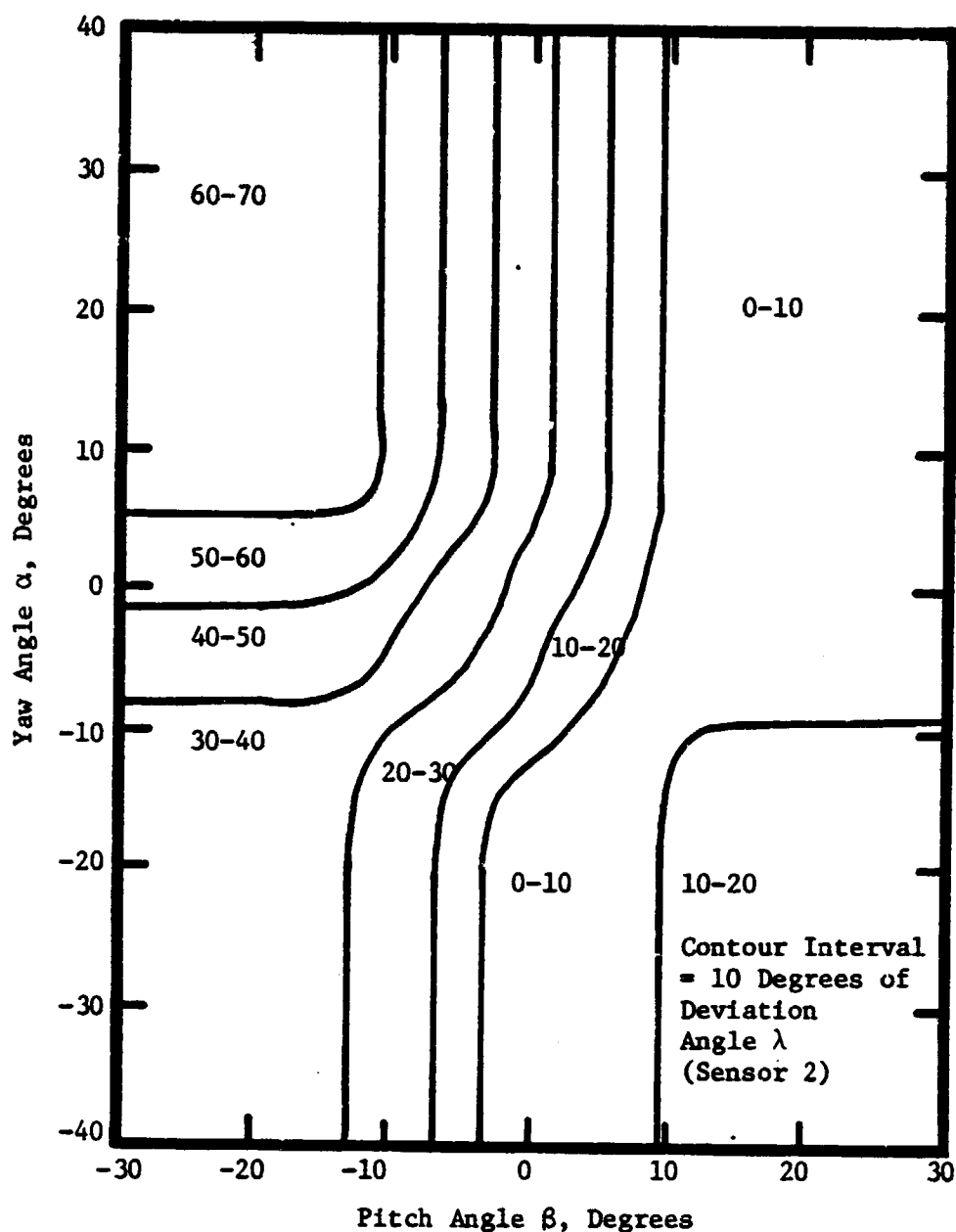


Figure 21. Flow Deviation Angle of Sensor-Two with Three-Sensor Probe Yaw and Pitch Angle Variation.

ORIGINAL PAGE IS
OF POOR QUALITY

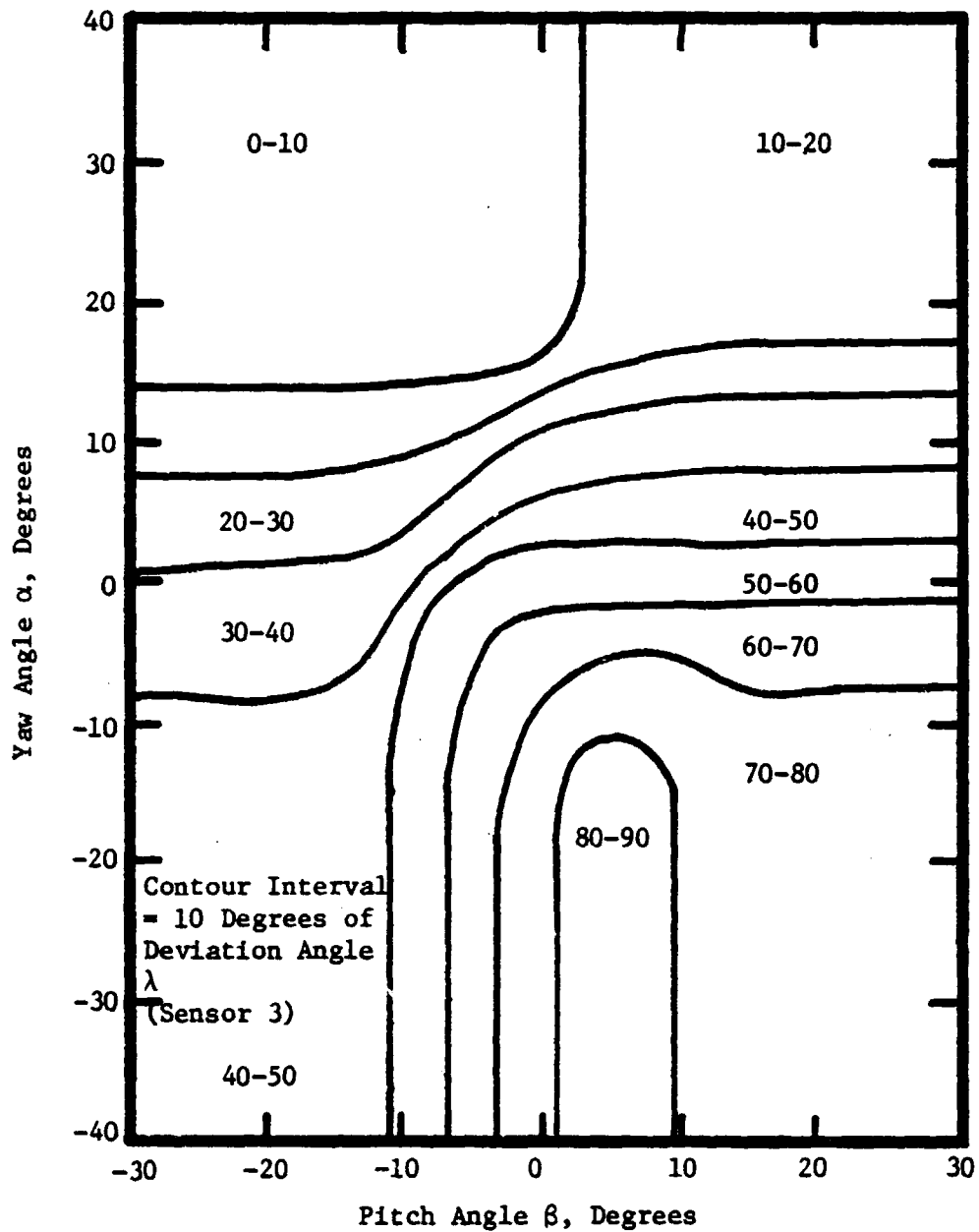


Figure 22. Flow Deviation Angle of Sensor-Three with Three-Sensor Probe Yaw and Pitch Angle Variation.

these deviation angles the normalized cooling velocity deviates considerably from the cosine law, thus allowing for large error. Sensor 3, similarly, is at a large deviation angle with respect to the incident flow at increasing values of negative yaw and positive pitch angles. Figure 19 indicates a moderate error associated with the data in this yaw and pitch range. Each sensor, due to its orientation, experiences different deviation angles at various angles of yaw and pitch. One sensor may be aligned properly to the main flow while another sensor could be at a large deviation angle and experiencing a large error in velocity measurement due to the component of velocity parallel to the sensor axis. The resulting velocity sensed by the composite probe is a combination of the individual errors associated with each sensor. To determine accurately the flowfield, each sensor must be corrected to the cosine law for the various values of yaw and pitch angle.

As Figures 17, 18, and 19 indicate, the normalized cooling velocities fall within a band which fans out at various values of the deviation angle. The deviation angle λ is a function of the yaw and pitch angle of the probe. Thus the fanning of the data within the band is a function of the yaw and pitch angle. This trend can be understood by referring to Figure 7. The nature of this deviation from the cosine law is believed to be a result of complex aerodynamic and thermal interactions between the sensors. These interference effects occur when one sensor is ill-positioned relative to another sensor or to the incident flow.

The error ϵ_T is given by Figure 16 can now be interpreted as a combination of each individual sensor's deviation from the cosine law.

A correction of the overall error of the three-sensor hot-wire probe, when it is subjected to varying angles of incidence with respect to the flowfield, is obtained by first correcting the response of the individual sensors. This was approached by correcting the normalized cooling velocity through the use of a deviation angle sensitivity function $g(\lambda)$ given by:

$$U_{\text{eff}} = U_1 g(\lambda) \quad (10)$$

The deviation angle λ which is a function of the yaw and pitch angles is the angle between the incident velocity and the normal to the wire. This is similar to the yaw angle α associated with the single-sensor probe. The yaw or deviation angle sensitivity functions suggested by previous investigators were used as a first attempt to fit the data for the three-sensor probe given in Figures 17, 18, and 19. These functions as given by Champagne et al. (1967), Friehe and Schwarz (1968), and Roberts et al. (1975) are given, respectively, as:

$$g(\lambda) = (\cos^2 \lambda + k^2 \sin^2 \lambda)^{1/2} \quad (11)$$

$$g(\lambda) = [1 - b_1(1 - \cos^{1/2} \lambda)]^2 \quad (12)$$

$$g(\lambda) = [1 - b_2(1 - \cos^m \lambda)]^2 \quad (13)$$

where λ is the deviation angle which is determined from the yaw and pitch angles. These functions should accurately fit the data through equation (10). The behavior of these functions is given in Figures 23, 24, and 25. Figure 23 shows a family of lines given by equation (11) where k varies in value from 0.0 to 1.0 in 0.1 increments. Equation (12)

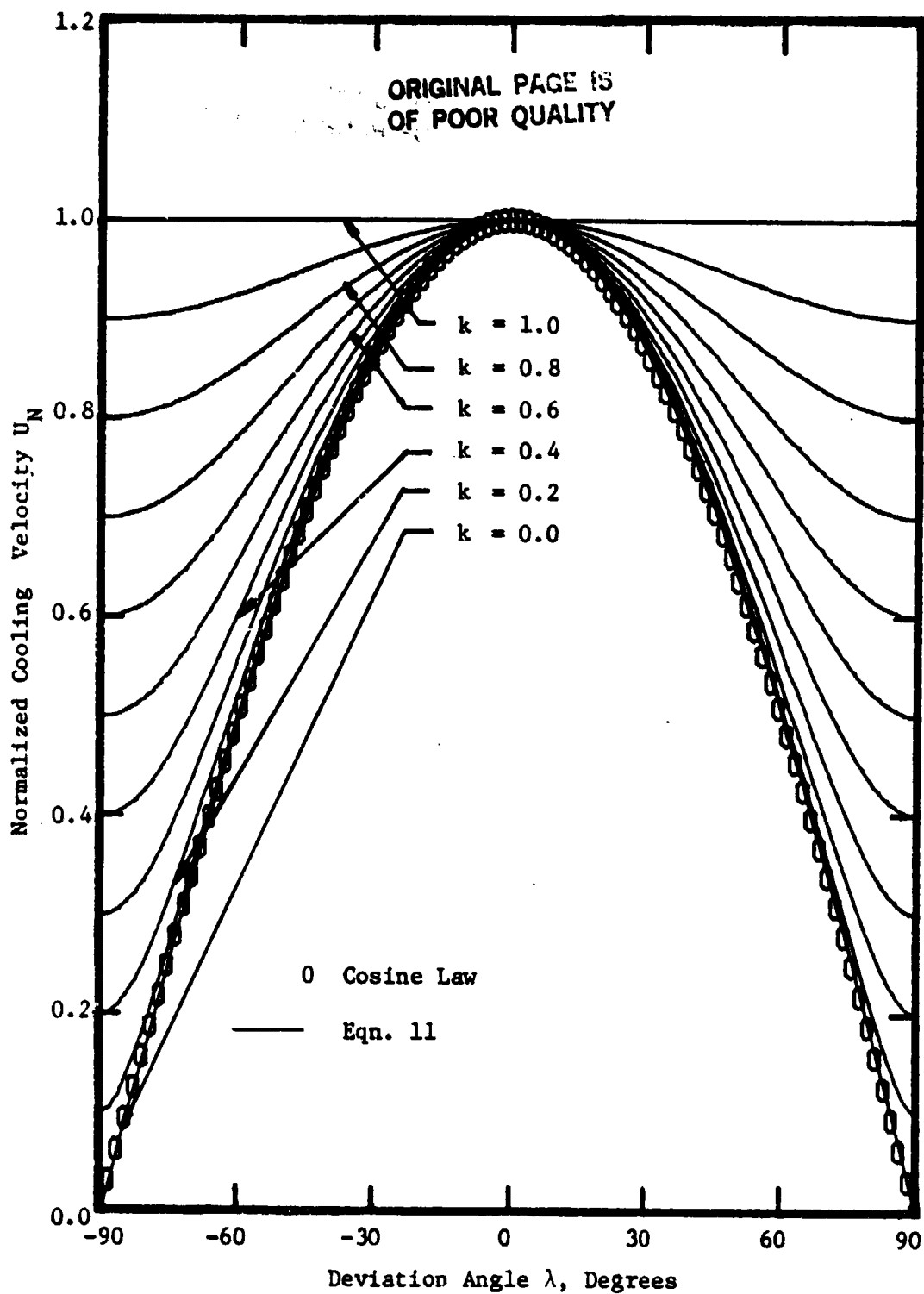


Figure 23. Behavior of Deviation Angle Sensitivity Function (Eqn. 11) with Deviation Angle Variation.

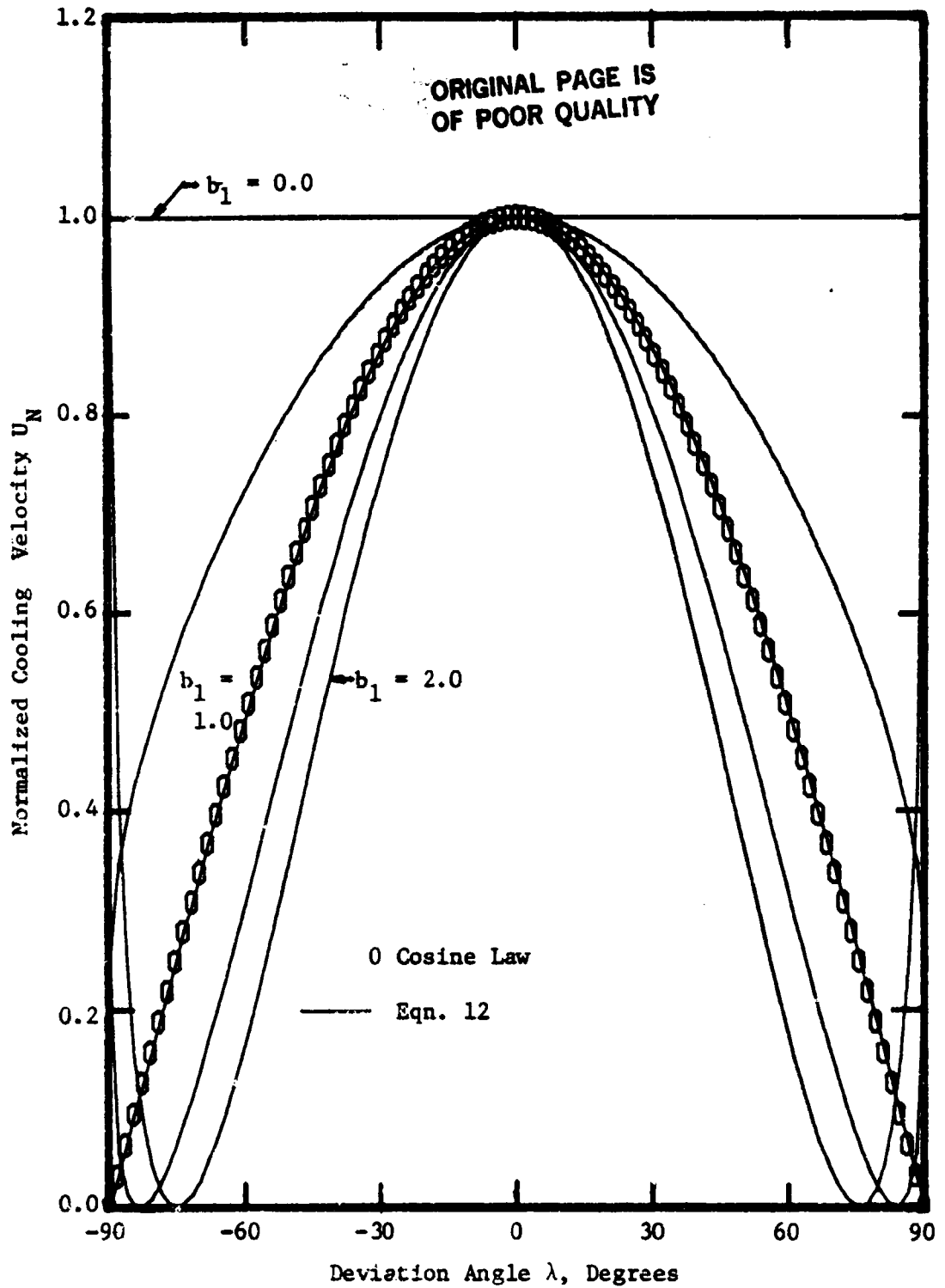


Figure 24. Behavior of Deviation Angle Sensitivity Function (Eqn. 12) with Deviation Angle Variation.

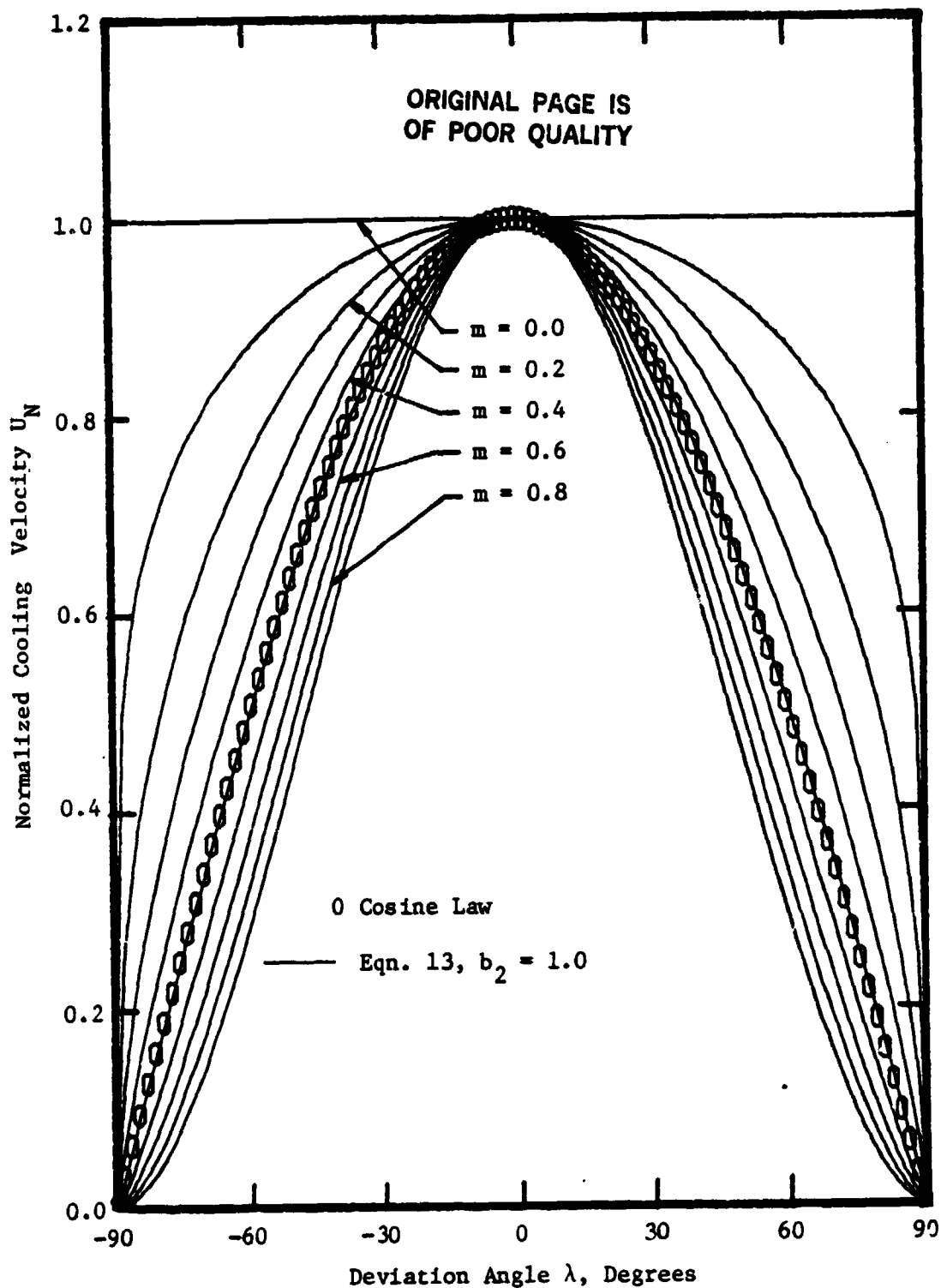


Figure 25. Behavior of Deviation Angle Sensitivity Function (Eqn. 13) with Deviation Angle Variation.

is represented in Figure 24 by a family of lines where the value of b_1 varies from 0.0 to 2.0 in 0.5 increments. Figure 25 shows a family of lines given by equation (13) where the values of $b_2 = 1.0$ and m varies from 0.0 to 0.9 in increments of 0.1. In all three figures, the circles represent data which behave according to the cosine law. None of these functions were found to fit the response of the individual sensors accurately for all values of the deviation angle. The interference effects induced by the complex configuration of the three sensors cannot be accurately modeled through the deviation angle sensitivity functions given.

By considering the behavior of the data presented in Figures 17, 18, and 19 a deviation angle sensitivity function of the form:

$$g(\lambda) = [k_1 (\cos^2 \lambda + k_3 \sin^2 \lambda)]^{1/2} \quad (14)$$

is proposed. Figures 26, 27, and 28 show the family of curves generated by altering various parameters of the function. This variation was determined by observing the deviation from the cosine law for the various sensors shown in Figures 17, 18, and 19. These curves accurately define the band of data generated by the three sensors normalized cooling velocities. Figure 26 shows a family of curves using equation (14) with k_1 varying from 0.8 to 1.3 in 0.05 increments, k_2 equal to 2.0, and k_3 equal to 0.0. This family of lines represents an accurate variation of the sensitivity function at various values of yaw and pitch angle for sensor 1. The normalized cooling velocity of sensor 2 was accurately fit using equation (14) with k_1 varying from 1.08 to 0.88 in 0.025 increments, k_2 varying similarly from 2.00 to 4.66 in 0.334

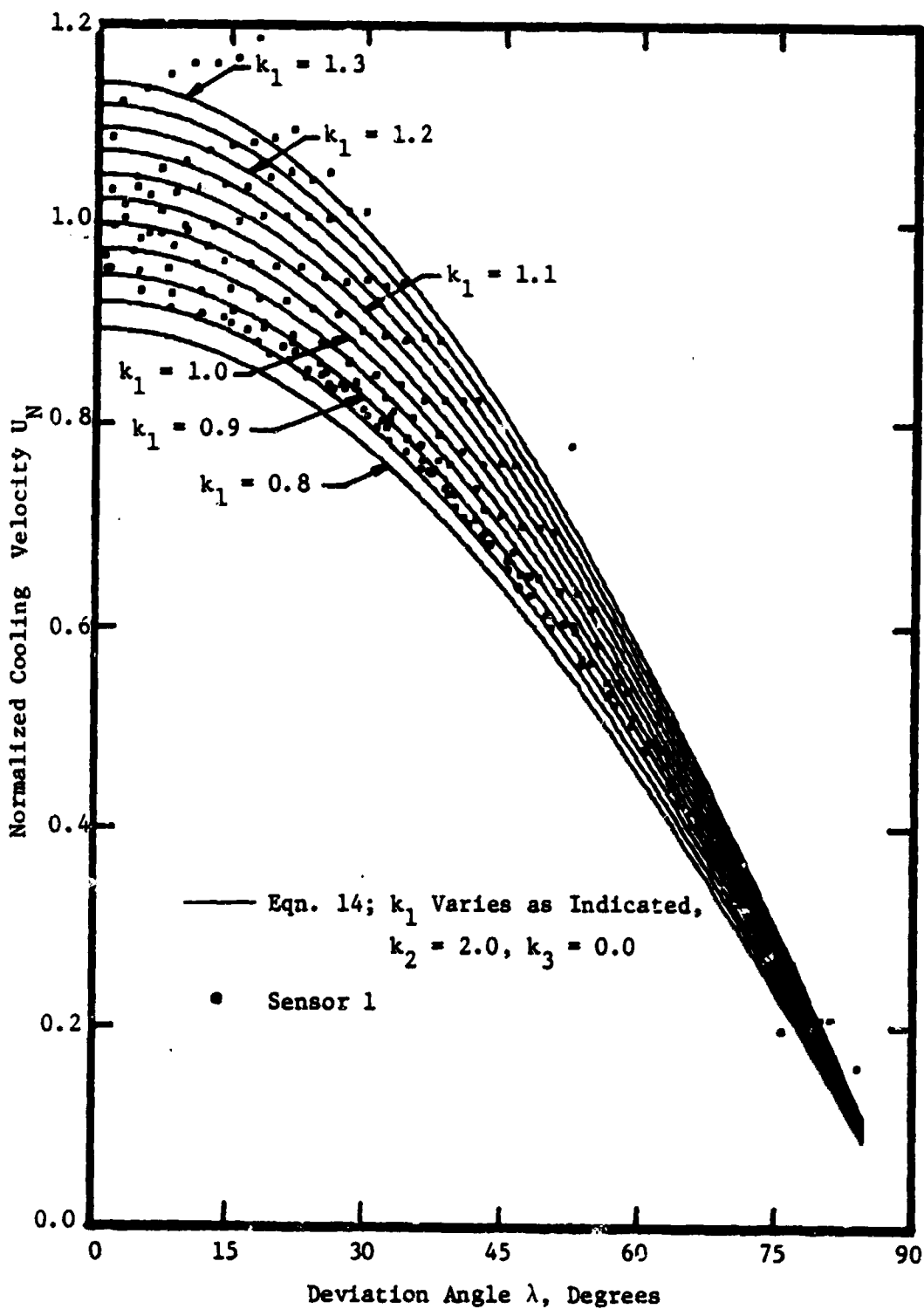


Figure 26. Comparison of Sensor-One Response and Deviation Angle Sensitivity Function (Eqn. 14) with Deviation Angle Variation.

ORIGINAL PAGE IS
OF POOR QUALITY

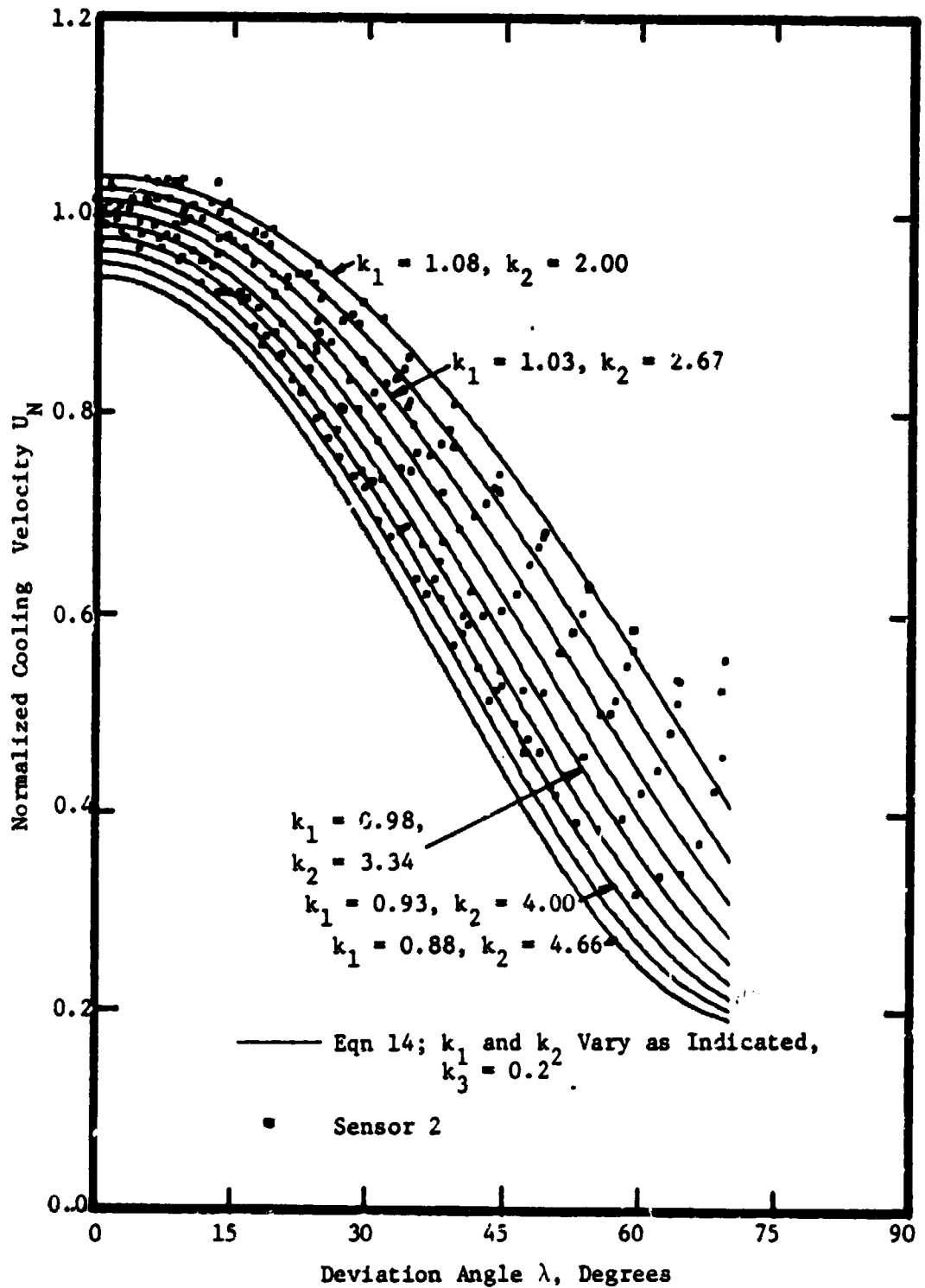


Figure 27. Comparison of Sensor-Two Response and Deviation Angle Sensitivity Function (Eqn 14) with Deviation Angle Variation.

ORIGINAL PAGE IS
OF POOR QUALITY

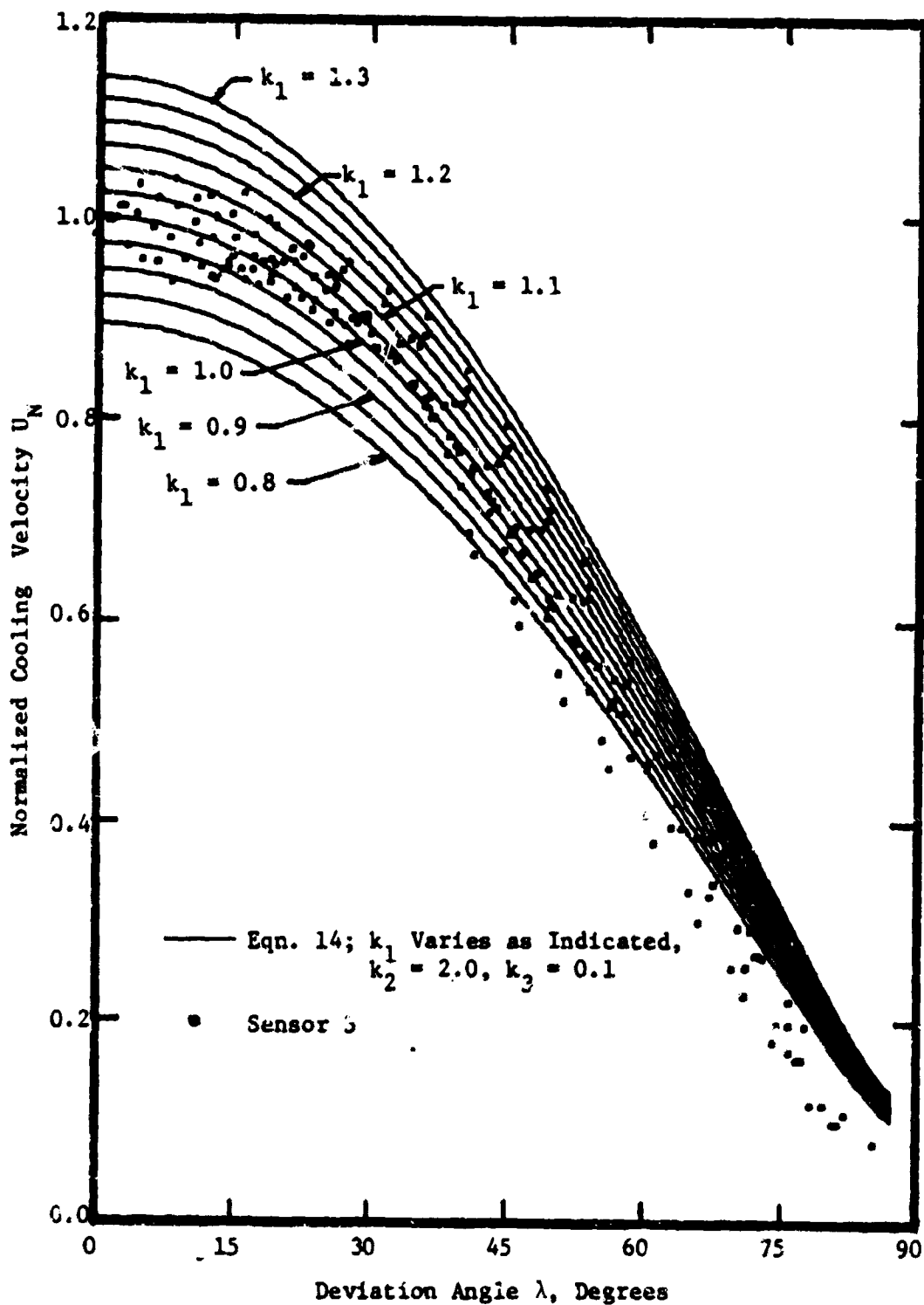


Figure 28. Comparison of Sensor-Three Response and Deviation Angle Sensitivity Function (Eqn. 14) with Deviation Angle Variation.

increments, and k_3 equal to 0.2. This fit is illustrated by Figure 27. Figure 28 illustrates a family of lines given by equation (14) with k_1 varying from 0.8 to 1.3 in 0.05 increments, k_2 equal to 2.0, and k_3 equal to 0.1. Thus the normalized cooling velocity of the three sensors can be accurately modelled by the deviation angle sensitivity function given by equation (14). The parameters k_1 , k_2 , and k_3 which determine the shape of the sensitivity function vary with the yaw and pitch angle of the probe.

The sensitivity function given by equation (14) was employed to calculate the total velocity sensed by the entire probe. The response of each sensor was corrected through equation (14). The exact value of the parameters k_1 , k_2 , and k_3 were chosen to give the best fit between the data and the sensitivity function as indicated by Figures 26, 27, and 28. This procedure was employed for all three sensors. The corrected response of each sensor was then used with the direction cosines of the sensors to determine the total incident flow U_T as a function of yaw and pitch angle. These values of U_T were then compared to the reference flow velocity U_{ref} through equation (8) to derive the resultant error. This error ϵ_T is shown in Figure 29 in the form of a contour plot for the various angles of yaw and pitch. The effect of employing the deviation angle sensitivity function is evident by viewing Figures 16 and 29. Figure 16 shows that initially an error of 10 percent or greater occurred beyond a yaw or pitch angle of ± 10 degrees. By employing the correction due to the deviation angle sensitivity function $g(\lambda)$, errors less than 4 percent occur at yaw and pitch angles of ± 20 degrees. Even at larger angles of yaw and pitch, the maximum error is reduced to 8 percent. This is a substantial improvement in the total response of the probe.

ORIGINAL PAGE IS
OF POOR QUALITY

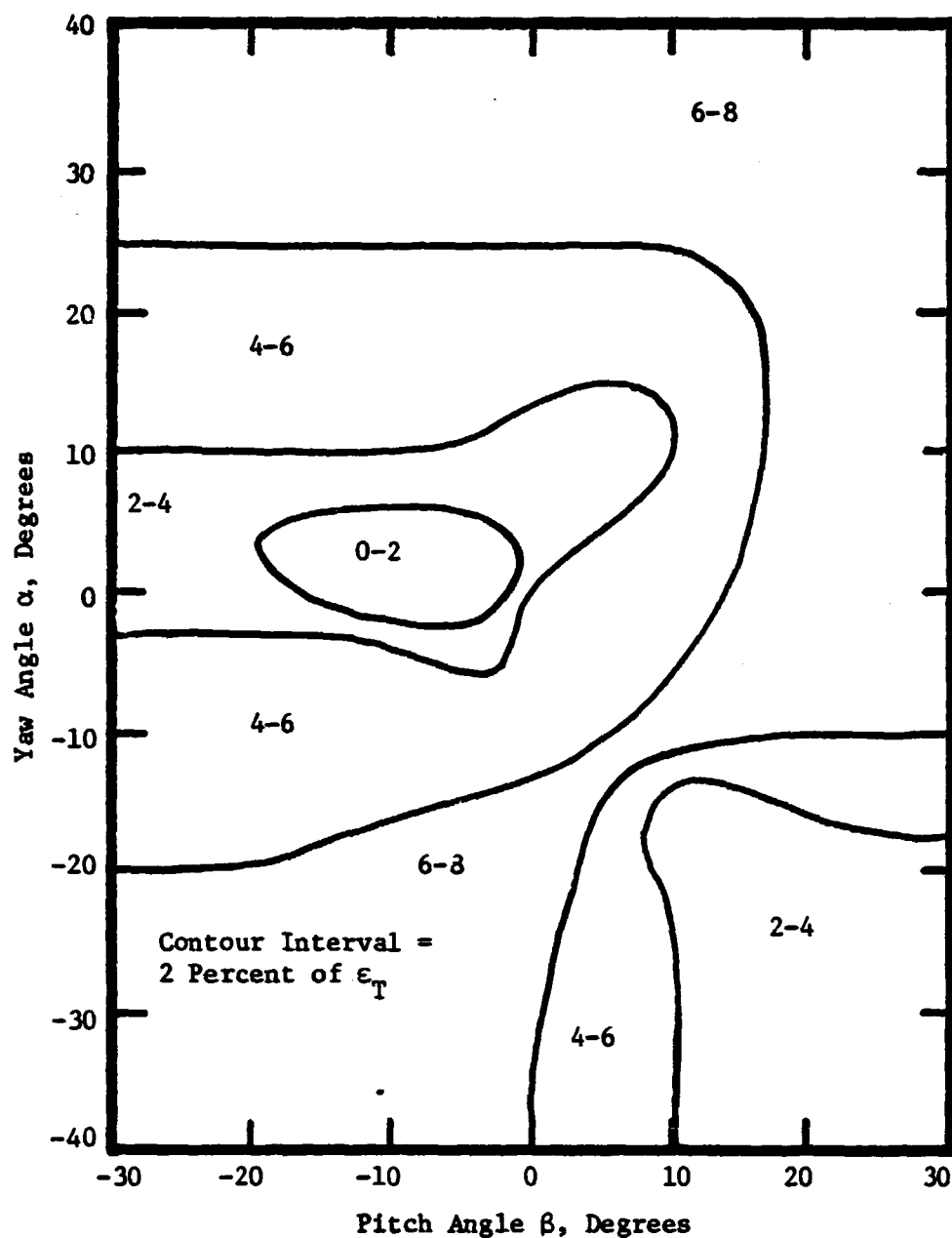


Figure 29. Error of Corrected Three-Sensor Hot-Wire Response with Yaw and Pitch Angle Variation.

C-2

The response of a three-sensor hot-wire probe to a varying incident velocity vector is quite different from that of a single-sensor hot-wire probe. The calibration of the probe is highly dependent upon the configuration of the sensors. Because of this characteristic, the probe sensors should be calibrated at the null or zero yaw and zero pitch angle position. This procedure calibrates each sensor to the magnitude of the incident velocity at the null position of the incident velocity vector. With this calibration procedure the constants of equation (2) can be determined for each sensor.

The three-sensor hot-wire probe should also be calibrated to the direction of the velocity vector if the flow under investigation will deviate appreciably from the null position. This procedure is necessary due to each sensor's unique orientation with respect to the incident flow direction and the other sensors. At high angles of yaw and pitch the response of the probe is subject to aerodynamic and thermal interference effects. These effects are due to the component of the incident velocity parallel to the sensors and to the shed wakes of the sensor prongs. The response of the probe must be corrected for these effects by a flow direction calibration.

In view of the results of this investigation, the following correction procedure is proposed. The response of the three-sensor probe should be determined for a variation of yaw and pitch angle which corresponds to the maximum flow angle deviation anticipated during the experimental investigation. For these values of yaw and pitch angle, figures similar to Figure 15 can be derived for the total velocity U_T normalized by the jet velocity U_{ref} and the three components of velocity U_i ($i = 1, 2, 3$) normalized by the appropriate component of the calibration

jet velocity $(U_{\text{ref}})_i$ ($i = 1, 2, 3$). These figures will determine the probe sensitivity to yaw and pitch angle during the experimental investigation. The probe can then be used to derive the uncorrected values of U_T and U_i ($i = 1, 2, 3$) of the flowfield under investigation. The three components of velocity U_i determine the yaw and pitch angle of the flow relative to the probe. These angles can be then used to determine the ratios U_T/U_{ref} and $U_i/(U_{\text{ref}})_i$ ($i = 1, 2, 3$) from the yaw and pitch angle calibration figures. From these ratios, the values of U_T and U_i for the flowfield under investigation, corrected for yaw and pitch angle induced errors, can be determined.

3.5 Error in Three-Sensor Hot-Wire Probe Measurements Subjected to a Fluctuating (Unsteady) Velocity Vector

The method of rotating a three-sensor hot-wire probe in a blade passage has many advantages. This method allows data to be acquired inside the blade passage from the pressure side to the suction side of a blade. In this region the probe must be rotated with the blading. The response of the three-sensor hot-wire probe using this method has been discussed in the previous sections. However, exit-flow measurements behind the blade passage do not require a rotating probe. Here the probe can be located outside of the blade passage. This allows for a much simpler data acquisition system. The exit-flow in the annulus-wall region was investigated using such a system and the results are reported in Chapter 4. An ensemble-average technique was employed to analyze the data acquired by a three-sensor hot-wire stationary probe located behind the blade passage. This method employed a simple probe holding arrangement since rotational stresses on the

probe were not involved. Also, the data acquisition time was considerably reduced. The speed of rotation of the compressor rotor was 1066 r.p.m. Since the rotor has 21 blades, one wake passage took 0.0027 seconds to sweep past the probe. The response of the probe was recorded on analog tape and analyzed at a later time. Details of this data acquisition system are given in Chapter 2.

The objective of this investigation was to determine the nature of some errors that are involved by subjecting a three-sensor hot-wire probe to a fluctuating velocity vector. These errors can be due to a physical constraint such as the angle between the incident flow direction and the axis of the cone of sensitivity formed by the three sensors. They can also be due to a data processing constraint such as the sample size. These two sources of error were felt to be particular to the annulus-wall exit-flow data presented in Chapter 4.

3.5.1 Effect of Probe Angle in the Stationary Frame of Reference with Respect to the Average Absolute Flow Direction

The probe employed for this investigation and the orientation of its sensors with respect to the probe axis is given in Figure 9. The direction cosines of the sensors with respect to the probe axes is given in Table 4. This probe was fixed to the casing of the axial flow compressor research facility and positioned behind the blade passage. The facility was operated at its design condition with the flow coefficient $\phi = 0.56$. The probe was positioned at $R = 0.730$, $z = 1.136$ and rotated about its axis such that the absolute probe angle γ (Figure 9) had the values: 30 deg, 40 deg, 50 deg, 60 deg, and 70 deg. With each angular position the probe was traversed in the axial

direction to compensate for the overhang of the sensors from the turning axis. This movement was done employing a micrometer with a precision of ± 0.00254 cm. The reference axial position at $\gamma = 40^\circ$ behind the blading, which is the design absolute flow angle, was thus maintained. At each angular position the response of the three sensors and a reference pulse signal synchronized to the rotor blade passage were recorded. This method resulted in the measurement of the same flow phenomena at varying angles between the flow direction and the axis of the cone of sensitivity formed by the three sensors. The data were analyzed and important information was extracted. This included the profiles of the three components of mean velocity in the streamwise coordinate system.

The resulting mean velocity profiles, using 200 samples, are given in Figures 30, 31, and 32. Beyond the probe angle of 70 deg, severe high frequency oscillations were observed in the sensor signals and no measurements were taken. Figure 30 shows the resulting streamwise velocity profiles which are normalized by the indicated free-stream value of the streamwise velocity W_{so} . These profiles are plotted against the tangential distance behind the blade passage which is normalized by the blade spacing. The abscissa $Y_e/S = 0.5$ represents the mid-passage and $Y_e/S = 0.0$ corresponds to the centerline of the rotor blade wake. The notation SS and PS indicate the suction and pressure sides of the blade passage, respectively. Figure 30 indicates that as the probe is turned further away from the ideal orientation at $\gamma = 40$ deg, a modification of the streamwise velocity profile exists. Up to 20 deg of turning the magnitude of the velocity defect due to the wake is only altered by approximately 3.0 percent. However, at 30 deg

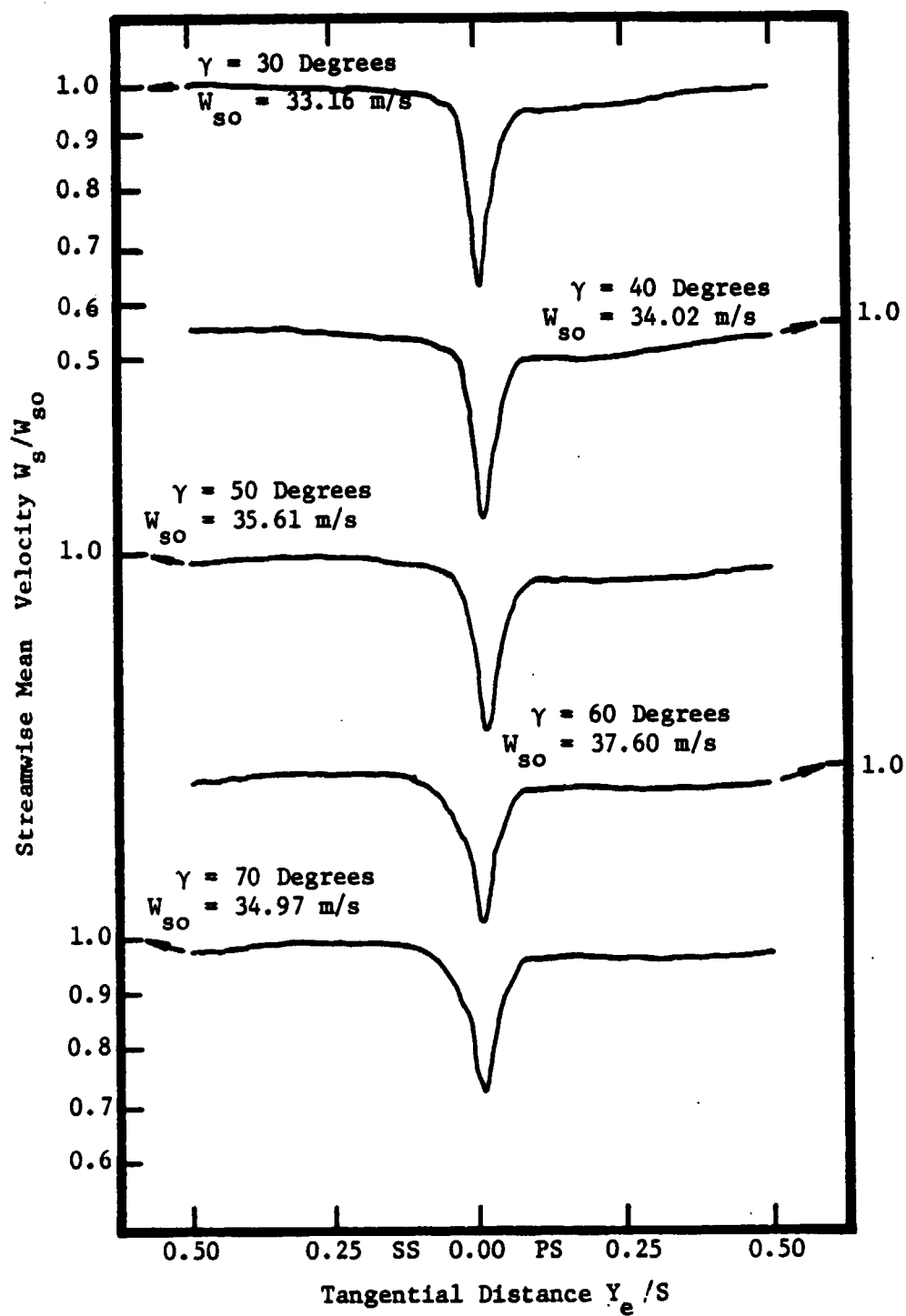


Figure 30. Streamwise Mean Velocity Profile Variation with Three-Sensor Probe Yaw Angle.

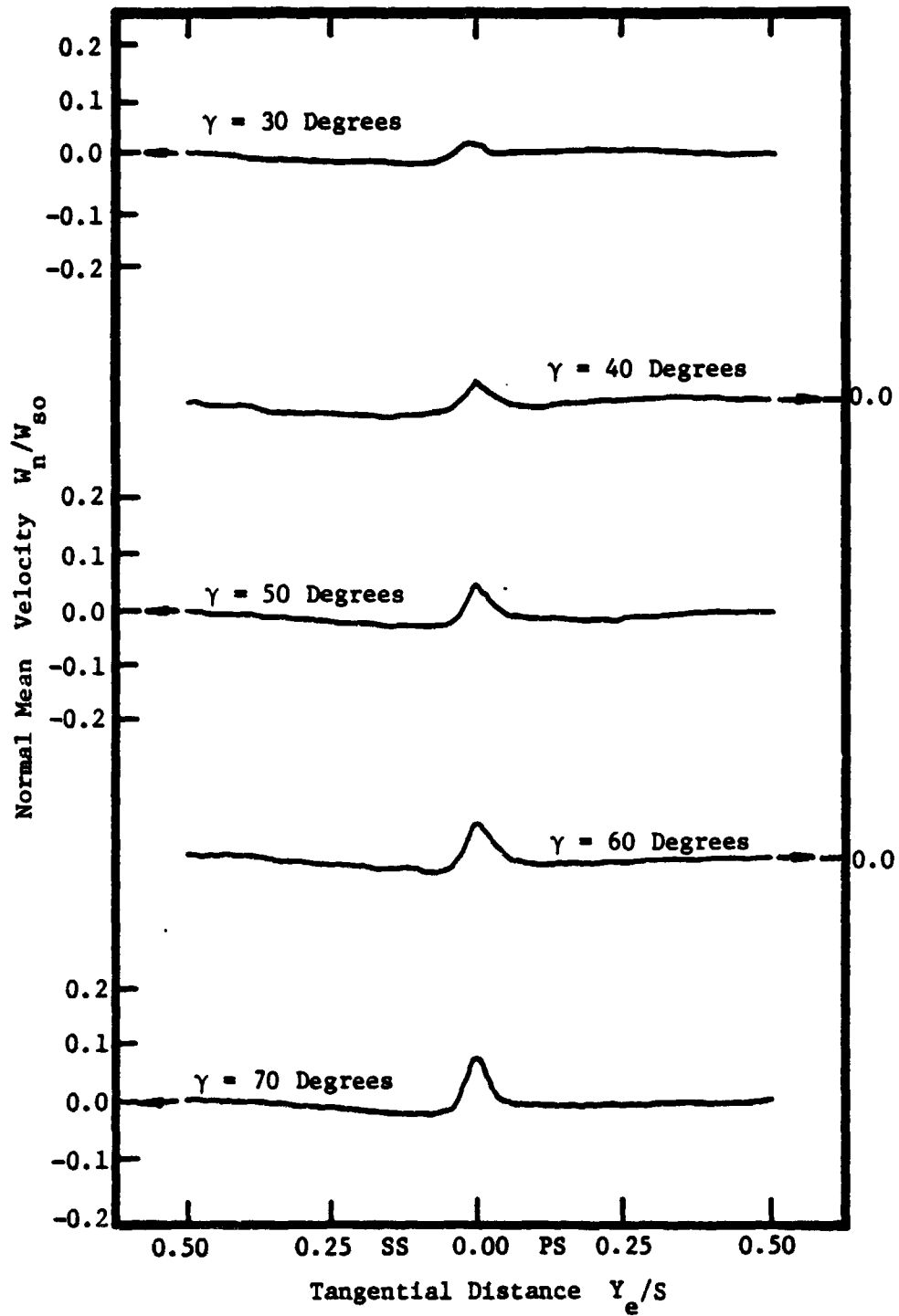


Figure 31. Normal Mean Velocity Profile Variation with Three-Sensor Probe Yaw Angles.

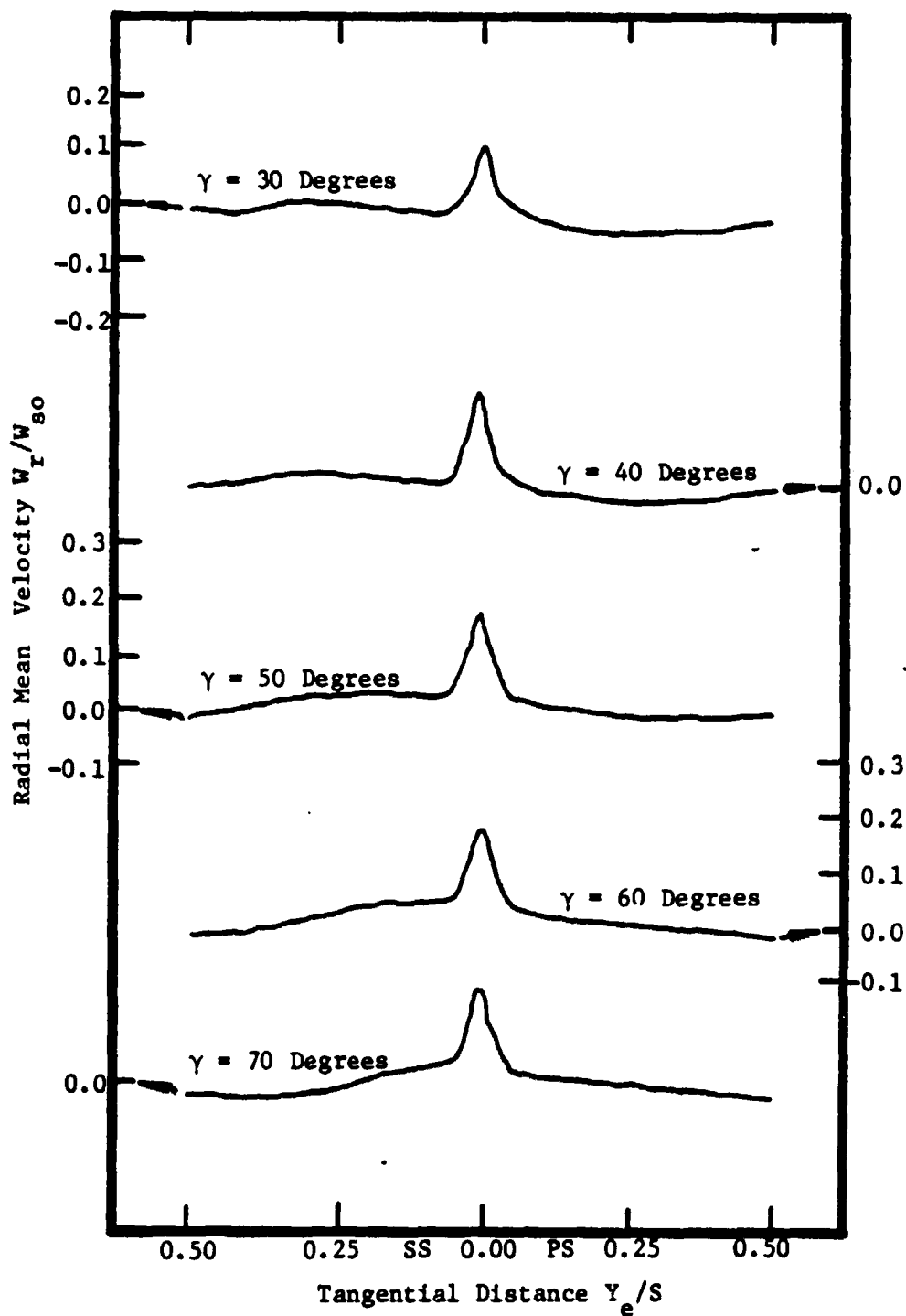


Figure 32. Normal Mean Velocity Profile Variation with Three-Sensor Probe Yaw Angle.

of turning the magnitude of the velocity defect is reduced by 9.5 percent and the wake width is shown to increase. Serious errors, up to 9.6%, were observed in the values of W_{s0} . However, since the error in W_s would be nearly the same as the error in W_{s0} , the ratio W_s/W_{s0} is the almost free of error. The misalignment of the sensor at $\gamma = 70$ deg results in a considerable deviation from the actual velocity profile. The effect of this deviation is qualitatively similar to that experienced by the yawing and pitching of a probe as reported in the previous section. Both probes yielded results which were approximately 10 percent in error at a turning angle of 30 deg.

Figure 31 shows the effect of the turning angle γ upon the normal velocity profiles. With increased turning angle, the normal velocity profile of the wake was seen to increase in value. Abnormally high values of normal velocity were sensed in the wake region. Figure 32 shows the radial velocity profile at various turning angles. The effect of the turning angle is not as severe; however, slight deviations in the profile do occur.

This initial look at the turning of a three-sensor hot-wire probe away from its ideal orientation during an ensemble-average type of measurement illustrates some errors involved. The response of the probe shown in Figures 30, 31, and 32 is the result of the complex interaction of the cooling velocities sensed by the three sensors. These cooling velocities may be subject to interference effects at probe orientations where one sensor shadows another. This shadowing could introduce errors of the type illustrated. The investigation reported here was a preliminary step in investigating some errors associated with employing the

ensemble-average data acquisition technique for the annulus-wall exit-flow with misorientation of the probe. It has been shown that for angles which deviate up to 20 deg from the ideal probe orientation to the absolute flow direction, errors of approximately 3 to 5 percent are encountered. This error is acceptable and within the experimental error of the annulus-wall flow investigation.

3.5.2 Effect of Ensemble-Average Sample Size

The sample size employed during the ensemble-average processing of the stationary measurements has been determined to influence the accuracy of the data. The resulting error has been discussed by investigators such as Bendat and Piersol (1958). This error was found to be associated with many factors such as the nature of the flow (steady or unsteady) and the physical characteristics of the probe. The intent of this investigation was to determine quantitatively the effect of sample size upon the mean velocity profiles.

Figures 33, 34, and 35 typically show the effect of sample size upon the mean velocity profiles obtained in the exit-flow of the blade passage at the annulus-wall region. As in the previous section, the mean velocities are normalized by the streamwise velocity at the free-stream location and the tangential distance behind the blade passage is normalized by the blade spacing. The sample size N and the value of W_{so} is indicated for each profile. The effect of sample size is seen to be appreciable. One effect observed in Figures 33, 34, and 35 is a smoothing of the irregular features of the velocity profile. Some of these features, particularly in the free-stream, are due entirely to

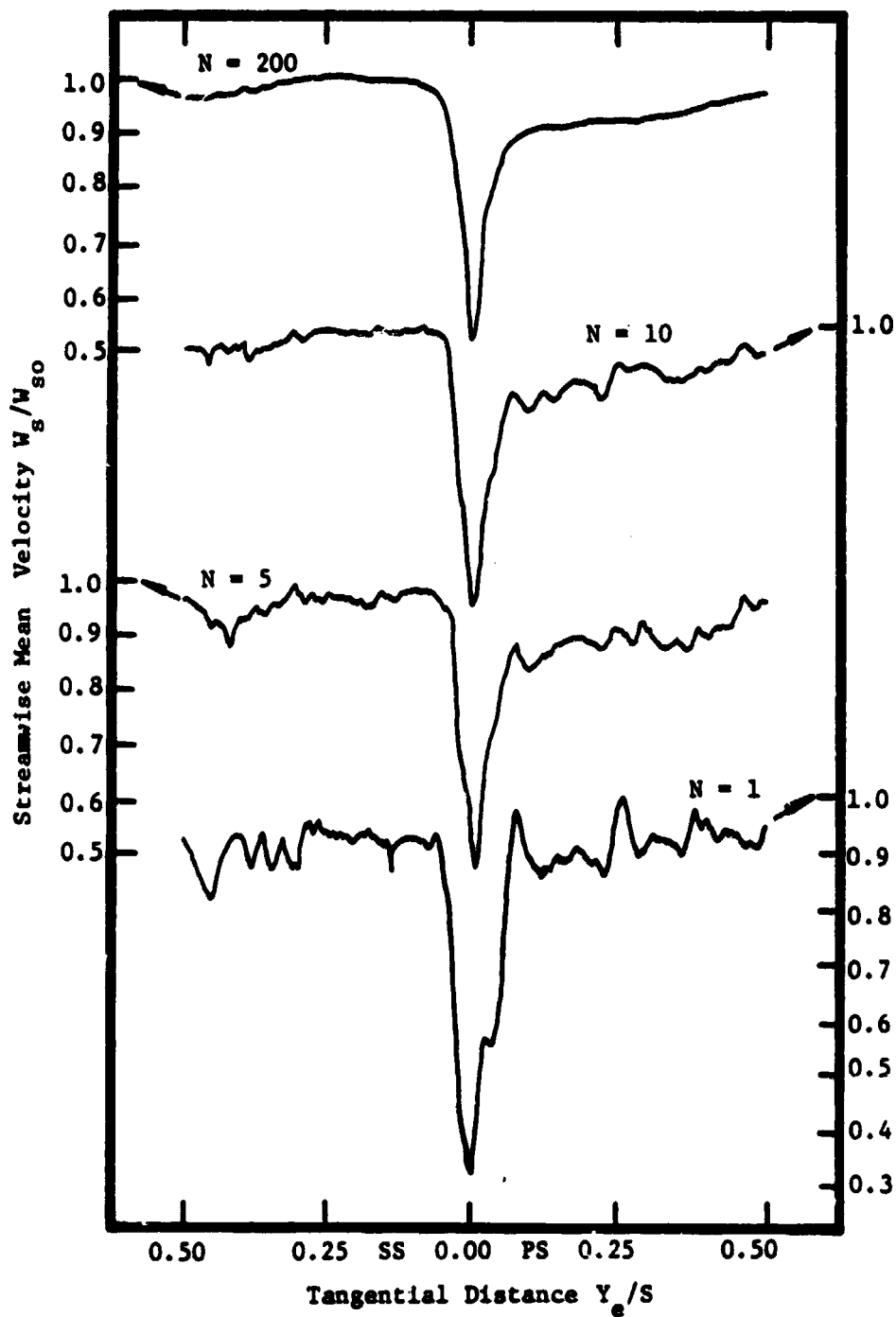


Figure 33. Streamwise Mean Velocity Profile Variation with Sample Size.

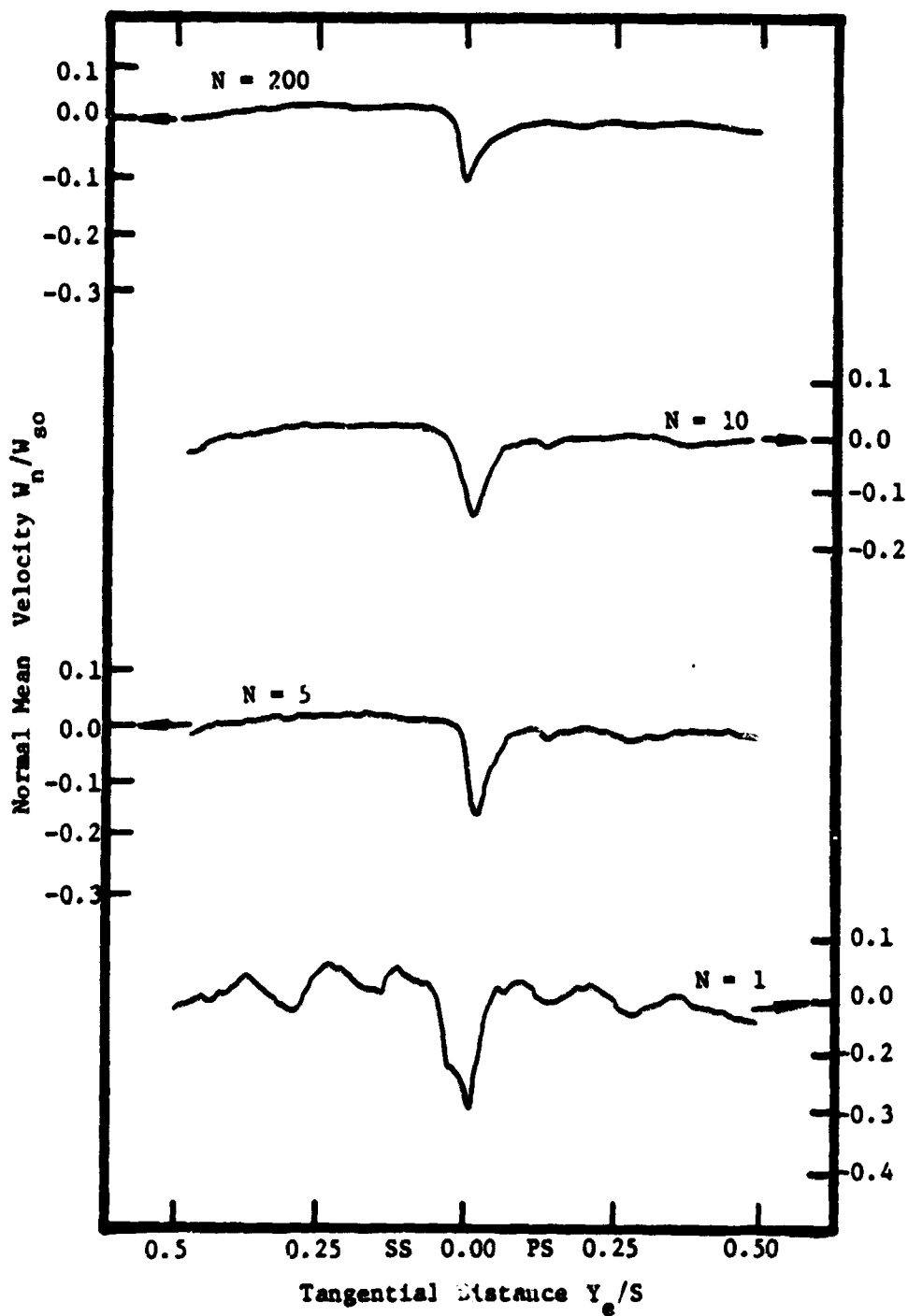


Figure 34. Normal Mean Velocity Profile Variation with Sample Size.

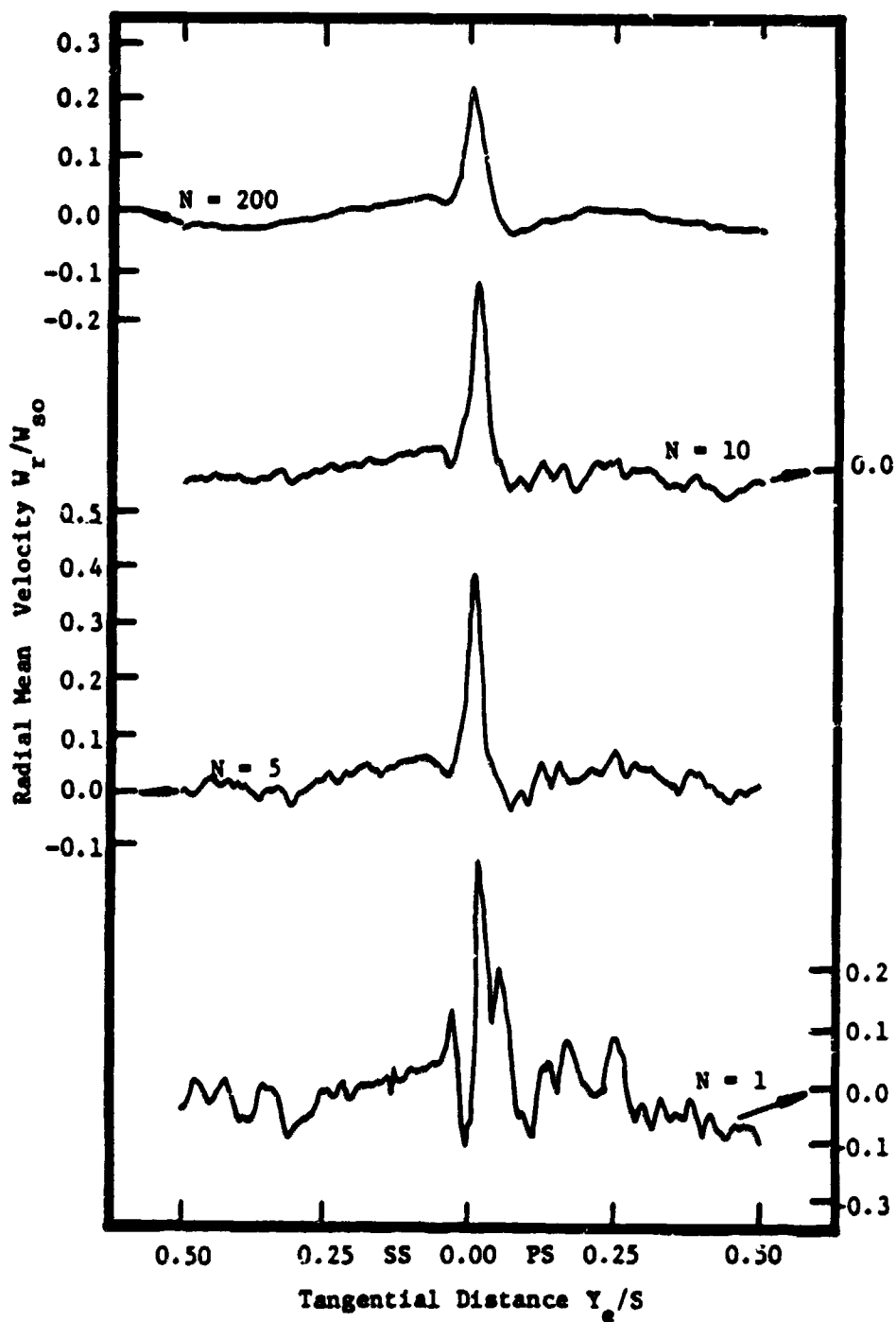


Figure 35. Radial Mean Velocity Profile Variation with Sample Size.

the turbulent nature of the flow. As the sample size is increased these turbulent fluctuations are averaged out. The averaging of these turbulent features is characteristic of most measurement techniques and the information lost in the mean velocity profiles which can be derived from the same signal.

Another effect of increased sample size is a loss of information about unsteady phenomena. Figures 33, 34, and 35 show an indication of this effect. With $N = 1$, each profile shows the location of a flow phenomenon which varies spatially from one revolution of the blade passage to another. The variation is small (2.4 percent of the blade passage); however with increasing N , the detail of the unsteady phenomena is reduced considerably. The dip in the streamwise and radial velocity profiles at $N = 1$ becomes a gradual curve at $N = 10$. Thus the nature of an unsteady flow phenomenon cannot be accurately determined with even a few samples for the ensemble-average.

As Figures 33, 34, and 35 indicate, the magnitude of the velocity defect of the rotor wake changes with the sample number. The profile of a single wake is shown with $N = 1$. This profile is probably not representative of the blade wake because of many factors which change a single blade's operating conditions randomly. However, as the sample size is increased a more representative profile is obtained because more typical profiles are included in the ensemble-average. This effect is evident by viewing Figure 33. The streamwise velocity defect in the wake is $0.61 W_s/W_{s0}$ for $N = 1$. As more samples are included ($N = 5, 10, \text{ and } 200$), a constant wake defect of $0.50 W_s/W_{s0}$ is obtained. Similar trends are seen for the normal and radial velocity profiles. The mean

velocity profiles obtained with a large number of samples show an accurate definition of the rotor wake.

The sample size used for an ensemble-average technique of data processing affects the resulting mean velocity profiles. The nature of the effect is to determine more accurately predominant flow phenomena, such as the blade wake, when large sample sizes are employed. However, the large sample size tends to average out any unsteady flow phenomena. Thus, the sample size employed should depend upon the nature of the flow phenomenon under investigation.

CHAPTER 4

EXPERIMENTAL RESULTS AND INTERPRETATION OF THE FLOWFIELD IN THE ANNULUS-WALL REGION

4.1 Rotor In-Flow Conditions

The rotor in-flow conditions strongly affect the development of the flow in the rotor blade passage with the mainflow. An accurate knowledge of the flowfield upstream of the rotor is essential before any attempt is made to study the rotor passage-flow and rotor exit-flow. The mean velocity and turbulence structure as well as the pressure field upstream of the rotor are important.

The rotor for The Pennsylvania State University axial-flow compressor facility is preceded by an inlet guide vane assembly, as shown in Figure 2. Typical pressure and velocity surveys upstream and downstream of the inlet-guide-vane assembly are presented in the following sections. These surveys display the effect of the assembly on the mean velocity and turbulence structure of the flow.

4.1.1 Surveys Upstream of the Inlet-Guide-Vane

Mean velocity and turbulence intensity profiles upstream of the inlet guide vanes were determined by Sitaram (1980). These data were measured using a hot-wire probe and a spherical-head static-stagnation pressure probe. The velocity distribution that exists in the annulus just upstream of the inlet-guide-vanes is presented in Figure

36. The velocity derived from wall-static measurement is also given in Figure 36. The velocity variation across the annulus from hub to tip is less than two percent. This indicates nearly uniform entry flow to the inlet guide vane.

4.1.2 Surveys Downstream of the Inlet-Guide-Vanes

Mean velocity and turbulence intensity profiles downstream of the inlet-guide-vanes were determined by Sitaram (1980), who employed a hot-wire probe and a spherical-head static-stagnation pressure probe. Figures 37 and 38 show the typical tangential variation of the axial velocity at positions just downstream and one chord downstream of the inlet guide vanes. The axial velocity is normalized by the value in the free stream, V_z/V_{z0} . An axial velocity defect of 0.16 in the wake at 0.041 chords downstream and at $R = 0.878$ was found to become 0.07 at 1.000 chords downstream of the inlet guide vanes. Further downstream, at $Z = 2.000$ and $R = 0.878$, the axial velocity defect was found to become $0.03 V_z/V_{z0}$. Similar decay rates of the axial velocity defect were observed at the other radial locations. An axial turbulence intensity in the wake of 30 percent of the free-stream velocity at $Z = 1.041$ and $R = 0.878$ was found to reduce to less than two percent at two chords downstream of the inlet guide vanes. As these surveys indicate, the inlet-guide-vane wakes have decayed considerably before reaching the rotor. Detailed measurements of the inlet-guide-vane wakes have been reported by Lakshminarayana and Davino (1980).

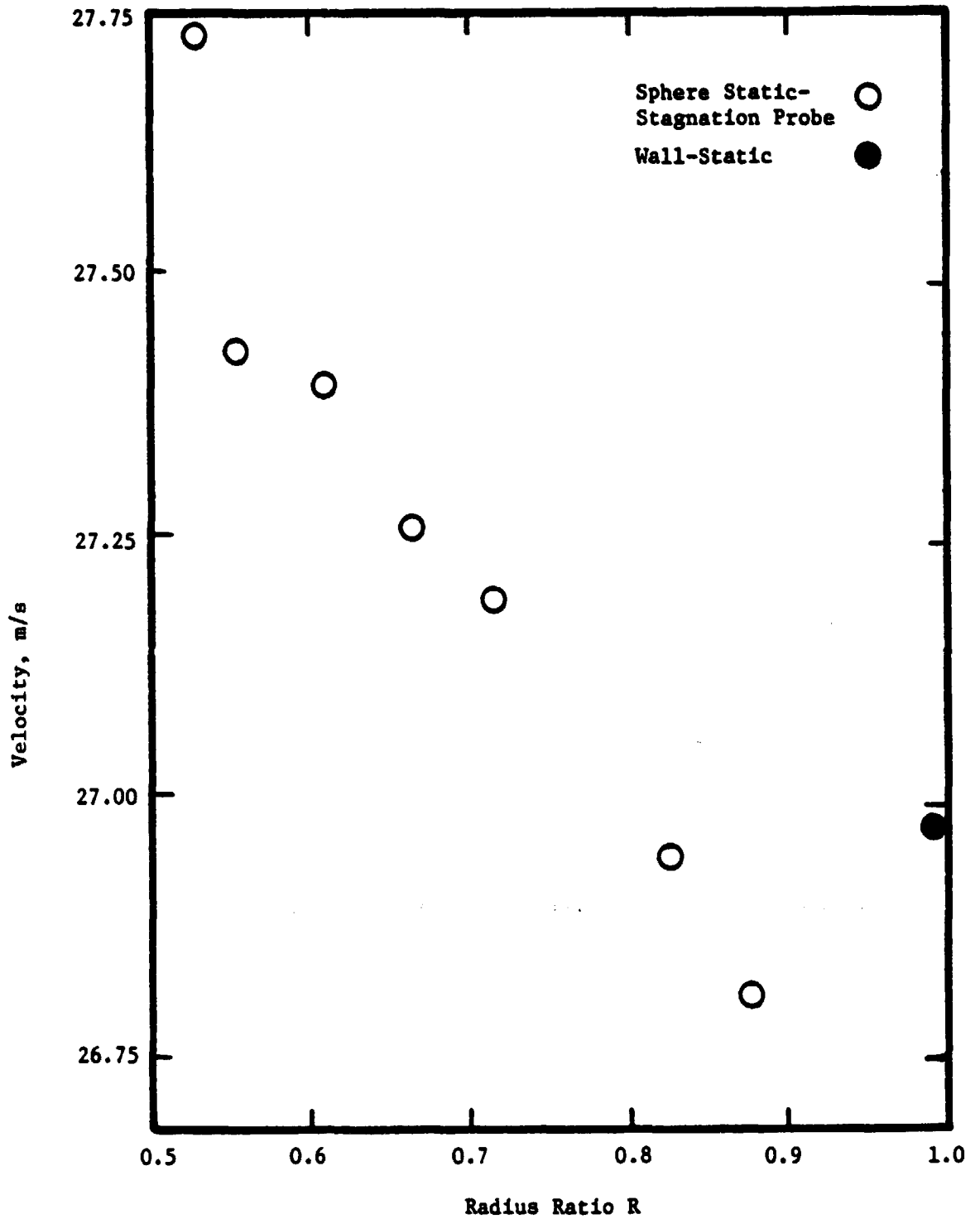


Figure 36. Velocity Across the Annulus Upstream of the Inlet Guide Vanes

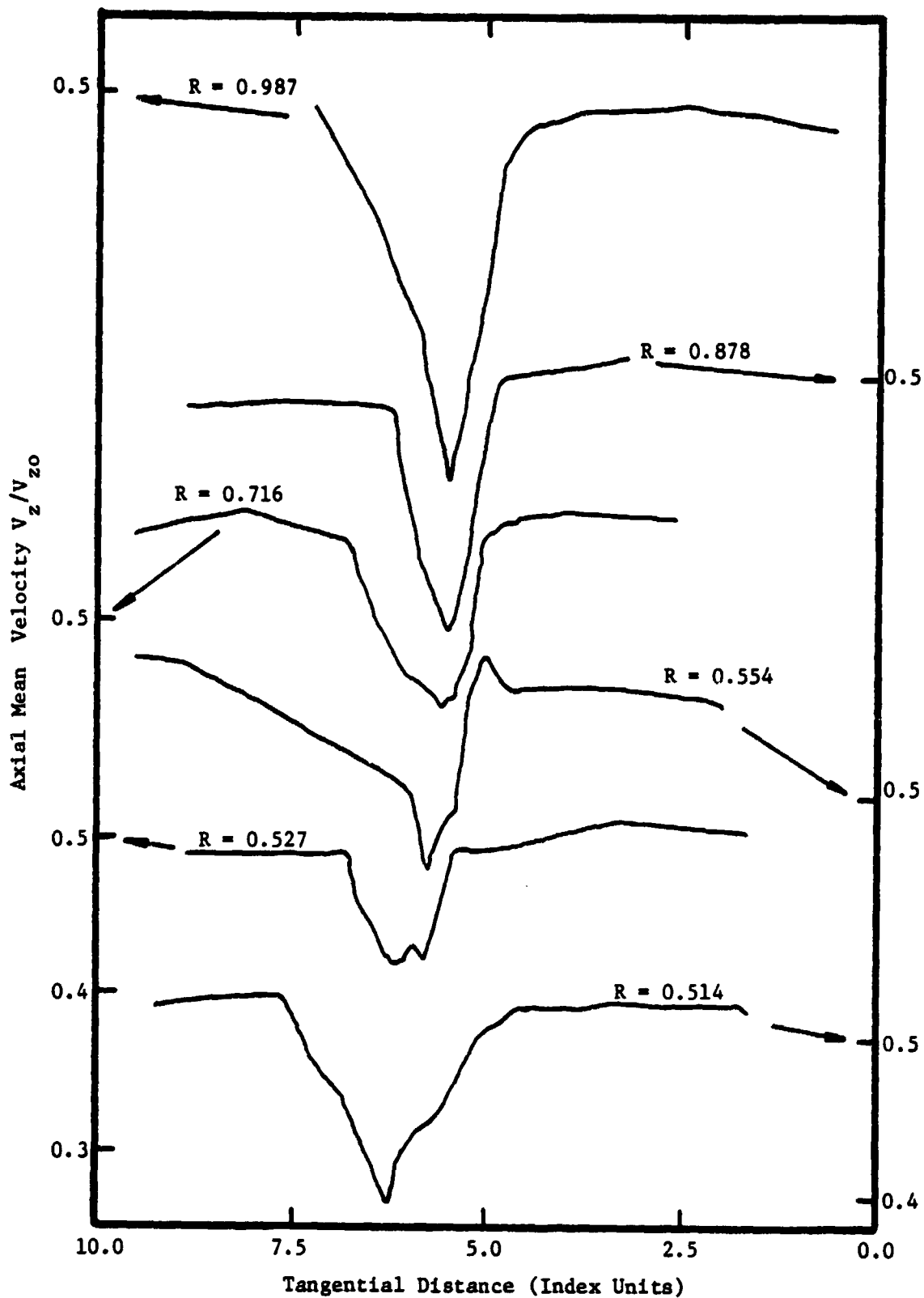


Figure 37. Tangential Variation of Axial Velocity Behind the Inlet Guide Vanes, $Z' = 0.042$, $\phi = 0.56$.

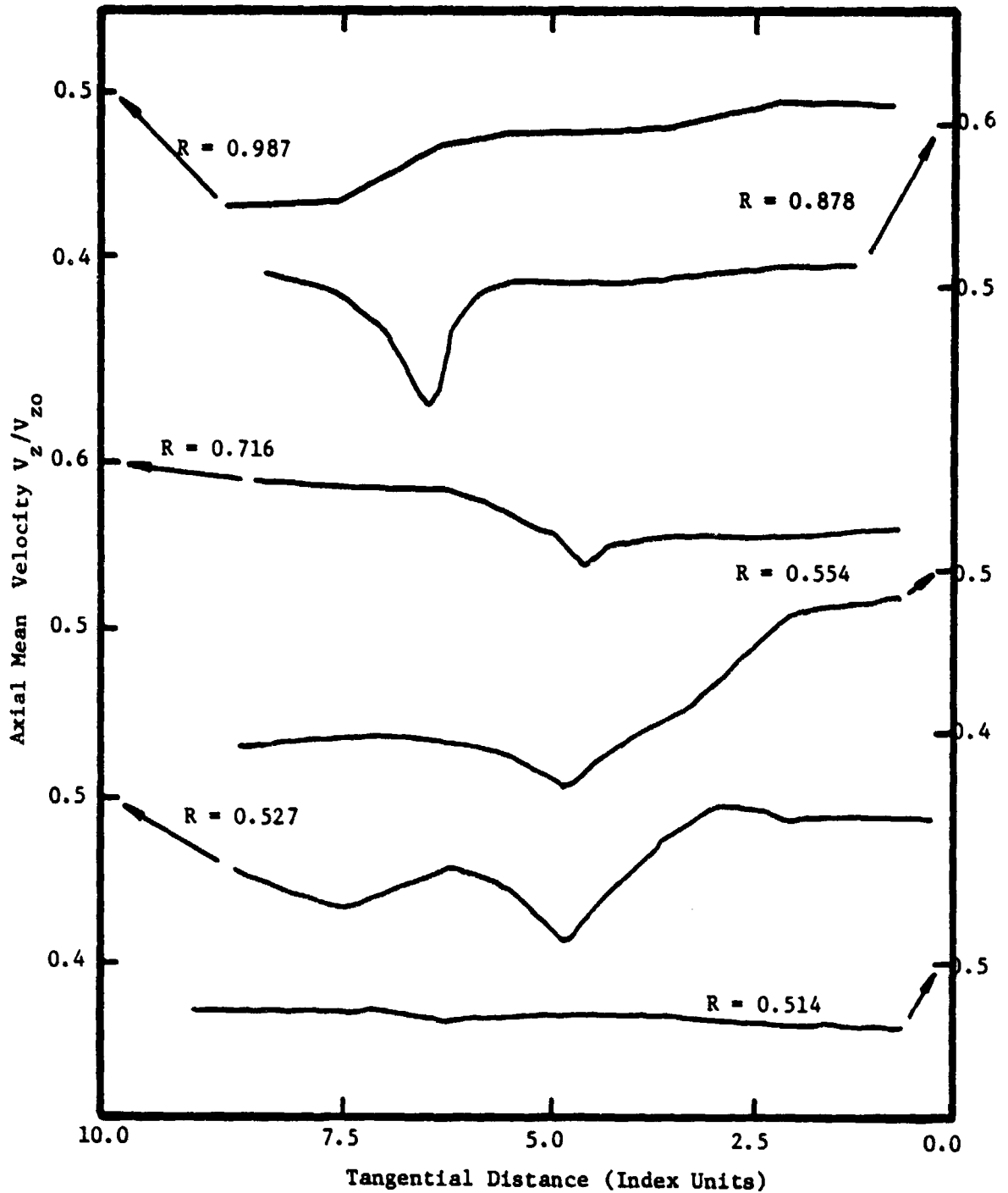


Figure 38. Tangential Variation of Axial Velocity Behind the Inlet Guide Vanes. $Z' = 1.000$, $\phi = 0.56$.

The inlet guide vanes are located 1.50 chords at the tip and 2.03 chords at the hub upstream of the rotor. At this position no appreciable distortion in mean velocity is introduced. However, a turbulence level of two percent upstream of the inlet guide vanes is amplified to approximately three percent downstream of the guide vanes. This amplification would possibly add to the overall turbulence level of the rotor passage-flow.

4.2 Mean Velocity Profiles in the Annulus-Wall Region

Tri-axial hot-wire probe measurements were used to study the properties of the rotor annulus-wall flow of a moderately loaded compressor. Mean velocity, turbulence intensity, and Reynolds stress profiles were derived from these measurements. These quantities were derived in a coordinate system which is shown in Figure 39. The orientation of this coordinate system (s, n, r), as well as the flow angle α and the meridional angle β , with respect to the compressor coordinate system (z, θ, r) is indicated. The (s, n, r) coordinate system follows the projection of the flow at the mid-passage in the radial plane for the various axial measurement stations. These measurements consisted of surveys across the rotor blade passage at various radial and axial locations. These locations are specified in Table 5. Measurements were obtained employing rotating and stationary probe data acquisition schemes. These schemes are presented in Figure 8. The rotating three-sensor probe was employed for relative velocity measurements within the rotor blade passage. The measurement surveys completed using this technique are indicated in Table 5. The stationary three-sensor probe was employed for absolute velocity measurements of

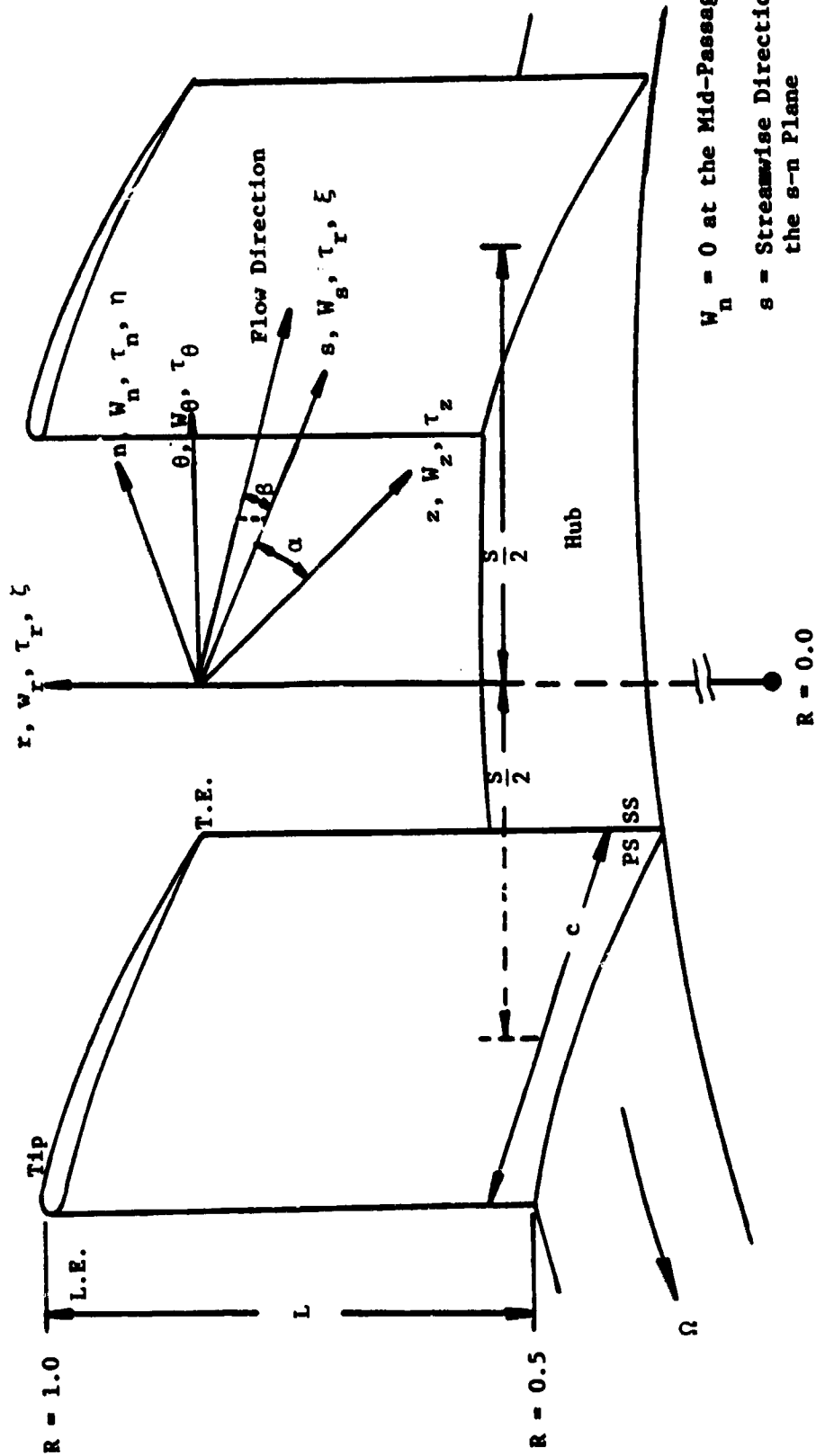


Figure 39. Definition of Streamwise Coordinate System

Table 5. Rotor Blade Annulus-Wall Flow Axial and Radial Measurement Stations

R \ Z, Z'	Passage - Flow (rotating probe)		Exit Flow (stationary probe)			
	0.750	0.979	0.021	0.042	0.125	0.458
0.986	-	-	*	*	*	*
0.980	*	*	*	*	*	*
0.973	*	*	*	*	*	*
0.959	*	*	*	*	*	*
0.945	*	*	*	*	*	*
0.918	*	*	*	*	*	*
0.891	*	*	*	*	*	*

the rotor annulus-wall exit-flow. These measurements were obtained in the stationary frame of reference and were transformed to a relative frame of reference. The radial and axial locations of these measurements are also indicated in Table 5. The data obtained by these two methods of flow measurement were analyzed by data reduction programs developed by the Penn State Turbomachinery group. A listing and brief description of the rotating and stationary data reduction programs are given by Ravindranath (1979) and Hah (1980), respectively. The rotating and stationary probe measurement programs reported in this chapter have incorporated the three-sensor hot-wire calibration and operation techniques discussed in Chapter 3. The yaw and pitch angle sensitivity of the passage-flow probe response was determined through the mat-plotting of the sensor response. The stationary probe was aligned within ± 5 degrees of the incident flow direction and a sample size of 200 was used for the data reduction. These procedures insured a good accuracy of the annulus-wall flow data.

All velocity profiles presented in this section are relative velocities. The blade passage-flow data are normalized with respect to the corresponding maximum streamwise velocity in the blade passage. The blade exit-flow data are normalized by the corresponding maximum streamwise velocity in the passage free-stream. This normalization convention allows a more continuous viewing of the data. Table 6 provides the normalization values.

It should be noted that the blade passage measurements begin at the axial location of $Z = 0.750$. Measurements were initiated at this location as a part of a comprehensive annulus-wall flow and secondary

Table 6. Maximum Streamwise Velocity* for the Reported Measurement Stations

R \ Z, Z'	Passage-Flow**		Exit-Flow**			
	0.750	0.979	0.021	0.042	0.125	0.458
0.986	---	---	0.514	0.527	0.429	0.318
0.980	0.550	0.432	0.554	0.559	0.490	0.373
0.973	0.707	0.588	0.573	0.580	0.531	0.425
0.959	0.593	0.580	0.548	0.573	0.547	0.479
0.945	0.579	0.553	0.563	0.531	0.547	0.531
0.918	0.680	0.539	0.591	0.542	0.547	0.528
0.891	0.740	0.610	0.588	0.558	0.527	0.518

*Values are normalized by the rotor blade tip speed ($\Omega_{\text{Tip}} = 51.51 \text{ m/s}$).

**Various flow parameters and scales of turbulence encountered are presented in Appendix A.

flow investigation. Complimentary measurements at upstream locations will be reported by Sitaram (1980).

4.2.1 Streamwise Mean Velocity

The variation of the streamwise velocity across the rotor blade row for various axial locations is shown plotted in Figures 40 through 45. The measurements obtained within the blade passage are given in Figures 40 and 41. These data are presented as discrete points varying tangentially across the blade passage. These data were found to be in good agreement near the blade surface with blade static-pressure measurements obtained by Sitaram (1980). Each figure presents the radial (indicated by various symbols) and tangential variation of the mean velocity where progressive figures present an axial variation of the annulus-wall flow. The tangential distance of Y_p within the blade passage and Y_e at the exit of the blade passage are normalized by the blade spacing. Within the blade passage (Figures 40 and 41), the data are plotted from the centerline of one blade to the centerline of the adjacent blade. A tangential traverse from $Y_p/S = 0.0$ to $Y_p/S = 1.0$ indicates a traverse from the suction side to the pressure side of the blade passage. The blade thickness is indicated on the abscissa of the figures. Due to the travel limitations of the probe traversing mechanism, the surveys do not extend completely to the blade surfaces. The symbols indicating radial location in Figure 40 apply to all blade-passage data and are not repeated in subsequent figures. Figures 42 through 45 present streamwise velocity profiles obtained downstream of the rotor blade passage. Due to the data

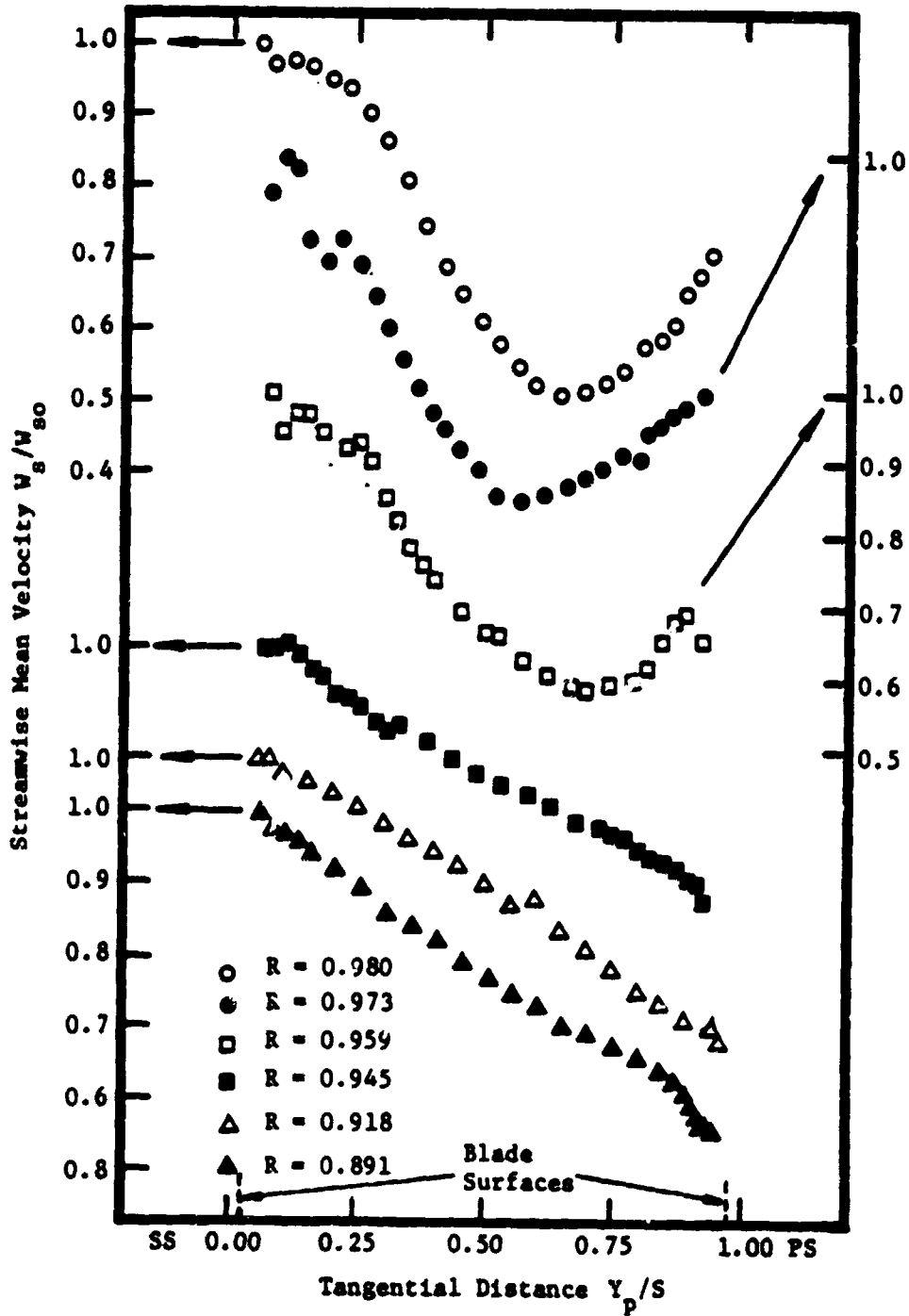


Figure 4Q Streamwise Mean Velocity Profiles, $Z = 0.750$

ORIGINAL PAGE IS
OF POOR QUALITY

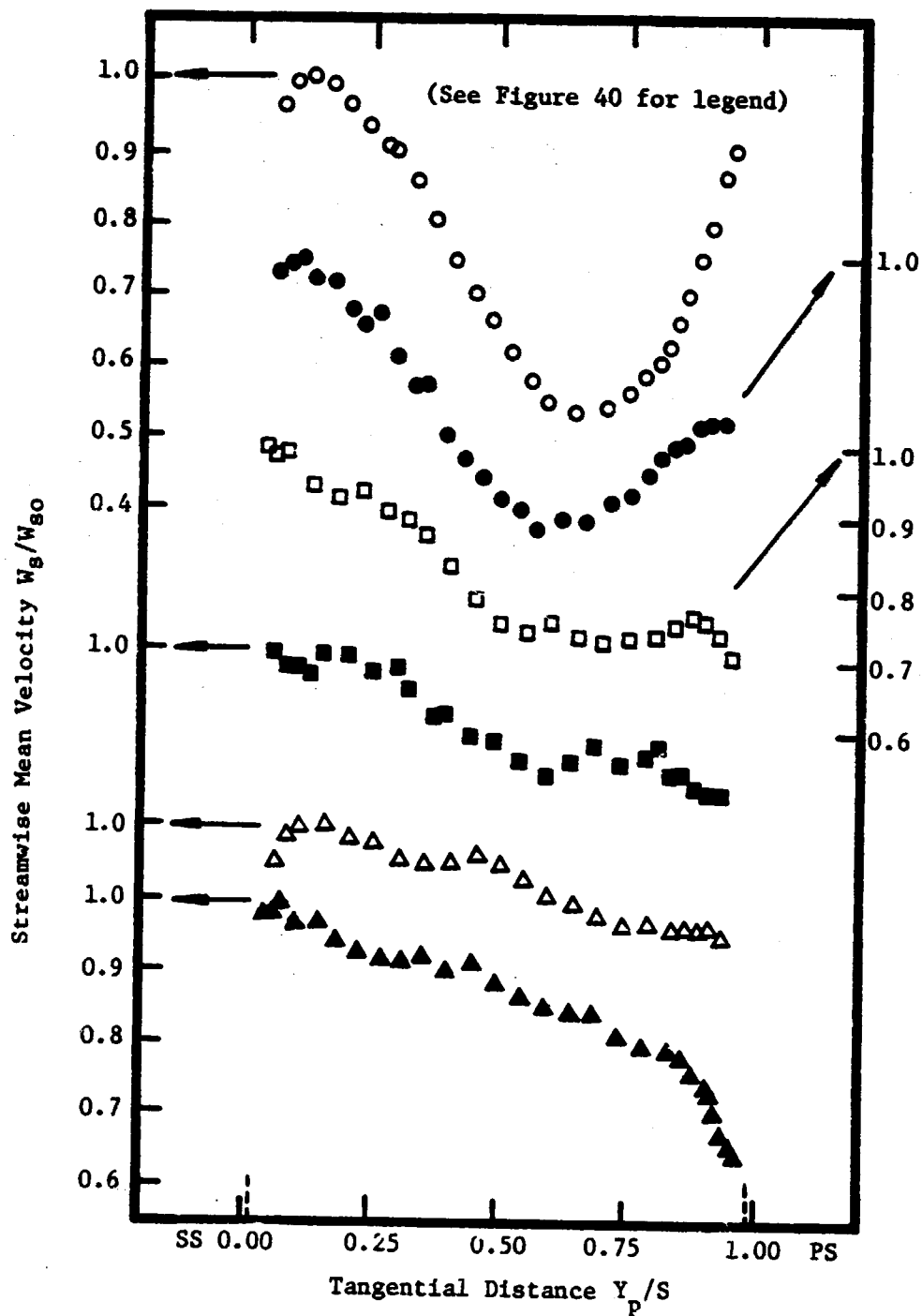


Figure 41. Streamwise Mean Velocity Profiles, $Z = 0.979$.

ORIGINAL PAGE IS
OF POOR QUALITY

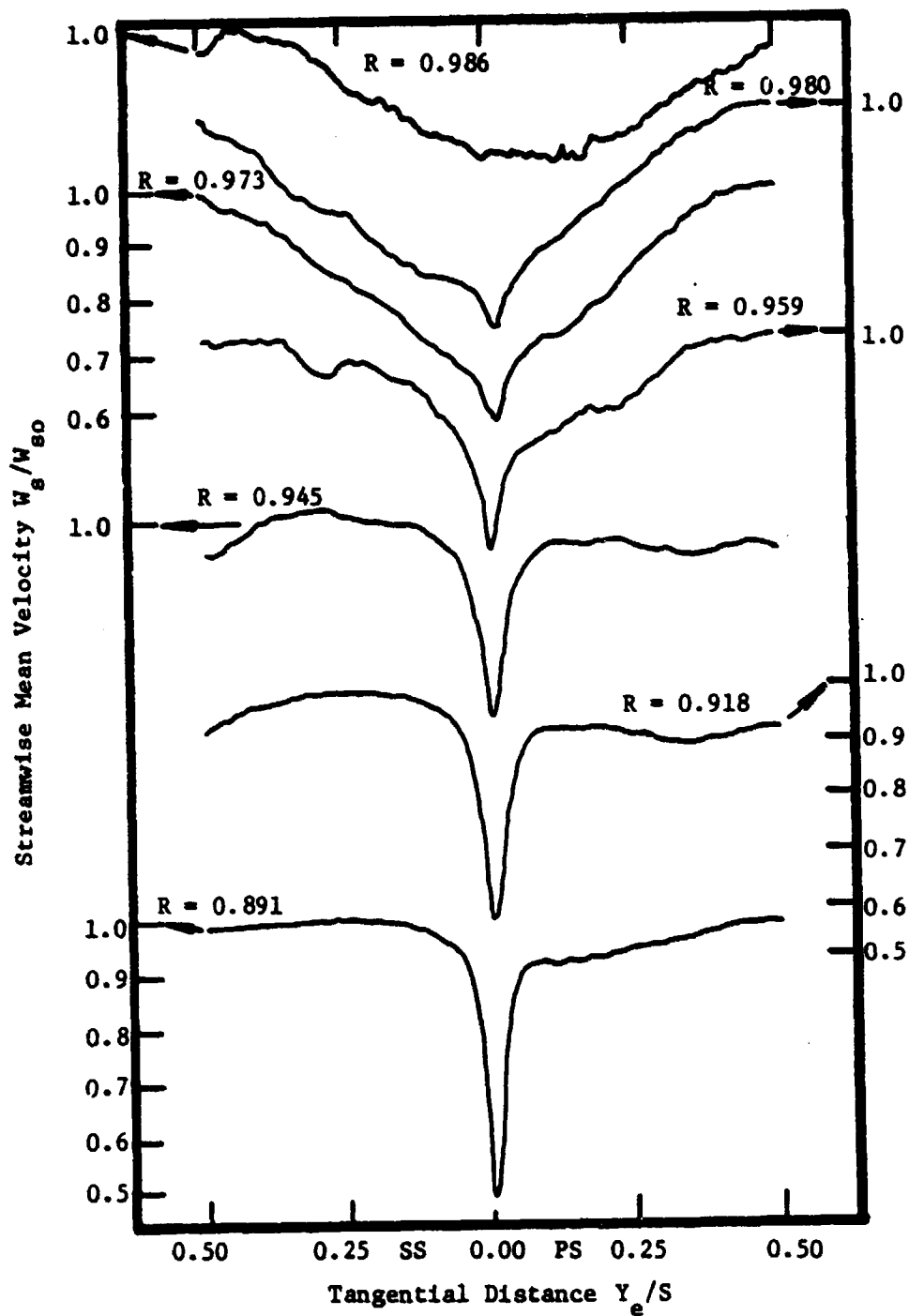


Figure 42. Streamwise Mean Velocity Profiles, $Z' = 0.021$.

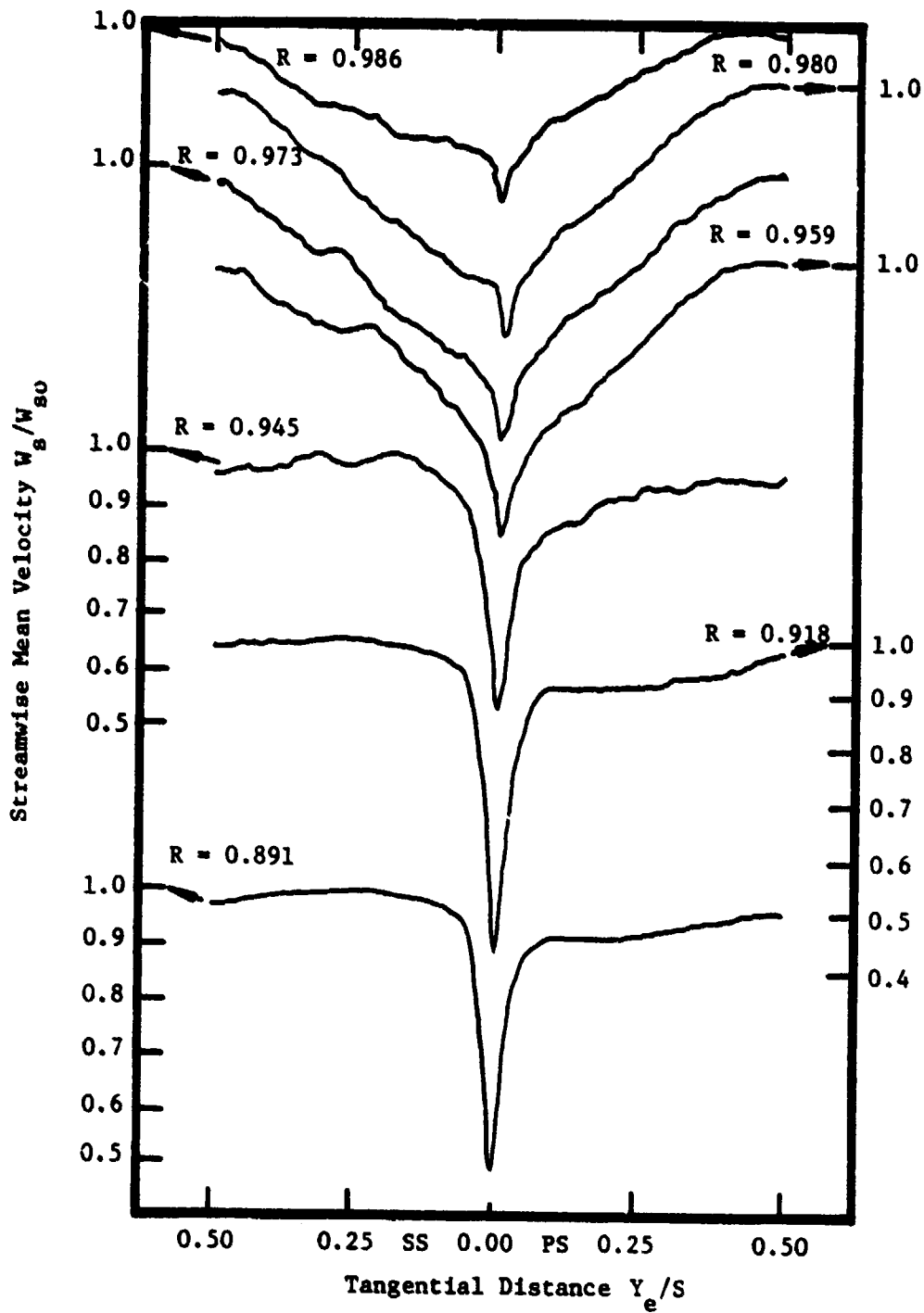


Figure 43. Streamwise Mean Velocity Profiles, $Z' = 0.042$.

ORIGINAL PAGE IS
OF POOR QUALITY

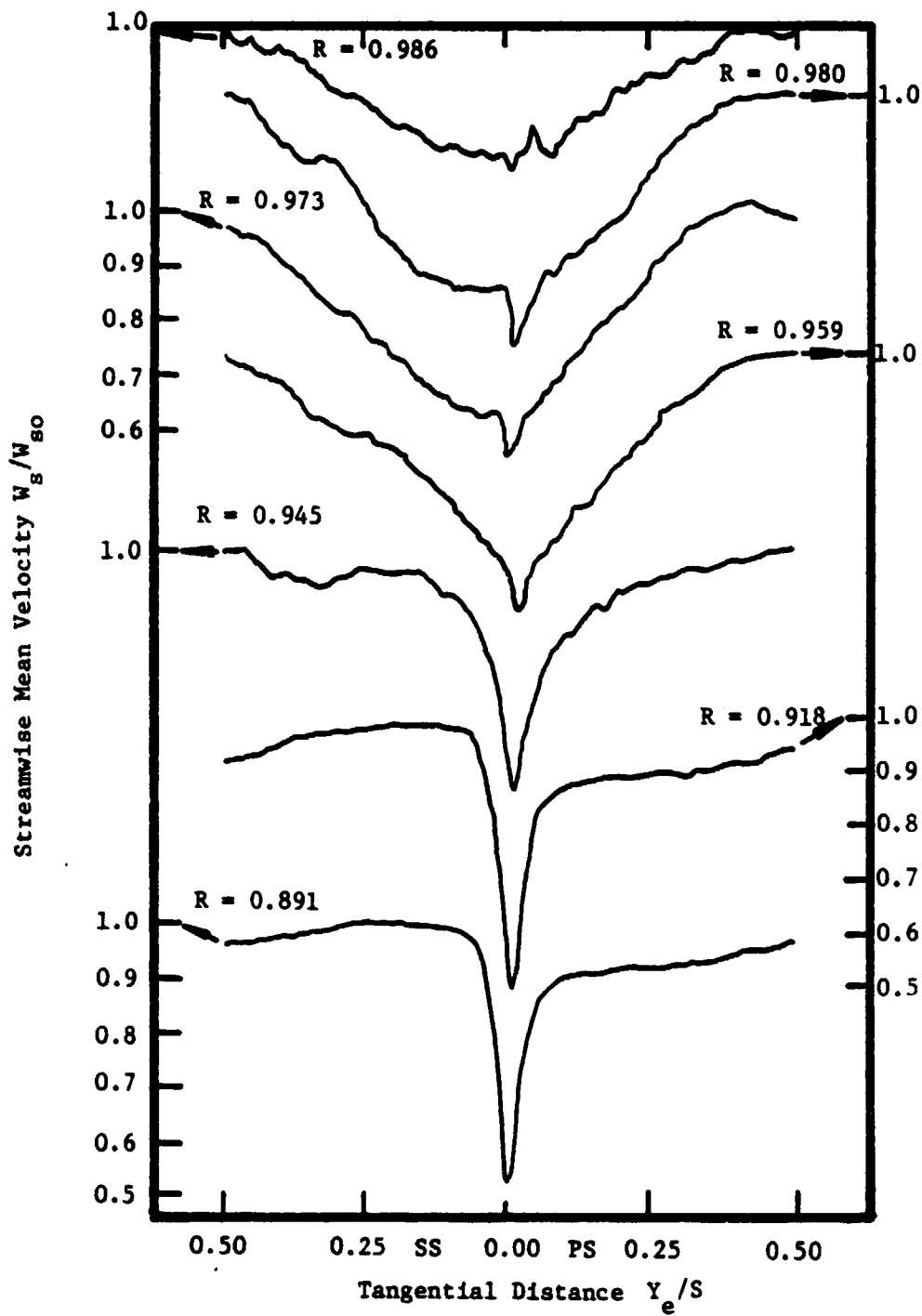


Figure 44. Streamwise Mean Velocity Profiles, $Z' = 0.125$.

ORIGINAL PAGE IS
OF POOR QUALITY

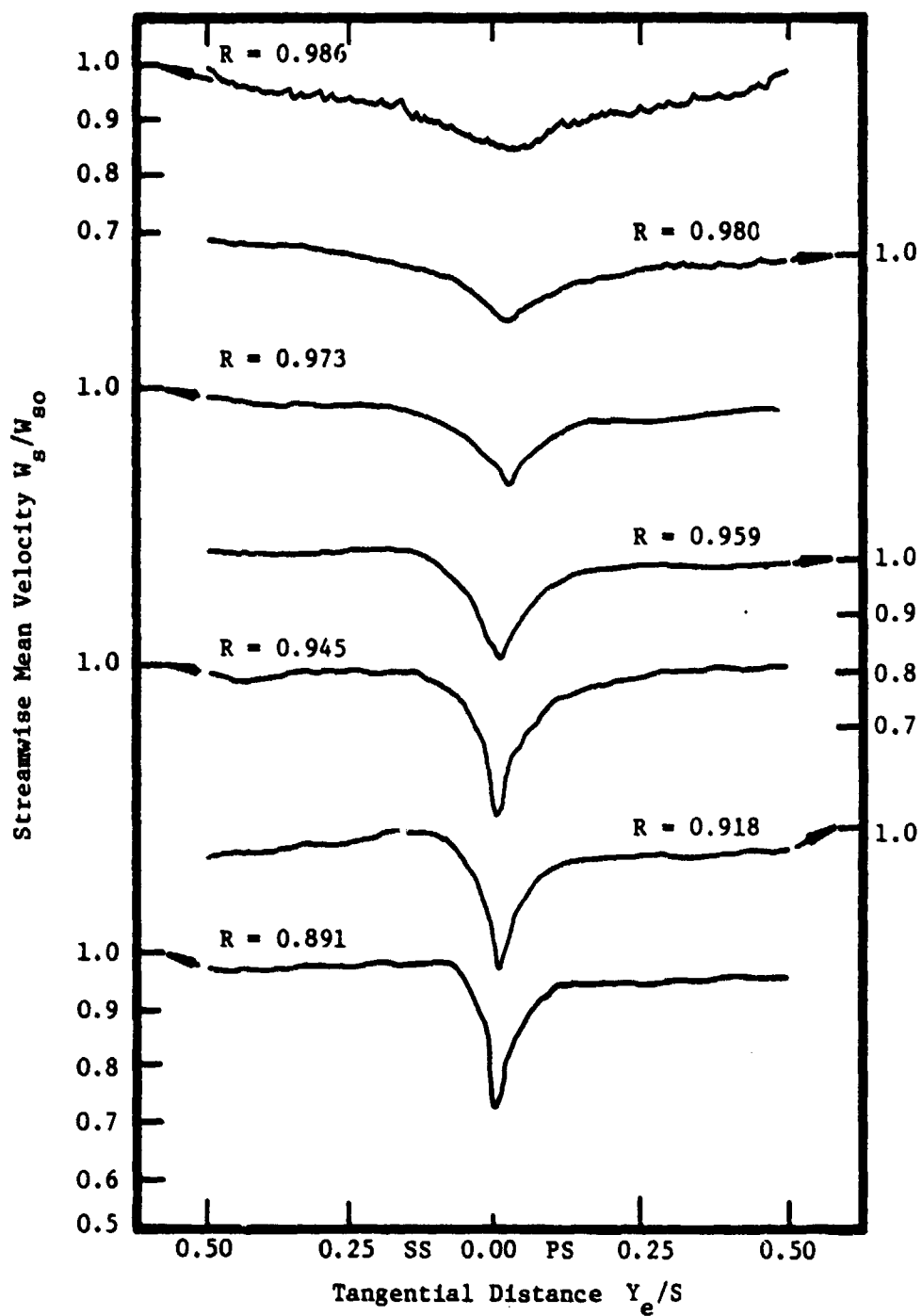


Figure 45. Streamwise Mean Velocity Profiles, $Z' = 0.458$.

acquisition and reduction techniques, these measurements are presented as a continuous profile. For each figure, these profiles present a radial and tangential variation of the annulus-wall flow. The tangential distance has been shifted by half a blade spacing from Figures 40 and 41 to more readily obtain information concerning the rotor blade wake. The pressure and suction sides of the blade wake are indicated with a tangential distance of $Y_e/S = 0.00$ indicating the wake center, and a tangential distance of $Y_e/S = 0.5$ indicating mid-distance between successive wakes. All the data presented in Figures 40 to 45 were obtained from the same rotor blade passage with the compressor stage operating at the design point with $\phi = 0.56$.

The radial variation of the flow is evident from Figures 40 and 41. At the axial location $Z = 0.750$, a distinct velocity deficiency is noted at radial locations above $R = 0.959$. Below this radius the flow shows a predominantly inviscid trend with some indications of the blade boundary layer at $R = 0.891$. The blade passage data, however, cannot accurately describe the blade boundary layer due to spatial limitations of the three-sensor hot-wire probe and the probe traversing mechanism. The inviscid flow at the lower radial locations shows a uniform increase in streamwise velocity from a value of $0.60 W_{so}$ at the pressure side, to $1.00 W_{so}$ at the suction side of the blade passage. With increasing radial location, a region of streamwise velocity deficiency becomes apparent. This deficiency is maximum at $R = 0.980$ with a value of $0.48 W_{so}$ at 65% of the blade passage width. This velocity deficiency is superimposed upon the inviscid flow. This deficiency is caused by the interaction of the blade boundary layer and the annulus-wall boundary layer. It is also possible that the

tip leakage flow and the secondary flow contribute to this deficiency. The interaction of these flows forms a region of low momentum fluid near the mid-passage of the blade tip. This results in an unconventional type of velocity profile near the blade tip, as seen in Figure 40. The existence of this "wake type" of profile is attributed to inward radial flow which is described in section 4.2.3.

A similar trend in the measurements is observed in Figure 41 for the axial location of $Z = 0.979$. At this location the predominantly inviscid flow is observed at the lower radius; however, the region of the velocity deficiency has extended to the lower radial location of $R = 0.945$. At this axial location the velocity reduction from the suction to pressure surface of the blade passage is not as large as that at $Z = 0.750$. A velocity gradient of only $0.10 W_{so}$ to $0.20 W_{so}$ is apparent. This reduction is due to the decreasing blade pressure distribution as the trailing edge of the rotor blade is approached. With increasing radius the region of the streamwise velocity deficiency becomes apparent. This velocity defect is again a maximum at $R = 0.980$ with a value of $0.60 W_{so}$ below an assumed inviscid trend at $Y_p/S = 0.65$. The region of velocity deficiency has increased with axial distance and it has also increased the value of the maximum velocity defect by 25 percent over an axial distance of approximately 0.25 blade chords. The tangential location of this region has remained the same, however.

The region of the streamwise velocity deficiency becomes especially pronounced at radial locations near the tip of the rotor blade. This is a region of maximum loss and considerable flow mixing which

results in strong eddies and associated energy dissipation. A concentration of high turbulence intensities was measured in this region and is reported in a later section of this chapter.

The blade to blade variation of the streamwise velocity at various radial locations behind the blade row is presented in Figure 42 through 45 for various axial locations. The dominant feature of these profiles is the character of the rotor blade wake and its interaction with the annulus-wall flowfield. At radial locations below $R = 0.945$, there is little flow interaction and the wake profiles are clearly defined. These wake profiles are asymmetrical about the wake center. This indicates the differential growth of the boundary layers on the two surfaces of the rotor blade. This is to be expected as the suction-surface boundary layer is thicker than the pressure-surface boundary layer. This asymmetry is maintained even at the last axial location which is approximately half-a-chord downstream of the rotor blade trailing-edge and is observed in the normal and radial velocity profiles. The existence of the pressure gradient across the blade passage is evident from Figures 40 and 41; however, it is also shown to exist immediately downstream of the blade trailing-edge. This is reflected in the free-stream velocity distributions of Figure 42 through 45. The streamwise velocity is greater on the suction side of the wake than on the pressure side of the wake. This effect persists to approximately half-a-chord downstream of the blade row.

For the radial locations at $R = 0.945$ and above, the rotor blade exit-flow interacts strongly with the annulus-wall boundary layer. This is a region of predominately viscous flow. The blade passage-flow

with a region of velocity deficit combines with the blade boundary layers and the annulus-wall boundary layer. This flow interaction results in a marked decrease in velocity behind the rotor blade which encompasses more tangential distance with increasing radial location. The merger of the blade boundary layer with the annulus-wall boundary layer results in a large increase in the wake width as the annulus wall is approached. This radial trend is observed at all axial locations behind the rotor.

The effect of radial location upon the wake defect (w_s/W_{so}) is seen from Figures 42 through 45. At the axial location $Z' = 0.021$, the wake defect is 0.51 at $R = 0.891$ which reduces to 0.25 at $R = 0.986$. This trend is similar for all the axial locations. The wake exhibits the tendency to become symmetrical with radial distance. This tendency is due to the radially outward transport of mass, momentum, and energy in the blade boundary layer and is observed in the normal and radial wake profiles. This radially outward flow interacts with the annulus-wall boundary layer to create a region of considerable flow mixing in the blade wake.

The development of the annulus-wall blade wake in the axial direction can be seen in Figures 42 through 45. For the wake near the trailing-edge, the velocity gradients in the tangential direction are very large. The steep gradient at the lower radial locations represents highly unstable and developing flow conditions. The gradient becomes smaller as the flow moves downstream because of the wake spreading and mixing with the free-stream. At radial locations above $R = 0.945$, the wake covers the entire blade passage and hence reflects the effect of the complex flow interactions. In this region

the wake also decays with axial distance. A wake defect of $w_s/W_{so} = 0.25$ at $R = 0.986$ and $Z' = 0.021$ decays to 0.15 at $Z' = 0.458$. This decay is due to the wake mixing with the free-stream and the annulus-wall boundary layer.

The maximum defect in streamwise velocity is greater at the lower radial location of $R = 0.945$ than at the tip. This indicates the faster decay rate of the wake near the blade tip and is presumably caused by the flow mixing described earlier. A comparison of Figures 42 and 45 shows that the wake near the tip decays faster than the wake at lower radii.

4.2.2 Normal Mean Velocity

The variation of the normal mean velocity within the rotor blade passage is presented in Figures 46 and 47. Due to the definition of the coordinate system shown in Figure 39, the normal velocity is zero at the mid-passage location. Figure 48 presents the variation of the passage-flow angle α at the suction-surface, mid-passage, and pressure-surface tangential location within the blade passage with radial distance. Figures 46, 47, and 48 allow an interpretation of the passage-flow relative to the blade geometry.

At the axial location of $Z = 0.750$ and radial locations below $R = 0.959$, the data indicates an increase in normal velocity from the suction-surface to the pressure-surface of the blade. This trend is due to the turning of the flow by the blade row. Figure 48 shows that at these locations the flow follows the blade surface, thus following the inviscid streamlines. Figure 48 also shows that the

ORIGINAL PAGE IS
OF POOR QUALITY

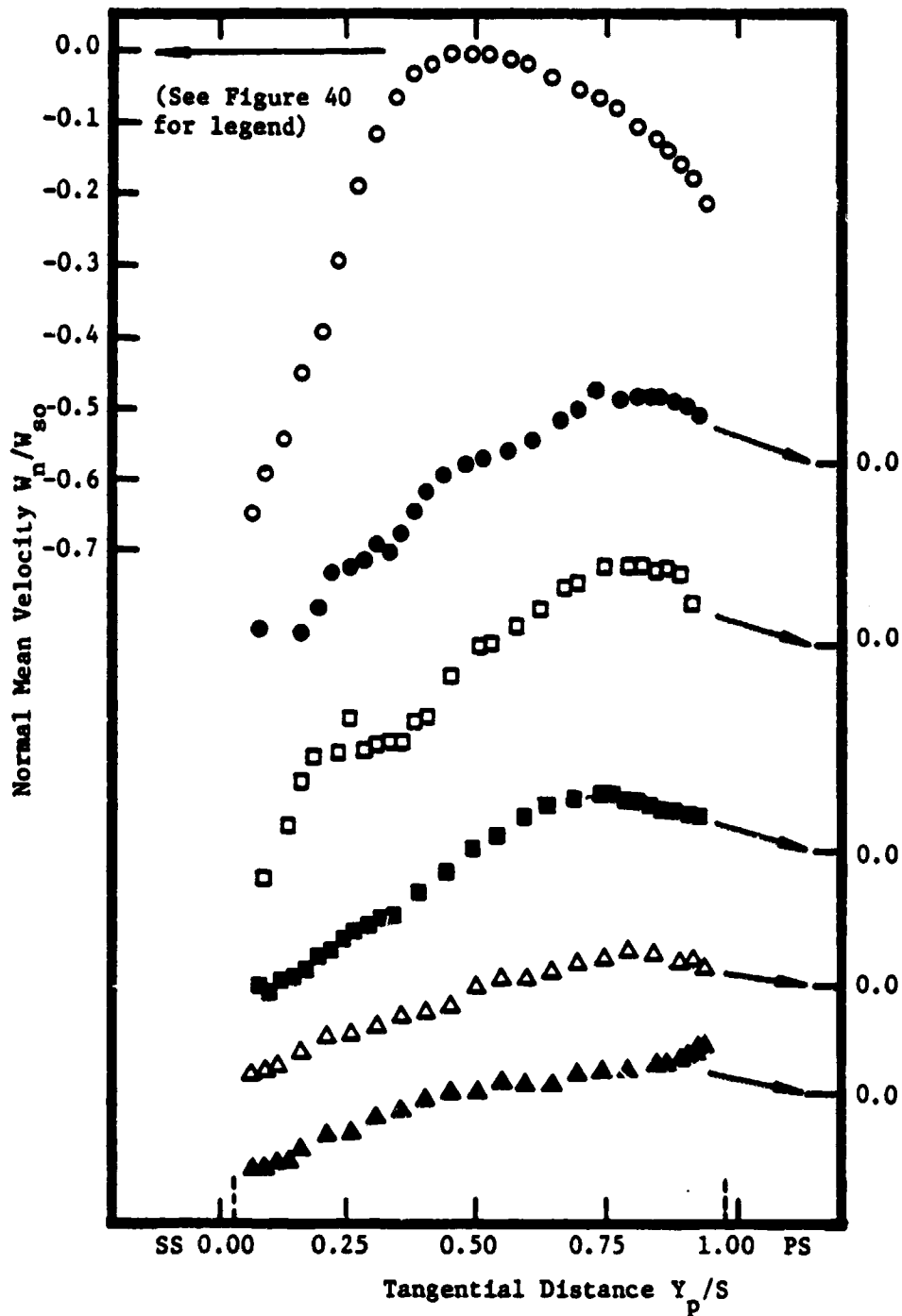


Figure 46. Normal Mean Velocity Profiles, $Z = 0.750$.

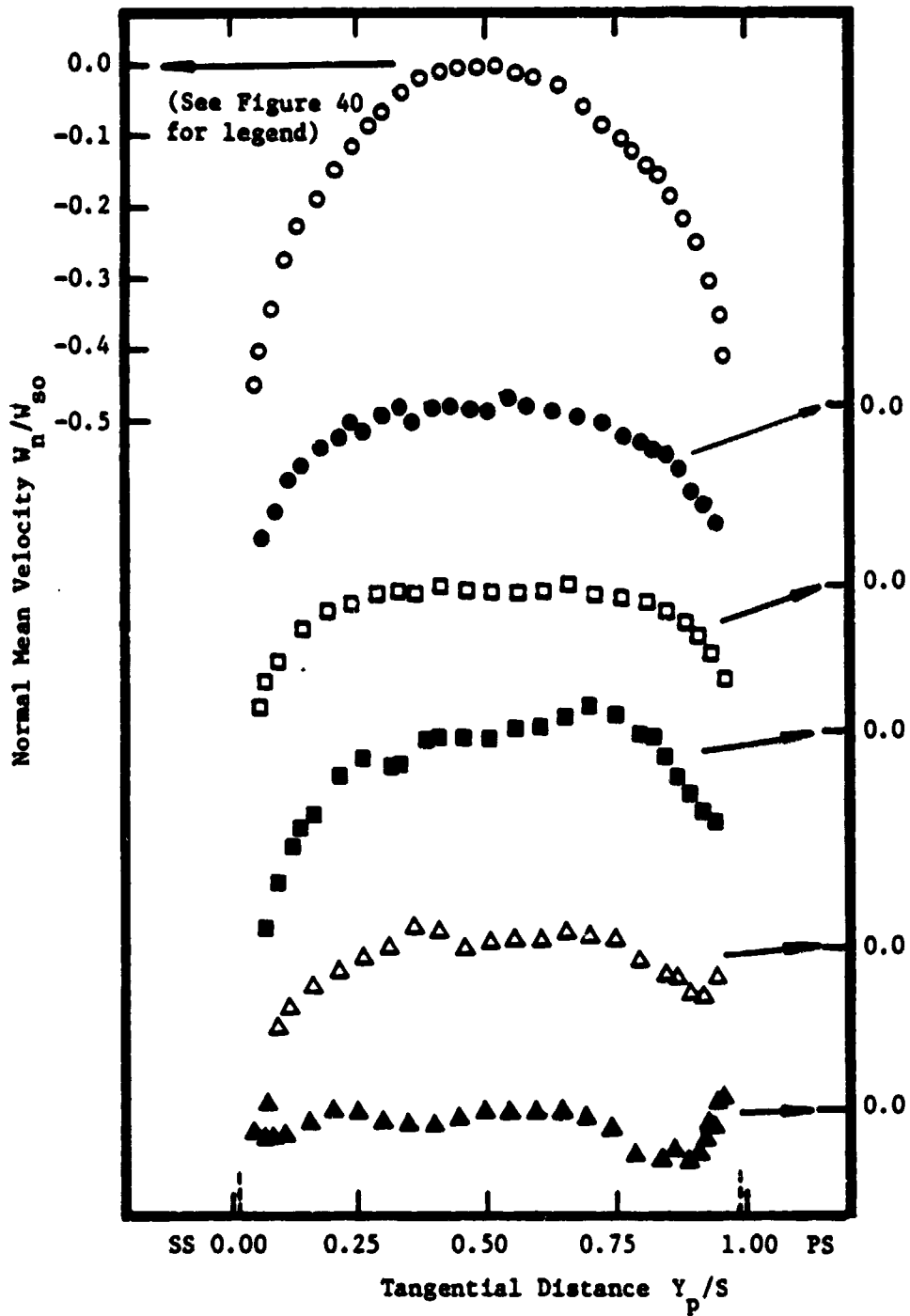


Figure 47. Normal Mean Velocity Profiles, $Z = 0.979$.

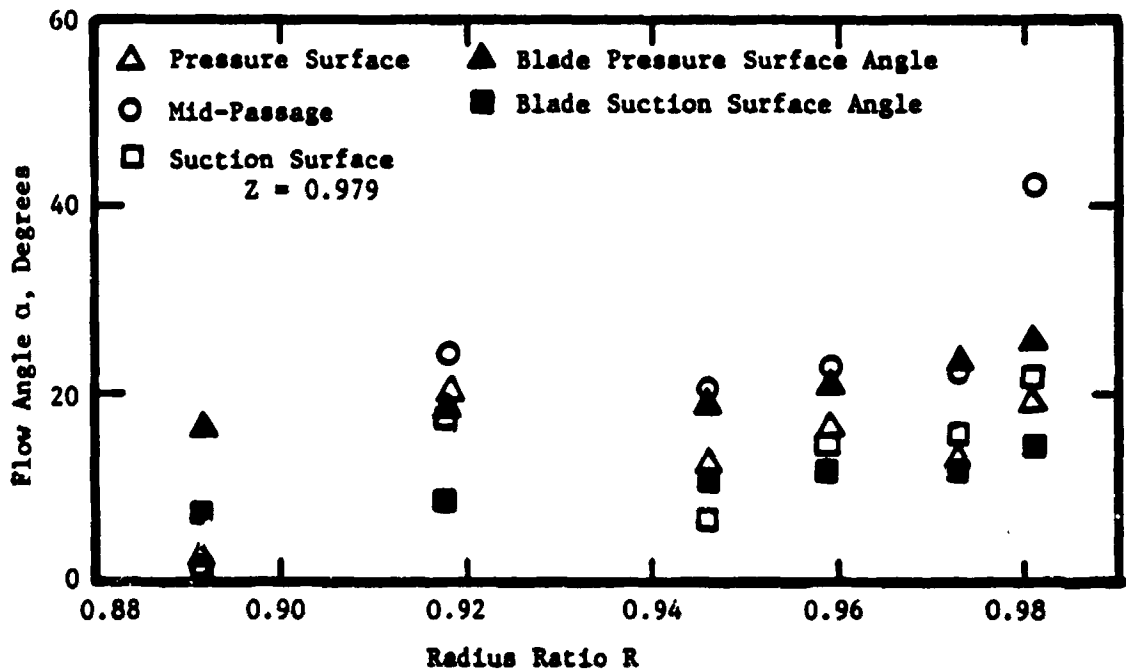
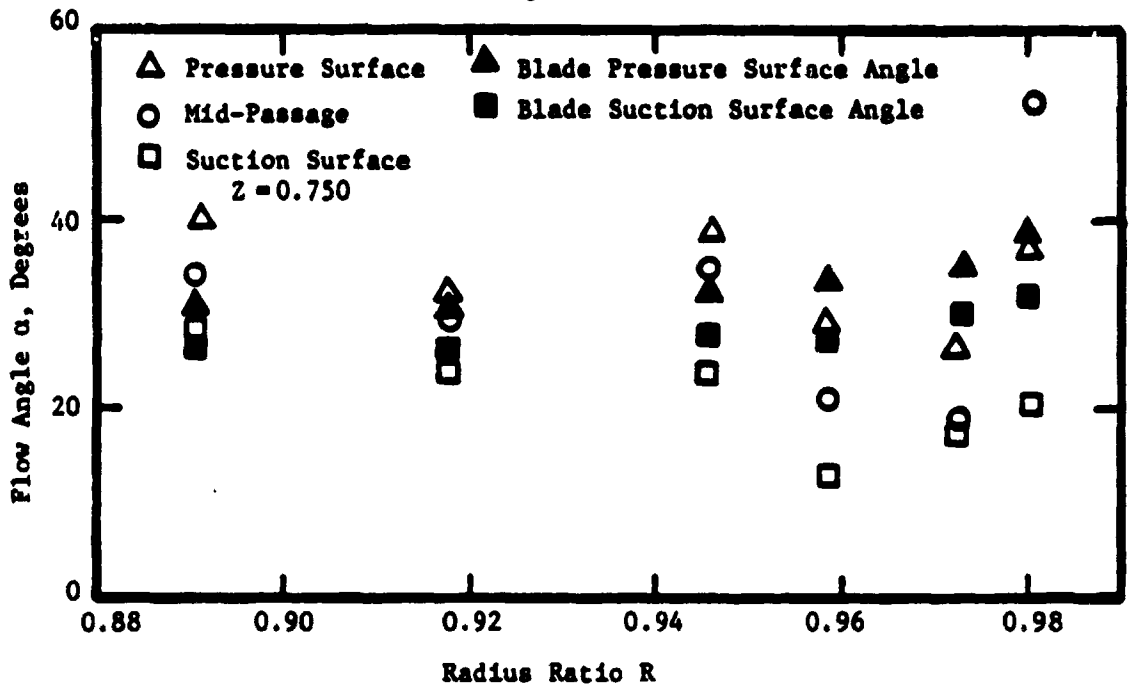


Figure 48. Variation of the Blade Passage-Flow Angle in the s-n Plane

flow is deflected away from the mean streamline near the suction-surface and visa-versa near the pressure-surface of the blade. The turning of the passage-flow is an inviscid flow phenomenon which is also observed at $Z = 0.979$.

Figures 46 and 47 show that substantial deviations from the inviscid trend occur at radial locations near the blade tip. At $Z = 0.750$ and radial locations above $R = 0.945$, the flow is overturned. A maximum of 15 degrees of overturning is seen to occur at $R = 0.959$. This flow overturning on the suction side of the blade passage is due to the interaction of the tip leakage flow and the main-stream flow. The tip leakage flow upon leaving the tip clearance gap begins to roll up and form a vortex which then proceeds downstream. This overturning may also have been caused by the presence of annulus-wall boundary layer. The entry flow is at a higher angle of attack and hence may deflect more through the passage. Another possible reason for the overturning is the secondary flow, whose vorticity is given by:

$$\xi_e - \xi_1 = 2\varepsilon \frac{\partial W}{\partial r} \quad (15)$$

Attempts are being made to measure the inlet velocity profile and calculate the secondary flow and hence the overturning/underturning from this expression. It is suspected that the leakage flow and the scraping vortex plays a major role in the overturning observed in these regions. At this location within the blade passage, the tip leakage flow rolls up toward the suction surface of the blade to produce substantial overturning of the flow.

At the axial location $Z = 0.750$ and radial locations above $R = 0.945$ the flow is overturned. This is evident by viewing Figures 46, 47, and 48. Only flow overturning is observed due to the restricted radial survey. The measurements were limited to radii below the clearance height due to the requirement that the rotating probe must maintain an adequate clearance between itself and the annulus wall. Figures 46 through 48 indicate the rolling up of the tip leakage flow in this region. However, this is complicated by the radially outward flow within the blade boundary layers. As a result, considerable flow interaction occurs in this region. The resulting flow interactions produce intense flow mixing and losses.

The existence of an interaction between the radially outward flow in the blade boundary layer and the main-stream flow is also observed at the pressure side of the rotor passage. This is shown in Figures 46 and 47. These figures show an overturning of the flow on the pressure side of the blade passage primarily at the axial location of $Z = 0.750$ and also at $Z = 0.979$. A deflection of the blade boundary layer towards the center of the blade passage is observed. This deflection produces a region of intense flow mixing and losses. This region of flow interaction was observed in the streamwise mean velocity profiles presented in the previous section.

Figures 46, 47, and 48 show that the normal velocity within the blade passage increases rapidly towards the rotor mid-passage. This

is seen to occur at radial locations above $R = 0.973$. This increase in normal velocity results in a large underturning of the flow in the region. The underturning of the flow is due to the viscous interaction between the annulus-wall boundary layer and the blade passage-flow. This interaction is characterized by a dragging of the low momentum fluid near the annulus-wall in the positive normal direction. This phenomenon is augmented by the tip leakage flow at this radial location. The combined effect is a large underturning of the flow at the rotor mid-passage location.

Figures 46 and 47 show that the region of flow interaction is confined to radial locations above $R = 0.918$. The characteristic intense flow mixing and large losses associated with radial locations near the blade tip are not seen below $R = 0.918$. Figures 46 and 47 indicate that a region of inviscid flow exists across the blade passage at the axial locations $Z = 0.750$ and $Z = 0.979$. At the axial location of $Z = 0.750$ the flow is seen to be substantially turned by the blade row. At $R = 0.891$ and $Z = 0.750$ a normal velocity of $-0.11 W_n/W_{so}$ on the suction surface of the blade increases to $0.9 W_n/W_{so}$ on the pressure surface of the blade. As the flow approaches the trailing edge of the blade it is only turned slightly by the blade row. This is observed at $R = 0.891$ and $Z = 0.750$ where the normal velocity is approximately the same on both blade surfaces.

The tangential variation of the normal velocity with radial and axial location downstream of the rotor passage is given by Figures 49 through 52. The exit-flow angle α at the mid-passage location for these axial locations is shown in Figure 53. The exit-flow exhibits inviscid trends below the radial location of $R = 0.945$. The normal

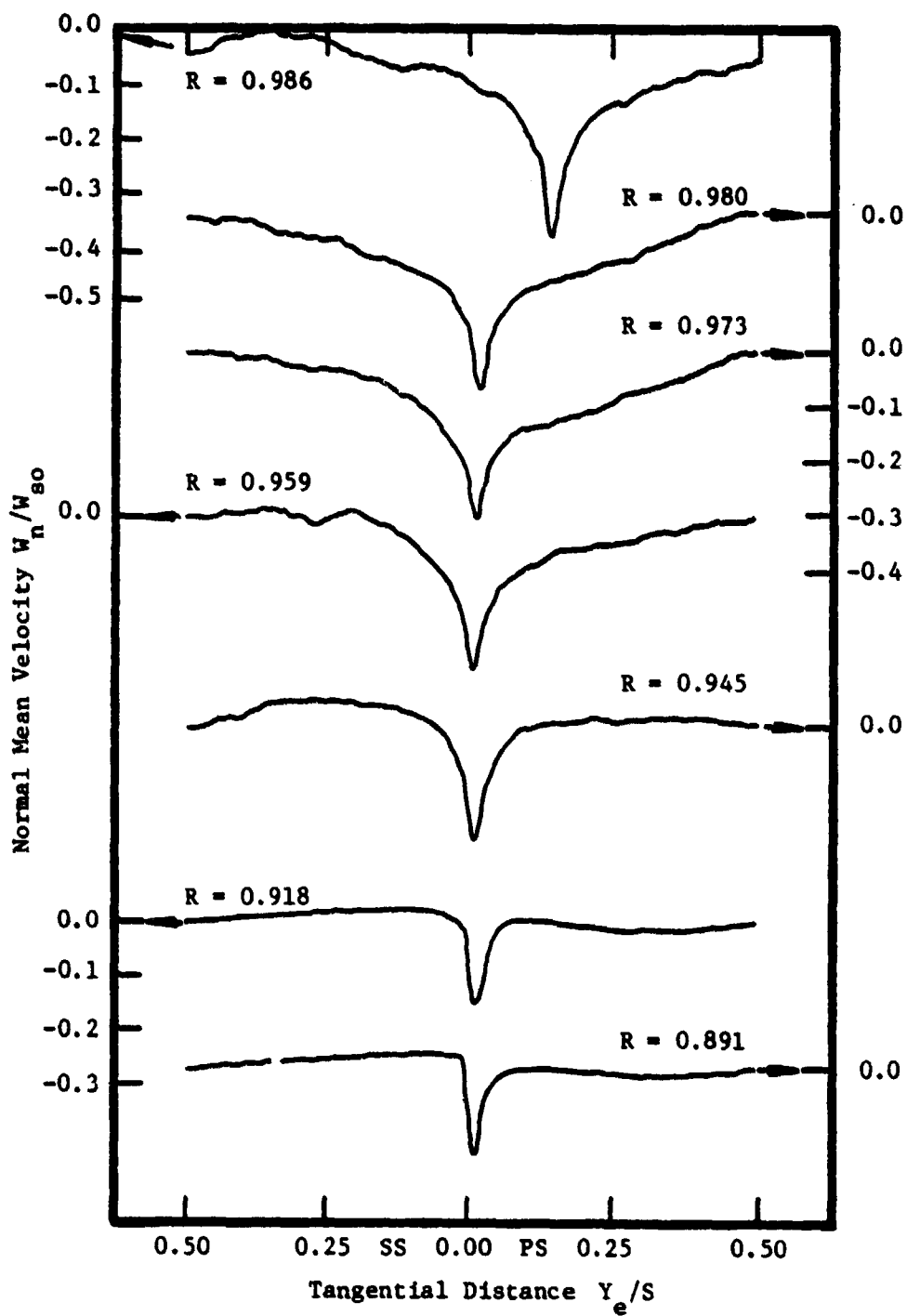


Figure 49. Normal Mean Velocity Profiles, $Z' = 0.021$.

ORIGINAL PAGE IS
OF POOR QUALITY

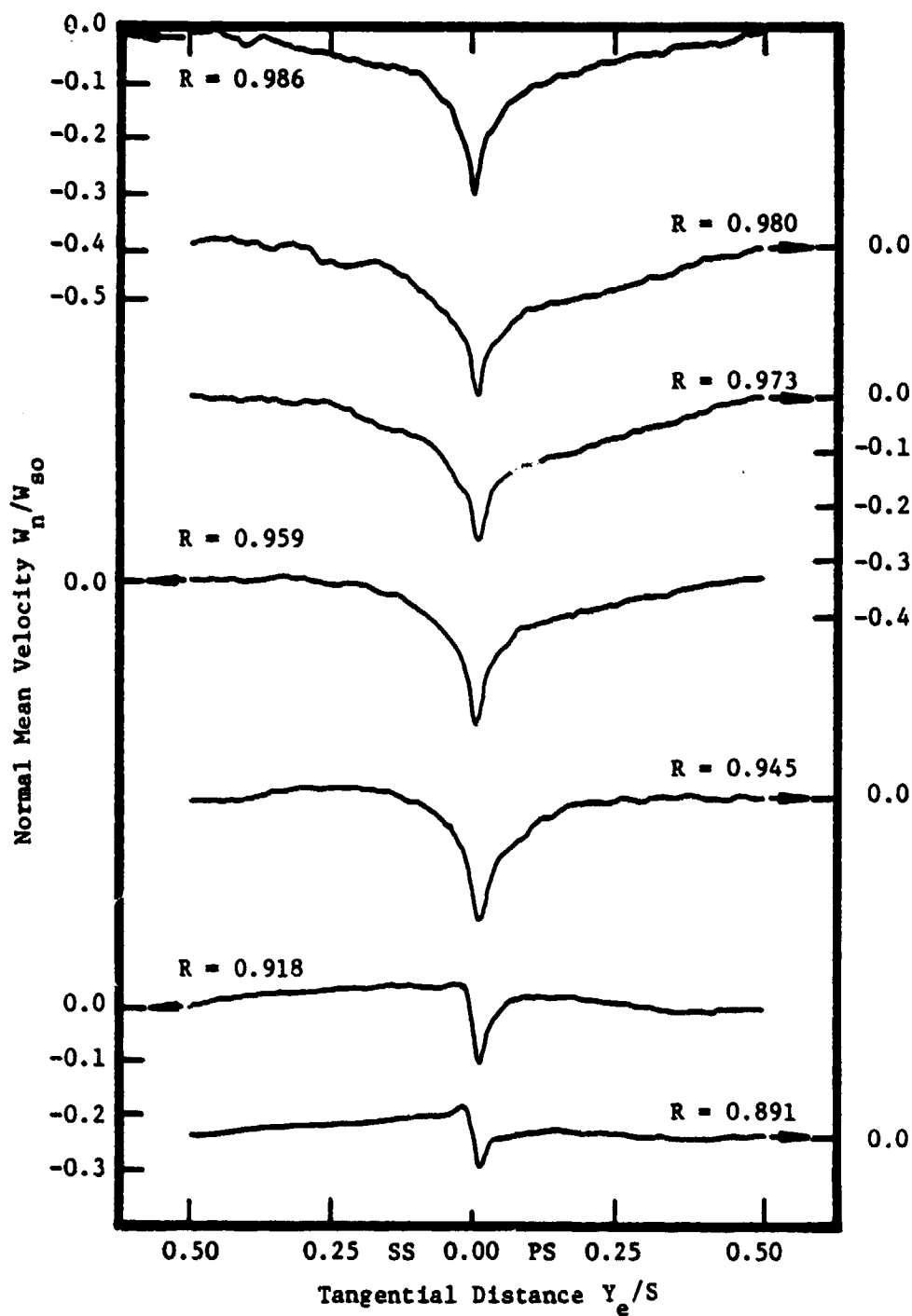


Figure 50. Normal Mean Velocity Profiles, $Z' = 0.042$.

ORIGINAL PAGE IS
OF POOR QUALITY

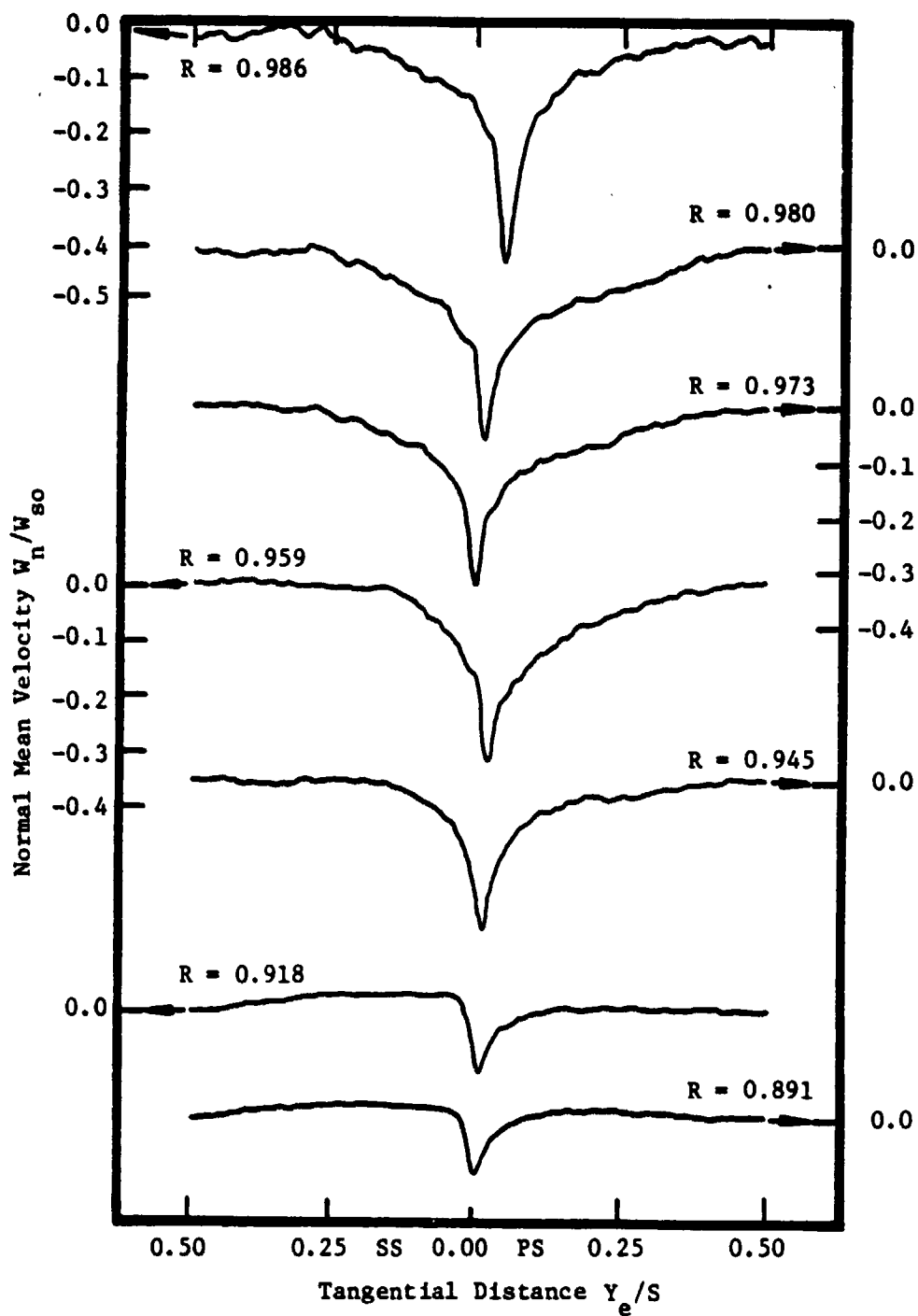


Figure 51. Normal Mean Velocity Profiles, $Z' = 0.125$.

ORIGINAL PAGE IS
OF POOR QUALITY

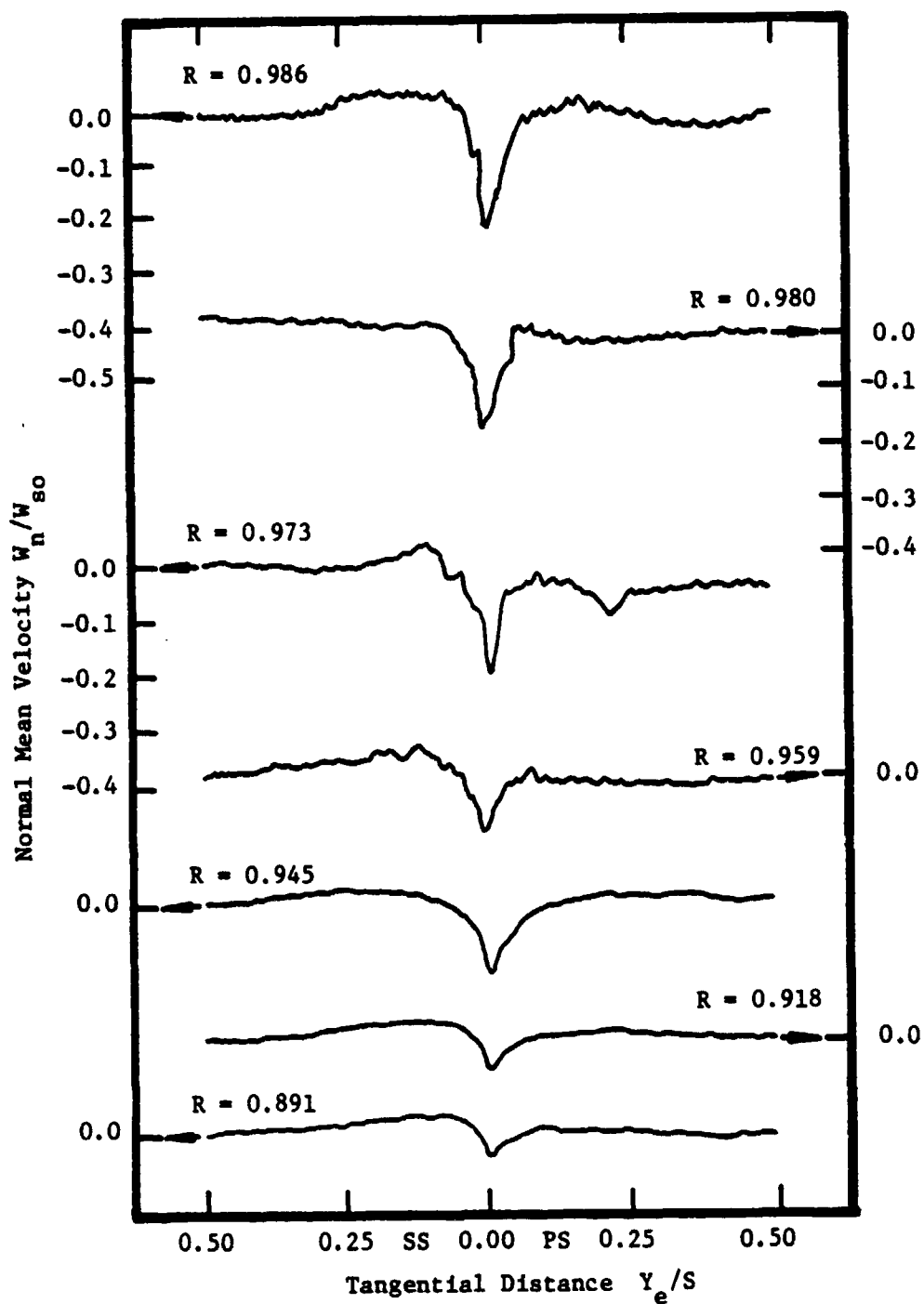


Figure 52. Normal Mean Velocity Profiles, $Z' = 0.458$.

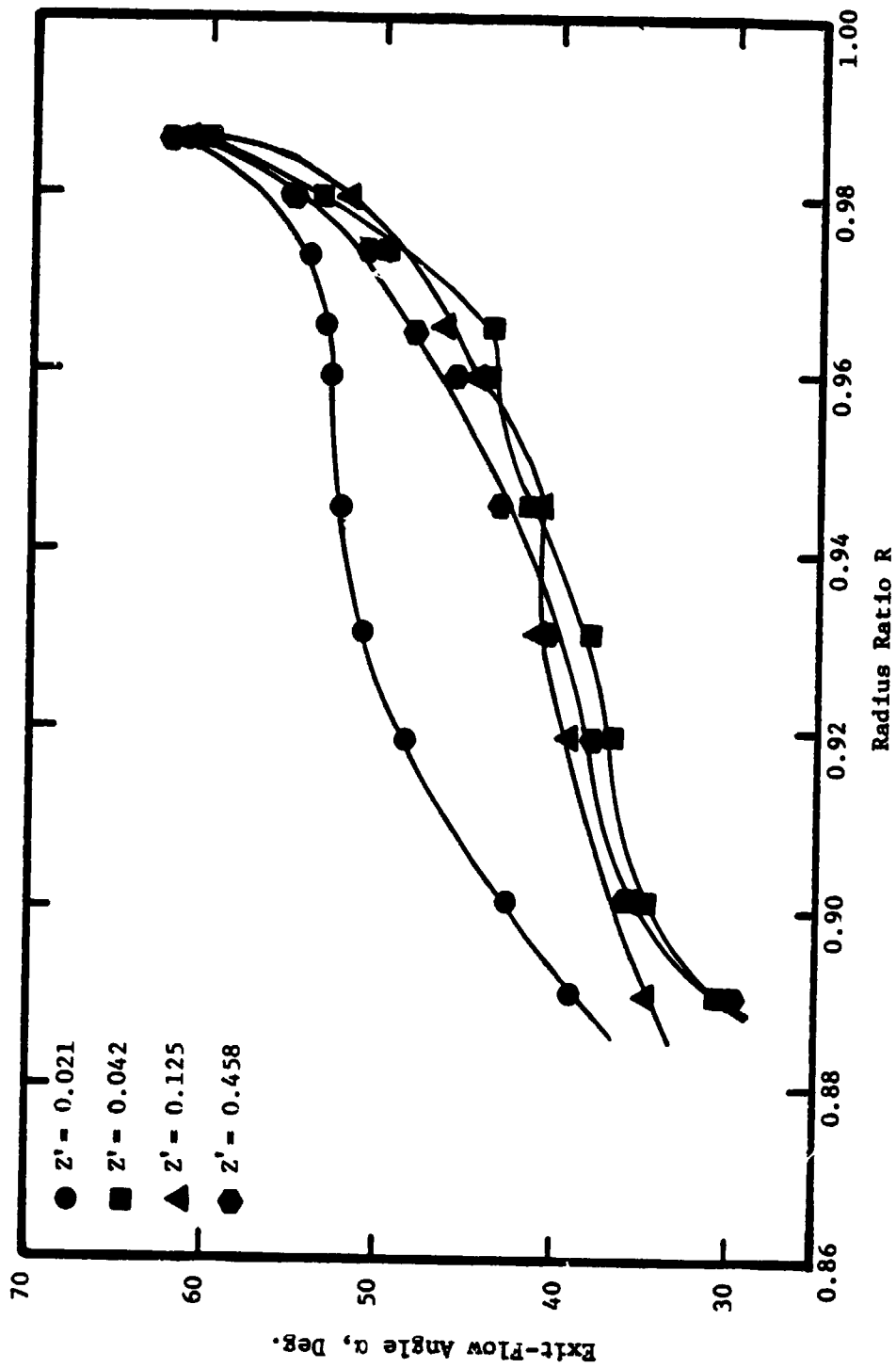


Figure 53. Variation of the Blade Exit-Flow Angle in the s-n Plane.

velocity decreases sharply at the tangential location of the wake and then gradually decays with axial distance. A normal velocity (W_n/W_{so}) of 0.17 at $R = 0.891$ and $Z' = 0.021$ decreases to 0.07 at $Z' = 0.458$. The diffusion and dissipation of the flow is due to the wake mixing with the free-stream flow.

The normal velocity in the wake increases with radial location. This increase is due to the increase of the boundary layers on the blade surface. Possible additional effects are due to the annulus-wall boundary layer and the tip leakage flow.

Figure 53 shows the variation of the exit-flow angle with radial and axial location. The various axial stations are indicated in the figure. The general trend of increasing flow angle with radius is similar to that observed within the blade passage. The effect of the annulus-wall boundary layer is seen at the blade tip where the flow angle of the relative flow remains about the same with axial distance. At this location, the flow is being dragged by the annulus-wall boundary layer. This results in the large overturning of the flow in this region.

Figures 49 through 52 reveal a very interesting fact. As with the streamwise and radial mean velocity profiles of the exit-flow, the normal velocity profiles do not indicate the presence of the tip leakage vortex. In Chapter 3 it was determined that an unsteady flow phenomena could not be determined through an ensemble-average technique of data reduction. This technique was employed for the stationary probe data obtained in the rotor exit-flow region. Thus the tip leakage vortex would not be discerned from the data, if it was unsteady in nature. The existence at the tip leakage flow inside

the blade passage was observed and discussed above. The formation and roll up of the tip leakage flow could be unsteady in nature due to non-uniform rotor tip clearance and non-identical blades. If this condition existed, it would be difficult to discern the tip leakage flow in the exit data.

4.2.3 Radial Mean Velocity

Radial velocity profiles for the various radial and axial locations are shown plotted in Figures 54 through 59. These profiles show that the radial velocities increase with an increase in radius.

The tangential variation of the radial velocity within the rotor blade passage is shown in Figures 54 and 55. These figures indicate negative radial velocities for the radii near the tip with maximum values occurring at approximately 30 percent of the tangential distance from the suction-surface of the blade. The radially inward flow at this location indicates the extent of interaction between the blade boundary layers and the annulus-wall boundary layer. The radial flows inside the suction- and pressure-surface boundary layers tend to roll toward mid-passage, interact, and produce strong vortices and radially inward flows. These flows are probably caused by the blade boundary layer interaction with the annulus-wall boundary layer and the tip leakage flow. This phenomenon was investigated by Lakshminarayana (1973) for the flow inside an inducer passage. Figures 54 and 55 show the variation of the radial velocity which indicates rapid flow mixing near the blade tip. The radial velocity (W_r/W_{so}) of 0.20 at $Z = 0.750$ and $R = 0.980$ has diminished drastically at $R = 0.973$. This rapid decrease of the radial velocity is also

ORIGINAL PAGE IS
OF POOR QUALITY

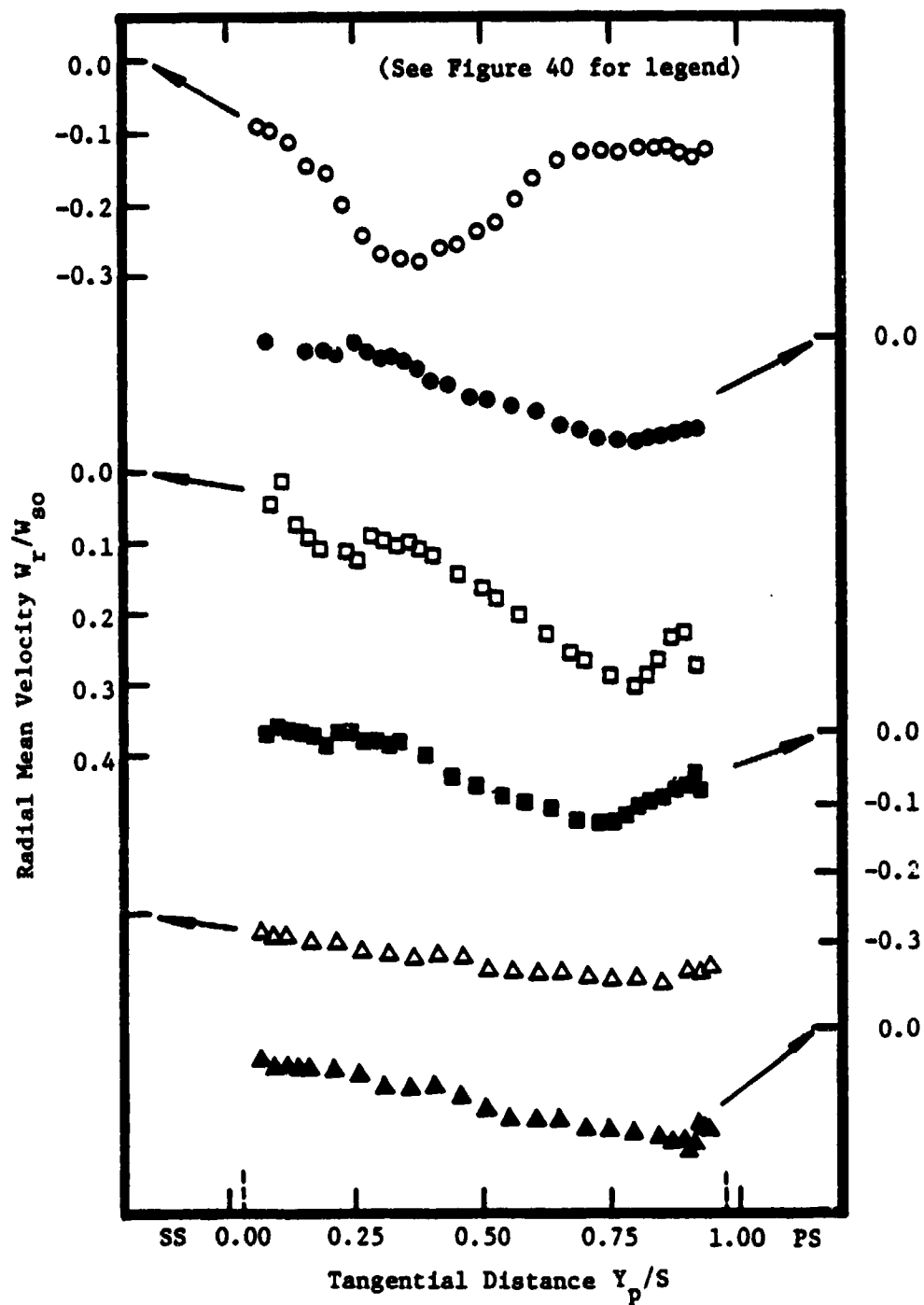


Figure 54. Radial Mean Velocity Profiles, $Z = 0.750$.

ORIGINAL PAGE IS
OF POOR QUALITY

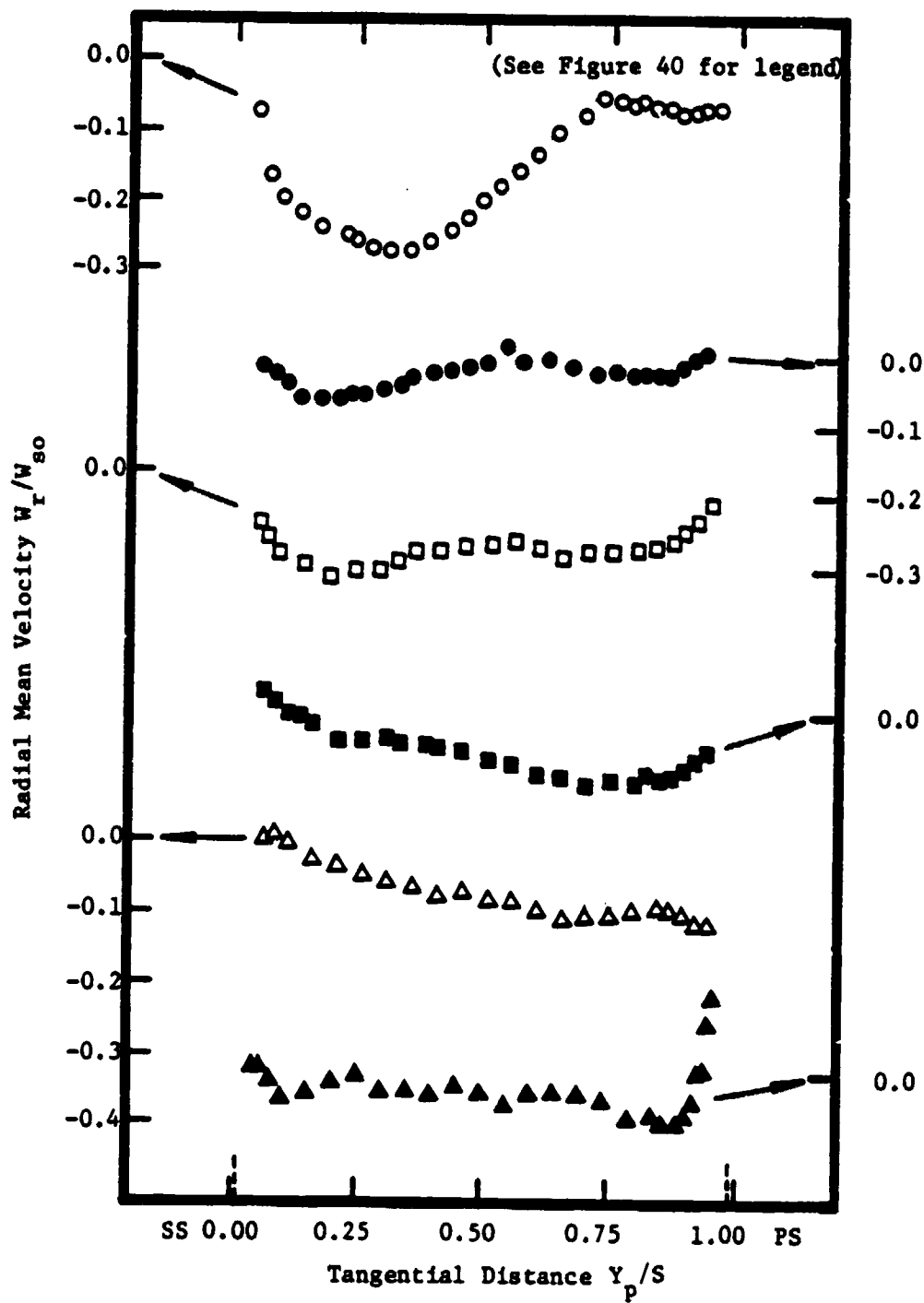


Figure 55. Radial Mean Velocity Profiles, $Z = 0.979$.

ORIGINAL PAGE IS
OF POOR QUALITY

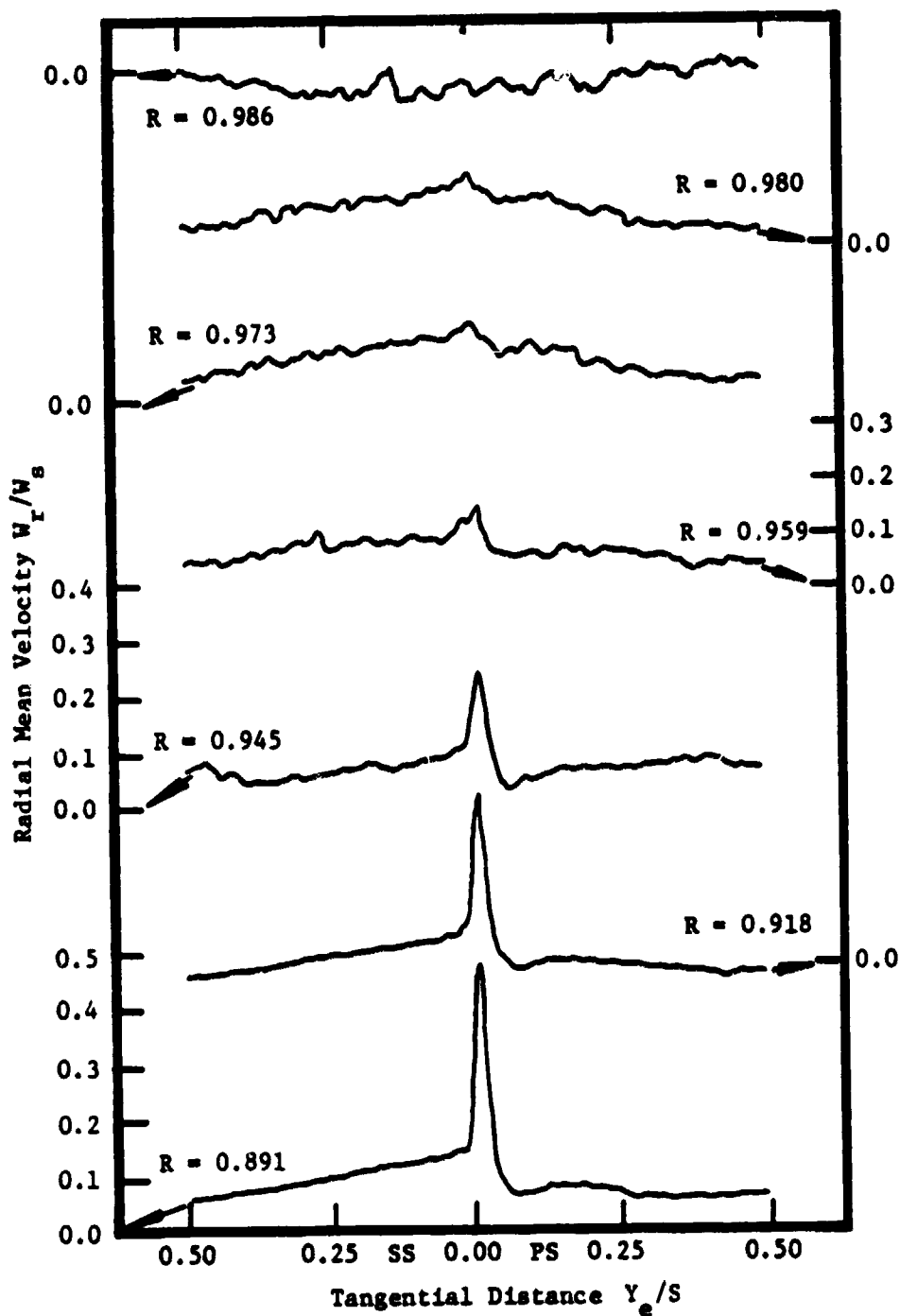


Figure 56. Radial Mean Velocity Profiles, $Z' = 0.021$.

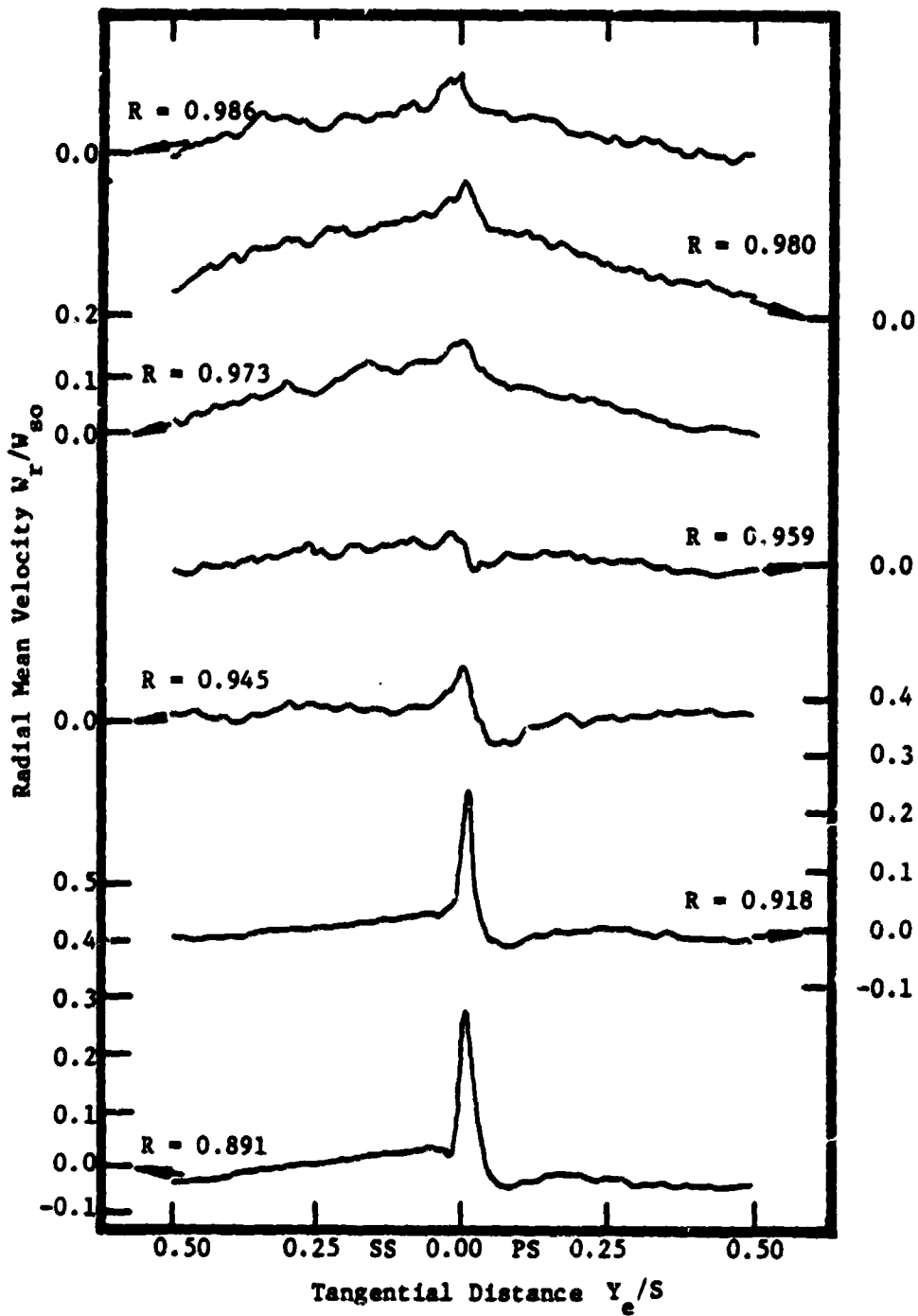


Figure 57. Radial Mean Velocity Profiles, $z' = 0.042$.

ORIGINAL PAGE IS
OF POOR QUALITY

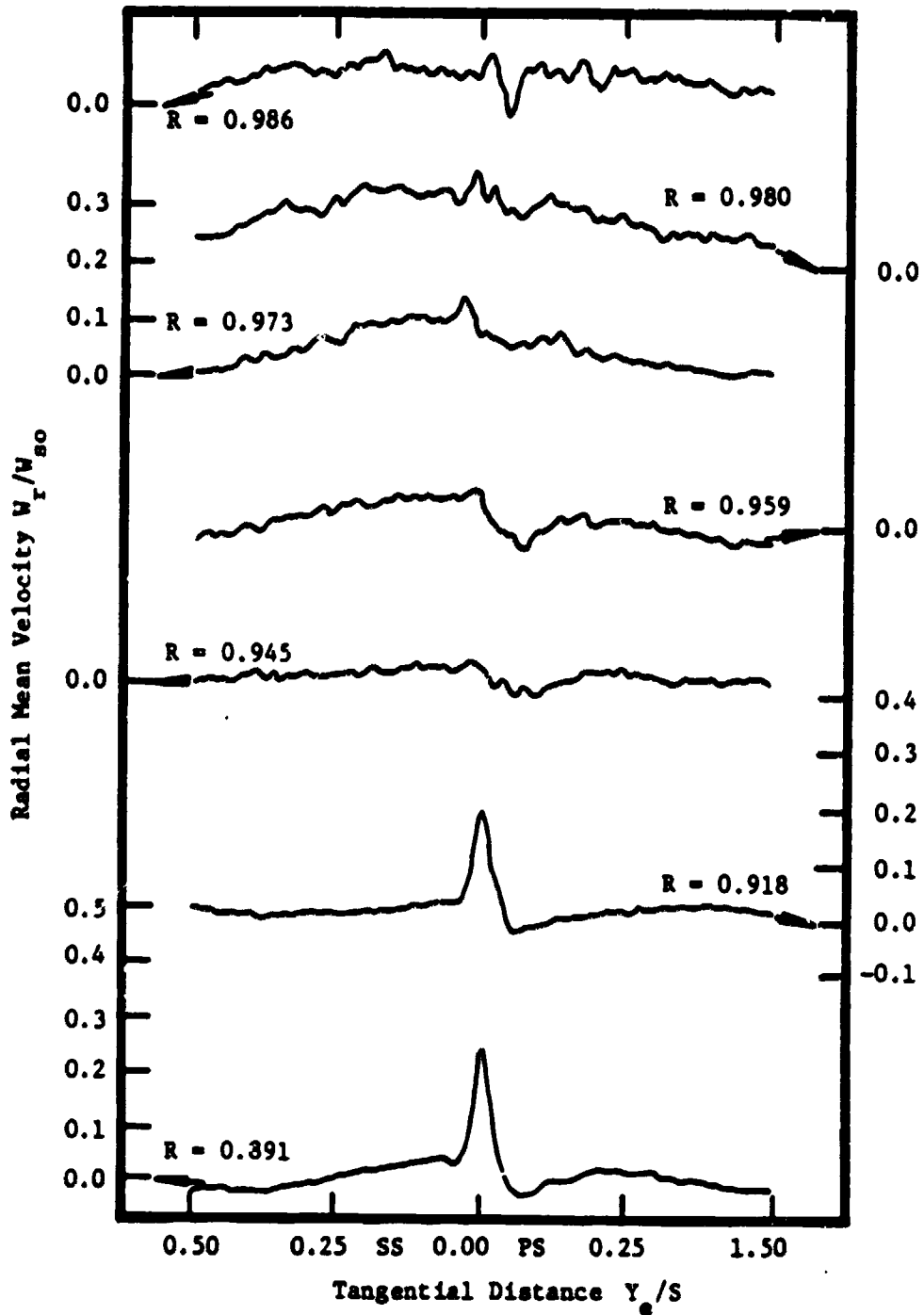


Figure 58. Radial Mean Velocity Profiles, $Z' = 0.125$.

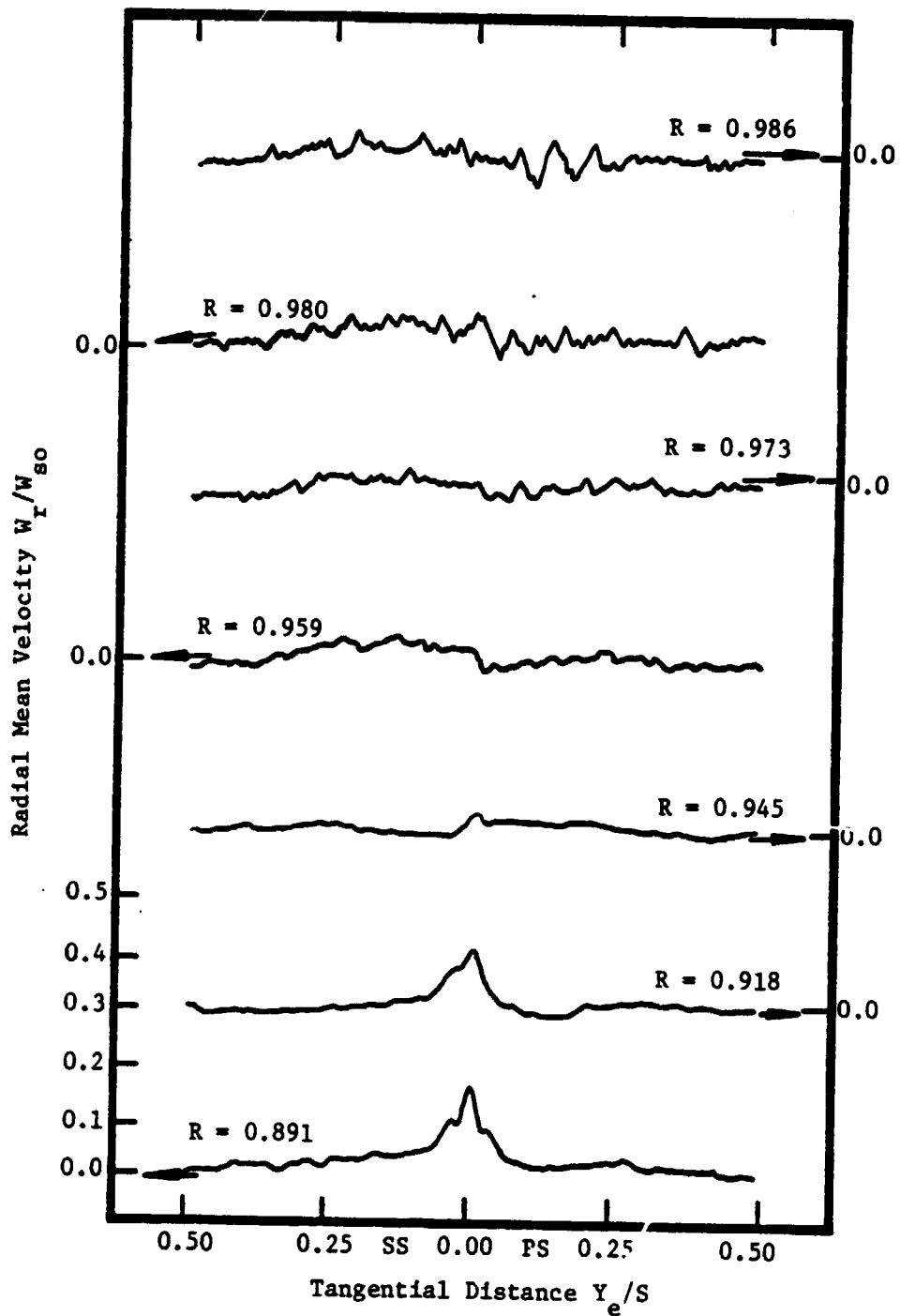


Figure 59. Radial Mean Velocity Profiles, $Z' = 0.458$.

seen at $Z = 0.979$. However, at $Z = 0.979$ the region of radially inward flow has increased to approximately 70 percent of the blade passage as compared to nearly 50 percent at $R = 0.750$. The region of maximum radial velocity has also moved toward the suction-surface of the rotor blade.

The radial velocities near the blade tip are believed to be influenced by the tip leakage flow. This flow produces a vortex which rolls up and travels downstream along the suction-surface of the blade. The complete structure of the tip leakage vortex is not evident from these data. Possible reasons for this are the limited radial traverse distance of the three-sensor probe and a possible unsteady character of the tip leakage flow.

Due to limitations of the probe traverse and mechanical difficulties, no measurement could be taken very close to the blade surface. Here the radial velocities should be outward. These radially outward flows, however, are present in the profile of the rotor blade wake as shown in Figures 56 through 59.

Radial velocities in a blade row are caused by an imbalance in the radial pressure gradient and the centrifugal forces. Physically, at either surface of the rotor blade the radial velocities must be zero. The maximum radial velocities occur slightly away from the blade surface in the blade boundary layer. The radial velocity in a compressor rotor is outward due to the larger centrifugal force than the radial pressure gradient inside the blade boundary layer.

The radial velocity profiles given in Figures 56 through 59 show the radial outward flow in the blade wake which results from the

shedding of the blade boundary layers. The radially outward flow in the wake decreases rapidly in the radial direction. At the axial location of $Z' = 0.021$, the maximum radial velocity (W_r/W_{so}) of 0.40 in the wake center reduces to nearly zero values at $R = 0.973$. This rapid decrease of the radial velocity is also present at the other axial locations downstream of the rotor. The interaction and subsequent mixing of the radial velocity in the wake with the annulus-wall boundary layer is the cause of this rapid decrease. The radial velocity profile in the wake is seen to decay with axial distance. At $R = 0.891$ and $Z' = 0.021$ a radial velocity (W_r/W_{so}) of 0.40 decays to 0.12 at $Z' = 0.458$. This decay rate is greater at higher radial locations where it is accelerated by the mixing of the blade wake and the annulus-wall boundary layer. The decay rate of the radial velocity profile downstream of the blade is rapid in this region. This is also due to the interaction between the blade wake and the annulus-wall boundary layer. The radial velocity in the free-stream behind the blade is zero. This indicates the balance which exists between the radial pressure gradient and the centrifugal forces.

4.2.4 Total Relative Velocity Inside the Blade Passage

Iso-contour plots of the total relative velocity within the rotor blade passage are presented in Figures 60 and 61. The tangential distance across the blade passage is normalized by the blade spacing and the radial distance within the blade passage is normalized by the blade tip radius. The total relative velocity is normalized by the blade tip speed and is presented at contour intervals of 0.1

$$W_T/U_{Tip}.$$

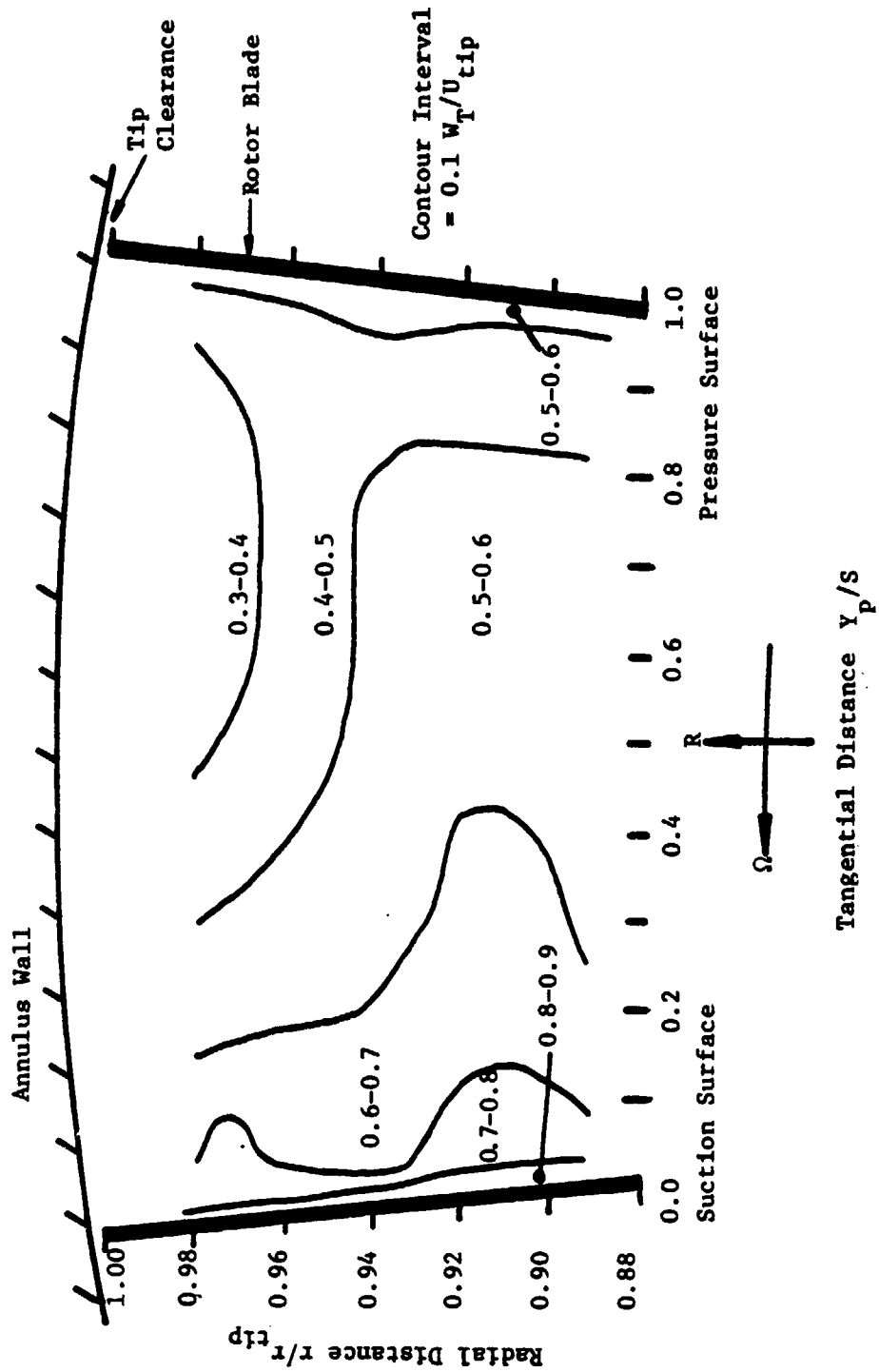


Figure 60. Total Relative Velocity at $Z = 0.750$.

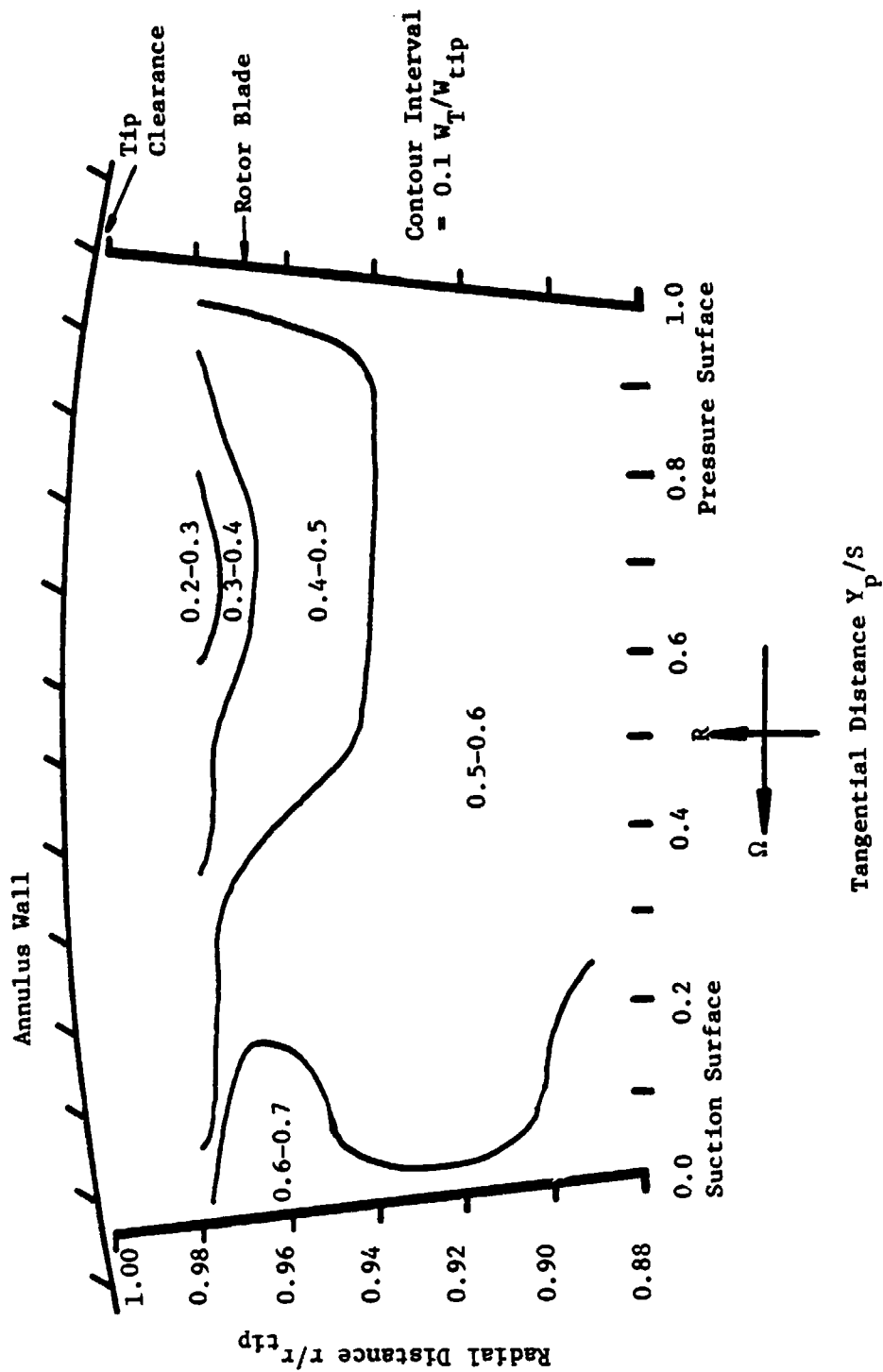


Figure 61. Total Relative Velocity at $Z = 0.979$.

Figures 60 and 61 show the distribution of the total relative velocity inside the blade passage at axial locations $Z = 0.750$ and $Z = 0.979$, respectively. The values of W_T/W_{Tip} near the blade surfaces were derived by blade static pressure measurements obtained by Sitaram (1980). These isocontour plots clearly indicate the three-dimensional nature of the blade-passage flow. The inviscid flow is also evident across the blade passage. A distinct velocity deficiency is noted at approximately 65 percent of the distance from the suction surface at radial locations above $R = 0.945$. The low relative velocities near the tip result in a large stagnation (absolute) pressure rise in this region. This large pressure rise is not due to flow turning but is caused by complex mixing and viscous interactions. This is a region of maximum loss. The radially outward flows inside the pressure- and suction-surface boundary layers are encountered by the annulus-wall at this region. They subsequently tend to roll toward the mid-passage, interact, and produce strong vortices and radially inward flows. This interaction region is an area of considerable flow mixing which results in strong eddies and energy dissipation. A concentration of high turbulence intensity levels was observed in this region and this is presented in subsequent sections. The interference region is seen to grow with axial distance. At $Z = 0.750$ the velocity deficiency is at a level of 0.3 to 0.4 W_T/U_{Tip} and at $Z = 0.979$ this velocity deficiency has increased to a level of 0.2 to 0.3 W_T/U_{Tip} . This drop in velocity may be due to the diffusion of the flow from one axial location to another. This is supported by the fact that the inviscid flow at lower radial

locations experiences a similar drop in velocity from one axial location to the next.

The inviscid flow at the radial locations below $R = 0.945$ is also evident from Figures 60 and 61. At $Z = 0.750$ the inviscid flow shows an increase in total velocity of approximately $0.3 W_T/U_{Tip}$ from the pressure- to suction-surface of the rotor blade. This inviscid trend is not as pronounced at $Z = 0.979$. Only a slight increase in the total relative velocity is seen at this axial location. This decrease in the velocity gradient is due to a decrease in the pressure gradient near the blade trailing-edge.

From Figures 60 and 61 the three-dimensional nature of the annulus-wall flow is evident. This characteristic of the flow is due mainly to the presence of the interference region between the blade boundary layers and the annulus-wall boundary layer. It is believed that this tip leakage flow also contributes to this three-dimensional nature, but due to the limited radial survey a complete structure of this flow was not obtained. The viscous effects in the annulus-wall region are thus found to be appreciable and should be properly considered for a flow prediction scheme.

4.3 Turbulence Intensity Profiles in the Annulus-Wall Region

Blade to blade distributions of the three turbulent intensity components (see Figure 39) at various radial and axial locations are shown in Figures 62 and 79. The turbulent intensity components are normalized by the local mean velocity, since the turbulence is dependent upon the local flow conditions. The tangential distance

ORIGINAL PAGE IS
OF POOR QUALITY

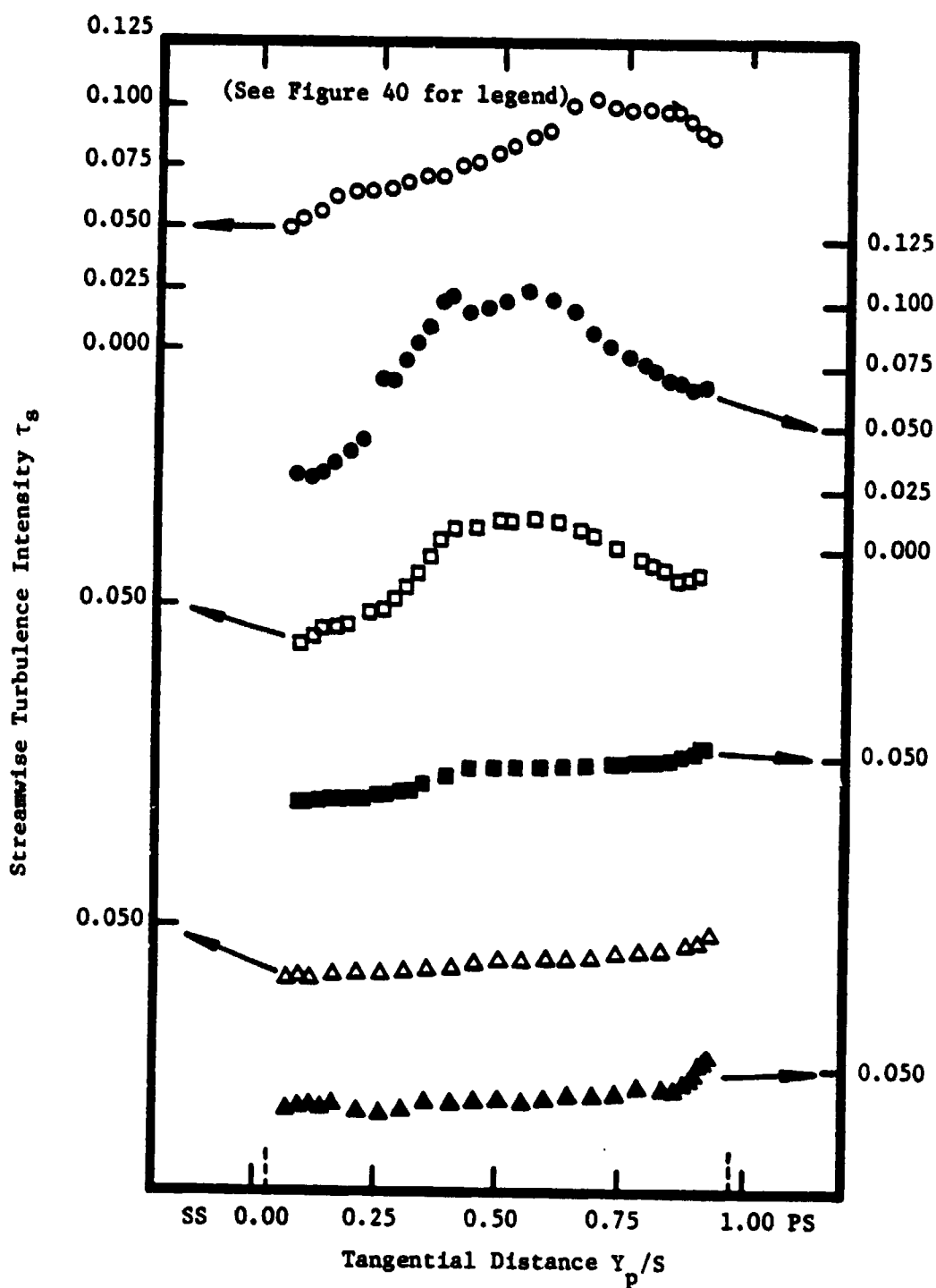


Figure 62. Streamwise Turbulence Intensity Profiles, $Z = 0.750$.

ORIGINAL PAGE IS
OF POOR QUALITY

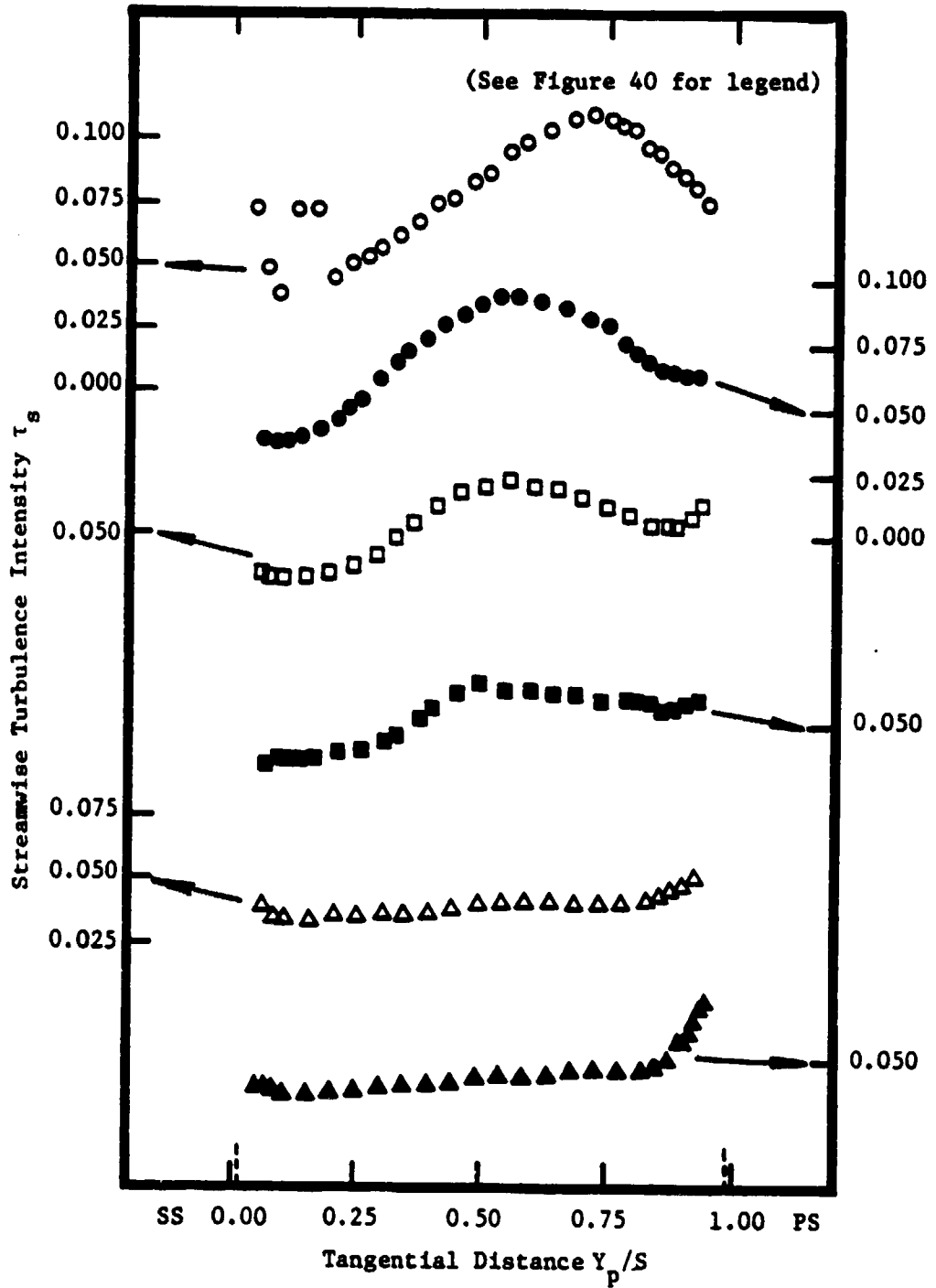


Figure 63. Streamwise Turbulence Intensity Profiles, $Z = 0.979$.

ORIGINAL PAGE IS
OF POOR QUALITY

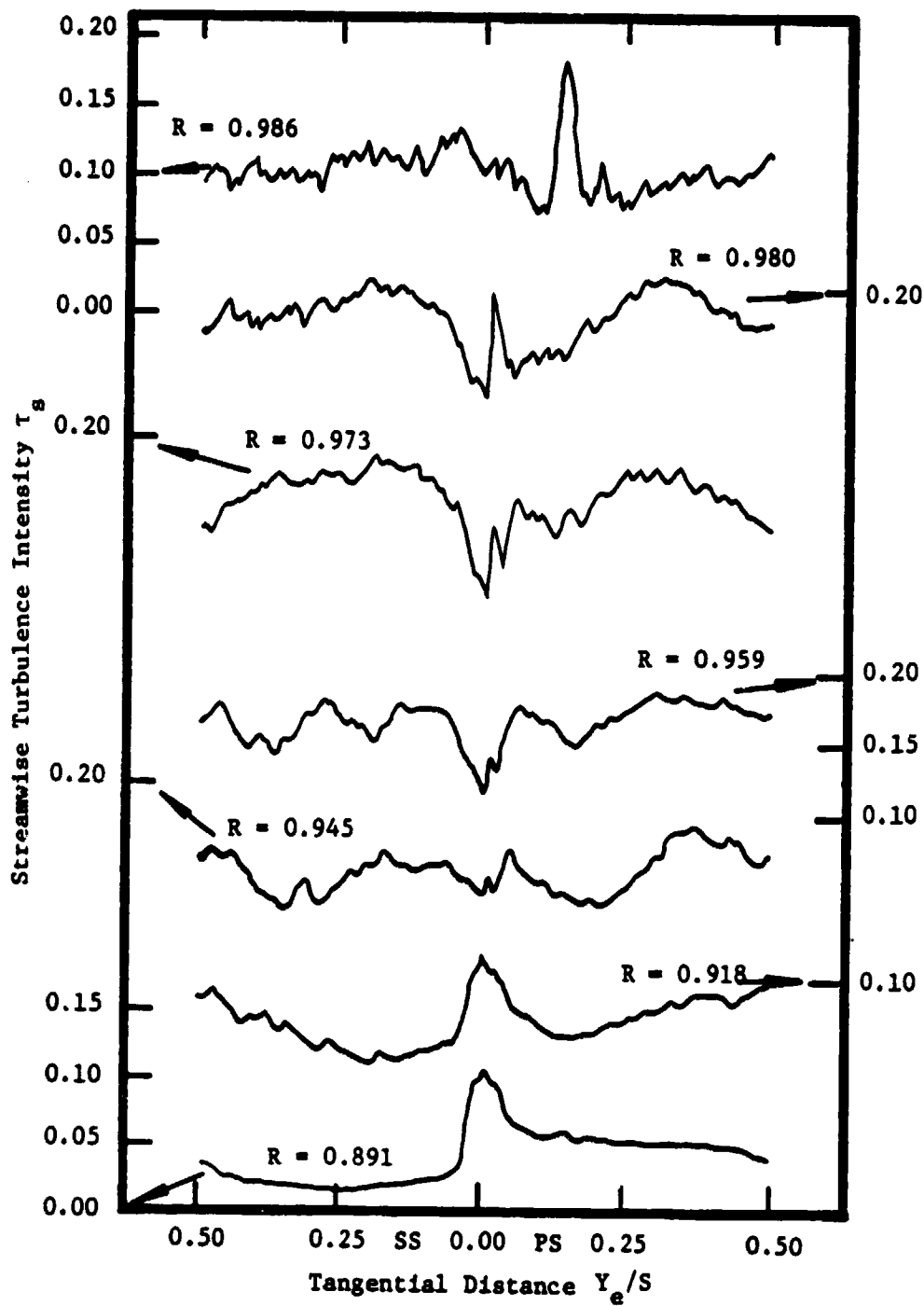


Figure 64. Streamwise Turbulence Intensity Profiles, $Z' = 0.021$.

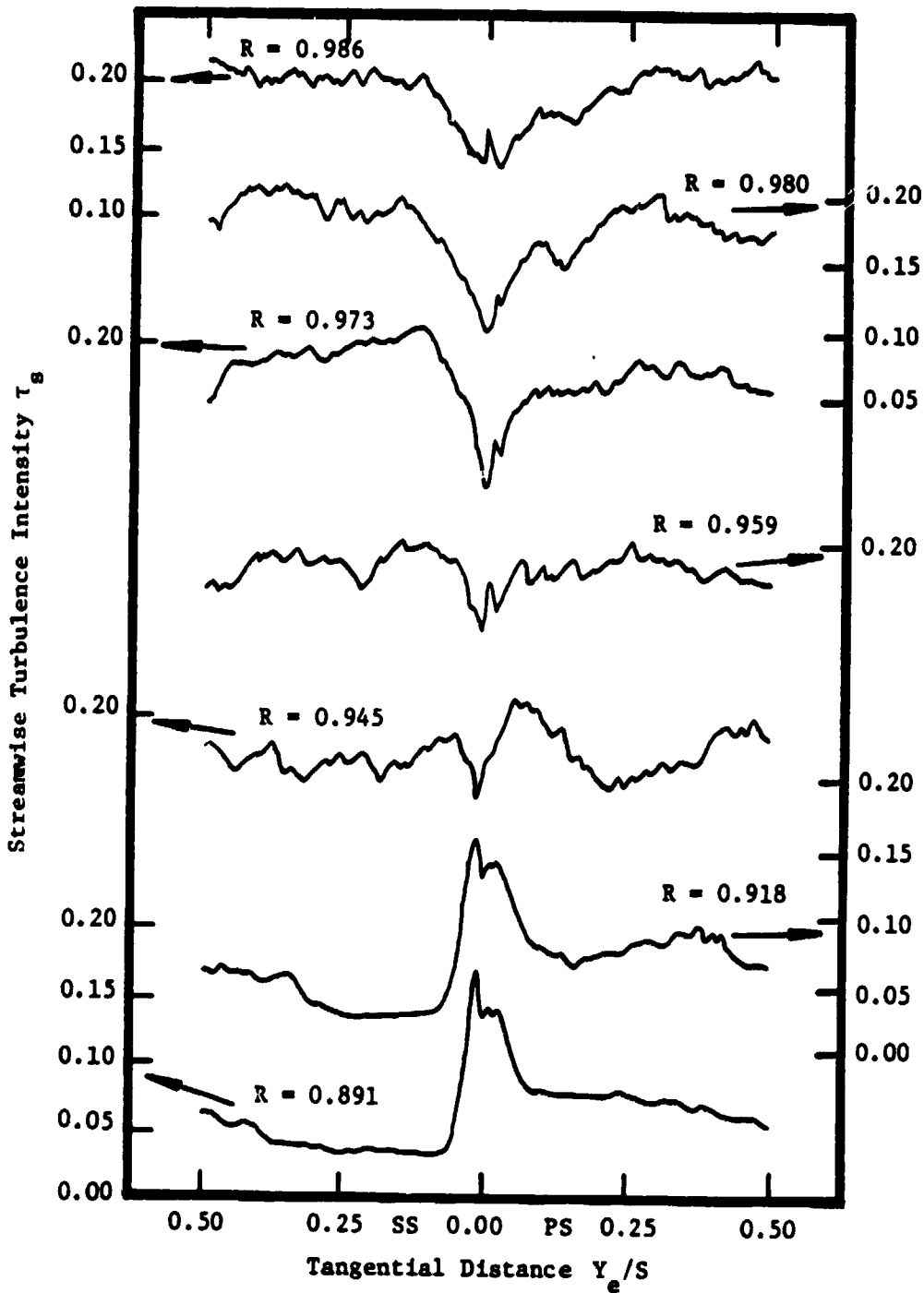


Figure 65. Streamwise Turbulence Intensity Profiles, $Z' = 0.042$.

ORIGINAL PAGE IS
OF POOR QUALITY

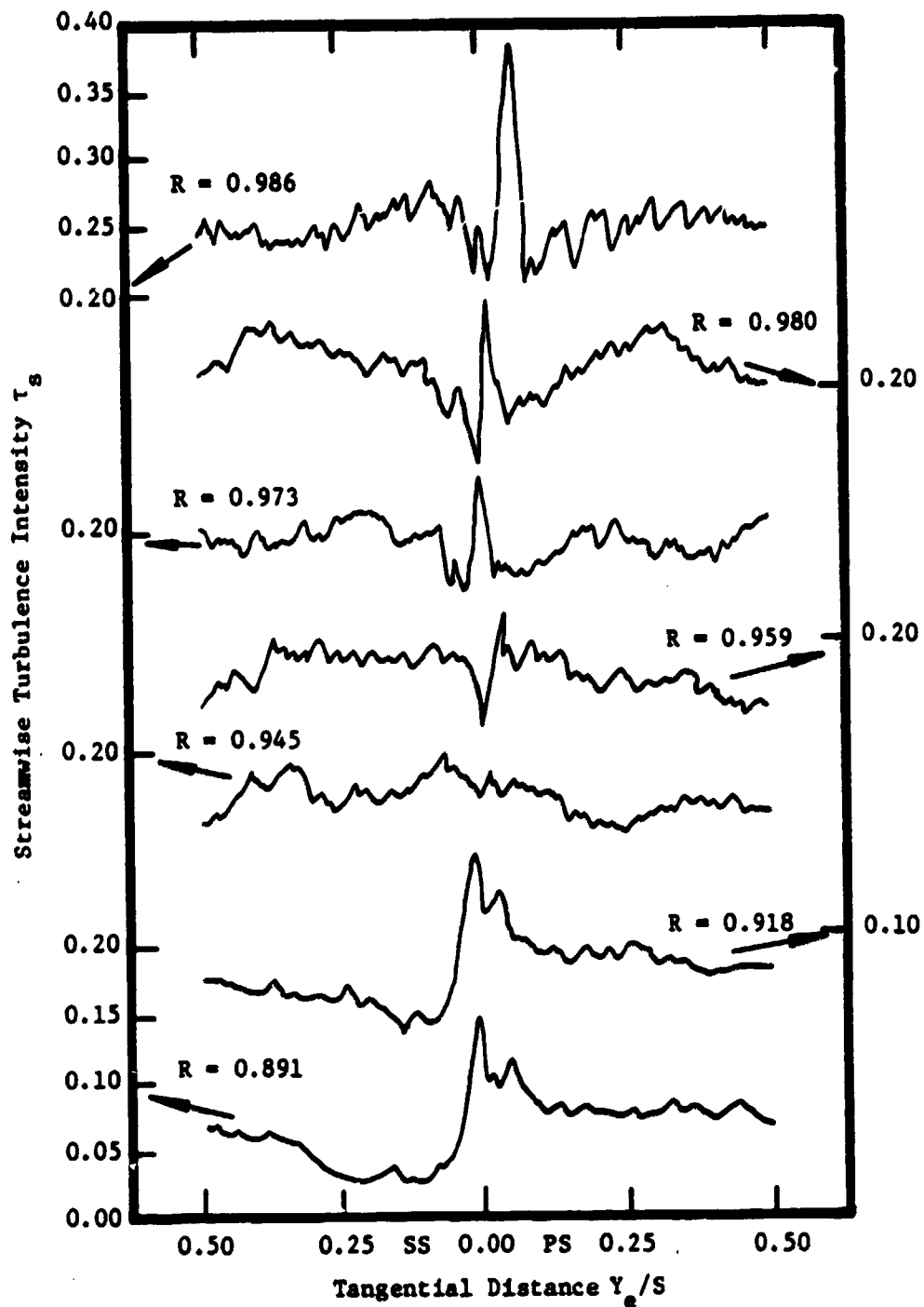


Figure 66. Streamwise Turbulence Intensity Profiles, $Z' = 0.125$.

ORIGINAL PAGE IS
OF POOR QUALITY

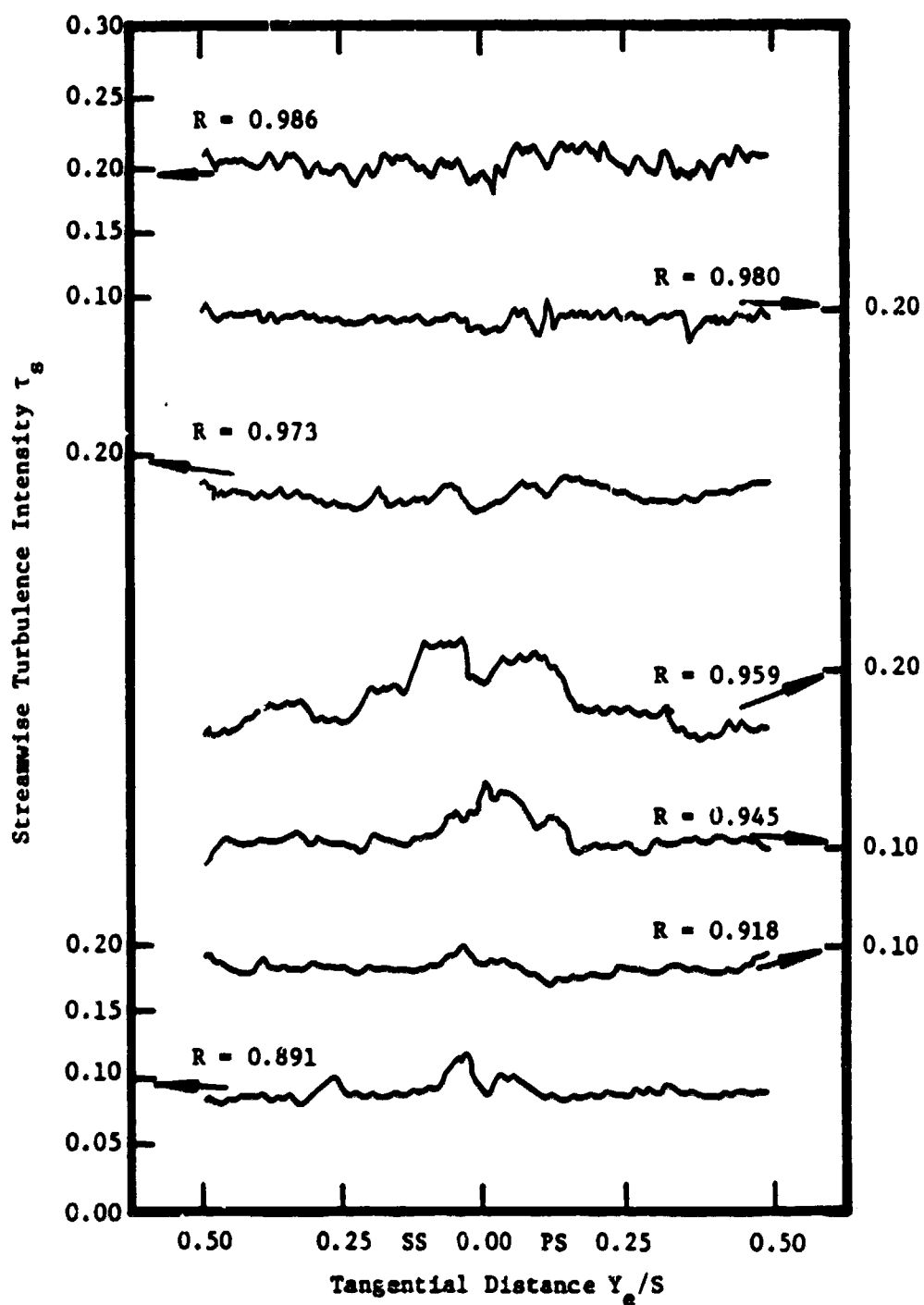


Figure 67. Streamwise Turbulence Intensity Profiles, $z' = 0.458$.

ORIGINAL PAGE IS
OF POOR QUALITY

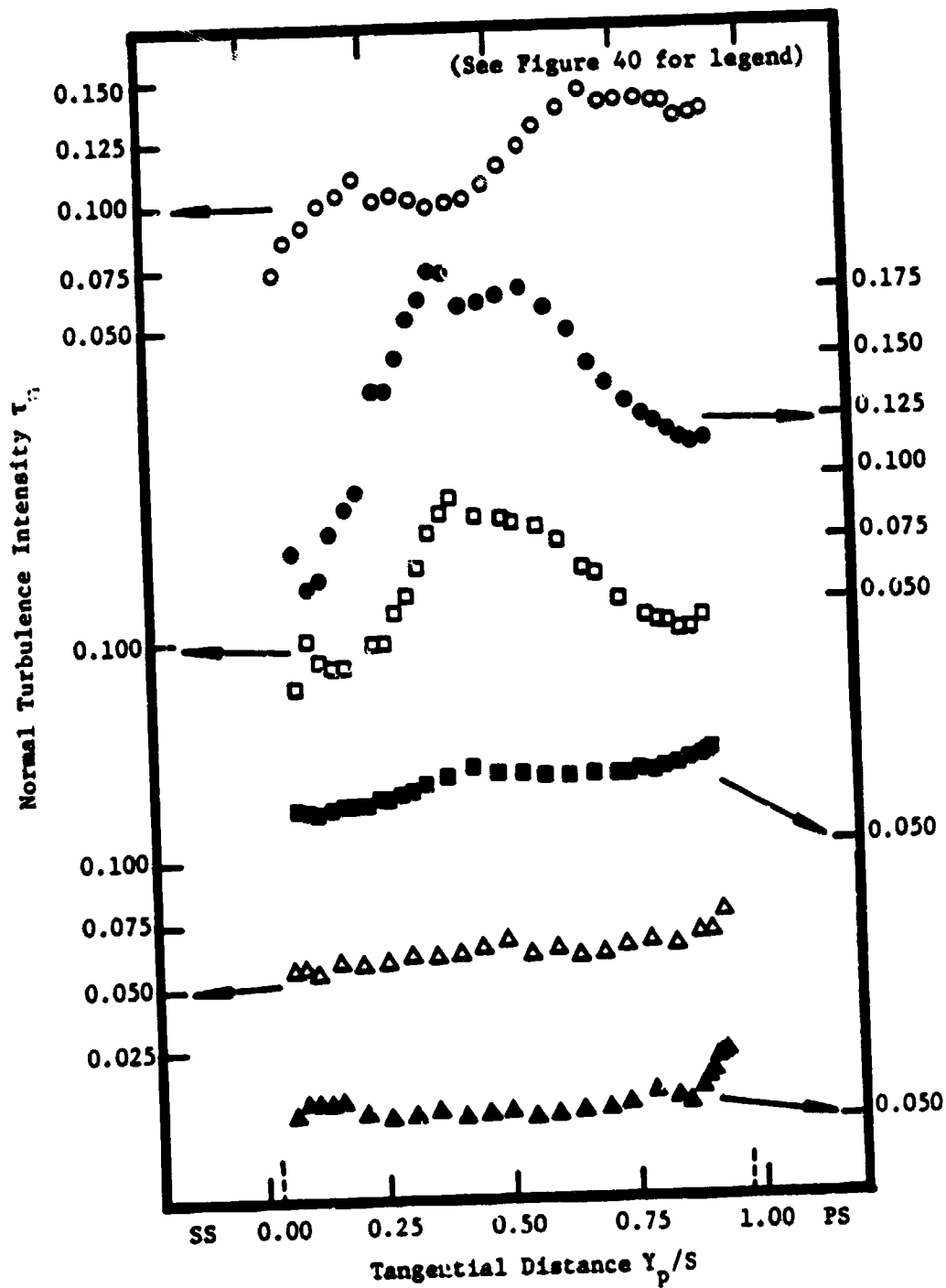


Figure 68. Normal Turbulence Intensity Profiles, $Z = 0.750$.

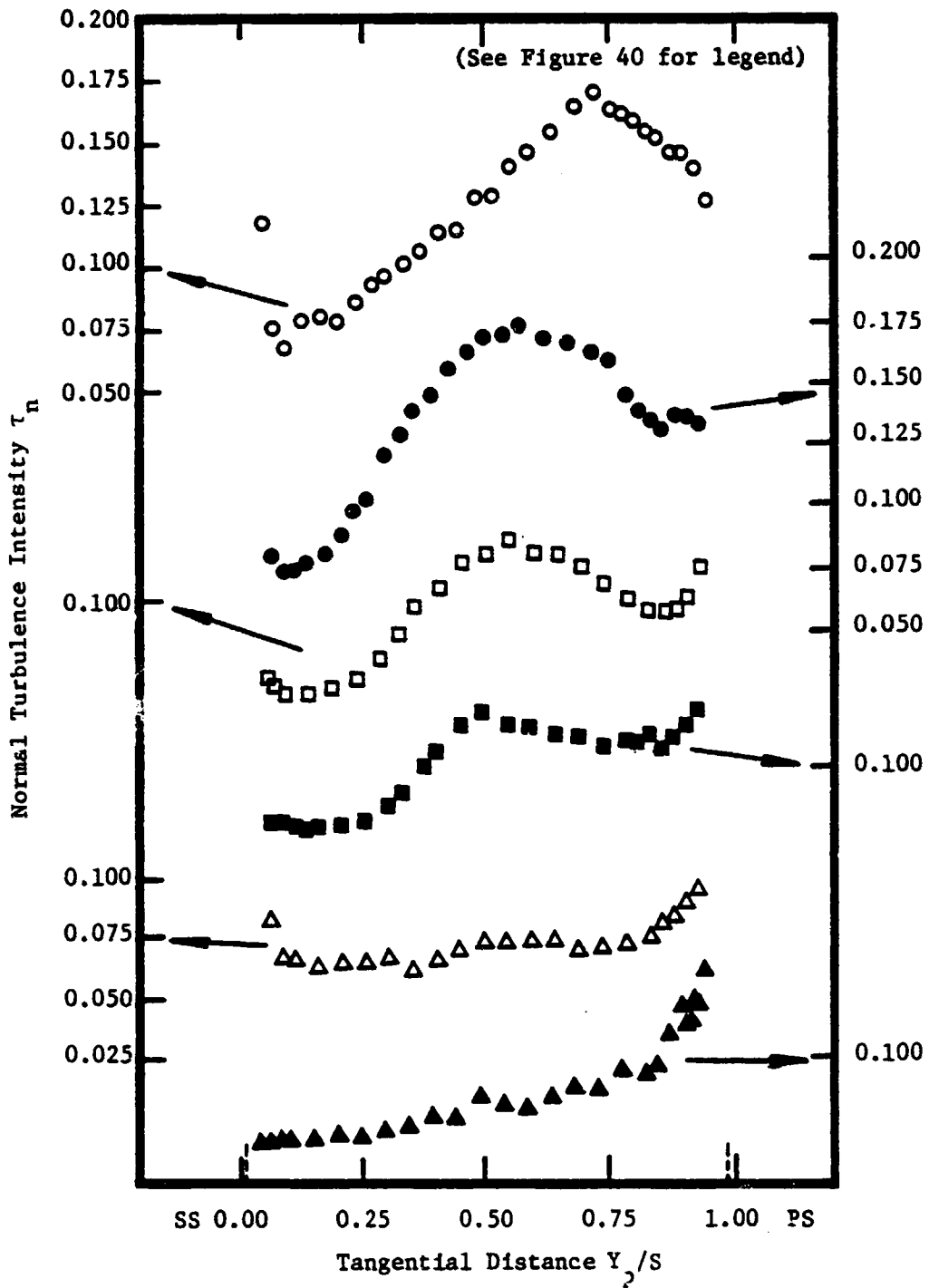


Figure 69. Normal Turbulence Intensity Profiles, $Z = 0.979$.

ORIGINAL PAGE IS
OF POOR QUALITY

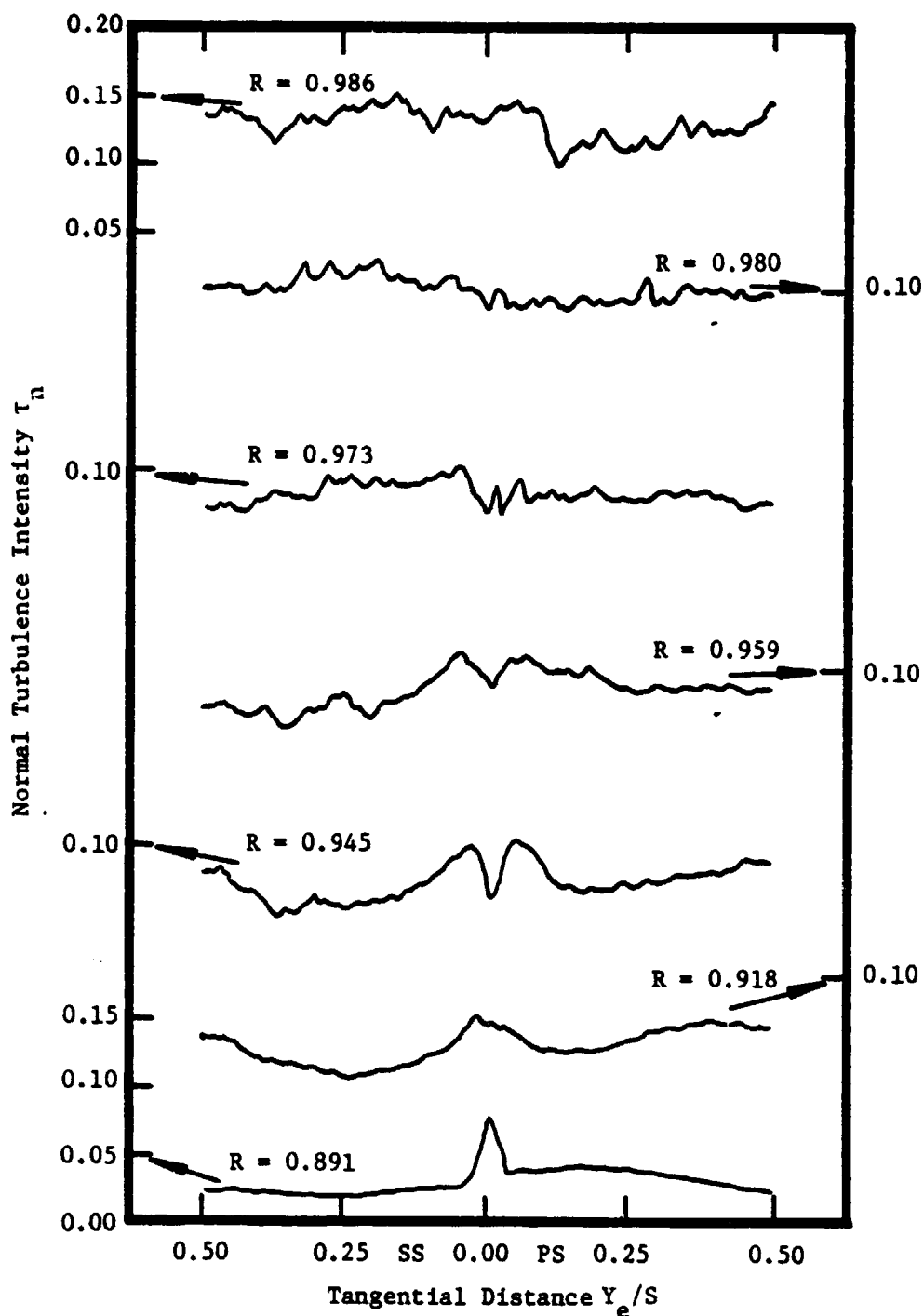


Figure 70. Normal Turbulence Intensity Profiles, $Z' = 0.021$.

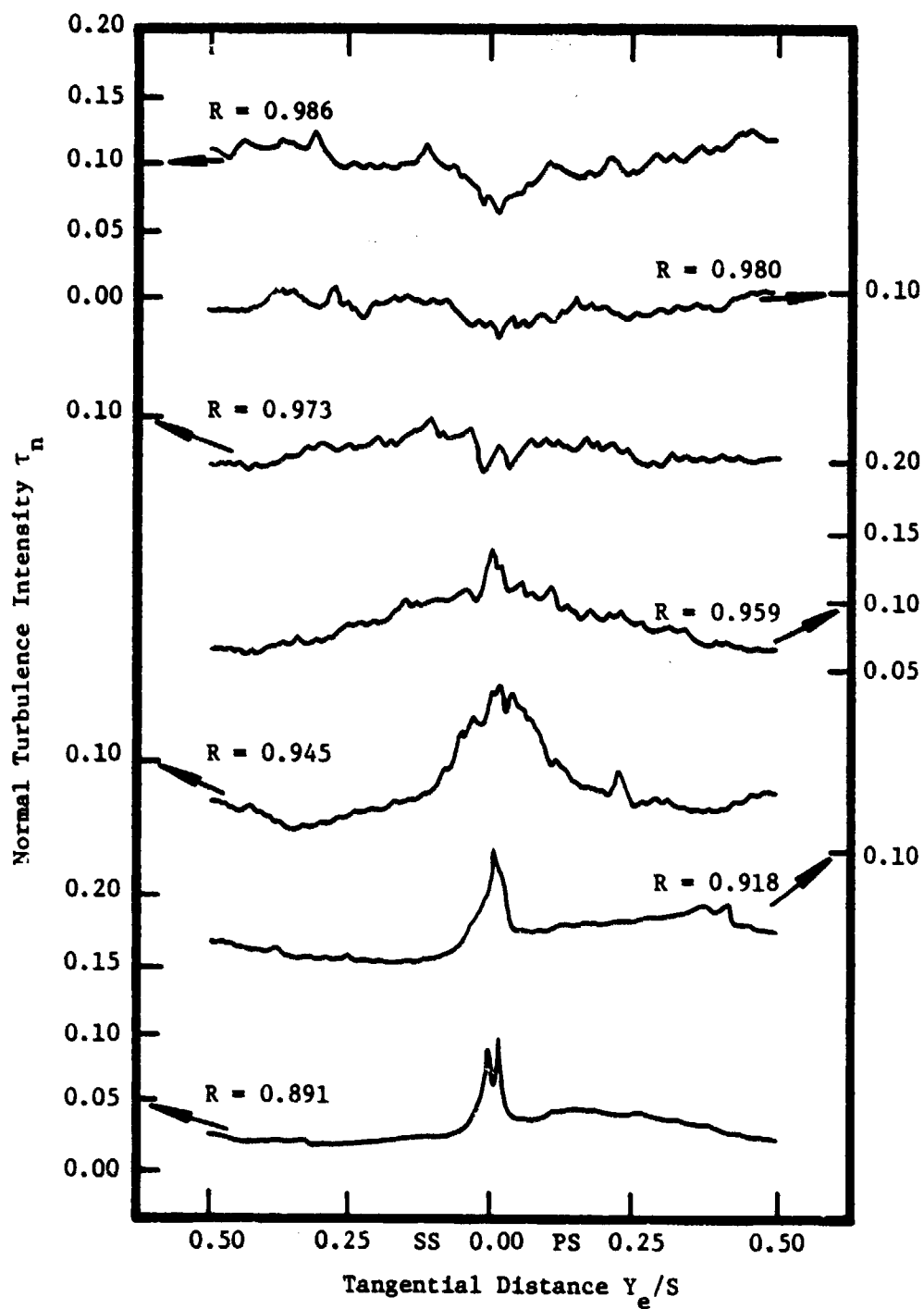


Figure 71. Normal Turbulence Intensity Profiles, $Z' = 0.042$.

ORIGINAL PAGE IS
OF POOR QUALITY

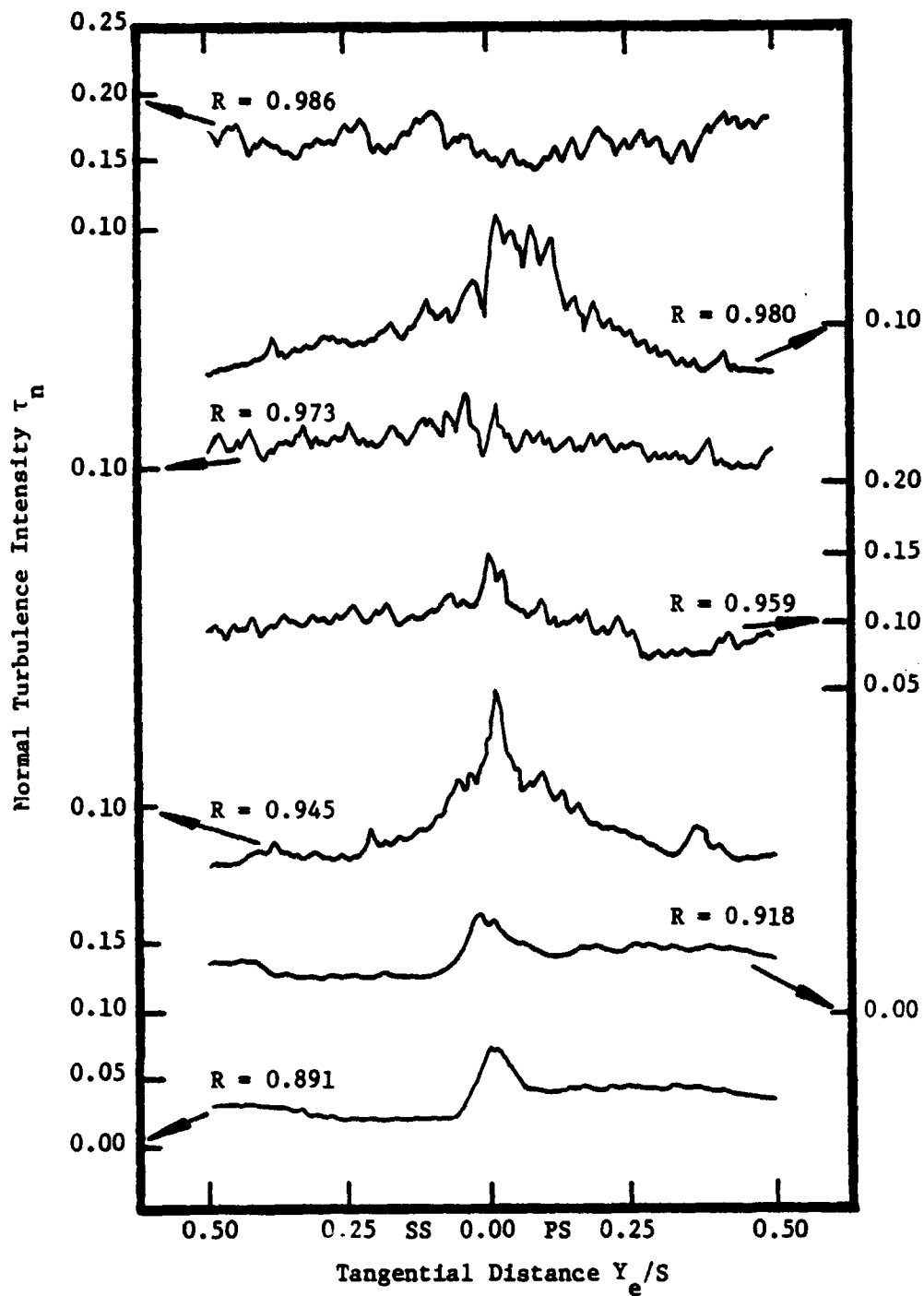


Figure 72. Normal Turbulence Intensity Profiles, $Z' = 0.125$.

ORIGINAL PAGE IS
OF POOR QUALITY

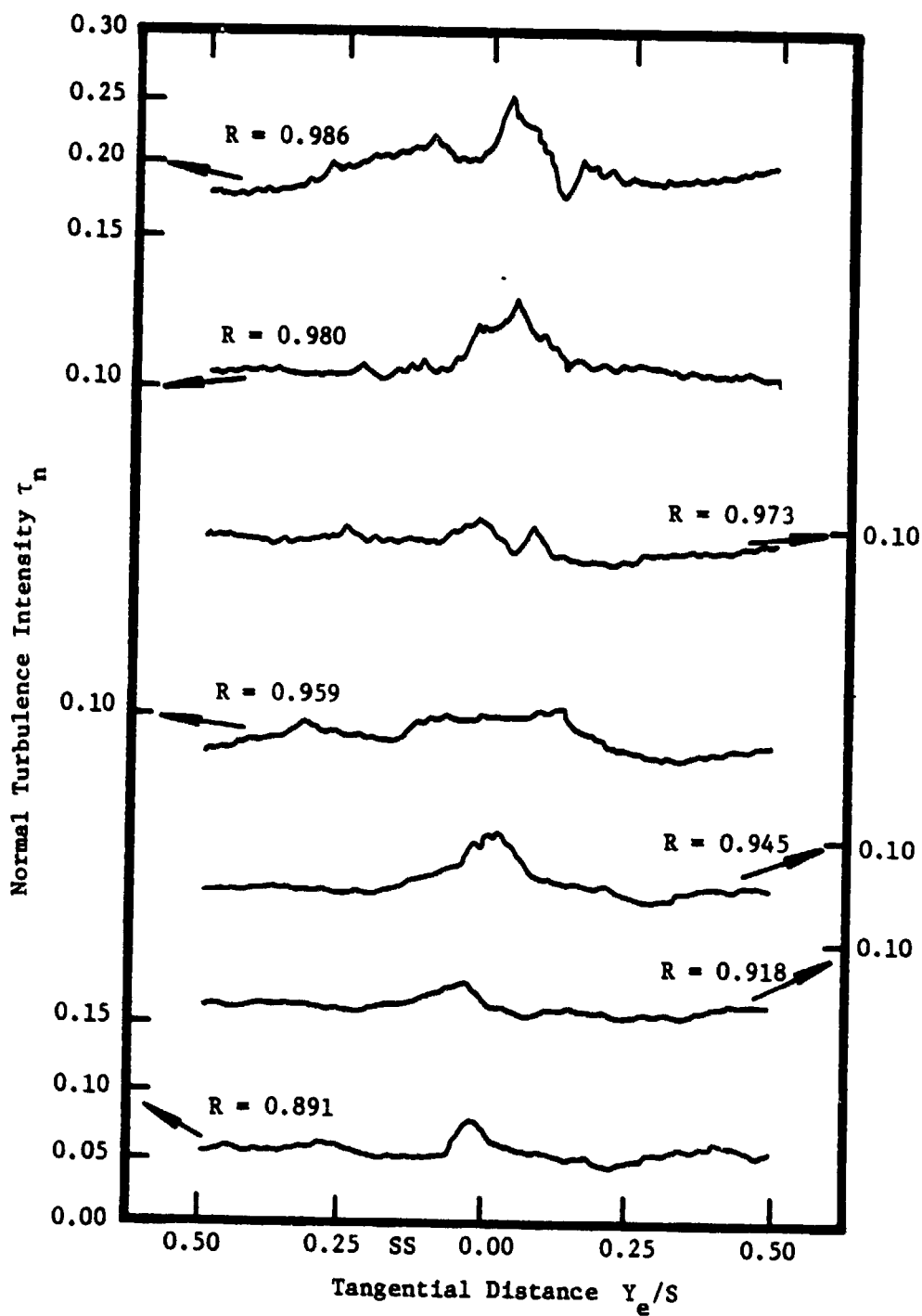


Figure 73. Normal Turbulence Intensity Profiles, $z' = 0.458$.

ORIGINAL PAGE IS
OF POOR QUALITY

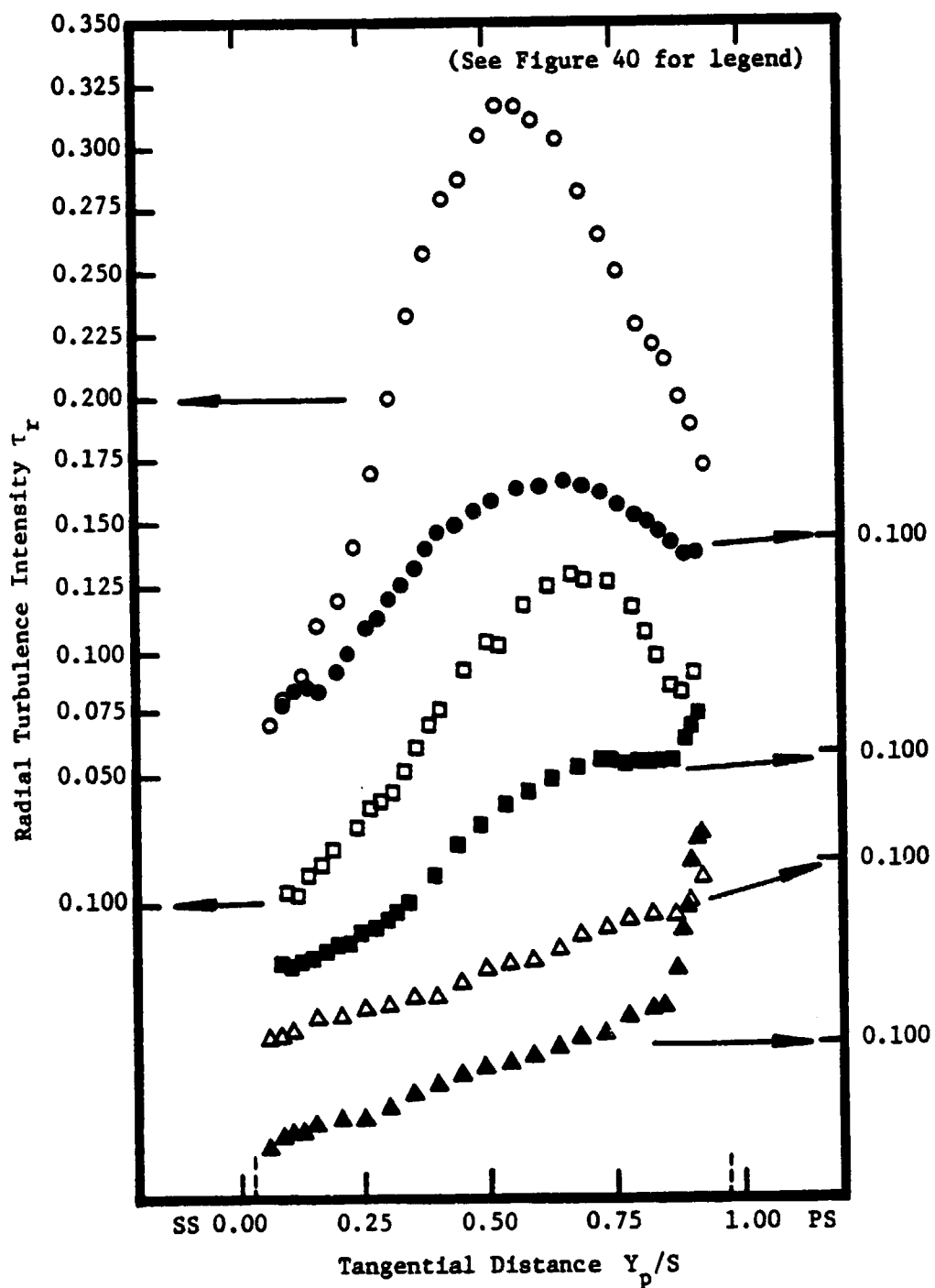


Figure 74. Radial Turbulence Intensity Profiles, $Z = 0.750$.

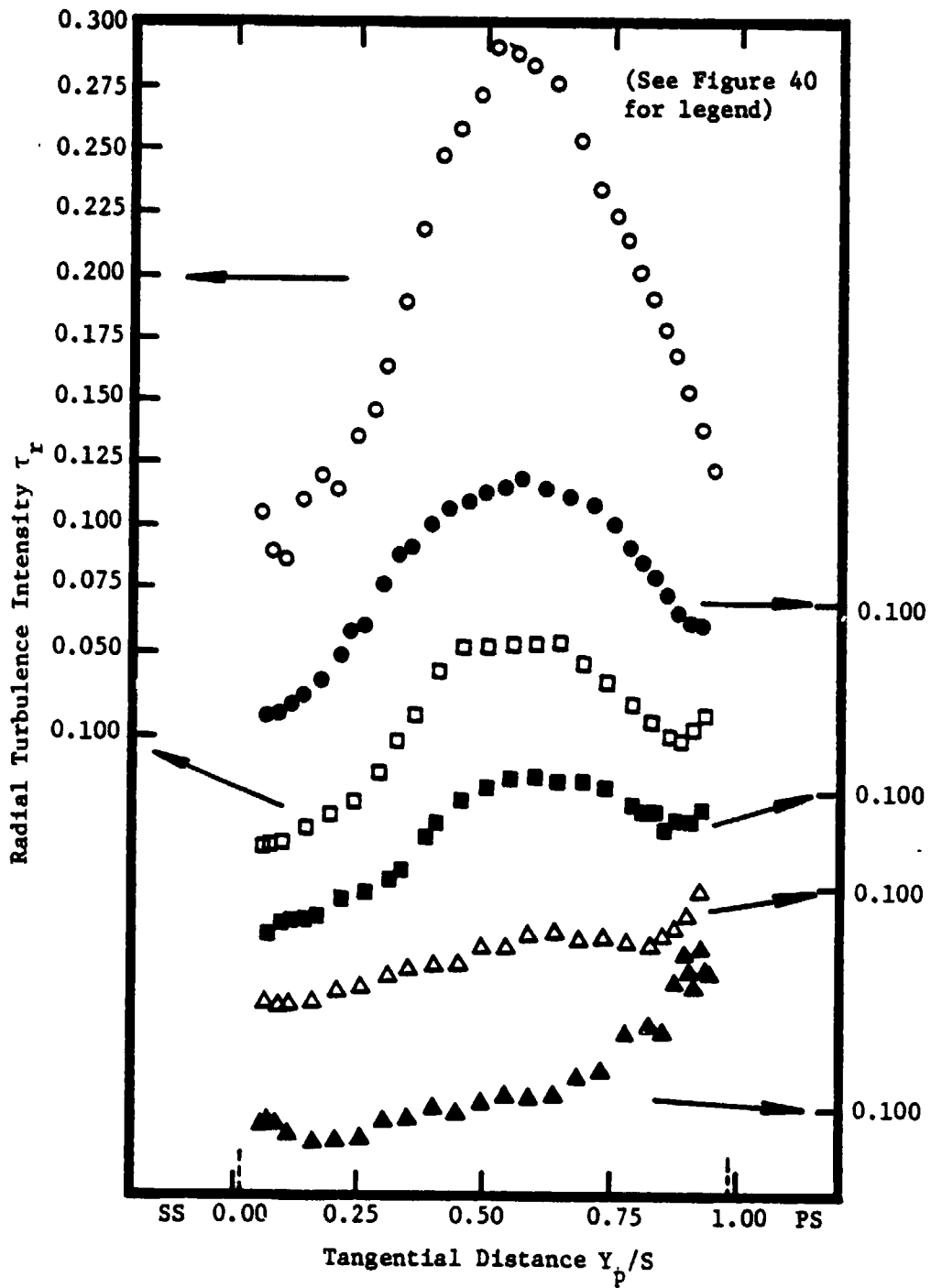


Figure 75. Radial Turbulence Intensity Profiles, $Z = 0.979$.

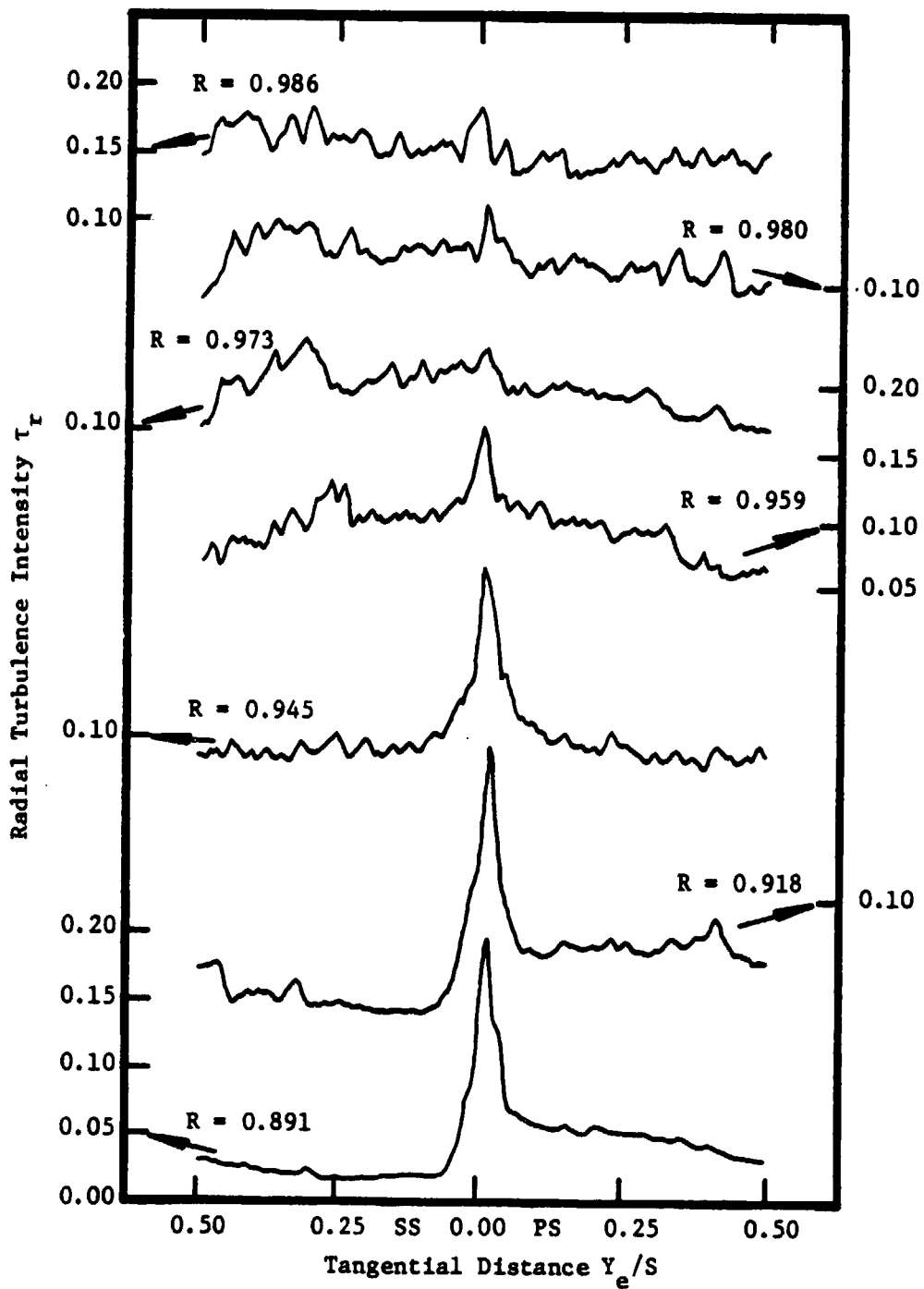


Figure 77. Radial Turbulence Intensity Profiles, $Z' = 0.042$.

ORIGINAL PAGE IS
OF POOR QUALITY

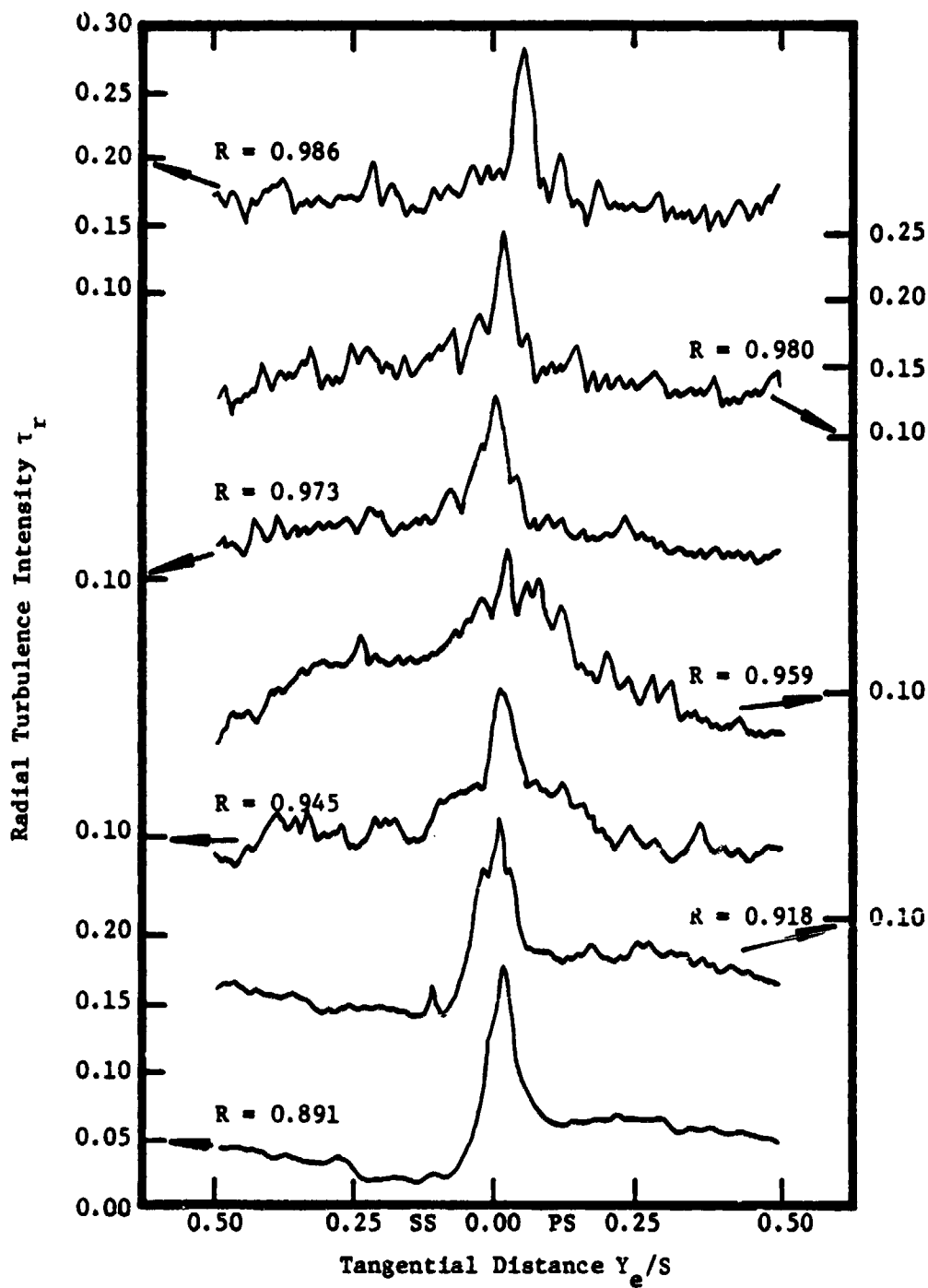


Figure 78. Radial Turbulence Intensity Profiles, $Z' = 0.125$.

ORIGINAL PAGE IS
OF POOR QUALITY

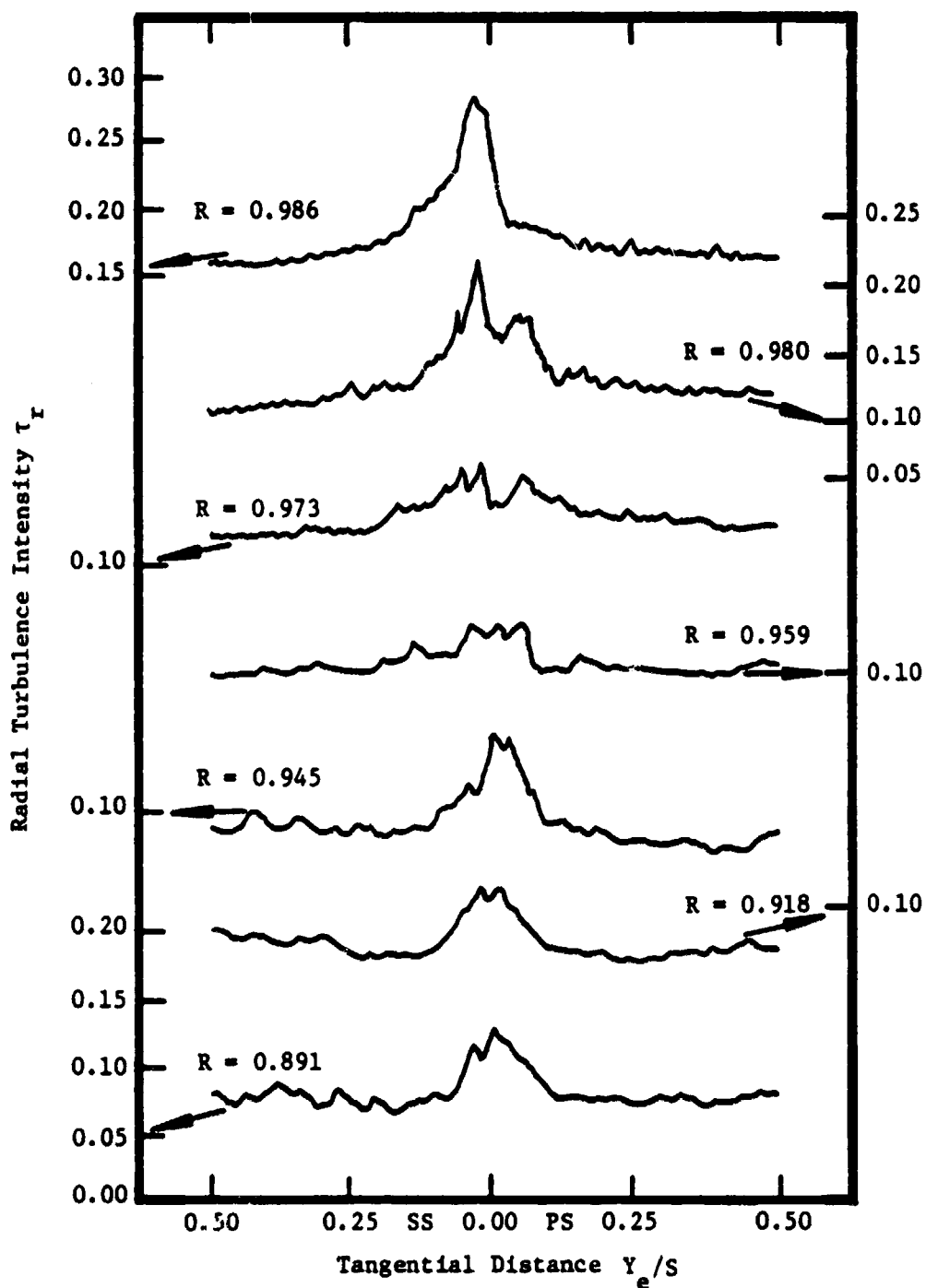


Figure 79. Radial Turbulence Intensity Profiles, $Z' = 0.458$.

across the blade passage is normalized by the blade spacing. As with the mean velocity data, a rotating measurement scheme was employed within the rotor blade passage and a stationary measurement scheme was employed downstream of the rotor blade passage. All conventions for the data presented in Figures 62 to 79 are identical to these used for the mean velocity data.

4.3.1 Streamwise Turbulence Intensity

The streamwise turbulence intensity profiles for the annulus-wall region are presented in Figures 62 through 67. Figures 62 and 63 show the structure of the streamwise turbulence intensity τ_s across the blade passage with radial and axial variation. High levels of streamwise turbulence intensity are observed at radial locations above $R = 0.945$. The turbulence level reaches 10% of the local mean velocity at $R = 0.980$ while levels of 4-5% are observed at the lower radial locations. The location of the high turbulence levels corresponds to the interference region where considerable flow mixing occurs. As shown by the mean velocity profiles, this region is located at approximately 65% of the blade passage from the suction-surface of the rotor blade. The region of increased turbulence intensity is seen to increase radially at the radial location of $R = 0.945$ and the axial location $Z = 0.750$. A similar radial trend is seen at $R = 0.918$ and $Z = 0.979$. This indicates the spatial growth of the interference region as the annulus-wall flow propagates downstream within the blade passage.

The streamwise turbulence intensity is also seen to increase near the blade surfaces in Figures 62 and 63. This increase is due to the

production of turbulence by the mean velocity gradients in the blade boundary layers. A decrease should then occur very near the blade surface in the viscous layer. However, this was not observed since measurements could not be taken in this region due to the finite size of the probe.

The streamwise turbulence intensity profiles for the blade exit-flow are presented in Figures 64 through 67. These profiles show very high values at the tangential location of the blade wake and at higher radial locations. As the flow leaves the rotor blade passage, the mainstream turbulence intensity is carried into the exit-flow. At high radial locations the level of streamwise turbulence intensity in the free-stream is amplified to a level observed in the interference region of the passage-flow. This redistribution of turbulence intensity is also observed at lower radial locations and for the other components of turbulence intensity.

In Figures 64 through 67 the influence of the annulus-wall is not readily observed below the radial location of $R = 0.945$. In this region the streamwise turbulence intensity profiles show typical trends. The profiles are asymmetrical but tend to become symmetrical beyond 0.125 chords downstream. This trend is also observed in the profiles of the other components of turbulence intensity. The asymmetry in the profiles results from the differential growth of turbulence on the suction- and pressure-surface of the rotor blade. Figures 65 and 66 show a dip in the profile at the centerline of the wake. The dip occurs because the turbulence intensity is zero on the blade surface due to the maximum value of intensity which will occur

slightly away from the blade surfaces. These figures also show the effect of the centrifugal forces which increase the intensity on the suction-surface and decrease the intensity on the pressure-surface of the blade. The magnitude of the turbulence intensity in the wake is seen to decrease with axial distance.

The streamwise turbulence intensity profiles at radial locations above $R = 0.945$ are also plotted in Figures 64 through 67. These profiles depict the complex turbulence structure in the annulus-wall region. The effect of the interaction of the secondary flow, tip leakage flow, and the blade wake is observed in these plots. The free-stream turbulence intensity has substantially increased at these higher radial locations. At $Z' = 0.042$ a free-stream value of approximately 5% at $R = 0.891$ has increased to 20% at $R = 0.986$. Immediately behind the blade, $Z' = 0.021$, the increase in free-stream turbulence is only 10%. This indicates that there is intense mixing in these regions. Areas of high turbulence tend to spread out and mix with the free-stream as the flow develops. From this location downstream the free-stream turbulence intensity is increasing. At these higher radial locations, the turbulence intensity within the wake structure is still observed and is magnified due to the complex flow interactions. The presence of the annulus-wall and the associated flow mixing causes the streamwise turbulence intensity to increase in both the rotor blade wake and the free-stream.

4.3.2 Normal Turbulence Intensity

Figures 68 through 73 present the normal turbulence intensity profiles for the annulus-wall region. Figures 68 and 69 show the structure of the normal turbulence intensity τ_n across the blade passage. Many of the trends displayed in these profiles are similar to those observed in the streamwise turbulence intensity profiles. At radial locations above $R = 0.945$, high levels of turbulence intensity are observed. The turbulence level reaches 15% of the local mean velocity at $R = 0.980$, where levels of 5% are observed at lower radial locations. The interference region within the blade passage is indicated by high levels of turbulence intensity. This region is seen to extend to lower radial locations at $Z = 0.979$ and is located at approximately 65% of the blade passage from the suction-surface of the blade. The production of turbulence by the mean velocity gradients in the blade boundary is indicated by an increase in normal turbulence intensity near the blade surfaces.

Figures 70 through 73 display the normal turbulence intensity profiles in the blade exit-flow. These profiles show high values of turbulence at the tangential location of the blade wake and at radial locations near the blade tip. Below the radial location of $R = 0.945$, the free-stream turbulence level is about 4% with the wake turbulence level reaching 10% of the local mean velocity. Above $R = 0.945$ the complex turbulence structure in the annulus-wall region is apparent. The effect of flow interactions is an increase in the overall level of turbulence in this region. At $Z' = 0.125$ the free-stream turbulence level has increased from 4% at $R = 0.891$ to 17% at $R = 0.986$. This

increase is not as high immediately behind the blade where the free-stream intensity level is 13% of the local mean velocity. This again indicates that the flow requires a small axial distance after exiting the blade row to induce maximum flow mixing. This region of flow mixing increases the turbulence level of the free-stream and rotor wake flow.

A comparison between the streamwise and normal turbulence intensity levels at the lower radial locations shows that these components of intensity are approximately equal in the free-stream. This indicates isotropic flow in this region. However, this is not true for the higher radial locations where the complex flow interactions are observed. In this interference region the level of τ_n is greater than the level of τ_s both inside the blade passage and at the exit of the blade passage.

4.3.3 Radial Turbulence Intensity

Radial turbulence intensity profiles for the annulus-wall region are presented in Figures 74 through 79. Figures 74 and 75 display the tangential variation of the radial turbulence intensity τ_r across the blade passage at various radial and axial locations. At both axial locations, there is a high level of turbulence intensity at radial locations above $R = 0.918$. The tangential location of these high intensities corresponds to the mixing region near the tip. Levels of radial turbulence intensity as high as 32% of the local mean velocity are shown in this region. Inside the blade passage boundary layer, the magnitude of the radial intensity component τ_r is larger

than both the streamwise τ_s and normal τ_n intensity components. This observed behavior is contrary to that known for stationary two-dimensional boundary layers where $\tau_s > \tau_r > \tau_n$. This indicates that the turbulence characteristics are markedly affected by the blade rotation. The experimental data obtained by Lakshminarayana and Gorton (1977) inside the rotor passage of a three-bladed rocket pump inducer and of Raj and Lakshminarayana (1976) obtained in rotor wakes confirms this conclusion. An analysis of this effect is given by Lakshminarayana and Reynolds (1979).

Radial turbulence intensity profiles for radial and axial locations in the exit-flow are shown plotted in Figures 76 through 79. The radial intensities below the radial location of $R = 0.945$ show predominately the wake structure. These intensities are larger than the streamwise and normal components in magnitude and reach values of 20% of the local mean velocity at the wake center. The free-stream level of turbulence is approximately 3%, with high values occurring on the pressure side of the wake. The existence of the large radial component of intensity at the wake location reflects the character of the rotor blade boundary layers under the influence of rotation. The existence of these large radial components of intensity also demonstrates the three-dimensional nature of the rotor wake.

At radial locations above $R = 0.945$, the flow is subjected to complex interactions resulting from the annulus-wall boundary layer, the rotor wake, the tip leakage flow, and the secondary flow. The result of this flow interaction is to increase the overall radial turbulence intensity. The free-stream value of turbulence increases

from 3% at the lower radial locations to 16% at the radial location of $R = 0.986$. However, this level occurs at $Z' = 0.042$ and slowly decreases with axial distance. At $Z' = 0.021$ and the same radial location, the radial turbulence intensity is only 12% of the local mean velocity. This increase and then decrease in radial turbulence intensity indicates that the development of the flow mixing region initially grows stronger before it begins to decay. A similar trend is observed in the wake at radial locations near $R = 0.959$. This suggests the presence of a trailing vortex which initially grows in strength before decaying. This phenomenon has been reported by Ravindranath and Lakshminarayana (1980).

4.3.4 Total Turbulent Energy Inside the Blade Passage

Isocontour plots of the total turbulent energy q^2 , within the blade passage are shown in Figures 80 and 81. The total energy of turbulence is defined as:

$$q^2 = \frac{\overline{w_s'^2} + \overline{w_n'^2} + \overline{w_r'^2}}{2 \overline{w_{so}^2}} \quad (16)$$

and is plotted at contour intervals of $0.01 q^2$. The tangential distance across the blade passage in the figures is normalized by the blade spacing and the radial distance within the blade passage is normalized by the blade tip radius.

Figures 80 and 81 show the distribution of the energy of turbulence inside the blade passage at axial locations $Z = 0.750$ and $Z = 0.979$, respectively. The three-dimensional nature of the blade passage-flow

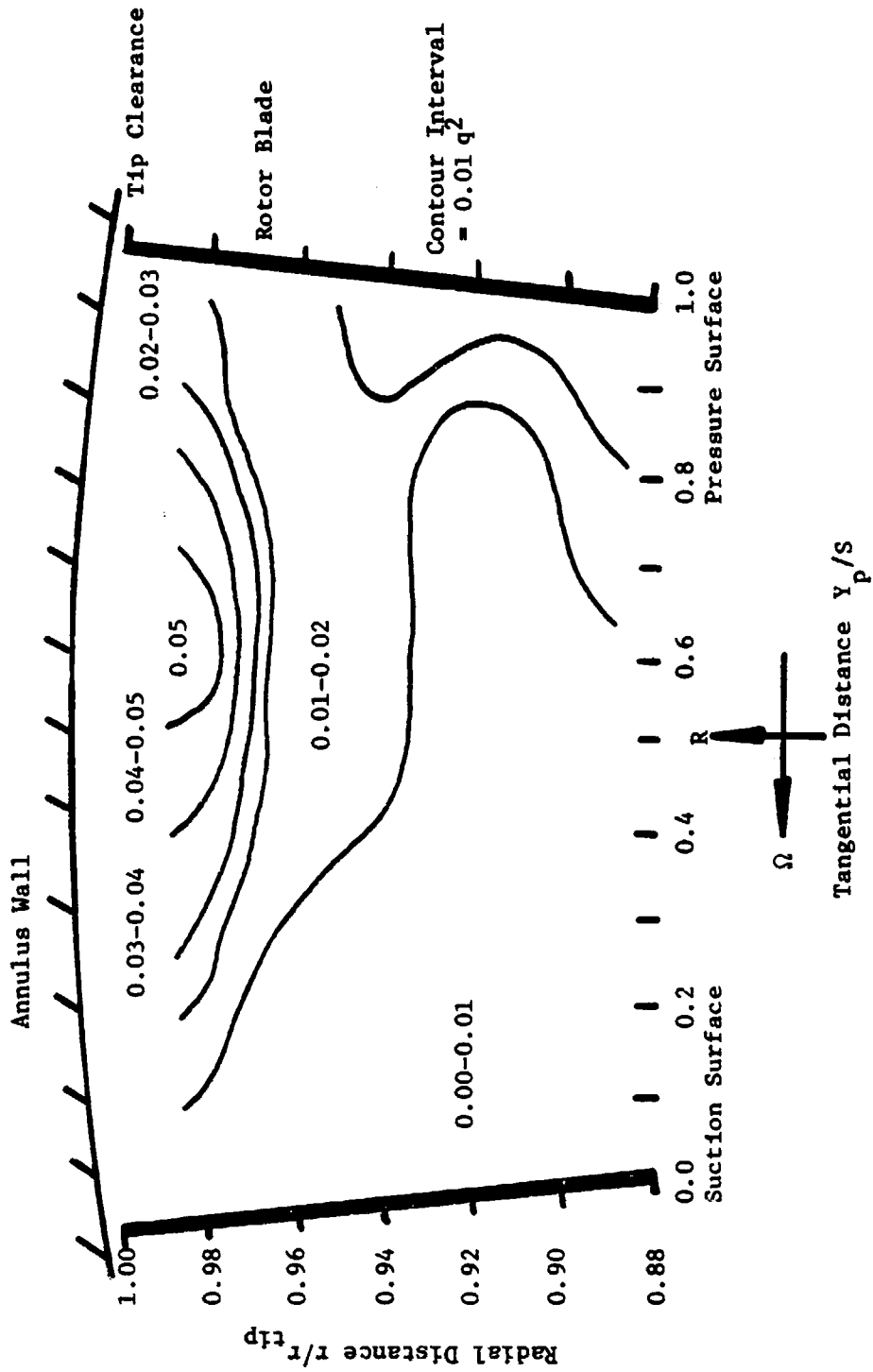


Figure 80. Total Turbulence Energy at $Z = 0.750$.

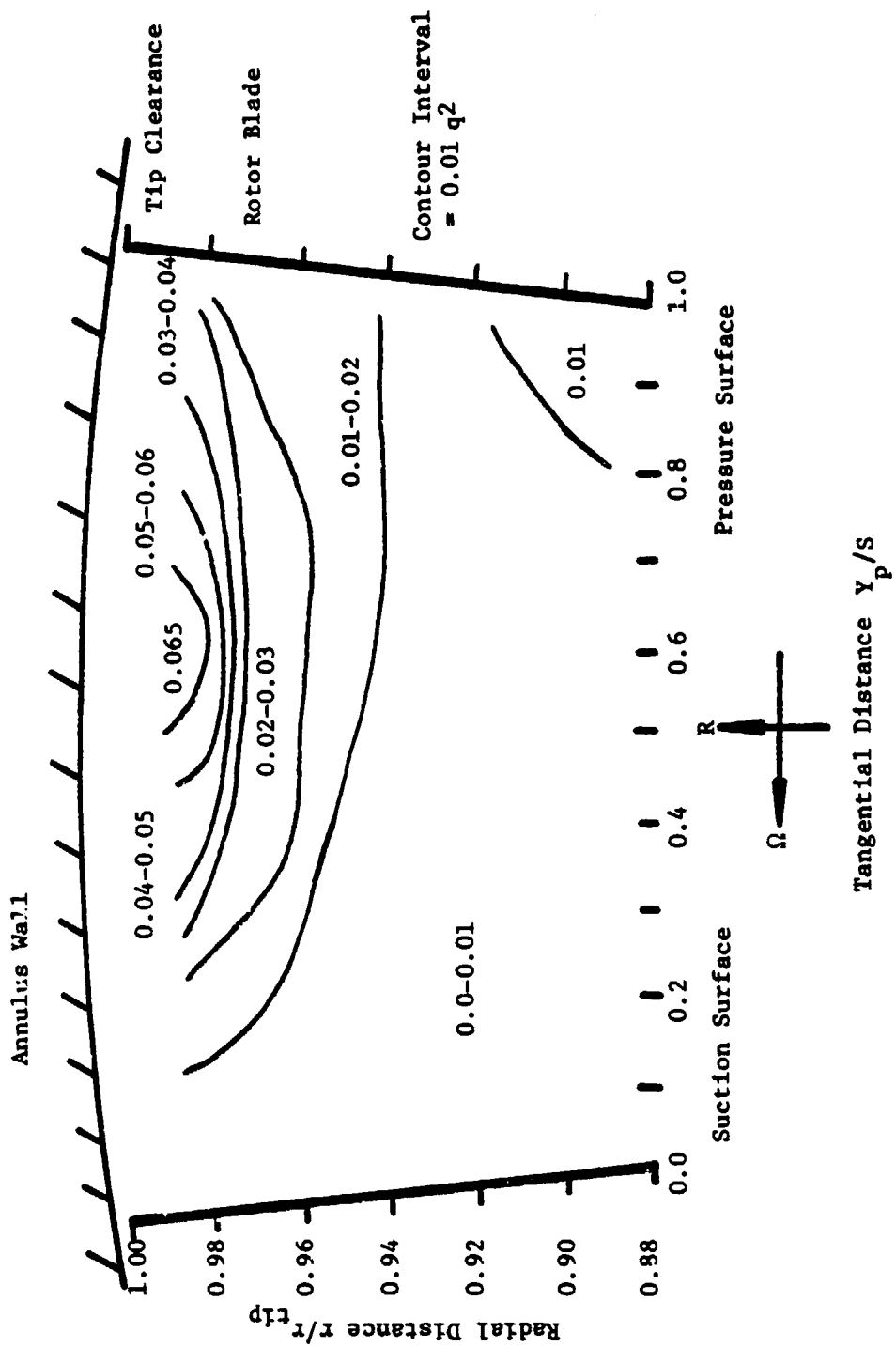


Figure 81. Total Turbulence Energy at $Z = 0.979$.

is clearly indicated. These contours show a core of high turbulence centered at approximately 65% of the passage width from the suction-surface. This core is seen to increase with axial distance. The core location and size increase coincide with the location of the maximum total relative velocity deficiency noted in Figures 60 and 61. At this location the two blade boundary layers are turned radially inward. Their interaction with the annulus-wall boundary layer and the tip leakage flow produces a large turbulent mixing zone. Unlike the two-dimensional fully developed boundary layers in stationary passages or pipes, the streamwise velocity profile in this interference region shows a dip with inward radial flows. Thus there exist finite mean velocity gradients even in the mid-passage. This results in an increased production of turbulence in this region. This increase of turbulence is shown by turbulence energy levels of 0.05 where levels of 0.00 to 0.01 are seen at radial locations where the flow is predominately inviscid.

4.4 Annulus-Wall Flow Turbulence Shear Stress Profiles

Figures 82 to 93 show the blade-to-blade distribution of the three turbulence shear stress correlations (see Figure 39) derived from the three-sensor hot-wire measurements described earlier. The stress correlations are normalized by the local streamwise velocity and the tangential distance is normalized by the blade spacing.

The measurements of the blade passage-flow show that outside of the interference region, the turbulence stresses are small. However, these stresses increase in magnitude as the blade surfaces are

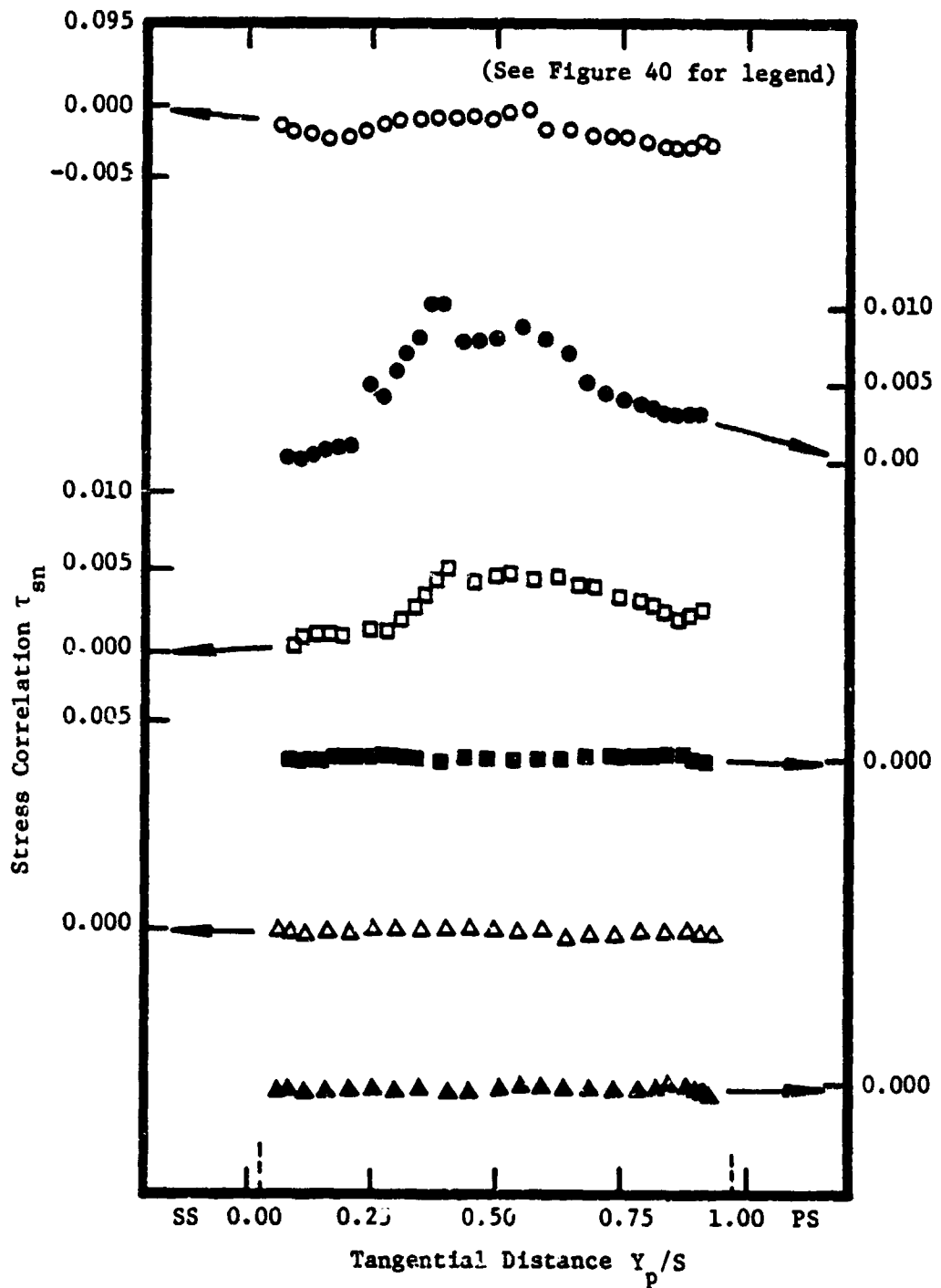


Figure 82. Stress Correlation τ_{sn} , $Z = 0.750$.

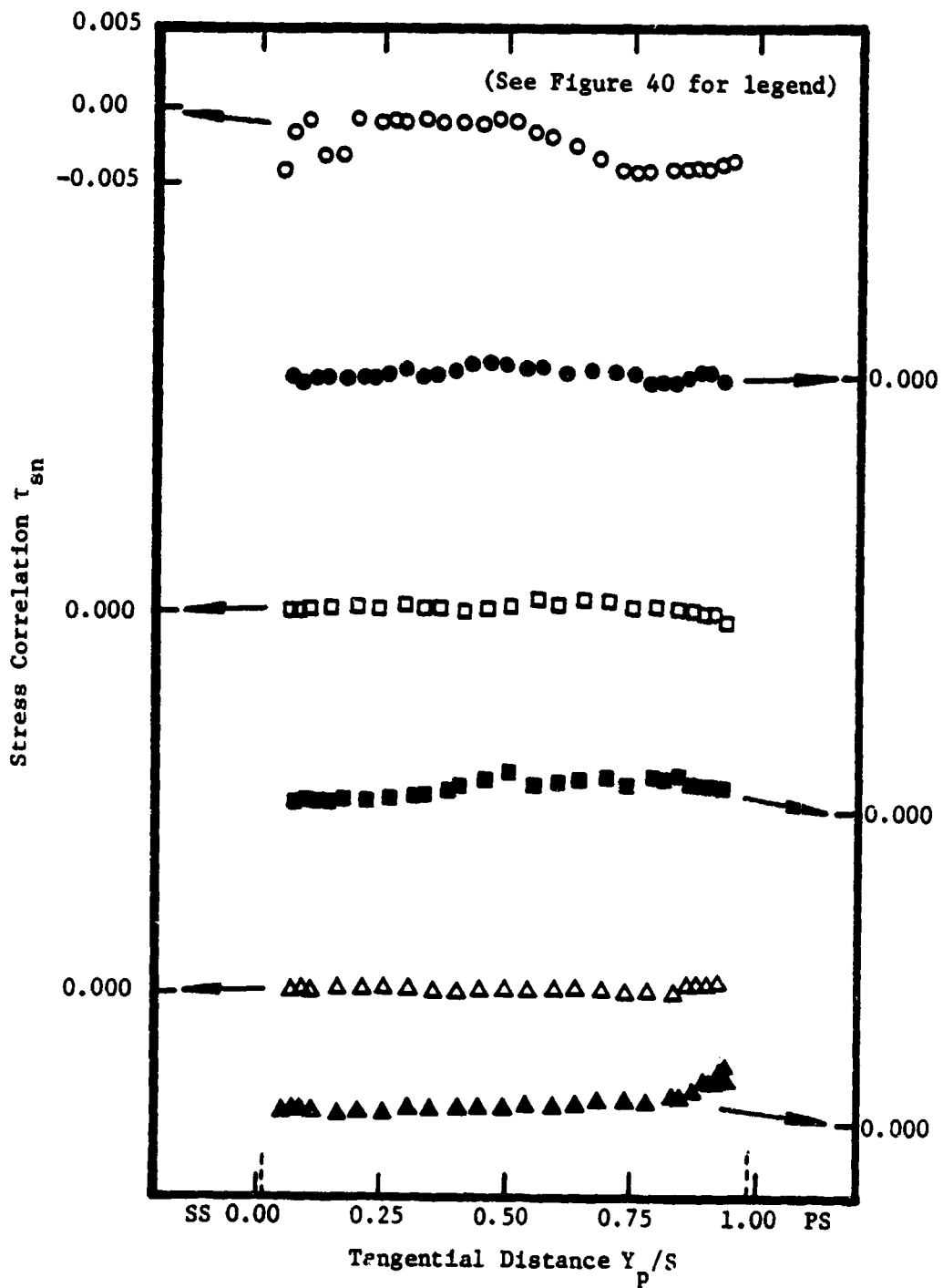


Figure 83. Stress Correlation τ_{sn} , $Z = 0.979$.

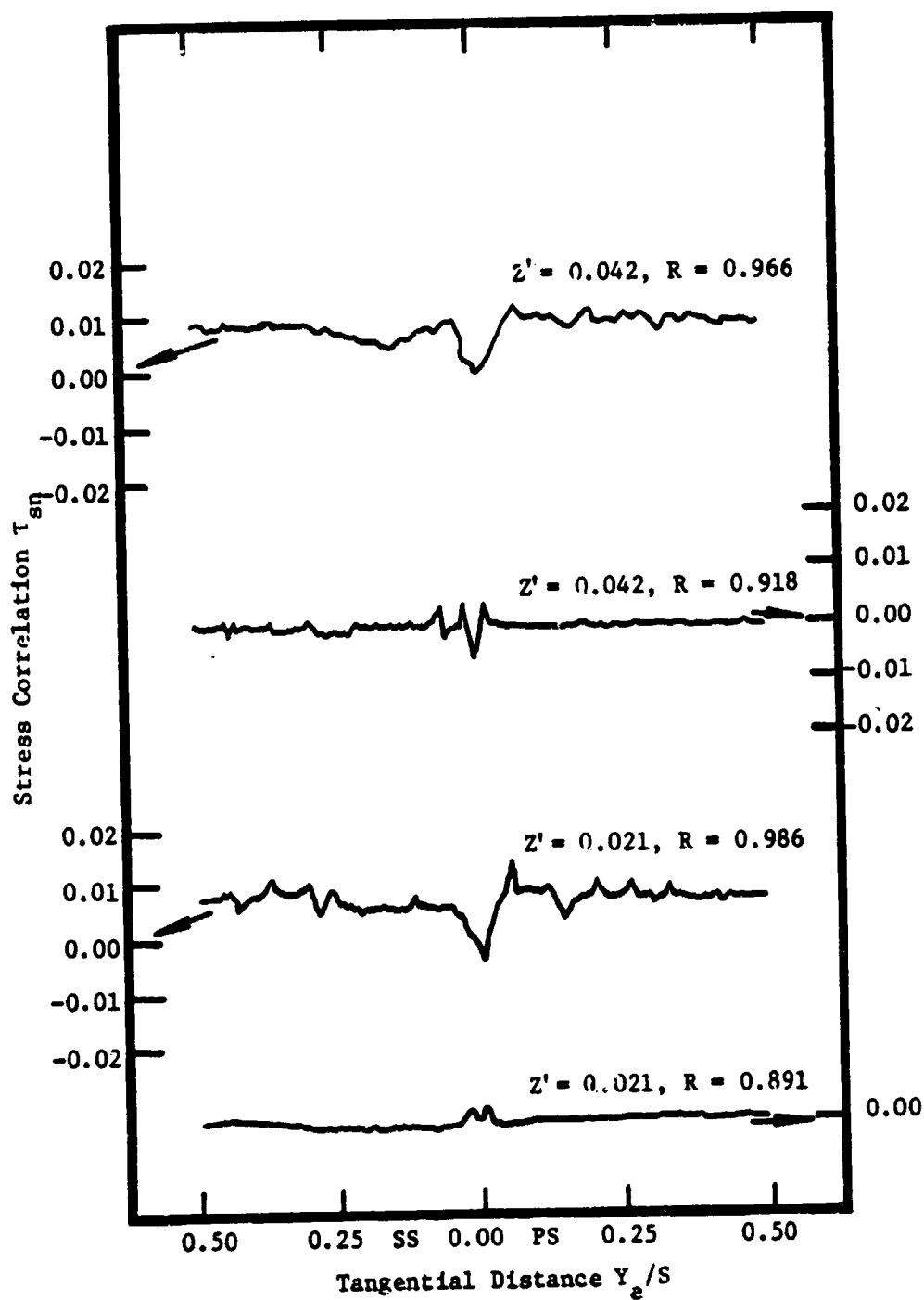


Figure 84. Stress Correlation τ_{sn} , $Z' = 0.021, 0.042$.

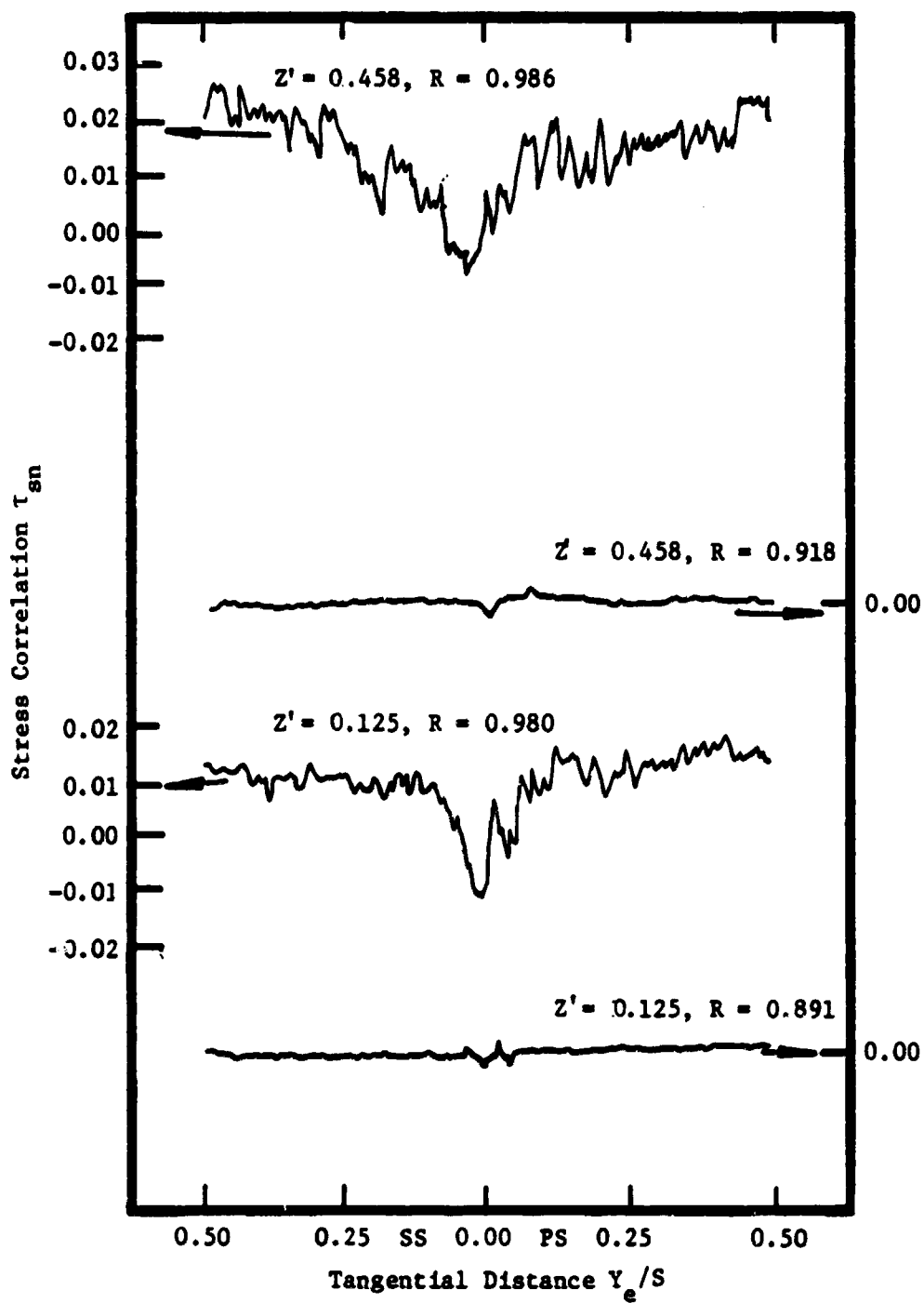


Figure 85. Stress Correlation τ_{sn} , $Z' = 0.125, 0.458$.

ORIGINAL PAGE IS
OF POOR QUALITY

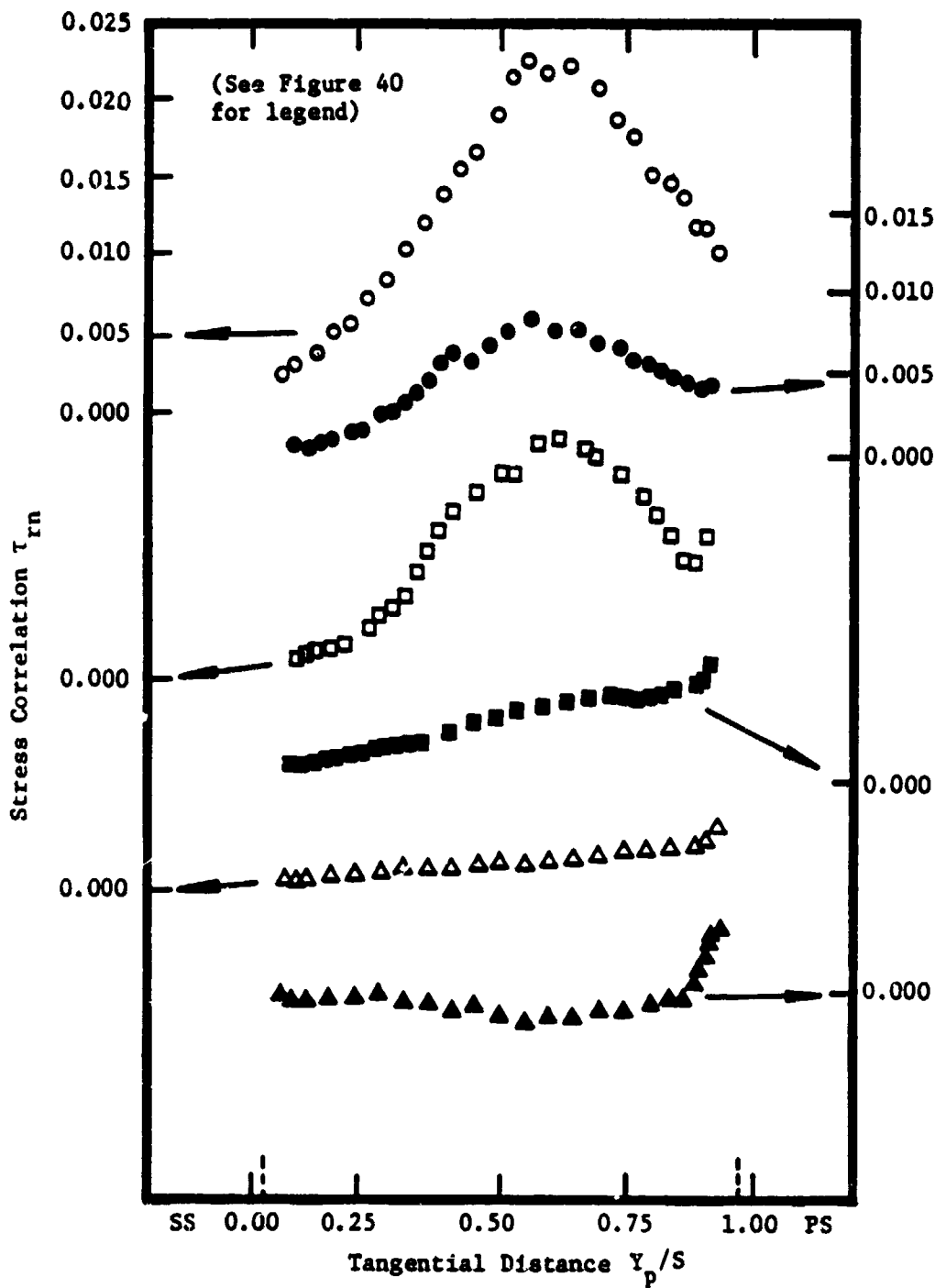


Figure 86. Stress Correlation τ_{rn} , $Z = 0.750$.

ORIGINAL PAGE IS
OF POOR QUALITY

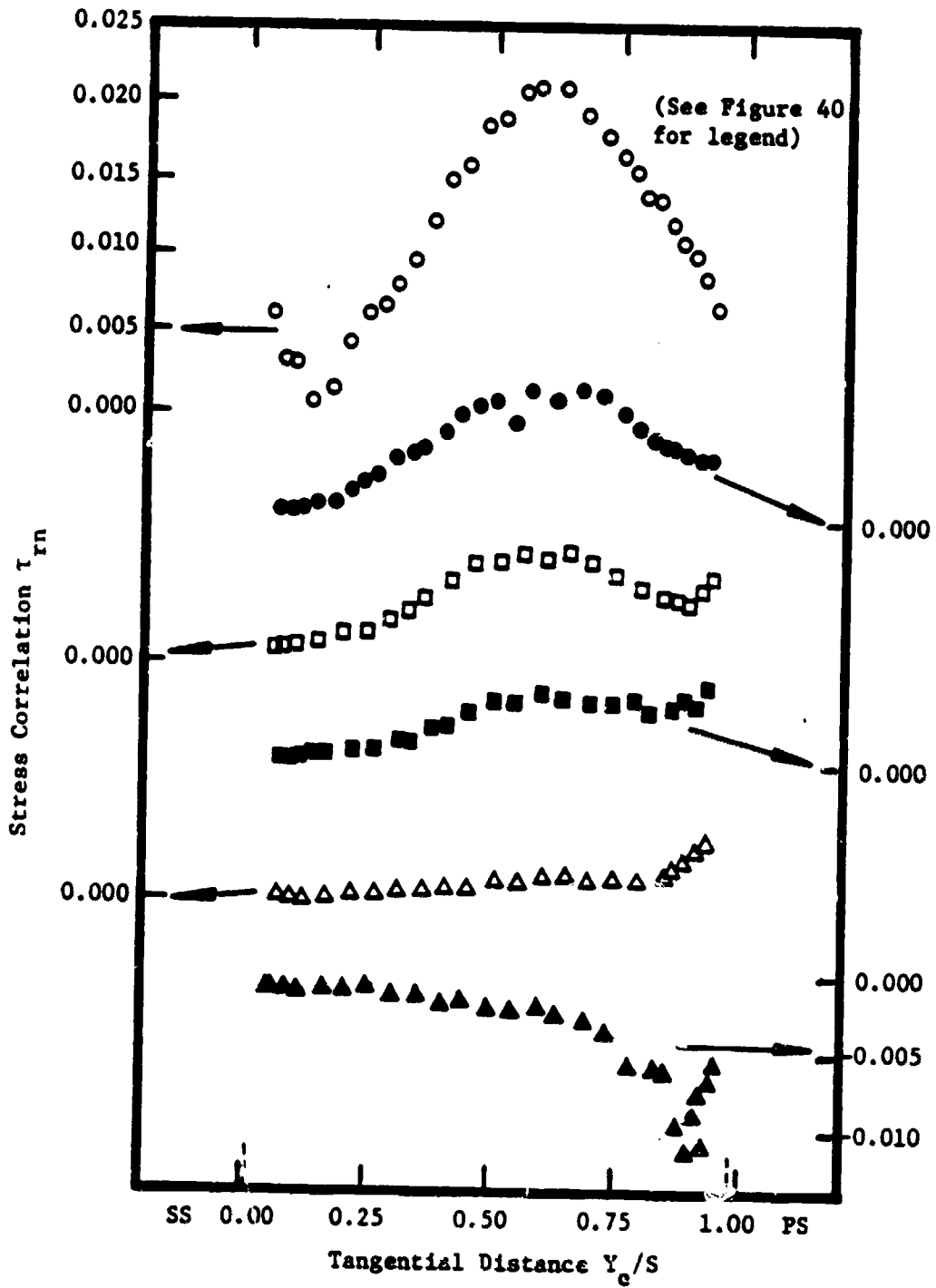


Figure 87. Stress Correlation τ_{rn} , $Z = 0.979$.

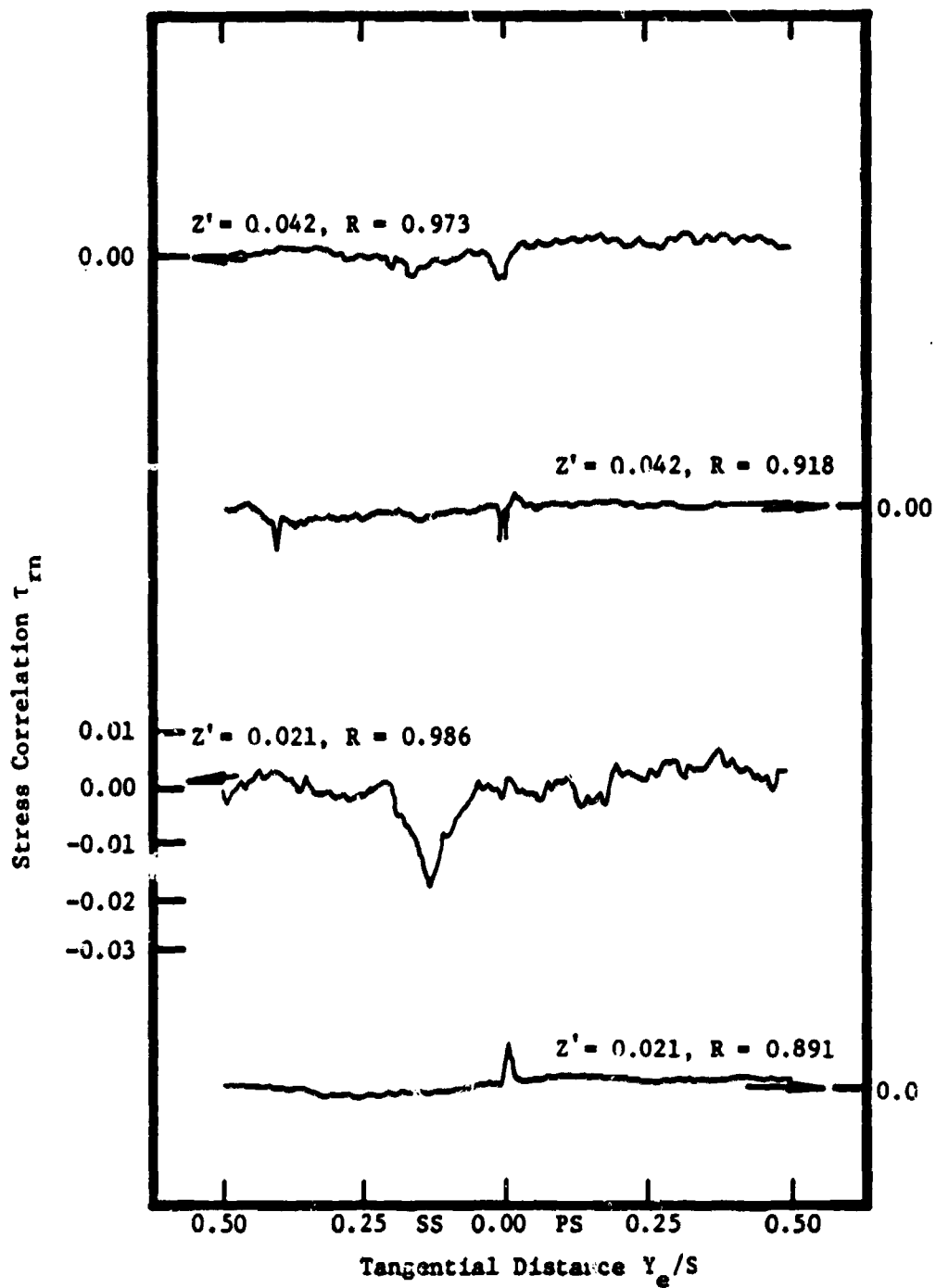


Figure 88. Stress Correlation τ_{rn} , $Z' = 0.021, 0.042$.

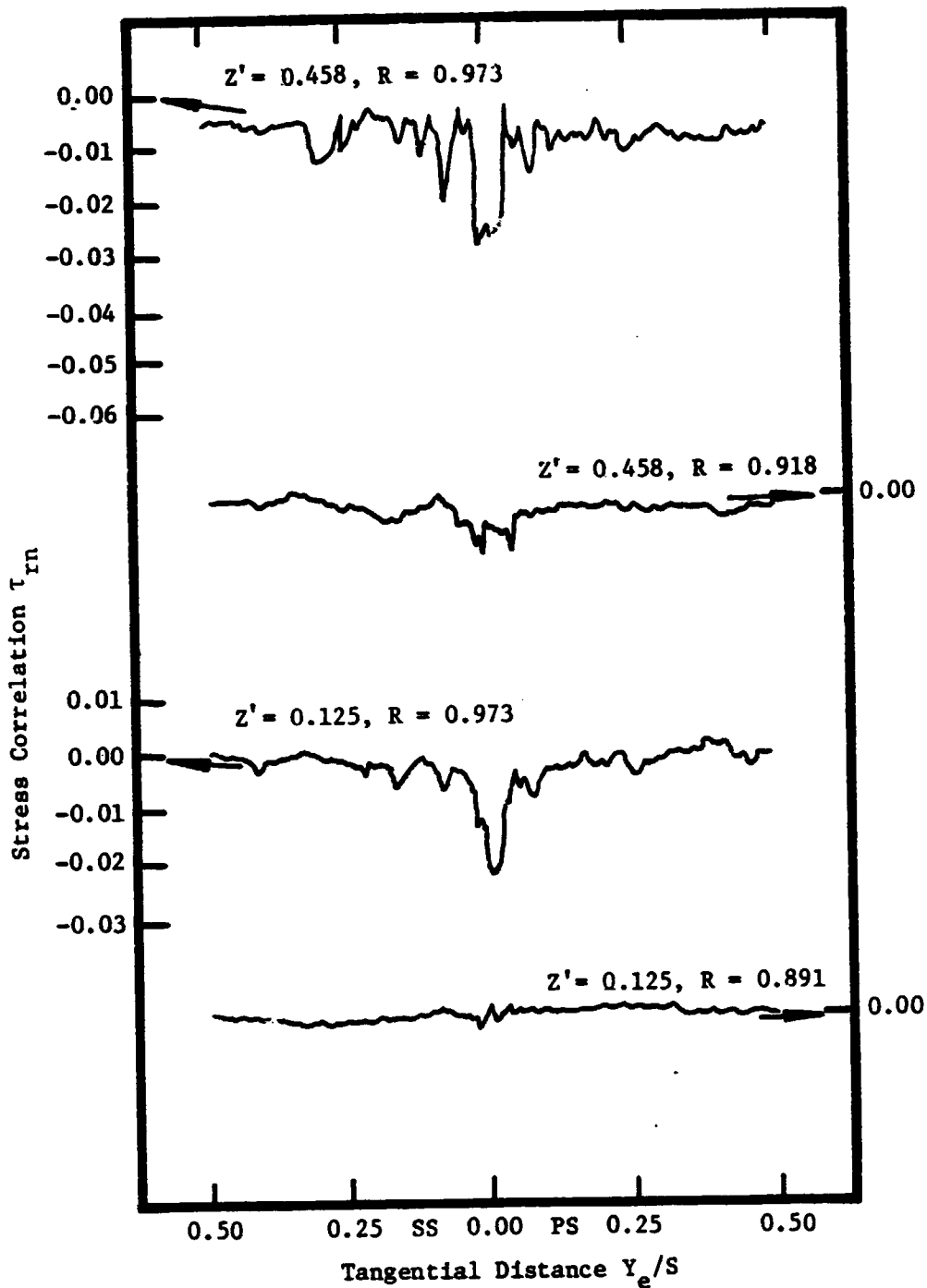


Figure 89. Stress Correlation τ_{rn} , $Z' = 0.125, 0.458$.

C-3

ORIGINAL PAGE IS
OF POOR QUALITY

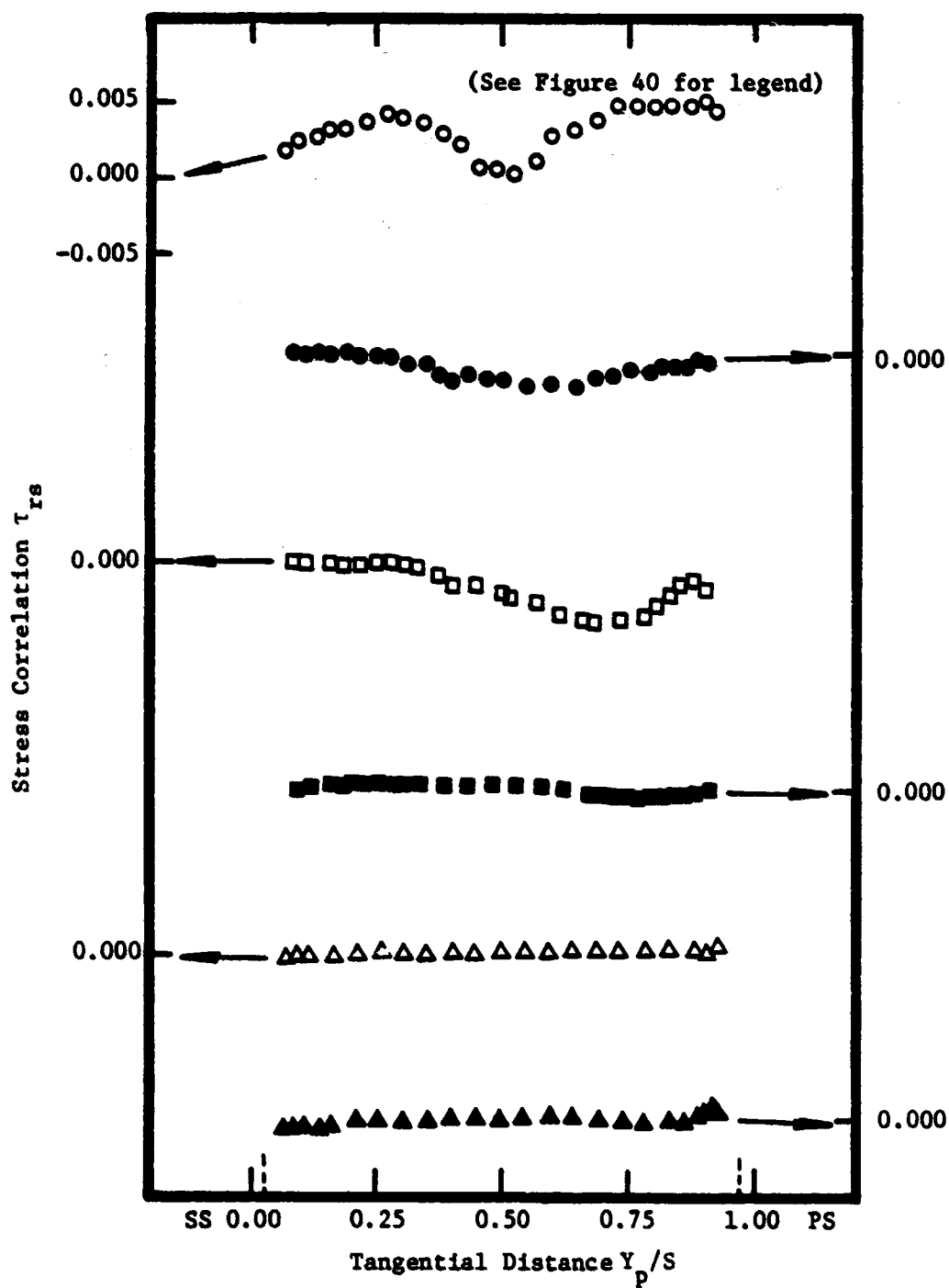


Figure 90. Stress Correlation τ_{rs} , $Z = 0.750$.

ORIGINAL PAGE IS
OF POOR QUALITY

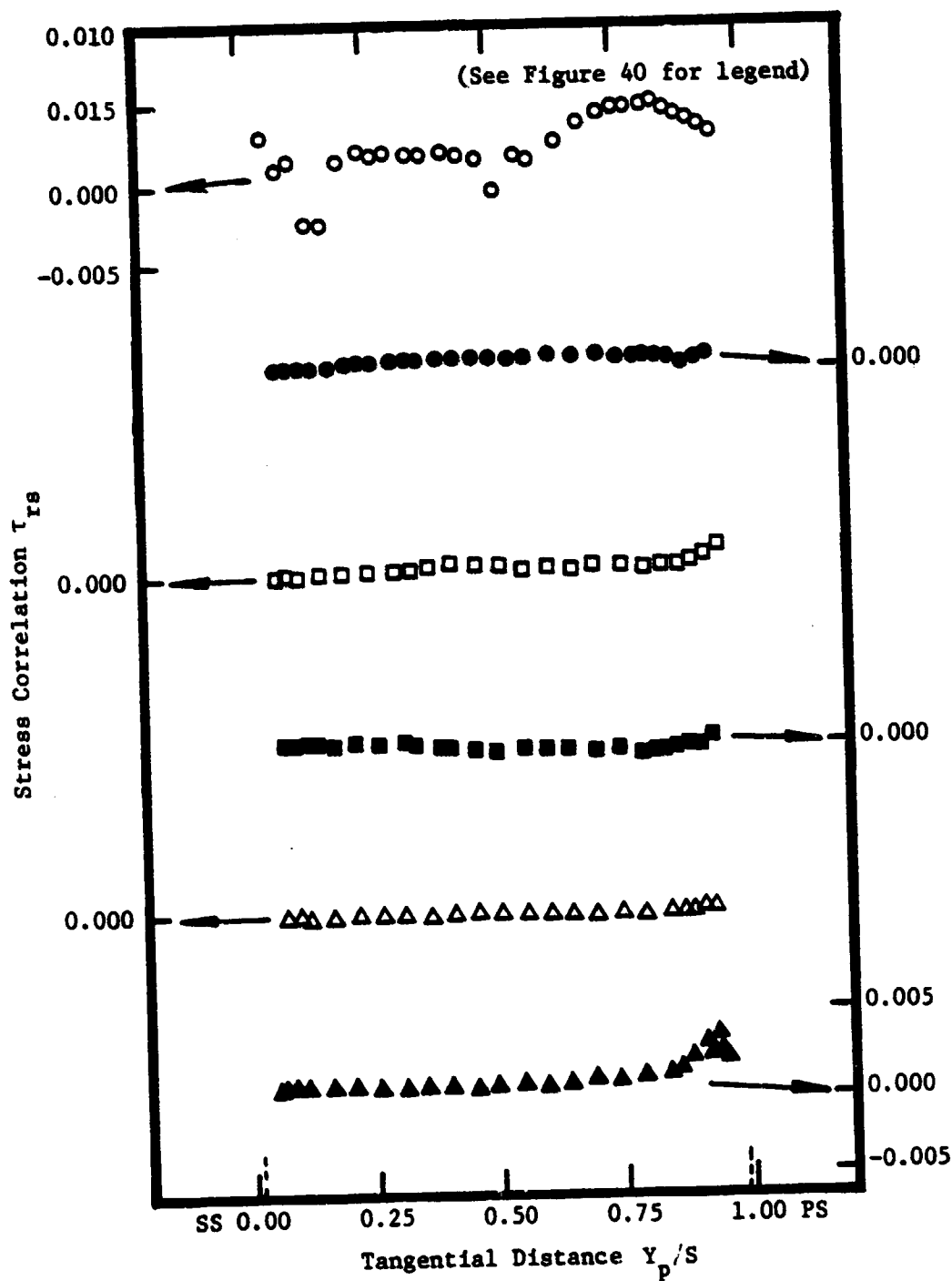


Figure 91. Stress Correlation τ_{rs} , $Z = 0.979$.

ORIGINAL PAGE IS
OF POOR QUALITY

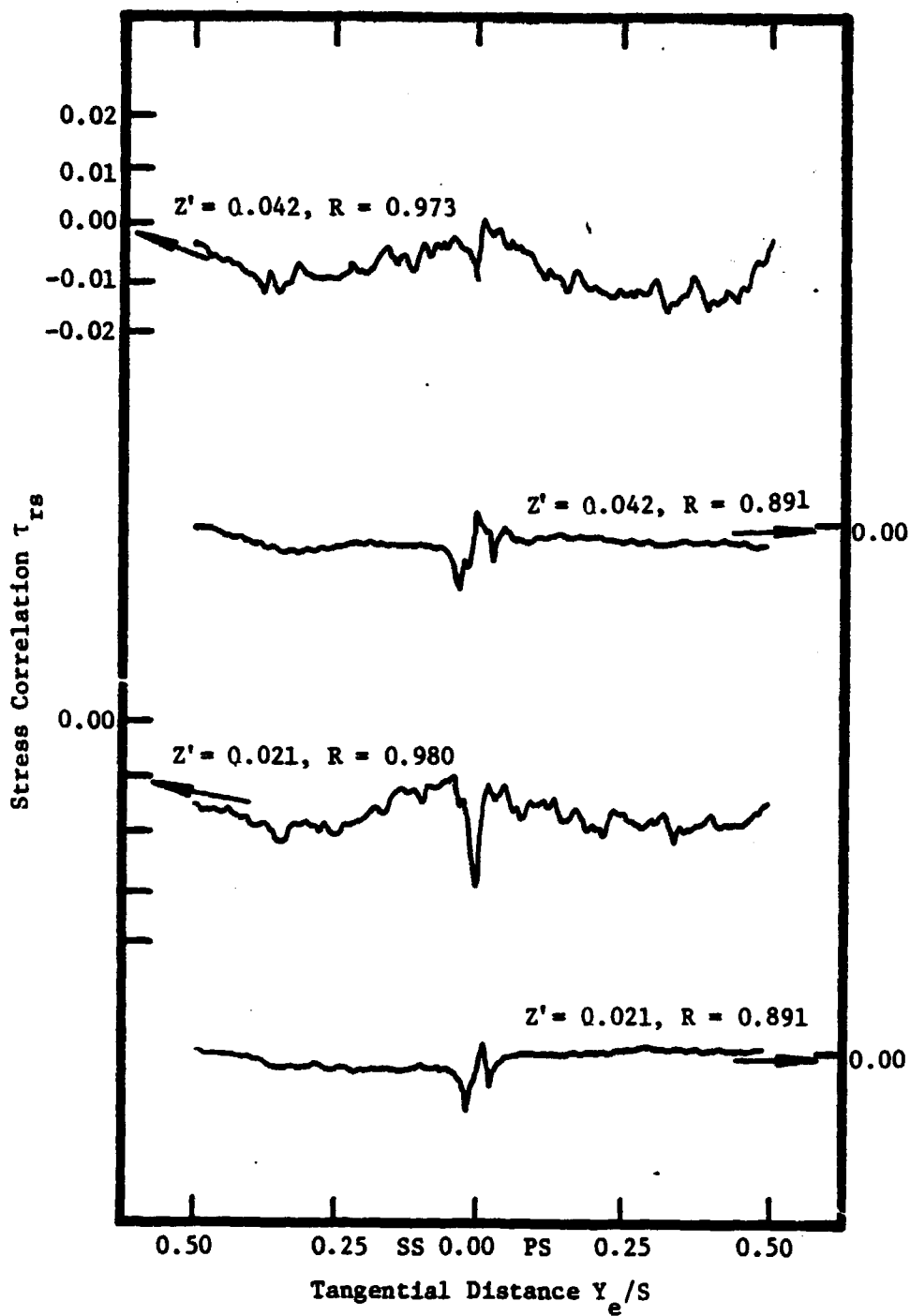


Figure 92. Stress Correlation τ_{rs} , $Z' = 0.021, 0.042$.

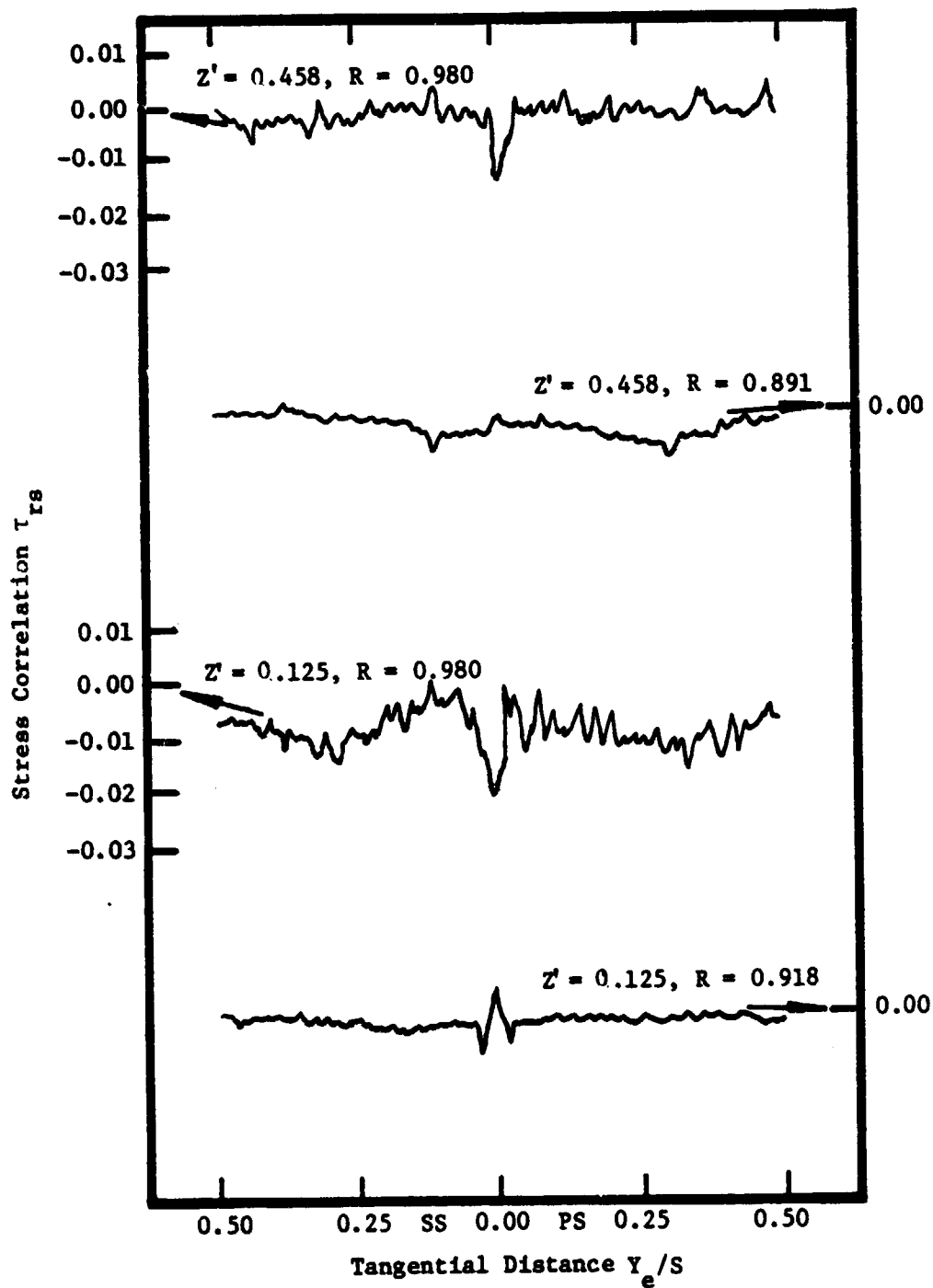


Figure 93. Stress Correlation τ_{rs} , $Z' = 0.125, 0.458$.

approached. This is due to the production of these stresses by the mean velocity gradients. This trend is common to all wall-bounded shear flows. Unlike two-dimensional boundary layers where only the stress correlation τ_{sn} is present, the data shows that the other two stress correlations (τ_{rn} and τ_{rs}) are also of the same order of magnitude. In the interference region, the turbulence stresses become large due to their production by the mean velocity gradients.

The turbulent stresses in the rotor exit-flow are very small in the free-stream and increase in magnitude near the wake center. At this location they reach their maximum value. This type of trend is brought about by gradients of the mean velocity and turbulence intensity. The variation of the stress correlation τ_{sn} shows the expected reversal of stress at the wake center. This reversal of stress is induced by opposite gradients of streamwise mean velocity about the wake center. The profiles are also asymmetrical about the wake center. The location of the zero stress correlation does not occur where $\partial W / \partial n$ is zero. This characteristic has also been reported by Raj and Lakshminarayana (1973) and Hah (1980). The profiles show a decay of the stress correlation τ_{sn} with axial distance; however, the stress correlation increases with radial distance. The interaction of the two shear layers, the annulus-wall boundary layer, and the rotor wake, produces large amounts of flow mixing which results in an increase of the stress correlations.

The stress correlation τ_{rn} also exhibits an asymmetric profile about the wake center. At the lower radial locations the radial velocities are smaller than the streamwise velocities, which give

τ_{rn} to be less than τ_{sn} . This trend is not fully realized by the data presented. At some low radial locations the stress correlations are equal in magnitude and in other instances it is seen that τ_{rn} is greater than τ_{sn} . This observation indicates the effect of rotation on the stresses. Lakshminarayana and Reynolds (1980) have argued, on the basis of the Reynolds stress equation in the rotating coordinate system, that the effect of rotation is to attenuate the stress component τ_{rn} . As the blade tip is approached, the situation becomes more complicated due to the viscous interactions associated with the annulus wall. The magnitude of the stress correlation τ_{rn} increases rapidly. The effect of the interaction of the annulus-wall boundary layer with the rotor wake, the tip leakage vortex, and the secondary flow is to amplify this stress component. The viscous interaction of the flowfield in this region compliments the effect of rotation.

The stress correlation τ_{rs} is seen to be of the same order of magnitude as τ_{sn} in the blade exit-flow. This stress correlation is asymmetric about the wake center and has the same sense on either side of the wake as τ_{sn} . The effect of the annulus wall is seen to increase the magnitudes of the stress correlation τ_{rs} to that observed for the stress correlation τ_{sn} . Again, the influence of the viscous flow interactions near the annulus wall is shown to increase the stress correlation τ_{rs} .

The stress correlations of the exit-flow near the annulus wall show an increase in the wake with axial distance. The exact nature of this increase is difficult to determine. However, due to the experimental set-up the smoothness of the annulus wall varied with

axial distance. The increase in the stress correlations might reflect an interaction between the exit-flow and the surface of the annulus wall. It should also be noted that the stress correlations presented in Figures 82 through 93 are subject to spatial errors which are inherent in a three-sensor hot-wire probe. An estimate of the scales of the flow and the expected order of error is given in Appendix A and Appendix B. However, the contribution to stress from eddies larger than the distance between the probe sensors was measured accurately.

4.5 Passage-Averaged Flow Angle Variation

The radial variation of the passage-averaged flow angle $\bar{\alpha}$ and the meridional angle $\bar{\beta}$ at various axial locations is plotted in Figures 94 and 95. The nature of these angles with respect to the streamwise coordinate system is shown in Figure 39. Figure 94 shows that the flow angle $\bar{\alpha}$ deviates from the design value (dashed lines) considerably at radial locations near the blade tip. This trend is evident for both the blade passage-flow and the blade exit-flow. For both figures the design value of $\bar{\alpha}$ is based upon inviscid flow calculations.

In Figure 94 the upper graph indicates that 10 to 12 degrees of flow overturning occurs for $Z = 0.750$ at the radial locations $R = 0.959$ and $R = 0.973$. At these locations the mean velocity profile indicated that on the suction side of the blade passage the tip leakage flow was rolling up due to its interaction with the mainstream flow. Also, the flow on the pressure side of the blade passage was shown to be deflected toward the mid-passage. Both of these viscous phenomena are seen to produce substantial flow angle deviations from the design

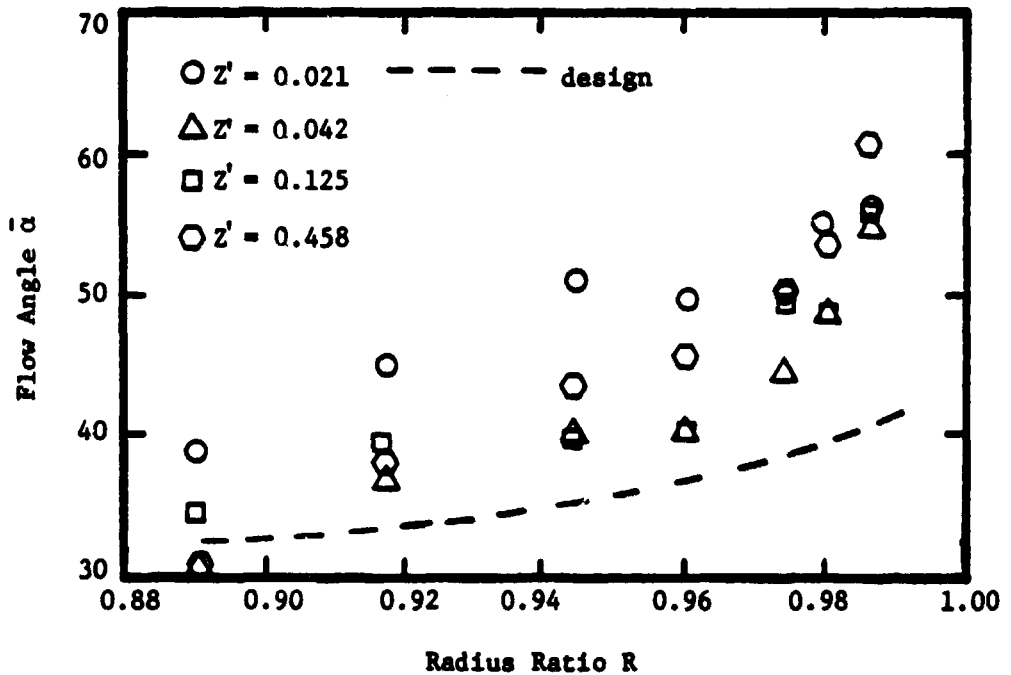
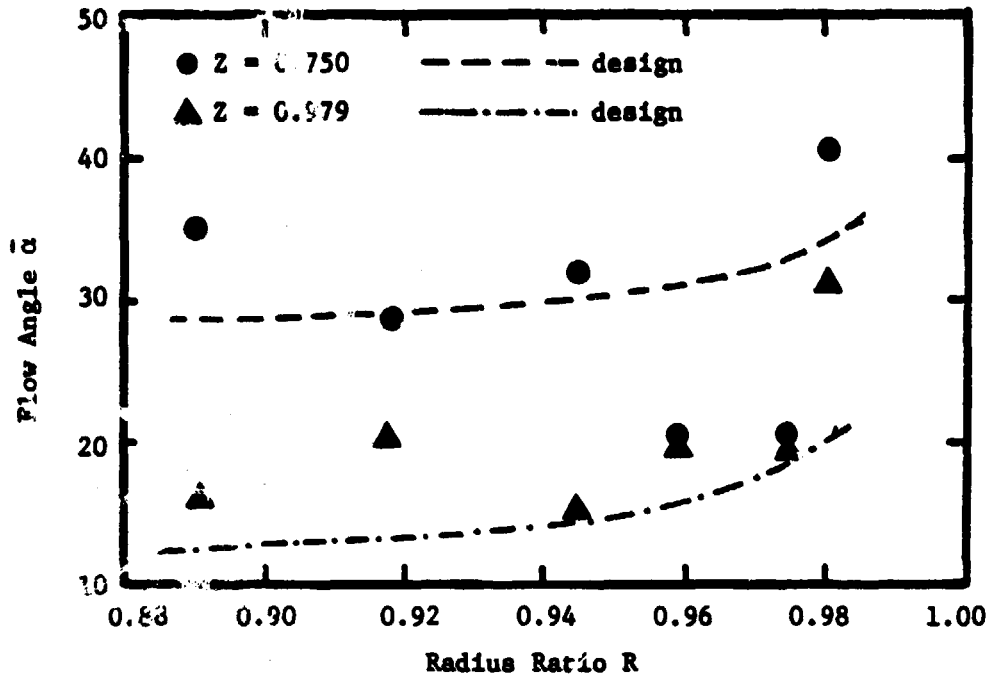


Figure 94. Radial Variation of Passage-Average Flow Angle at Various Axial Locations.

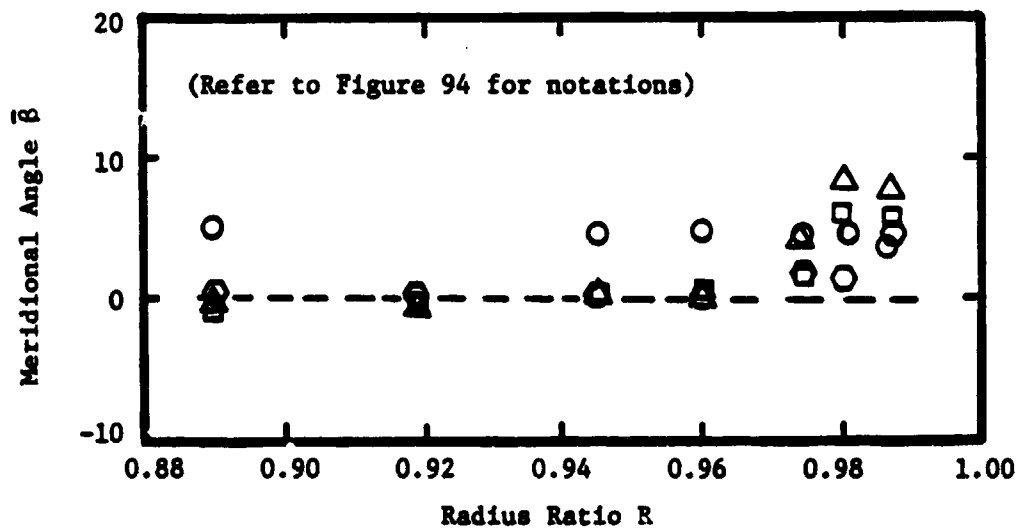
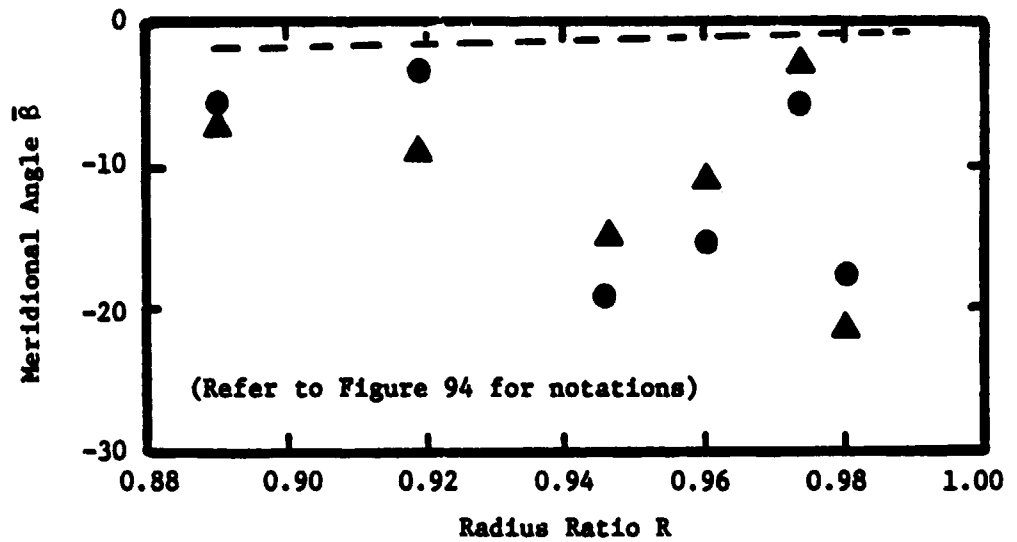


Figure 95. Radial Variation of Passage-Average Meridional Angle and Various Axial Locations.

or inviscid analysis. At these radial locations but at $Z = 0.979$, Figure 94 shows that the flow is slightly underturned. At this axial location the strength of the tip leakage flow is less due to the reduced pressure differential across the blade tip. The flow on the suction side of the blade passage is underturned due to the scraping of the annulus-wall boundary layer and the deflection of the blade boundary layer to the center of the passage due to the annulus wall. However, the flow on the pressure side of the blade passage is also deflected toward the center of the blade passage which results in flow overturning. The combination of these effects results in slight flow underturning. For both axial locations within the blade passage, the flow is severely underturned near the blade tip at $R = 0.980$ due to the combined effect of the tip leakage flow and the annulus-wall boundary layer. Thus substantial deviations from the design value of $\bar{\alpha}$ occur within the blade passage due to viscous flow phenomena.

The lower graph of Figure 94 shows the measured flow angle $\bar{\alpha}$ in the exit-flow compared to the design value. At the lower radial locations the flow angle deviates only slightly from the design value. However, as the radial location is increased, up to the blade tip, $\bar{\alpha}$ increasingly deviates from the design condition. At $R = 0.986$ the flow is underturned by approximately 16 degrees. This flow underturning is induced by the effect of the annulus wall. Upon leaving the blade passage the viscous dragging of the exit-flow by the annulus wall underturns the flow with increasing severity as the wall is approached.

Figure 95 shows a comparison of the meridional angle $\bar{\beta}$, which is averaged over the blade passage for the passage- and exit-flow, with

the design value of β . The flow is seen to deflect radially inward within the blade passage. This deviation from the design condition is primarily due to the viscous interaction of the flow phenomena near the blade tip. This includes the radially inward flow produced by the rolling up of the tip leakage flow and the deflection of the blade boundary layer radially inward due to the annulus wall. At the exit of the blade passage, the meridional angle β slightly deviates from the design value near the blade tip. A radially outward flow is indicated for the flow behind the blade passage.

4.6 Passage-Averaged Velocities and Annulus-Wall Mean Boundary Layer Properties

In the following sections the passage-average total velocity, momentum thickness, and shape factor are discussed.

4.6.1 Passage-Average Total Velocity

The radial distribution of the passage-average total velocity for the various axial measurement stations is shown in Figure 96. At each axial location the distribution of the passage-average total velocity W_{TA} , which is normalized by the rotor blade tip speed U_{Tip} , is presented graphically with the corresponding values of velocity indicated.

The passage-average value of W_T is found to be lower than the free-stream velocity that exists in an inviscid flow. This difference increases as the flow proceeds further downstream. The largest difference occurs near the blade tip where the two surface boundary layers have interacted with the annulus-wall boundary layer.

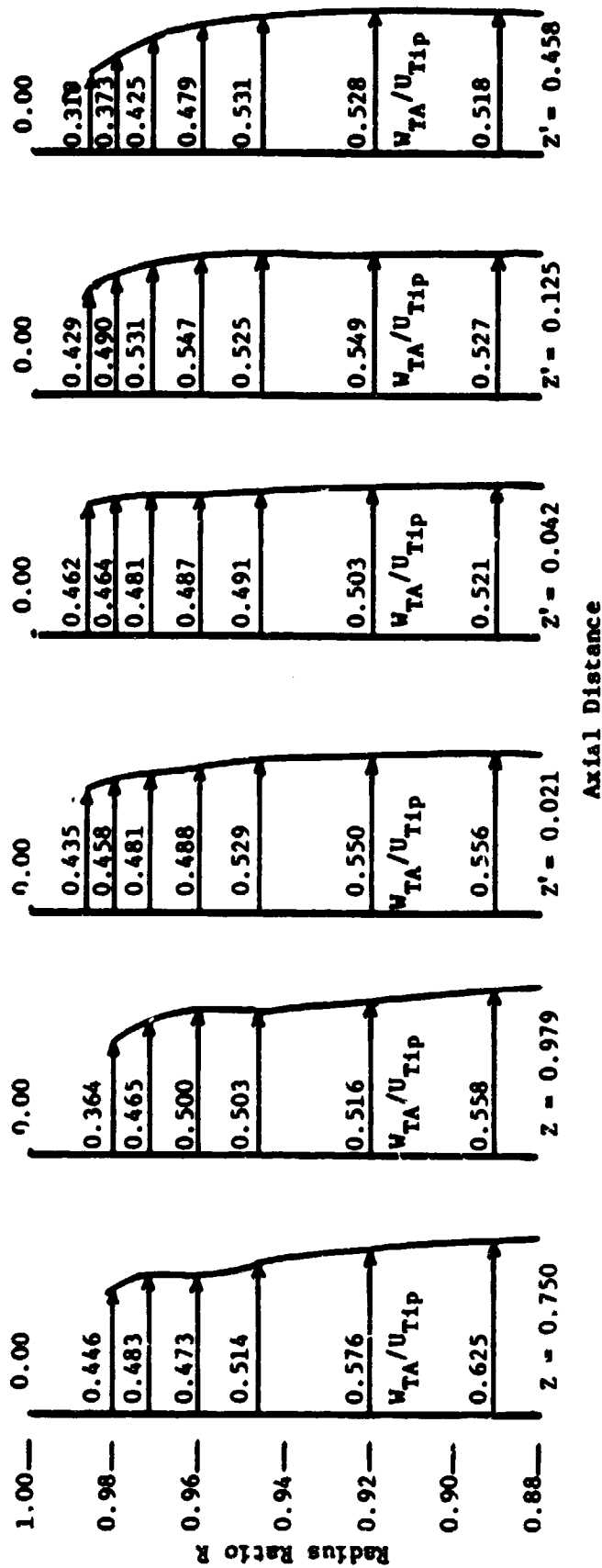


Figure 96. Radial and Axial Distribution of the Passage-Average Total Relative Velocity.

The large reduction of the passage-average velocity near the tip is due to the interference of the blade boundary layers and the annulus-wall boundary layer. At this location the flows are completely submerged into each other and are accompanied by radial inward flow. This phenomenon was observed in the radial mean velocity profiles discussed earlier. In this region it was observed that the value of the shear stress is considerable near the center of the passage. Also, the turbulence level observed in this region is maintained at the expense of the mainstream velocity gradient in the normal direction. These observations are reflected in the passage-average value of the total mean velocity presented in Figure 96.

4.6.2 Momentum Thickness and Shape Factor of the Annulus-Wall Boundary Layer

Momentum thickness is used as the characteristic boundary layer dimension. The momentum thickness implies the loss of momentum in the boundary layer, as compared with the potential flow. In the case of the annulus-wall region, this loss of momentum is associated with the annulus-wall boundary layer and the flow interactions between the blade boundary layers, the tip leakage flow, and the secondary flow. The integration of the momentum thickness θ^* was performed along the radial direction and is given by:

$$\theta^* = \int_{R=0.891}^{R=1.000} \frac{W_{TA}}{W_o} \left(1 - \frac{W_{TA}}{W_o}\right) dR \quad (17)$$

The data were extrapolated from $R = 0.980$ or $R = 0.986$ to the annulus-wall where $W_{TA}/W_o = 1.0$. The variation of the annulus-wall flow

momentum thickness with downstream distance is shown plotted in Figure 97. Downstream of the blade passage the momentum thickness increases with axial distance. This increase is due to the development of the annulus-wall boundary layer as the flow progresses downstream. Also, the various annulus-wall flows resulting from the interference region within the blade passage are decaying with axial distance. This decreases the momentum associated with the flow in this region.

The decrease in θ^* from the blade passage-flow to the exit-flow may be caused by blowing due to the tip leakage flow. The blowing would have the effect of energizing the flow and decreasing the momentum thickness.

The shape factor H is defined as the ratio of the displacement thickness to the momentum thickness and it is uniquely related to the velocity profile. The axial distribution of the shape factor obtained from the measurements of the passage-average velocity is plotted in Figure 98. The value of H is seen to increase rapidly at the trailing-edge of the rotor blade. The high value of 1.56 at $Z = 0.979$ indicates an interaction between the annulus-wall boundary layer and the interference region.

4.7 Variation of Rotor Wake Decay in the Radial and Streamwise Directions

The dominant flow phenomenon downstream of the blade passage is the rotor wake. The development of the wake in the radial and axial directions is influenced by the annulus wall. Various characteristics of the rotor wake are reported in the following sections which indicate this influence.

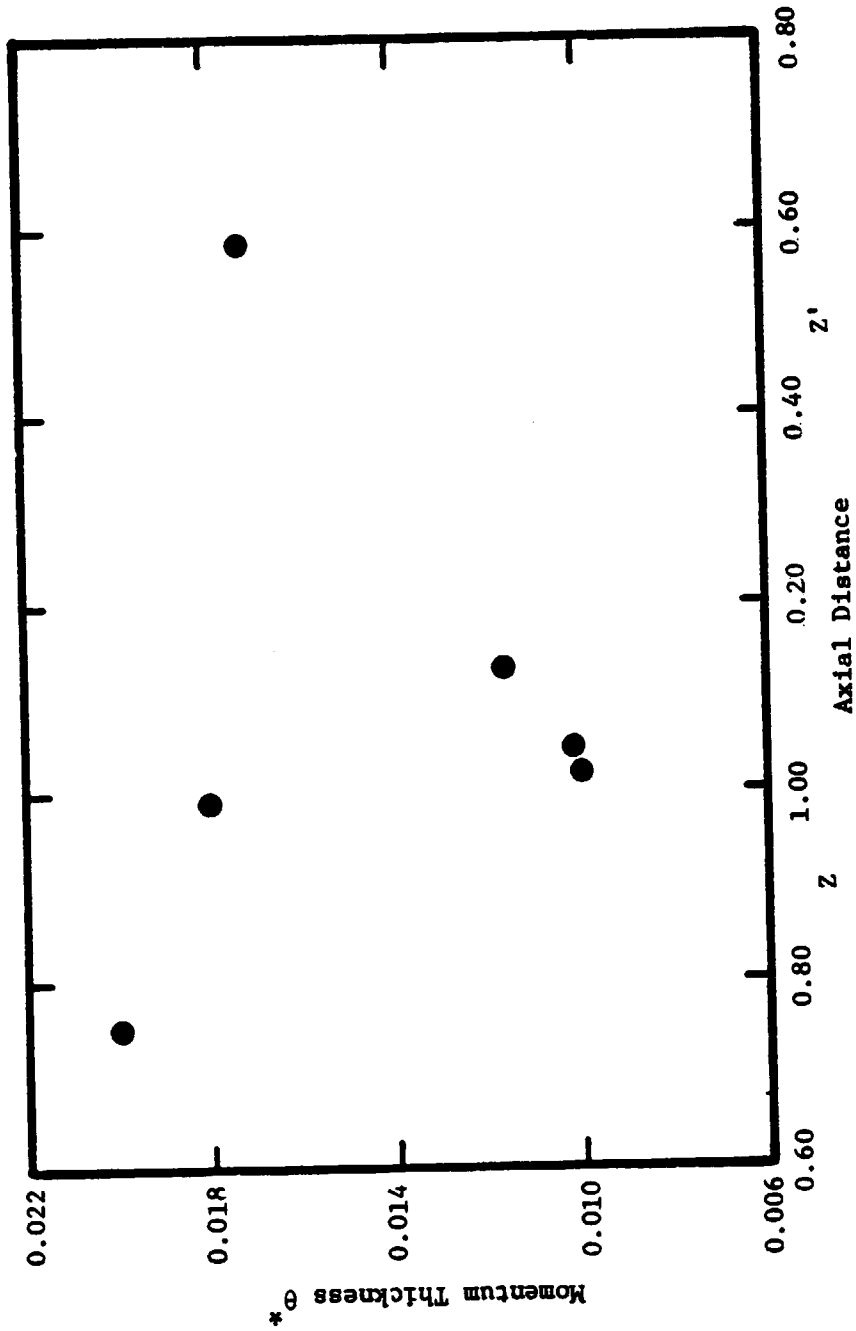


Figure 97. Annulus-Wall Flow Momentum Thickness Variation with Axial Distance.

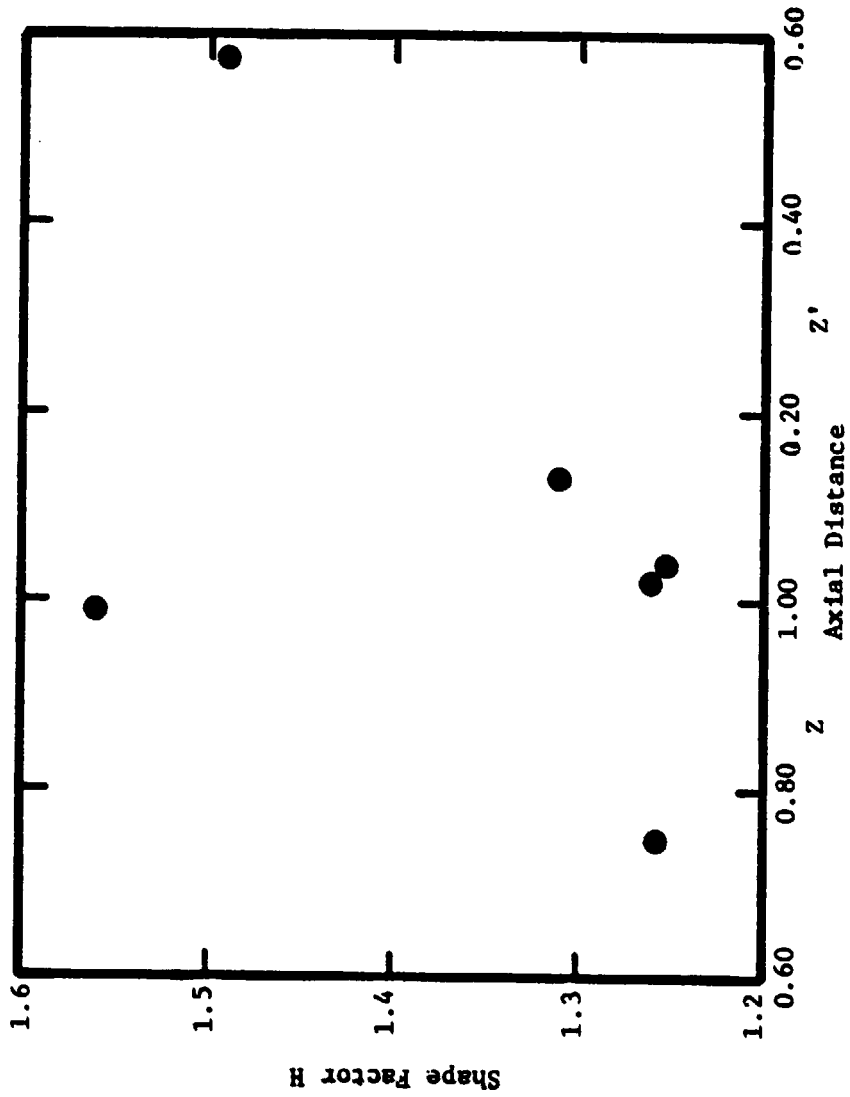


Figure 98. Annulus-Wall Flow Shape Factor Variation with Axial Distance.

4.7.1 Maximum Defect in Mean Velocities

The variation of the velocity deficit at the wake centerline reflects the decay rate or modification of the rotor wake. The decay of the mean velocity defect is greatly influenced by the pressure gradients and turbulence fluctuations downstream of the blade passage. The annulus-wall boundary layer, secondary flow, and tip leakage flow in the annulus-wall region also contribute to the variation of the wake profile.

The variation of the streamwise velocity defect and the maximum values of radial and normal velocity are shown plotted in Figures 99, 100, and 101. Due to the asymmetric nature of the wake profiles, the velocity defect with respect to both the pressure and suction sides of the wake is plotted. The variation of the wake velocity defect in the radial and axial direction is evident. Figure 99 shows this variation for the maximum streamwise mean velocity defect $(w_{so})_c / W_{so}$. The wake decay is maximum near the blade tip. This is brought about by the tip clearance flow, annulus-wall boundary layer, and secondary flow discussed earlier. The general trend observed is that the velocity defect decays rapidly in the axial direction. This trend is most pronounced at the lower radial locations where a velocity defect of 0.55 decays to 0.25 over an axial distance of half a blade chord. This rapid decay is attributed to large turbulence intensities, pressure gradients, and three-dimensional effects. The very wide wake profile at the higher radial locations reduces the streamwise velocity defect to a value of 0.25 near the blade which decays to 0.12 at $Z' = 0.458$. The shape of the profiles and the velocity defect at the radial

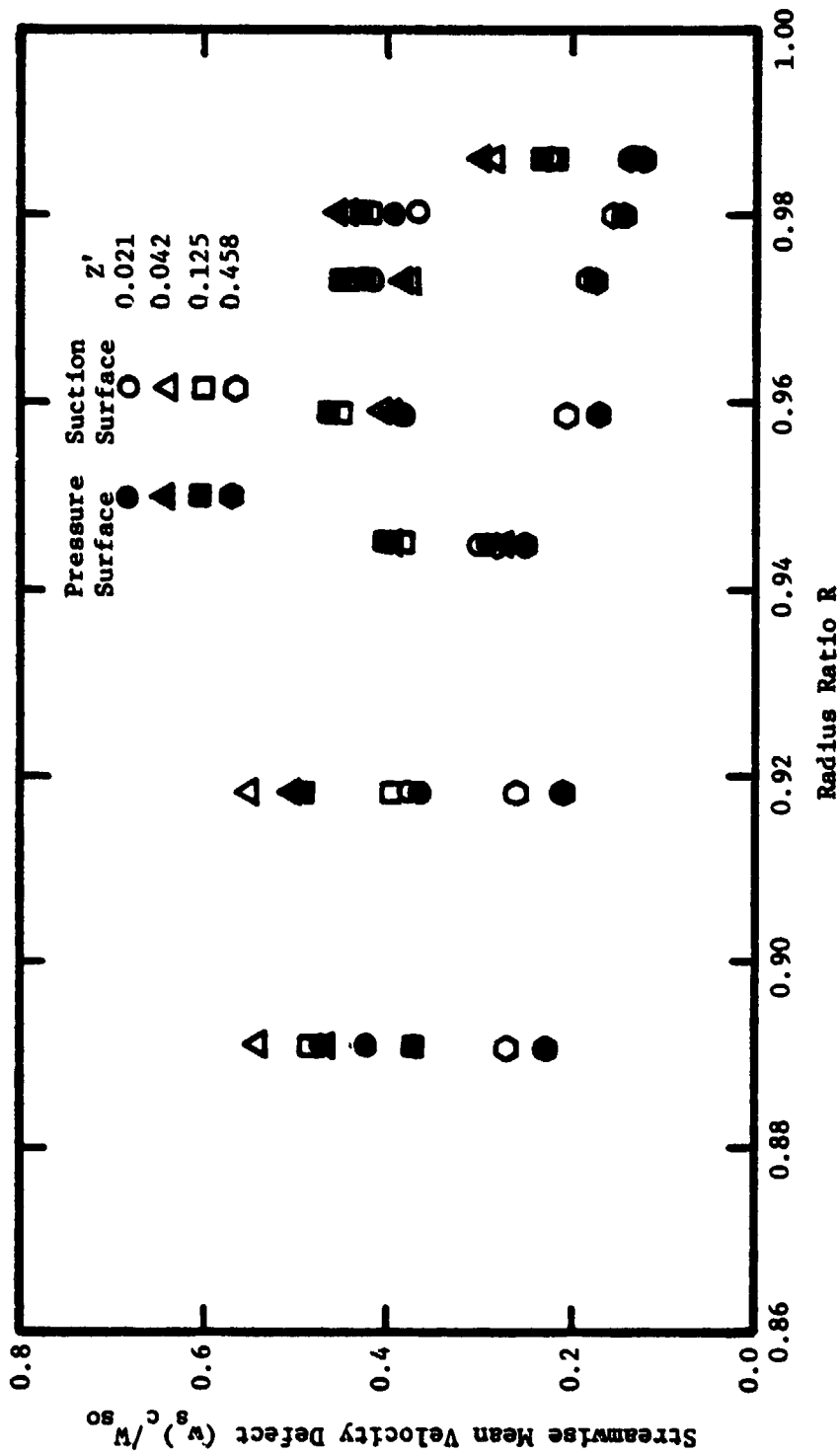


Figure 99. Radial and Axial Variation of the Streamwise Mean Velocity Defect.

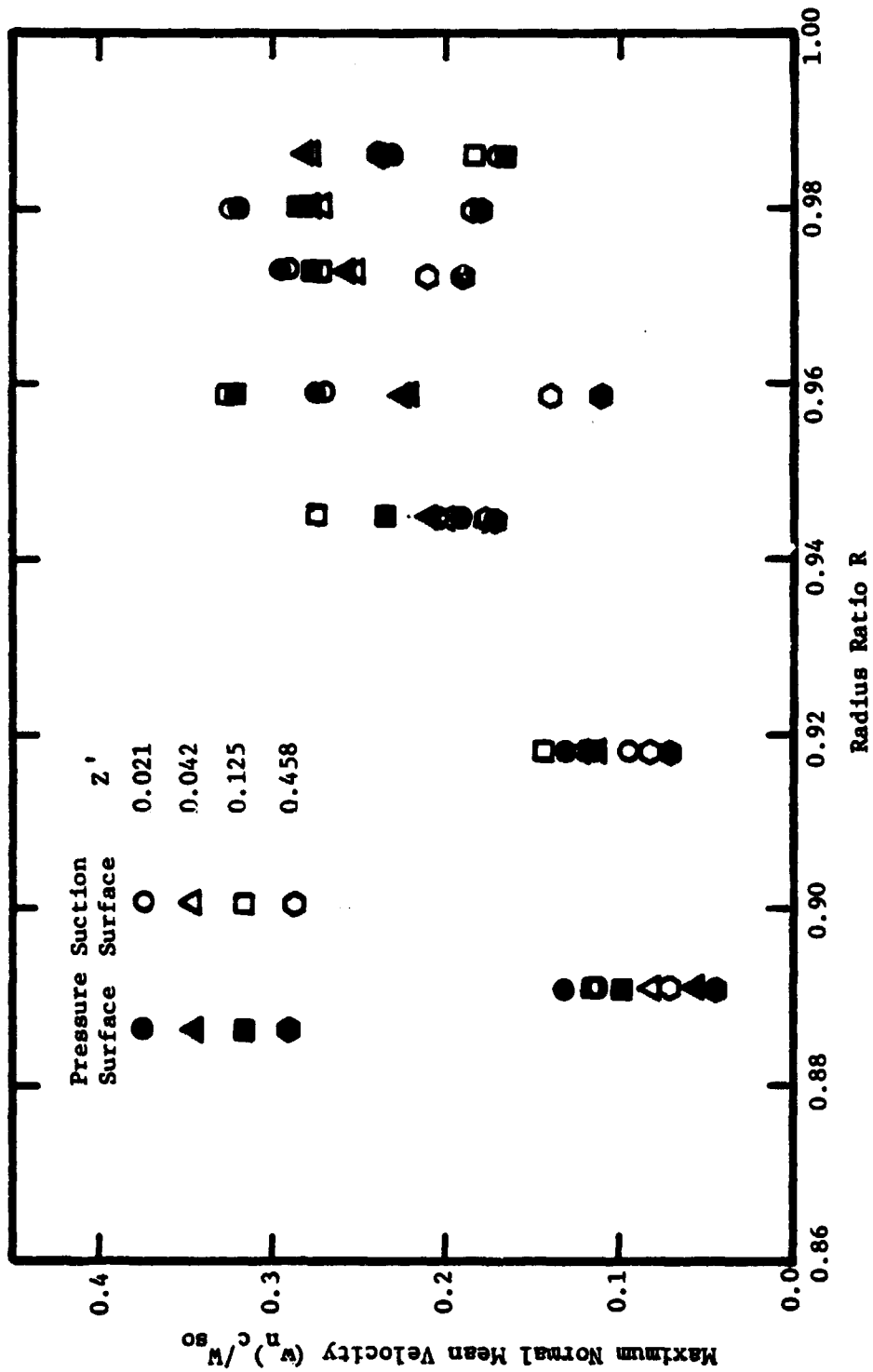


Figure 100. Radial and Axial Variation of the Maximum Normal Mean Velocity.

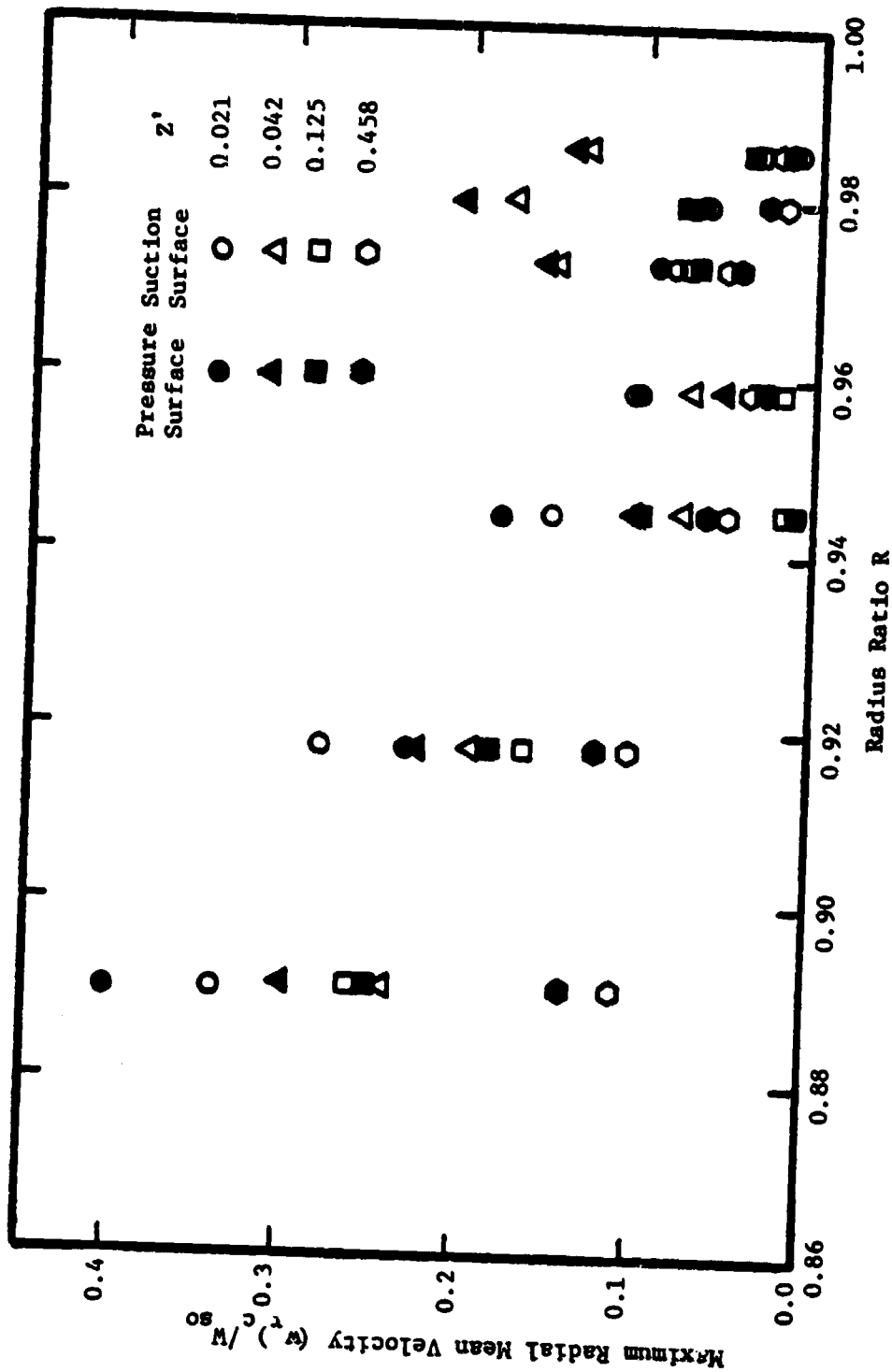


Figure 101. Radial and Axial Variation of the Maximum Radial Mean Velocity.

locations above $R = 0.945$ are due to the highly three-dimensional, viscous nature of the flow. The interaction of the annulus-wall boundary layer with the exit-flow induces a broader wake profile which extends over the entire blade spacing. This flow interaction dissipates the strong velocity gradients present in the wake trailing-edge region. The dissipation of the wake produces lower values of the streamwise velocity defect.

The variation of the maximum normal mean velocity $(w_n)_c/W_{so}$ in the radial and axial directions is presented in Figure 100. A substantial decay of the velocity is observed from the blade trailing-edge to the downstream locations. This decay is due to flow mixing and wake spreading as the wake travels downstream. With increasing radius, the normal velocity increases due to the viscous nature of the annulus-wall boundary layer and the tip leakage flow. The dragging of the flow in the normal direction and the passing of the leakage flow in the normal direction both contribute to a higher normal velocity. This increases the normal velocity of the wake in this region.

Figure 101 shows the variation of the maximum radial mean velocity $(w_r)_c/W_{so}$ in the radial direction and as the flow propagates downstream. The velocity is seen to decrease very rapidly with axial distance. At $R = 0.891$ a radial velocity of 0.40 at $Z = 0.021$ decays to 0.14 at $Z = 0.458$. This rapid decay rate is also observed at higher radial locations with a decrease in the decay rate as the blade tip is approached. The high levels of turbulence and viscous effects in this region promote a rapid decay rate. The radial velocity is

also seen to decrease rapidly in the radial direction. This is due to the presence of the annulus-wall boundary layer and its viscous nature which induces rapid flow mixing in the radial direction.

4.7.2 Maximum Turbulence Intensity in the Wake

The variation of the maximum streamwise, normal, and radial maximum turbulence intensities in the wake is shown plotted in Figures 102, 103, and 104. It is seen that the intensities are higher in the trailing-edge region, increasing towards the blade tip, and that the decay rate of the turbulence intensity is higher as the blade tip is approached.

Lakshminarayana and Reynolds (1979) have given a qualitative analysis of the effects of rotation on turbulence. They have shown that the turbulence structure of a rotating blade is different compared to a stationary blade. The radial turbulence intensities are likely to be higher than the streamwise and normal components. The present data confines their analysis at radial locations below $R = 0.945$. For the radius $R = 0.891$, the maximum radial component is 0.209 while the streamwise and normal components are 0.141 and 0.102 respectively. These data also partially confirm the analysis of Raj and Lumley (1976) who have shown that if the gradient of the radial component of mean velocity across the wake is larger than the angular velocity of the machine, then

$$\tau_r > \tau_n > \tau_s$$

At radial locations above $R = 0.945$, the viscous effects of the annulus-wall boundary layer, the secondary flow, and the tip leakage

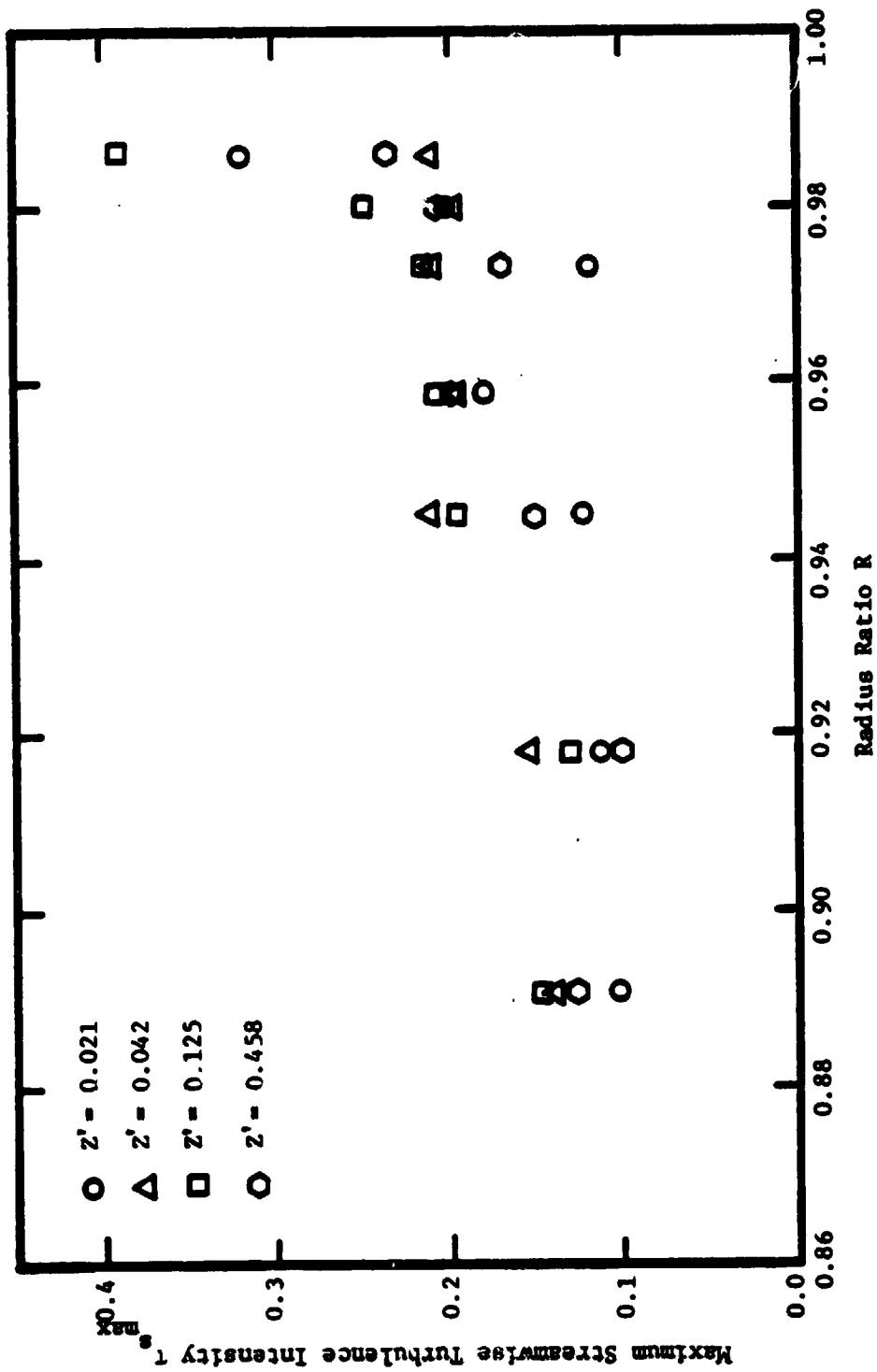


Figure 102. Radial and Axial Variation of the Maximum Streamwise Turbulence Intensity.

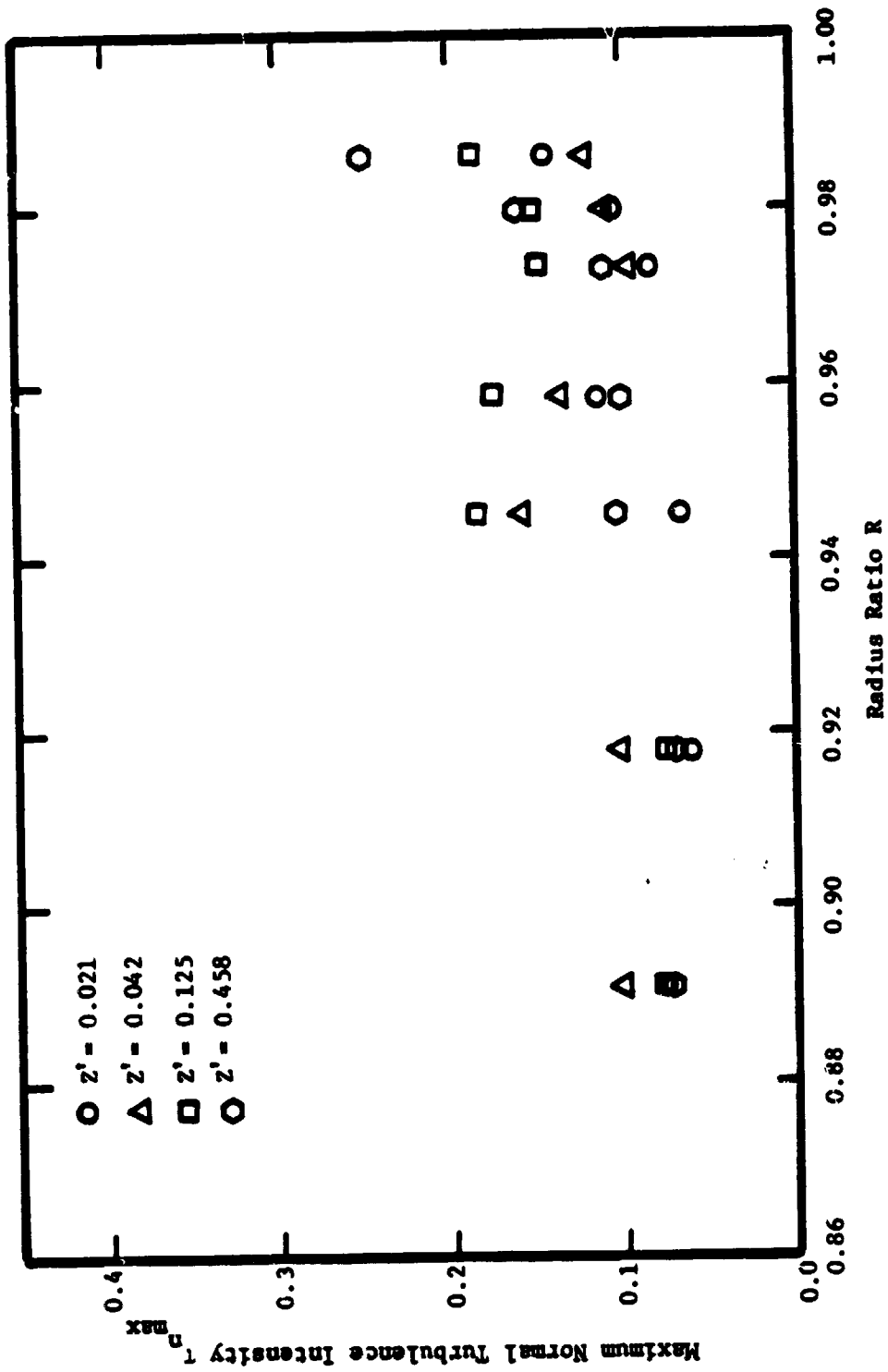


Figure 103. Radial and Axial Variation of the Maximum Streamwise Turbulence Intensity.

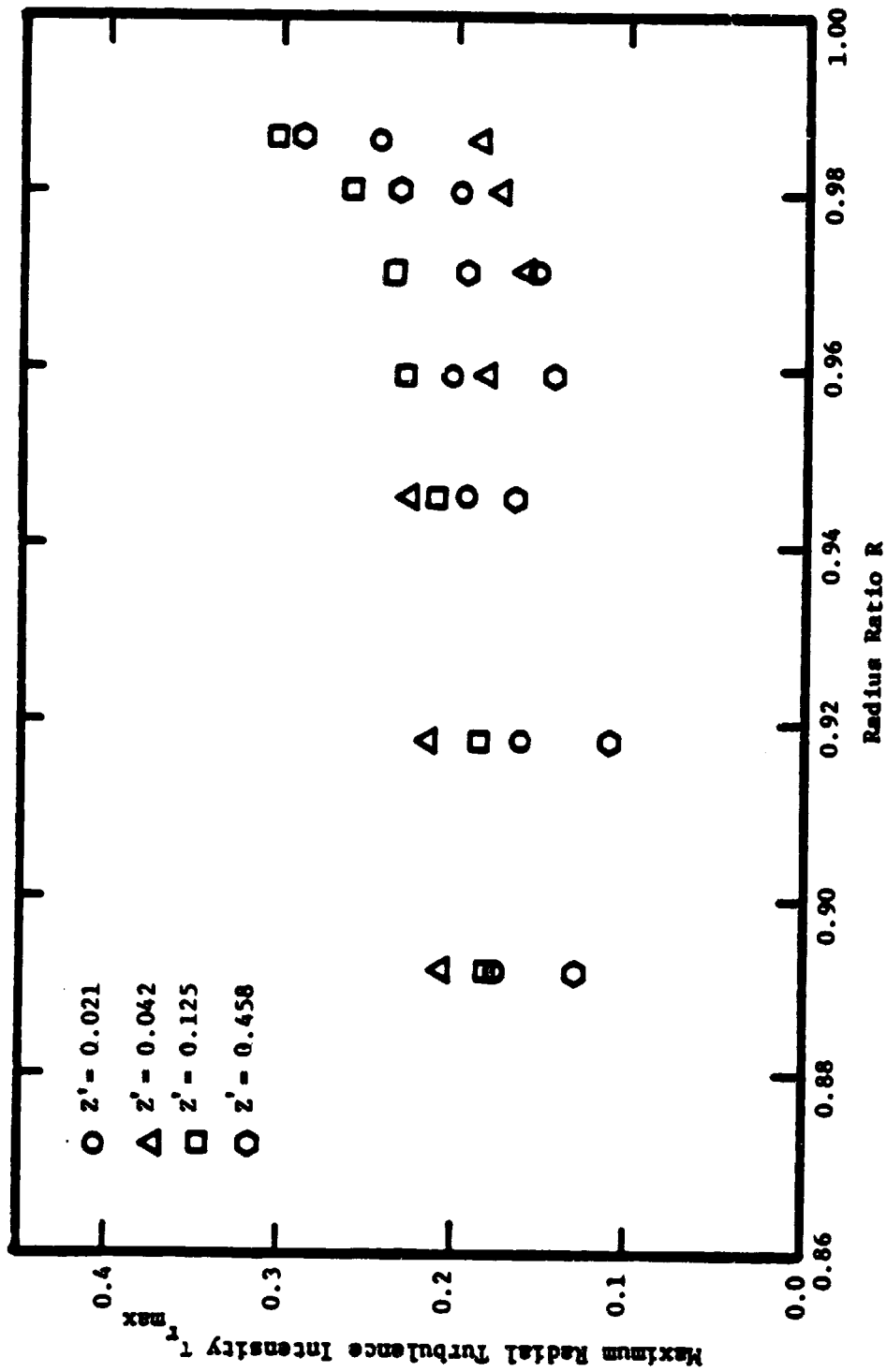


Figure 104. Radial and Axial Variation of the Maximum Radial Turbulence Intensity.

flow induce higher turbulence intensities. Both the streamwise and radial components of turbulence intensity reach values of 30 percent of the free-stream velocity. This indicates the severe flow mixing which occurs in the radial and streamwise directions as the wake is adjusting to the mainstream viscous flow.

4.7.3 Free-Stream Turbulence Intensity

Variations of the free-stream streamwise, normal, and radial turbulence intensities are shown plotted in Figures 105, 106, and 107. Near the blade tip, where the wake structure encompasses the entire blade passage, the free-stream location was taken to be at $Y_g/S = 0.5$. The free-stream turbulence structure does affect the rotor wake characteristics and losses in a compressor stage. It is useful to designers in evaluating the inlet flow conditions to a subsequent stage. It is interesting to note the turbulence amplification through the rotor blade row in the annulus-wall region. The effect of the blade force acting on the fluid is the probable cause of this amplification at the lower radial locations. Here a 2 percent free-stream streamwise and tangential turbulence intensity increases to approximately 4 percent behind the blade row. The radial turbulence intensity is seen to increase to values near 5 percent of the free-stream velocity. This clearly indicates the effect of centrifugal and coriolis forces on the radial turbulence intensity.

As the annulus wall is approached, all components of intensity experience a substantial increase. At $R = 0.986$ the streamwise turbulence intensity has increased to 20 percent while the normal and radial components of intensity approach a value of 15 percent of the mean

ORIGINAL PAGE IS
OF POOR QUALITY

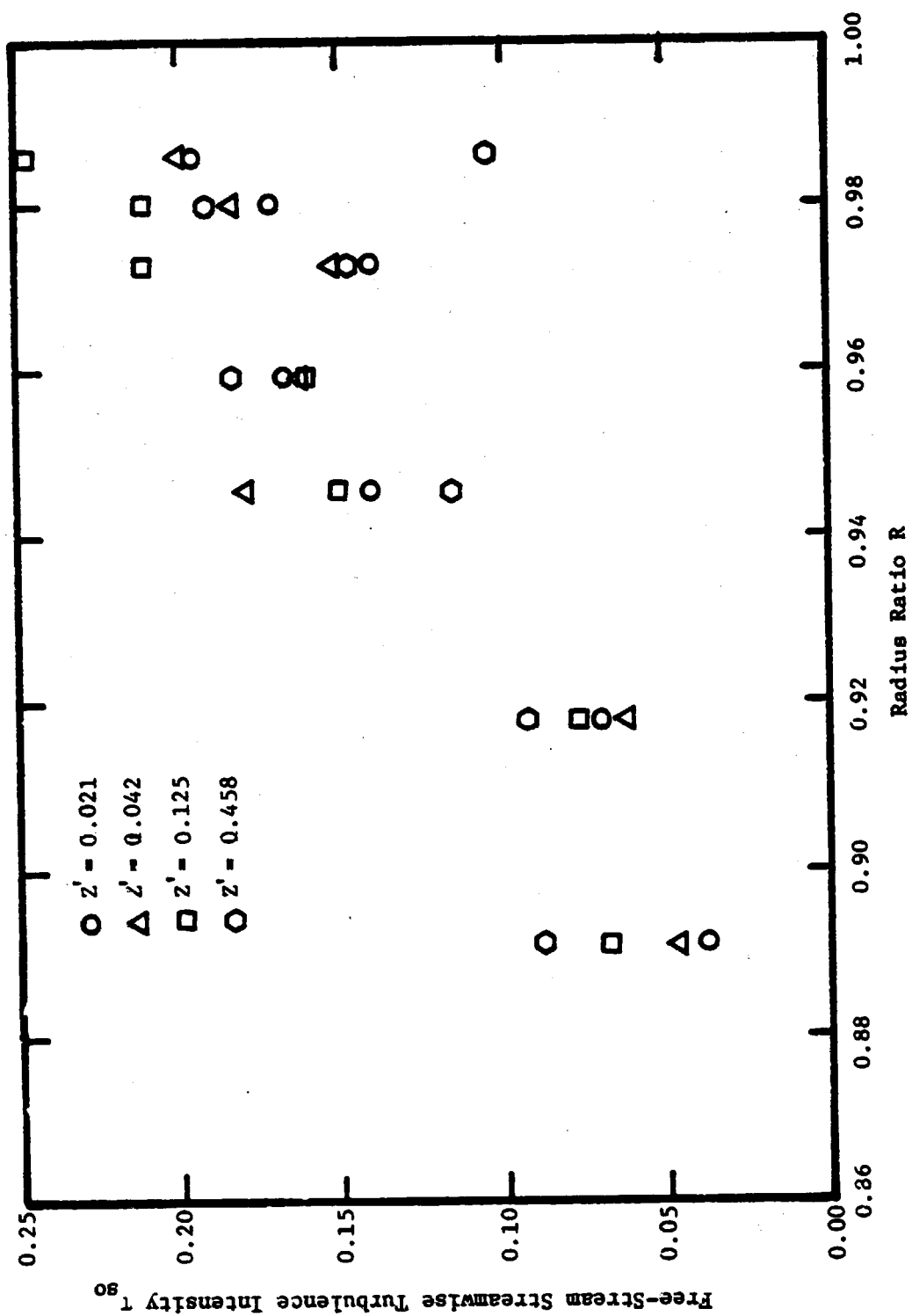


Figure 105. Radial and Axial Variation of the Free-Stream Streamwise Turbulence Intensity.

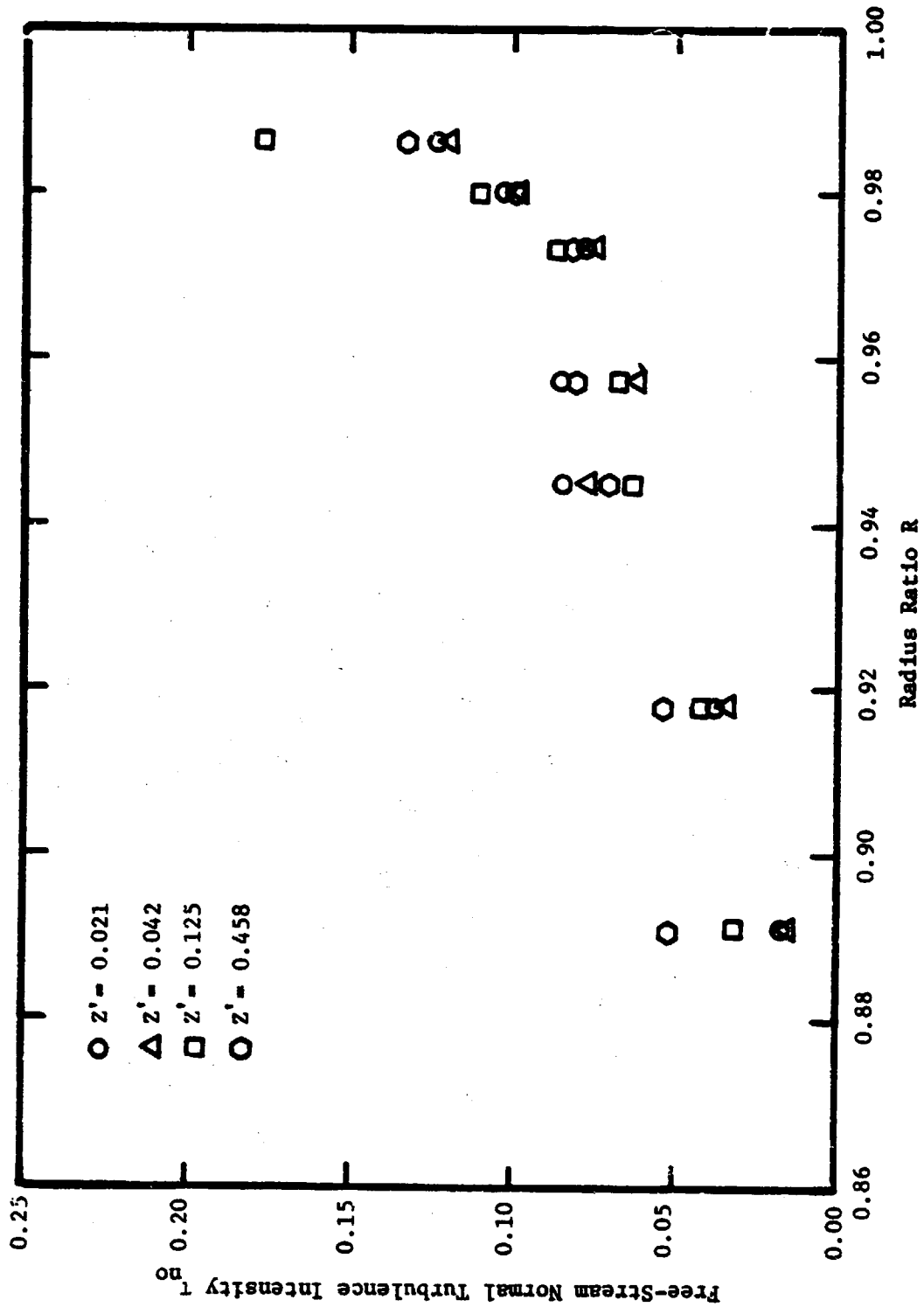


Figure 106. Radial and Axial Variation of the Free-Stream Normal Turbulence Intensity.

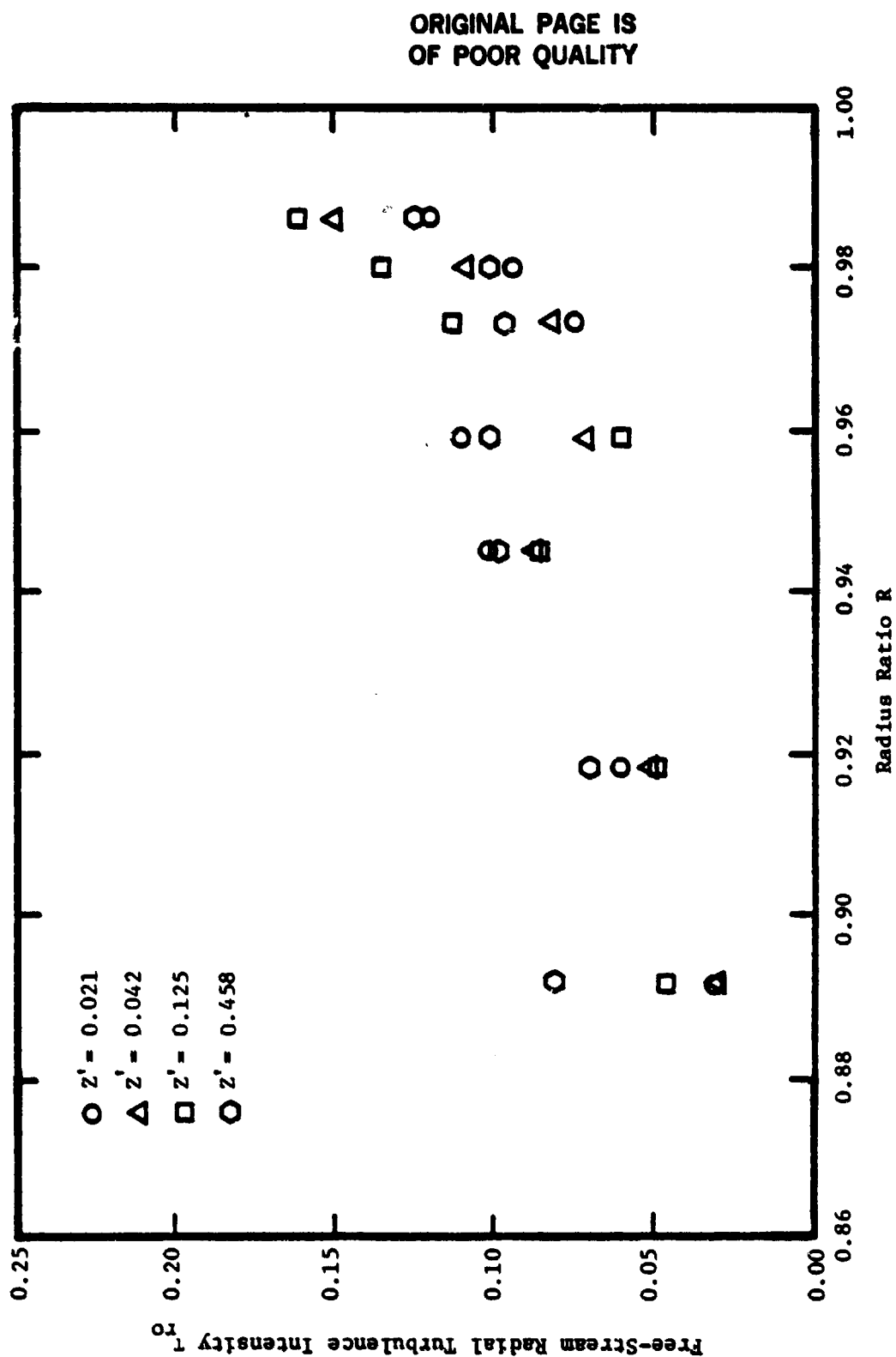


Figure 107. Radial and Axial Variation of the Free-Stream Radial Turbulence Intensity.

velocity. These high values of intensity indicate the interactions of the wake, leakage flow, annulus-wall boundary layer, and the secondary flow. The highest levels of intensity for all components occurs at approximately 12 percent downstream of the blade trailing edge. This indicates that the interference region of these flows occurs with maximum strength at a distance behind the blade. This distance is required by the wake and tip leakage flow to become fully developed.

As these figures show, in a multi-stage machine there is a spanwise and axial gradient in turbulence intensity. This gradient alters the flow distribution into a succeeding blade row which results in a spanwise and axial gradient in noise generation and propagation as well as stagnation pressure loss.

4.7.4 Semi-Wake Width

The variation of the semi-wake width L with radial and axial location is shown in Figure 108. The semi-wake width is controlled by many parameters including the section drag coefficient, the blade spacing, and the rate of decay of the wake. In the case of an airfoil the wake can expand in an infinite medium. In the case of a rotor, however, the wake growth is limited by the adjacent blade wake. At radial locations below $R = 0.946$, the semi-wake width is seen to be only 4-5 percent of the blade spacing. A gradual increase in the semi-wake width is also seen with axial distance.

The semi-wake width is seen to increase very rapidly towards the annulus wall. This is due partially to the radial transport of mass, momentum, and energy in the rotor wake by the radial velocity.

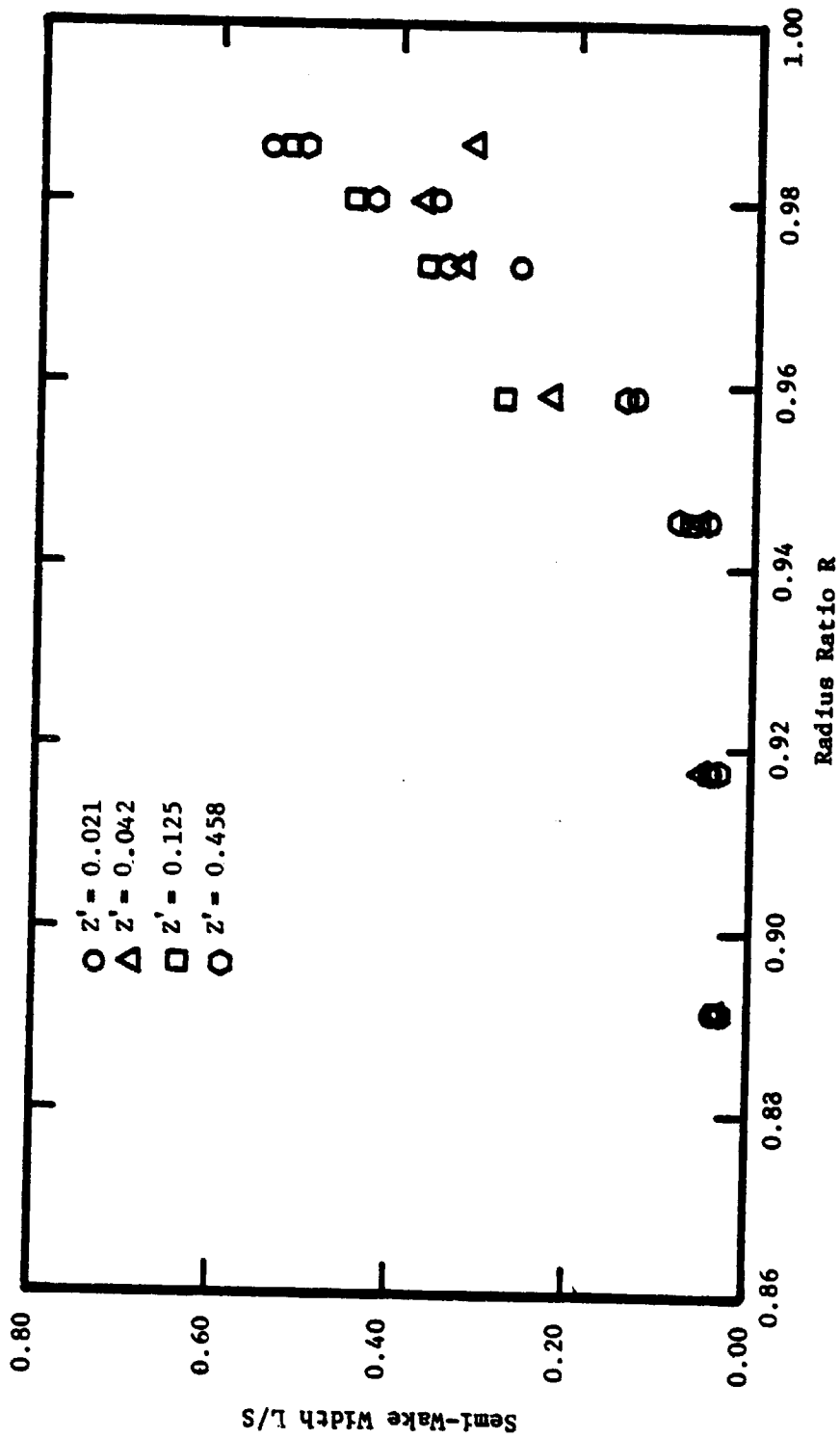


Figure 108. Variation of the Semi-Wake Width with Axial Distance.

Also, the interaction of the annulus-wall boundary layer with the blade wake in the interference region causes a rapid increase in the semi-wake width. At radial locations near the tip, the semi-wake width expands to 50 percent of the blade spacing. This indicates that the edge of one wake is adjacent to another. With this flow situation it is possible that the two wakes might merge together. This phenomenon has been reported by Ravindranath (1979).

4.8 Structure of Blade Passage Turbulence

Real time spectrum analysis was carried out to evaluate the spectral content of the turbulence in the flow behind the rotor blades. These energy spectra were taken at various axial, radial, and tangential locations within the blade passage employing the rotating three-sensor hot-wire probe. It is known and discussed by Hinze (1959) that the slope of the energy spectrum is $-5/3$ in the inertial range of isotropic turbulence and -1 in the viscous convective range. It is of interest to determine whether the blade passage-flow follows this boundary layer spectrum.

Figures 109 through 114 show the spectra taken at various portions inside the blade passage. Each figure displays the spectra obtained by the three sensors. Also at each axial and radial position the spectra obtained at the suction-surface, mid-passage, and pressure-surface is given. It is seen from these figures that most of the energy in turbulence at the lower radial location, $R = 0.891$, is confined to the low frequency range below 2 KHZ. However, at this radial location there is a sharp spike in the spectra. This spike

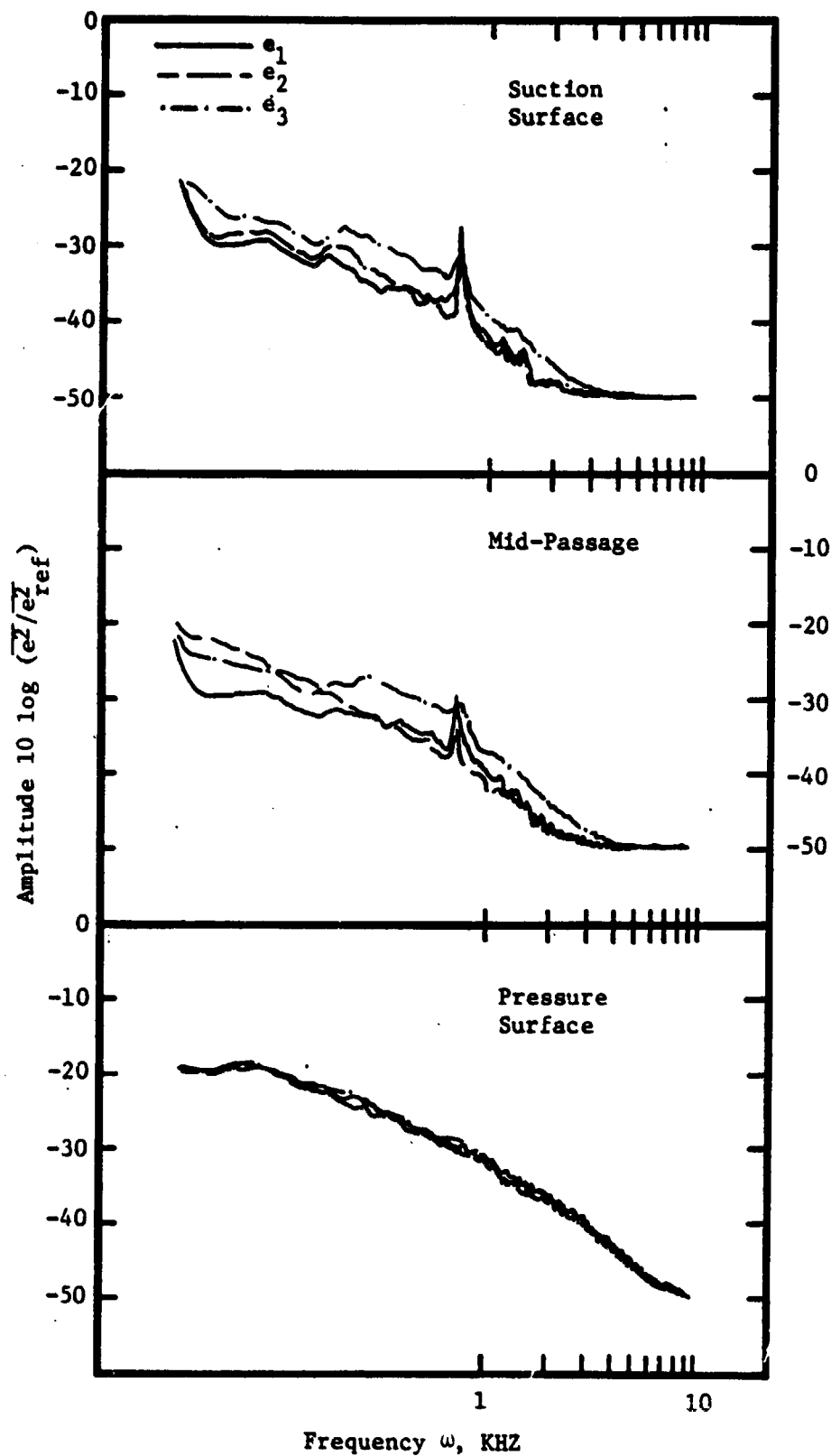


Figure 109. Turbulence Energy Spectra in the Relative Frame of Reference Inside the Blade Passage at $Z = 0.750$, $R = 0.891$.

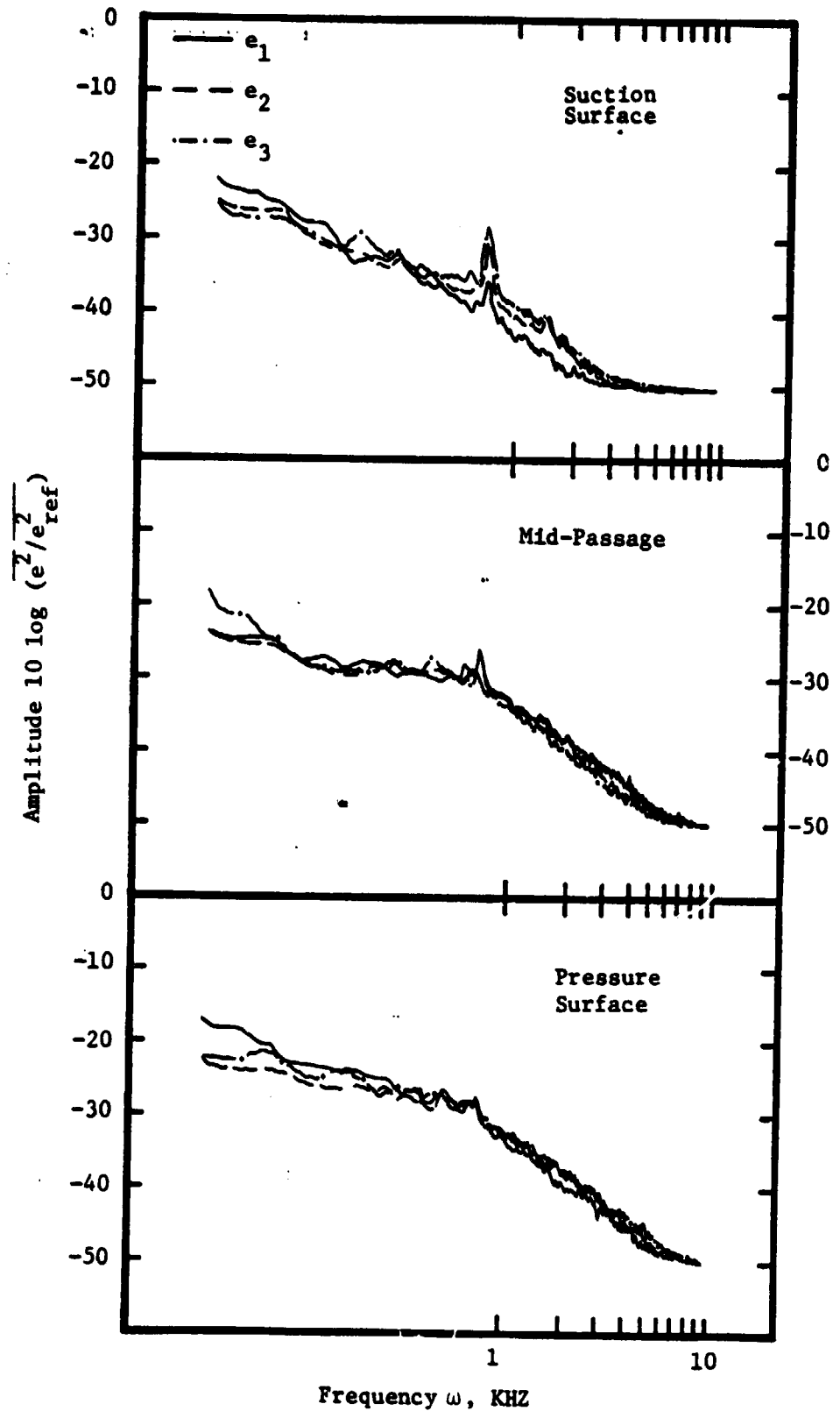


Figure 110. Turbulence Energy Spectra in the Relative Frame of Reference Inside the Blade Passage at $Z = 0.750$, $R = 0.946$.

ORIGINAL PAGE IS
OF POOR QUALITY

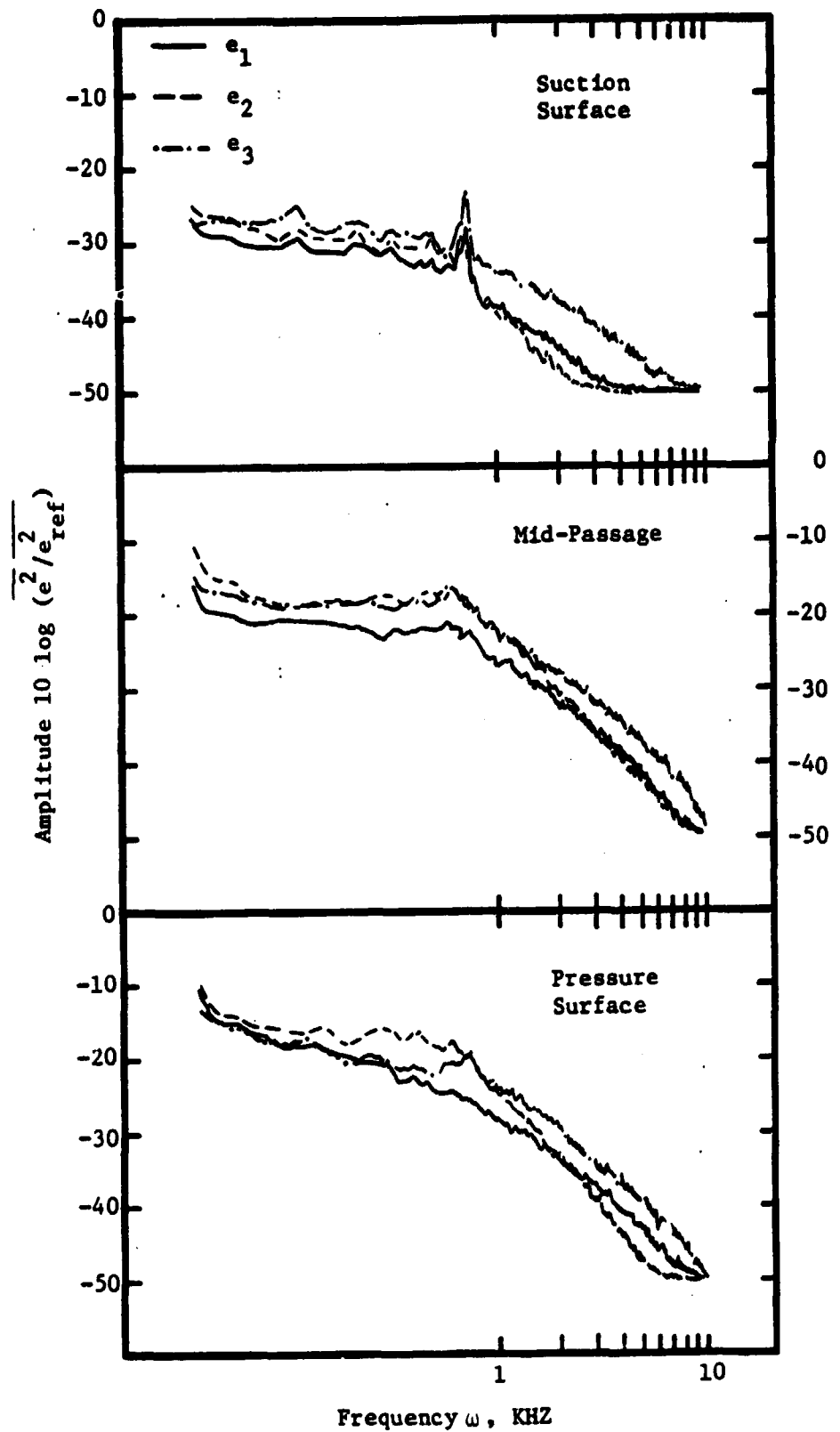


Figure 111. Turbulence Energy Spectra in the Relative Frame of Reference Inside the Blade Passage at $Z = 0.750$, $R = 0.980$.

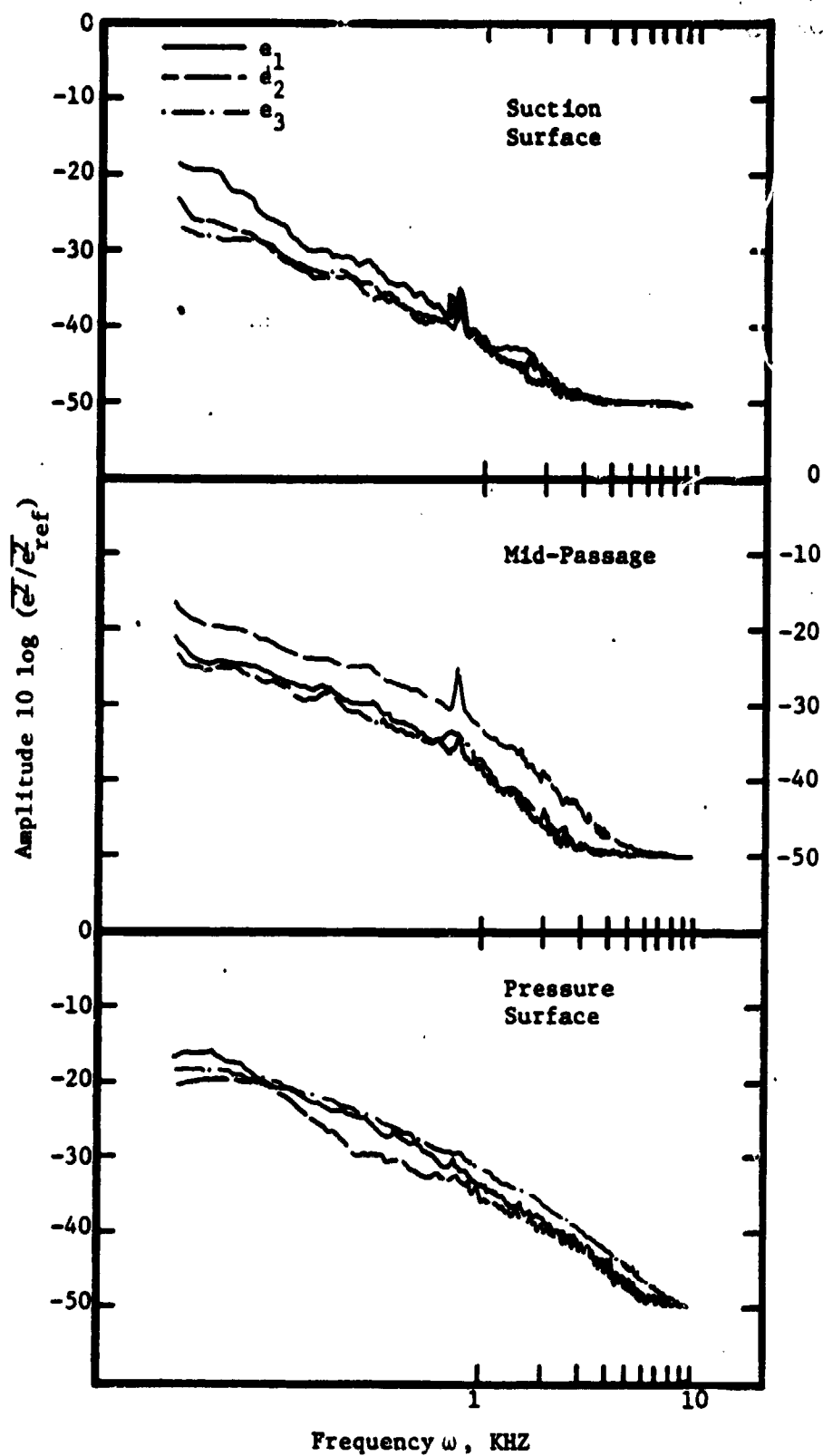


Figure 112. Turbulence Energy Spectra in the Relative Frame of Reference Inside the Blade Passage at $Z = 0.979$, $R = 0.891$.

ORIGINAL PAGE IS
OF POOR QUALITY

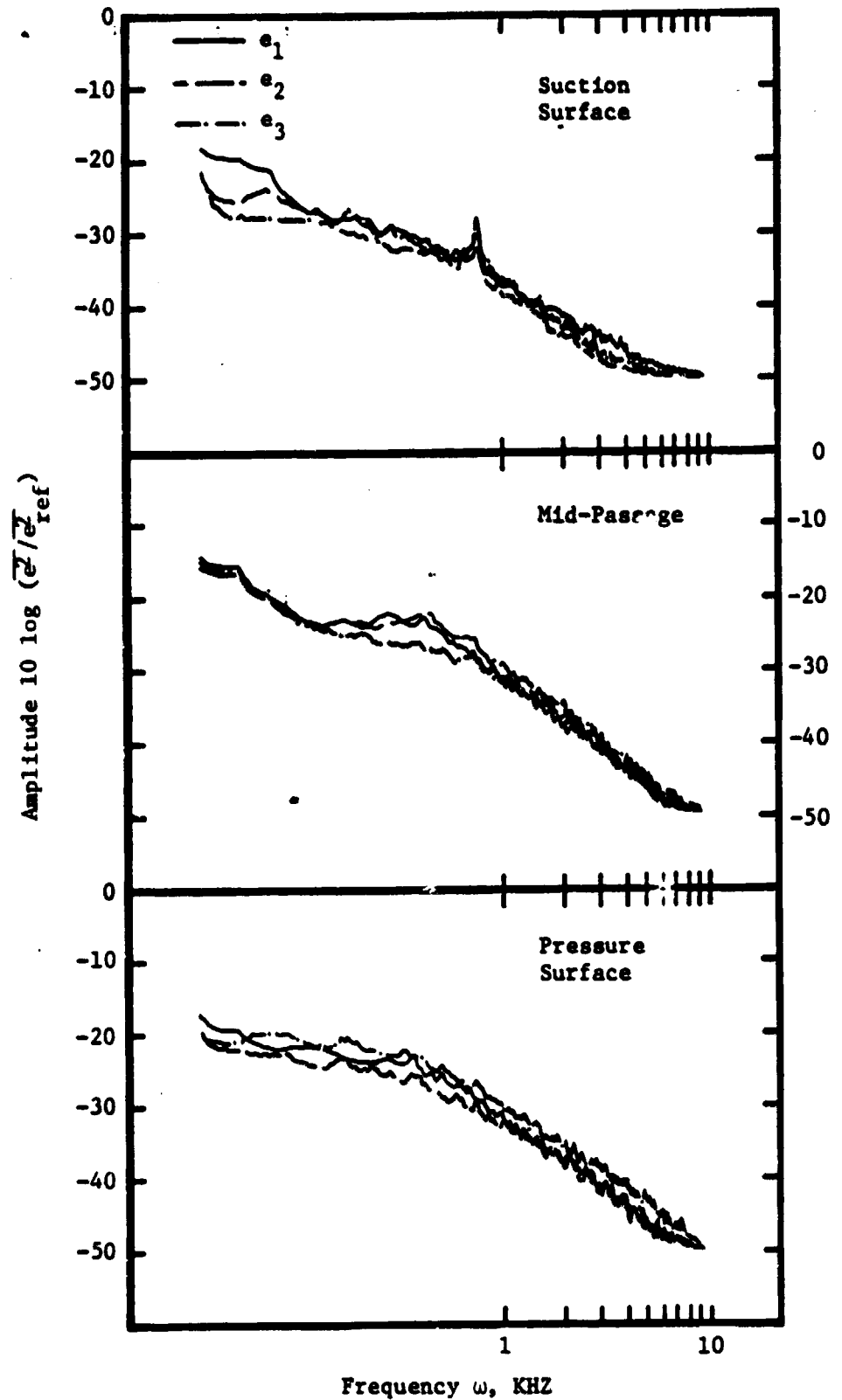


Figure 113. Turbulence Energy Spectra in the Relative Frame of Reference Inside the Blade Passage at $Z = 0.979$, $R = 0.946$.

ORIGINAL PAGE IS
OF POOR QUALITY

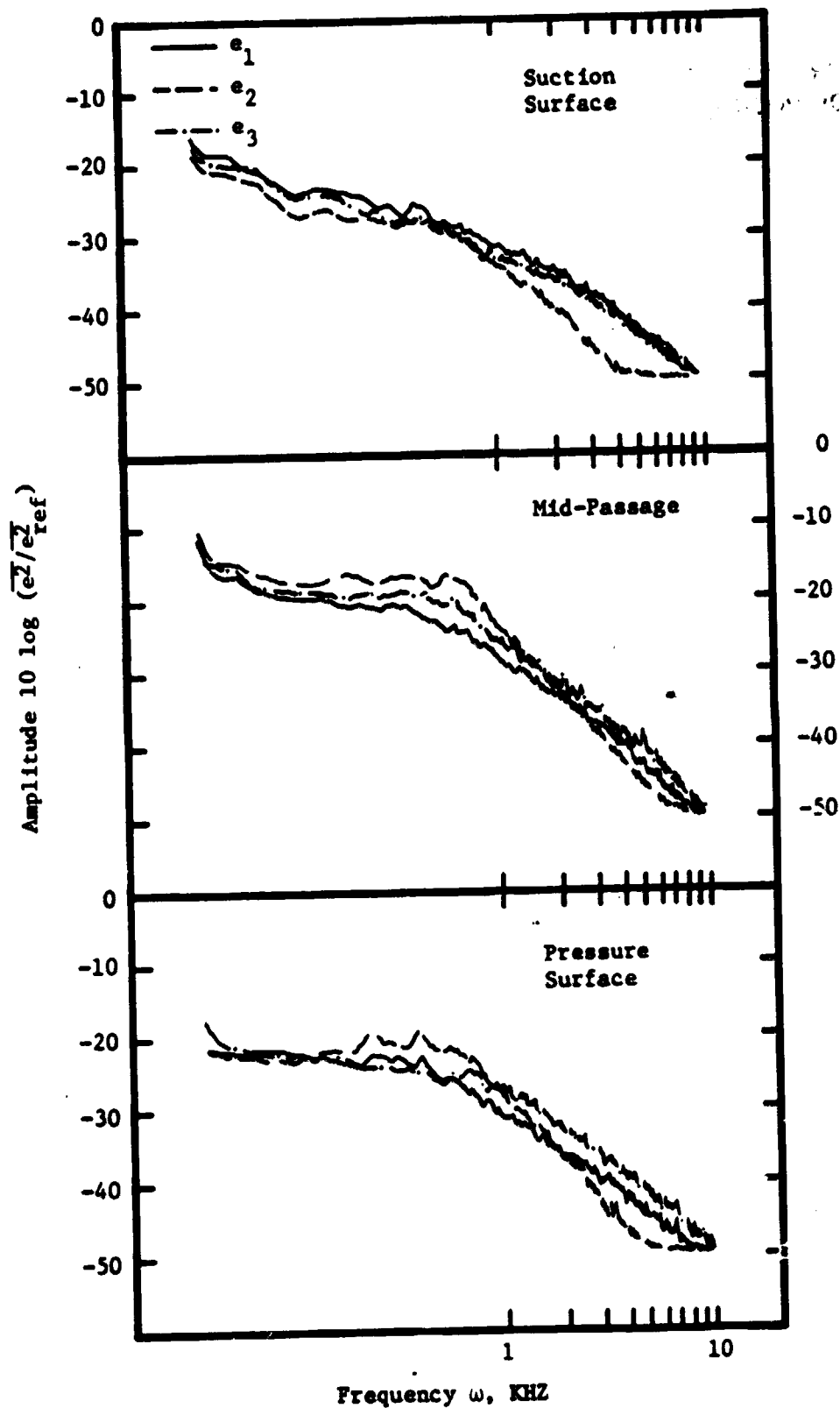


Figure 114. Turbulence Energy Spectra in the Relative Frame of Reference Inside the Blade Passage at $Z = 0.979$, $R = 0.980$.

corresponds to the blade passing frequency of the inlet-guide-vane wakes. The blade passing frequency (BPF) is obtained as:

$$\text{BPF} = \frac{\text{speed (rpm)} \times \text{no. of IGV blades}}{60} = 0.736\text{KHZ} \quad (18)$$

The area under the spikes represents the fraction of the total fluctuating energy contained in the periodic oscillations influenced by the upstream inlet guide vanes. The rotating hot-wire probe senses the inlet-guide-vane wakes as a source of turbulence.

Figures 109, 110, and 111 show the spectra taken at the axial location $Z = 0.750$. The energy content of the turbulence fluctuations increases as the rotor blade tip is approached. This is seen markedly on the pressure side of the blade passage and at the mid-passage location. The spike due to the inlet-guide-blade wake is overshadowed by the high turbulence in this region. The increase of the turbulence energy content is due to the development of the interference region discussed earlier. Associated with this region is a high degree of flow mixing and interaction of shear layers such as the blade boundary layers and the annulus-wall boundary layer.

Spectra obtained at $Z = 0.979$ are presented in Figures 112, 113, and 114. The radial increase of the turbulence energy is again apparent. The spectra exhibit typical energy distributions that exist in turbulent flows with most of the energy contained within 10 KHZ. At the lowest radial station most of the turbulent energy is confined below 2 KHZ. However, with increasing radius the limiting frequency approaches 10 KHZ. This is seen at $R = 0.981$. Here the slope of the energy spectra is -1 which indicates that the turbulence is in the

viscous conductive range. The radial locations above $R = 0.945$ show the higher values of turbulence occurring at tangential locations 65% of the distance from the suction-surface of the rotor blade. This is the location of the loss core due to strong flow interactions of the blade boundary layers, the tip leakage flow, the secondary flow, and the annulus-wall boundary layer.

CHAPTER 5

SUMMARY AND CONCLUSIONS

The use of a three-sensor hot-wire probe in a rotating blade passage and the response of this probe to a varying incident flow direction was investigated. This was a preliminary procedure performed before measurements were obtained of the flowfield under investigation. The characteristics of the annulus-wall flow of a moderately loaded compressor rotor blade was subsequently investigated. The present set of measurements represent the first set of data obtained within the rotor blade passage which include the three components of mean velocity, turbulence intensity, and stress correlations. Some of the important conclusions that can be drawn based on the results of the present investigations are presented below.

5.1 Sensitivity of Three-Sensor Hot-Wire Probe

1. The three-sensor hot-wire probe does not experience a change of calibration from the stationary to the rotating mode of operation, up to a centrifugal acceleration of 1100 g. The response of the sensor during rotation is identical to that obtained without rotation.
2. A combined sensor calibration must be performed to obtain accurate measurements. All three sensors should be simultaneously calibrated to a reference flow which varies throughout

a velocity range. For this calibration of the probe to the magnitude of the incident velocity, the probe should remain aligned to the incident flow at a position of zero degrees of yaw and pitch angle.

3. The three-sensor hot-wire probe should also be calibrated to the direction of the incident flow, due to substantial deviations from the cosine law which occur beyond certain values of yaw and pitch angle. These deviations are dependent upon the incident flow direction to each sensor, the heat transfer characteristics of each sensor, and the orientation of each sensor with respect to the other sensors. A mat plotting of the probe response for the various angles of yaw and pitch anticipated during the usage of probe can be used to correct the probe response. A sensitivity function of the form:

$$U_{\text{eff}} = U_1 [k_1 (\cos^2 \lambda + k_2 \sin^2 \lambda)]^{1/2}$$

was found to reduce the error in the probe response where the constants k_1 , k_2 , and k_3 are adjusted for the various yaw and pitch angles. Through the usage of the mat plot of the sensor response and the sensitivity function given above, the response of the three-sensor probe can be corrected for errors which exist at large angles of yaw and pitch.

4. The ensemble-average method of processing measurements of a periodic flow obtained with a stationary three-sensor hot-wire probe was found to be sensitive to two primary factors. These are the orientation of the probe with respect to the incident

flow direction and the number of samples used during processing of the data. The non-dimensionalized velocity profiles behind the blade passage were determined to be accurate for misalignment angles of ± 20 degrees. Beyond this range, the magnitude of the three components of velocity in the wake were seen to be erroneous. Also the width and shape of the wake profile was modified. A small number of examples used for processing the data revealed unsteady flow phenomena; however, the steady characteristics of the flow were seen to differ from that obtained with a larger number of samples. For the measurement of steady flow phenomena, a large number of samples (200) is desired. For the measurement of unsteady flow phenomena, a small number of samples (1 to 5) is desired.

5.2 Annulus-Wall Flow Characteristics

1. The flowfield near the annulus-wall region is primarily
• inviscid in nature at radial locations below 10 percent of the blade span from the blade tip. However, due to the effect of rotation, radially outward flows are present in the blade boundary layers.
2. At locations within approximately 10 percent of the blade span near the blade tip, a region of intense viscous flow interaction and mixing occurs at 65 percent of the tangential distance from the suction to the pressure side of the blade passage. This region expands radially inward as this proceeds downstream toward the blade trailing-edge.

3. A streamwise velocity deficiency which reaches values of 0.60 of the mainstream flow occurs in the blade passage at the location of the viscous flow interaction near the blade tip. The resulting "wake-type" of profile is attributed low momentum fluid and inward radial flows generated by the interaction of the blade boundary layers and the annulus-wall boundary layer. The magnitude of this velocity deficiency increases with axial distance inside the blade passage. The region of the streamwise velocity deficiency becomes more pronounced at radial locations near the tip of the rotor blade.
4. Within the blade passage and at radial locations within 10 percent of the blade tip, the normal velocity indicates large amounts of flow underturning and overturning which reveal the nature of the viscous flow interactions. At radial locations just above the inviscid flow ($R = 0.945$ to $R = 0.973$) the normal velocity turns toward the blade surface at the suction side of the blade passage. This flow overturning is due to the rolling up of the tip leakage flow by the mainstream flow. However, the normal velocity is reversed at higher radial locations near the blade tip. This underturning of the flow is due to the combined effect of the tip leakage flow and the dragging of the annulus-wall boundary layer by the mainstream flow. The radially outward flows within the blade boundary layers are deflected by the annulus-wall toward the mid-passage. This phenomenon produces flow overturning on the pressure side of the blade passage and flow underturning on the suction side of the blade passage.

5. Radial outward flows occur within the blade boundary layers due to an imbalance between the radial pressure gradient and the centrifugal forces. These flows, upon reaching the annulus wall, roll toward mid-passage, interact, and produce strong vortices and radially inward flow with the blade passage at approximately 65 percent of the passage distance from the suction side.
6. A reduction in the total relative velocity of approximately 50 percent occurred within the blade passage at approximately 65 percent of the distances from the suction side. This is the region of intense viscous flow interaction. The low relative velocities near the tip result in a large stagnation pressure rise due to the viscous interaction of the tip leakage flow, the blade boundary layers, the annulus-wall boundary layer, and possibly the secondary flow.
7. The exit-flow from the blade passage is dominated by the development of the rotor wake. The three components of relative mean velocity which described the wake profile are influenced by the annulus wall at approximately 10 percent of the blade span near the blade tip. These profiles are asymmetrical near the blade trailing-edge and tend to become symmetrical with axial distance. As the blade tip is approached, the streamwise velocity defect and radial velocity of the wake are reduced to near zero values and the normal velocity increased. This is due to the wake mixing with the free-stream and the annulus-wall boundary layer. The exit-flow is substantially underturned in this region.

8. The wake-width increases very rapidly in the radial direction to encompass the entire blade passage at the tip. This is due to the effect of the annulus-wall boundary layer and centrifugal forces. A gradual increase in the wake width is also seen with axial distance.
9. The decay of the blade wake is maximum near the blade tip which is due to mixing of mass, momentum, and energy with the annulus-wall boundary layer. The high levels of turbulence and viscous effects in the region promote a rapid decay rate in the axial direction.
10. The momentum thickness of the annulus-wall boundary layer increases with axial distance behind the blade due to the development of the annulus-wall boundary layer. A decrease in momentum thickness from the blade passage-flow to the exit-flow was observed and is caused by an energizing of the flow by the tip leakage flow.
11. Turbulence levels within the blade passage are high near the tip regions. A growing core of high turbulence is evident at 65 percent of the blade passage distance from the suction side which corresponds to the region of velocity deficiency mentioned above. The radial component of turbulence intensity has the largest magnitude in this core region which reaches values up to 32 percent of the local mean velocity. Within the blade passage, the total turbulence energy contours are similar to those of the turbulence intensities. Turbulence energy levels in the interference region reach values 6 times greater than levels in the inviscid flow region.

12. The turbulence structure of the rotor exit-flow is asymmetric behind the rotor blade and tends toward symmetry with axial distance. Near the blade tips, complex flow interactions result in an increase in turbulence intensity. This increase is most pronounced for the radial component. The turbulence intensities do not decay until a location 4 percent of the blade chord downstream. The flow mixing region initially increases in turbulence level before it begins to decay.
13. The effect of the blade force acting on the fluid causes an amplification of the turbulence level in the free-stream behind the rotor at radial locations below 10 percent of the blade span from the blade tip. As the tip is approached, the free-stream turbulence level increases due to the flow mixing with the annulus-wall boundary layer.
14. The locations of high turbulence stresses are concentrated in the high turbulence intensity areas of the mixing region near the blade tip. The effect of rotation is to attenuate the streamwise-stress component and amplify the radial-stress component.
15. The nature of the flowfield within the rotor blade passage at the annulus wall is the result of several viscous interacting flows driven by the blade rotation. A qualitative illustration of the flow interaction is proposed in Figure 115. This figure reflects the conclusions discussed above.

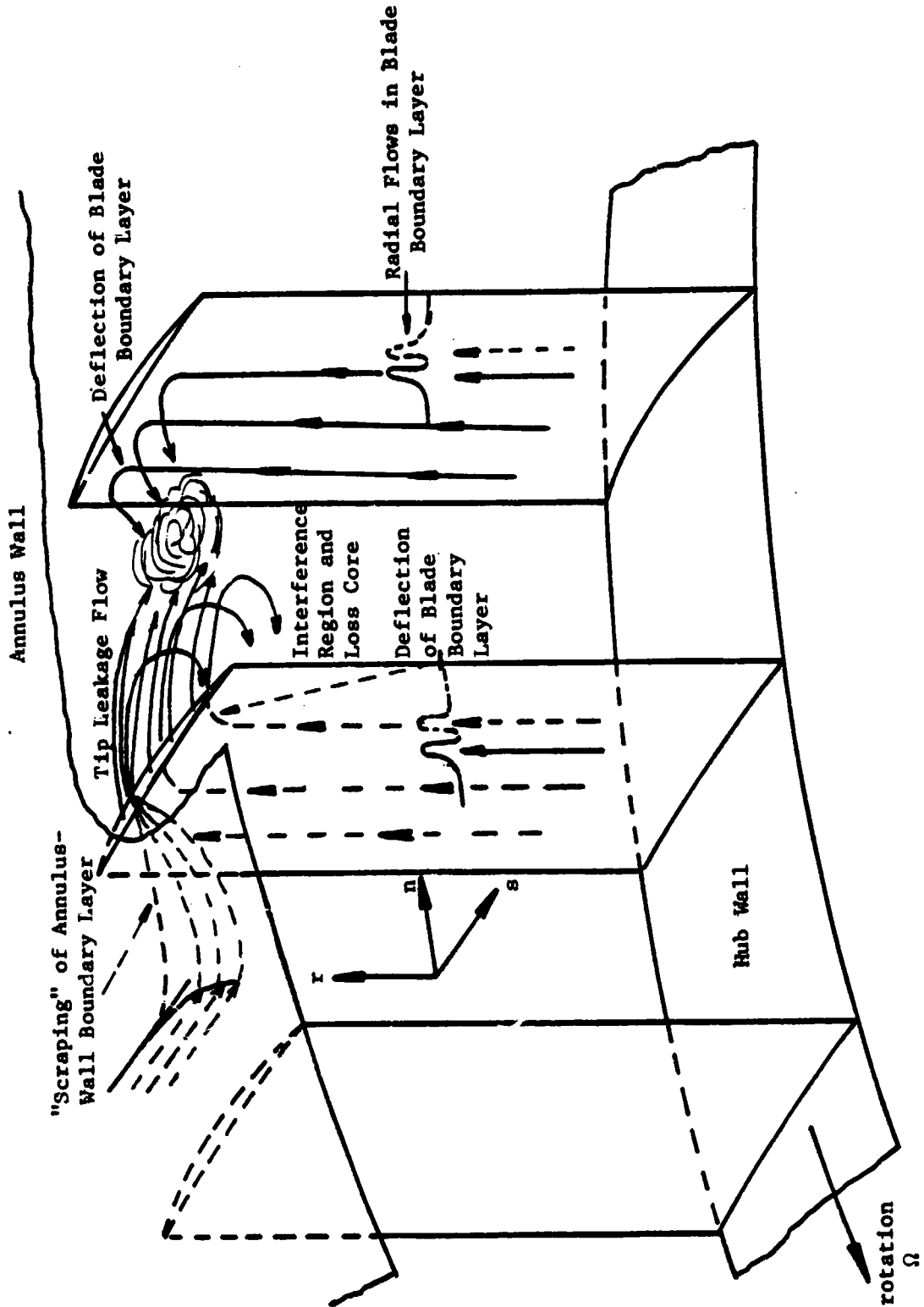


Figure 115. Qualitative Nature of Flowfield Near the Annulus Wall Due to Flow Interactions.

REFERENCES

- Anand, A. K., "An Experimental and Theoretical Investigation of Three-Dimensional Turbulent Boundary Layers Inside the Passage of a Turbomachinery Rotor," Ph.D. thesis, Department of Aerospace Engineering, The Pennsylvania State University, May 1976. (Also as NASA CR-2888, 1977).
- Anand, A. K. and Lakshminarayana, B., "Three-Dimensional Turbulent Boundary Layer in a Rotating Helical Channel," Journal of Fluids Engineering, Series I, Vol. 97, No. 2, pp. 197-210, June 1975.
- Bendat, J. S. and Piersol, A. G., Measurement and Analysis of Random Data, John Wiley and Sons, Inc., New York, N.Y., 1958.
- Betz, A., "The Phenomena at the Tips of Kaplan Turbines," Hydraulische Probleme, June 1925.
- Billet, M. L., "Secondary Flow-Related Vortex Cavitation," Ph.D. thesis, Department of Aerospace Engineering, The Pennsylvania State University, November 1978.
- Carter, A. D. S., "Three-Dimensional-Flow Theories for Axial Compressors and Turbines," Proceedings of the Institute of Mechanical Engineering, Vol. 159, pp. 255-268, 1948.
- Champagne, F. H., Sleicher, C. A., and Wehrmann, O. H., "Turbulence Measurements with Inclined Hot-Wires," Journal of Fluid Mechanics, Vol. 28, pp. 177-182, 1967.
- Dean, R. C., "Influence of Tip Clearance on Boundary Layer Characteristics in a Rectilinear Cascade," Rep. No. 27-3, Gas Turbine Lab., Massachusetts Institute of Technology, 1954.
- Friehe, C. A. and Schwarz, W. H., "Deviations from the Cosine Law for Yawed Cylindrical Anemometer Sensors," Transactions of the American Society of Mechanical Engineers, No. 35, pp. 655-662, 1968.
- Gearhart, W. S., "Tip Clearance Cavitation in Shrouded Underwater Propulsions," Journal of Aircraft, March-April 1966.

- Gorton, C. A., "Analytical and Experimental Study of Three-Dimensional Mean Flow and Turbulence Characteristics Inside the Passages of an Axial Flow Inducer," M.S. thesis, Department of Aerospace Engineering, The Pennsylvania State University, 1974.
- Gorton, C. A. and Lakshminarayana, B., "A Method of Measuring the Three-Dimensional Mean Flow and Turbulence Quantities Inside a Rotating Blade Passage," Journal of Engineering for Power, Vol. 98, April 1976.
- Hah, C., "A Numerical and Experimental Study of the Turbulent Wakes of Turbomachinery Rotor Blades, Isolated Airfoils, and a Cascade of Airfoils," Ph.D. thesis, Department of Aerospace Engineering, The Pennsylvania State University, 1980.
- Hah, C. and Lakshminarayana, B., "Effect of Rotation on a Rotating Hot-Wire Sensor," Journal of Physical Engineering: Scientific Instrumentation, Vol. 11, 1978.
- Hawthorne, W. R., "Secondary Circulation in Fluid Flow," Proceedings of the Royal Society (London), Vol. A206, 1951.
- Herrig, J. L., Emery, J. C., Erwin, J. R., "Systematic Two-Dimensional Cascade Tests of NACA 6⁵ Series Compressor Blades at Low Speeds," NASA TN 3916, 1957.
- Herzig, H. A., Hansen, A. G., and Costello, G. R., "A Visualization Study of Secondary Flows in Cascades," NACA TR 1163, 1953.
- Hinze, J. O., Turbulence, McGraw-Hill, New York, N.Y., 1959.
- Horlock, J. H., "Cross Flows in Bounded Three-Dimensional Turbulent Boundary Layers," Journal of Mechanical Engineering Science, Vol. 15, pp. 274-284, August 1973.
- Horlock, J. H., "Recent Developments in Secondary Flow," AGARD Conference Proceedings No. 214 in Secondary Flows in Turbomachines, pp. 1-1 to 1-18, March 1977.
- Horlock, J. H. and Lakshminarayana, B., "Secondary Flows: Theory, Experiment and Application in Turbomachinery Aerodynamics," Annual Review of Fluid Mechanics, Vol. 5, Annual Reviews, Inc., Palo Alto, pp. 247-280, 1973.
- Horlock, J. H. and Perkins, H. J., "Annulus Wall Boundary Layers in Turbomachines," AGARD-AG-185, May 1974.
- Horlock, J. H. and Wordsworth, J., "The Three-Dimensional Laminar Boundary Layer on a Rotating Helical Plate," Journal of Fluid Mechanics, No. 23, 1965.
- Hortog, D., Mechanical Vibrations, McGraw-Hill, Third Edition, 1947.

- Jones, R. T., NACA Technical Note 1402, 1947.
- King, L. V., "On the Convection of Heat from Small Cylinders in a Stream of Fluid," Philosophical Transactions of Royal Society (London), Vol. A214, pp. 373-432, 1914.
- Klein, A., "Influence of the Inflow B/L on Secondary Flow in the Blading of Axial Flow Turbines," Forschung Ingenieurwesens, Vol. 32, 1966.
- Kovaszny, L. S. G., "Turbulence Measurements," Applied Mechanical Review, Vol. 12, No. 6, p. 375, 1959.
- Lakshminarayana, B., "An Axial Flow Research Compressor Facility Designed for Flow Measurement in Rotor Passages," Proceedings ASME Symposium on Measurement Methods in Rotating Components of Turbomachinery, pp. 31-42, New Orleans, 1980 (to be published in Journal of Fluids Engineering).
- Lakshminarayana, B., "Methods of Predicting the Tip Clearance Effects in Axial Flow Turbomachinery," Journal of Basic Engineering, Vol. D92, pp. 467-482, September 1970.
- Lakshminarayana, B., "Three-Dimensional Flow Field in Rocket Pump Inducers, Part 1: Measured Flow Field Inside the Rotating Blade Passage and at the Exit," Transactions ASME, Journal of Fluids Engineering, Vol. 95, Series I, No. 4, pp. 567-578, December 1973.
- Lakshminarayana, B. and Davino, R., "Mean Velocity and Decay Characteristics of the Guidevane and Stator Blade Wake of an Axial Flow Compressor," Transactions ASME, Journal of Engineering for Power, Vol. 102, January 1980.
- Lakshminarayana, B. and Gorton, C. A., "Three-Dimensional Flow Field in Rocket Pump Inducers, Part 2: Three-Dimensional Viscid Flow Analysis and Hot-Wire Data on Three-Dimensional Mean Flow and Turbulence Inside the Rotor Passage," Journal of Fluids Engineering, Vol. 99, Series I, No. 1, pp. 176-186, March 1977.
- Lakshminarayana, B. and Horlock, J. H., "Secondary Flow in Turbomachines," International Journal of Mechanical Sciences, pp. 287-307, 1963.
- Lakshminarayana, B., Jabbari, A., and Yamaoka, H., "Turbulent Boundary Layer on a Rotating Helical Blade," Journal of Fluid Mechanics, Vol. 51, pp. 554-559, 1972.
- Lakshminarayana, B. and Poncet, A., "A Method of Measuring Three-Dimensional Wakes in Turbomachinery," Transactions ASME, Journal of Fluids Engineering, Vol. 96, No. 2, pp. 87-91, June 1974.
- Lakshminarayana, B. and Reynolds, B., "Turbulence Characteristics in the Near-Wake of a Compressor Rotor Blade," AIAA Paper 79-0280, 1979 (to be published in AIAA Journal, 1980).

- Lumley, J. L., "On the Interpretation of Time Spectra Measured in High Intensity Shear Flows," Physics of Fluids, Vol. 8, No. 6, 1965.
- Mellor, G. L. and Wood, G. M., "An Axial Compressor End Wall Boundary Layer Theory," Journal of Basic Engineering, Vol. 93, pp. 300-316, June 1971.
- Poncet, A. and Lakshminarayana, B., "Three-Dimensional Analysis and Measurement of the Flow in a Three Bladed Rocket Pump Inducer," NASA CR-2290, pp. 1-126, 1973.
- Prandtl, L., Ministry of Aircraft Production Volhenrohe, Reproductions and Transactions No. 64, 1946.
- Rains, D. A., "Tip Clearance Flow in Axial Flow Compressors and Pumps," California Institute of Technology, Mechanical Engineering Lab Report 5, 1954.
- Raj, R. and Lakshminarayana, B., "Characteristics of the Wake Behind a Cascade of Airfoils," Journal of Fluid Mechanics, Vol. 61, Part 4, pp. 707-730, December 1973.
- Raj, R. and Lakshminarayana, B., "Three-Dimensional Characteristics of Turbulent Wakes Behind Axial Flow Turbomachinery," Journal of Engineering for Power, Vol. 98, pp. 218-228, April 1976.
- Raj, R. and Lumley, J. L., "A Theoretical Investigation on the Structure of Fan Wakes," ASME Paper 76-WA/FE-22, 1976.
- Ravindranath, A., "Three-Dimensional Mean and Turbulence Characteristics of the Near Wake of a Compressor Rotor Blade," M.S. thesis, Department of Aerospace Engineering, The Pennsylvania State University, 1979.
- Ravindranath, A. and Lakshminarayana, B., "Structure and Decay Characteristics of Turbulence in the Near- and Far-Wake of a Moderately Loaded Compressor Rotor Blade," ASME Paper 80-GT-95, pp. 1-10, 1980 (to be published in the Journal of Engineering for Power, 1980).
- Reynolds, B. and Lakshminarayana, B., "Characteristics of Fully Loaded Fan Rotor Blade Wakes," NASA CR-3188, 180 pp., October 1979.
- Reynolds, B. and Lakshminarayana, B., "Turbulence Characteristics in the Near Wake of a Compressor Rotor Blade," AIAA Paper 79-0280, pp. 1-12, 1979 (accepted for publication in AIAA Journal, 1980).
- Roberts, F. A., Tan-Atichat, J., and Nagib, H. M., "A Further Generalization of the Cosine Relation for Cylindrical Anemometer Sensors Leading to Improved Turbulence Measurements," presented at the 28th Fluid Dynamics Meeting of the American Physical Society, College Park, Maryland, 1975.

- Seyb, N. J., "Determination of Cascade Performance with Particular Reference to the Prediction of Boundary Layer Parameters," Aeronautical Research Council Report 27, 1965.
- Sitaram, N., "Analytical and Experimental Investigation of End Wall Flow in an Axial Flow Compressor," Ph.D. thesis, Department of Aerospace Engineering (in preparation), 1980.
- Smith, L. H., "Secondary Flow in Axial Turbomachinery," Transactions ASME, Vol. 77, 1955.
- Smith, L. H., "Three-Dimensional Flow in an Axial Flow Turbomachinery," QADC, Technical Report 55-348, Vol. 2, John Hopkins University, 1956.
- Sockol, P. M., "End-Wall Boundary Layer Prediction for Axial Compressors," AIAA Paper 78-1139, 1978.
- Squire, H. B. and Winter, K. G., "The Secondary Flow in a Cascade of Airfoils in a Non-Uniform Stream," Journal of Aeronautical Science, No. 18, 1951.
- Sugeyama, Y., "On the Characteristics of a Wing with a Tip Clearance," Bulletin of the Japan Society of Mechanical Engineering, Vol. 18, No. 123, September 1975.
- Tennekes, H. and Lumley, J. L., A First Course in Turbulence, MIT Press, Cambridge, Massachusetts, 1972.
- Thwaites, B., "Approximate Calculation of the Laminar Boundary Layer," Aeronautical Quarterly, No. 1, 1949.
- Vagt, J. D., "Hot-Wire Probes in Low Speed Flow," Progress of Aerospace Science, Vol. 18, pp. 271-323, 1979.
- Vavra, M. H., Aerothermodynamics and Flow in Turbomachines, John Wiley and Sons, New York, 1960.
- Webster, C. A. G., "A Note on the Sensitivity to Yaw of a Hot-Wire Anemometer," Journal of Fluid Mechanics, Vol. 13, 1962.
- Wu, C. H. and Wu, W., "Analysis of Tip-Clearance Flow in Turbomachines," Polytechnic Institute of Brooklyn, Report No. 1, 1954.
- Wyngaard, J. C., "An Experimental Investigation of the Small-Scale Structure of Turbulence in a Curved Mixing Layer," Ph.D. thesis, The Pennsylvania State University, September 1967.

APPENDIX A

SCALES OF THE FLOW

The flow parameters and various scales of turbulence encountered in the present study are given below.

1. The free-stream velocity in the relative frame of reference varied from 15.5 to 46.5 m/s.
2. The overall turbulence level varied from 5% at free-stream locations to 15% inside the blade passage. In the rotor exit-flow the variation was from 5% to 20%.
3. The Reynolds number based on tip radius and peripheral velocity at the tip is 1.74×10^6 .
4. An estimation of the turbulent length scales is very important to categorize the type of turbulent flow, to understand its basic structure, and to calculate the various errors involved in the measurement of turbulent flow correlations. The three important scales of turbulence are:
 - a. Large eddy length scale (l)
 - b. Taylor's microscale (λ_g)
 - c. Kolmogorov scale (η)

The following Tennekes and Lumley (1972), the large eddy length scale is proportional to the mean flow strain rate. In the case of the passage-flow measurements, l is of the order of the mixing length of the boundary layer flow. For the rotor exit flow measurements, l is of the order of the semi-wake width. The Reynolds number (u'_{λ}/ν)

based on the turbulence intensity is also an important parameter in determining the structure of the turbulent flow. Here u' is the turbulence intensity and ν is the kinematic viscosity of the flow. The Reynolds number varies with radial and axial location of the flow. Typical values of the large eddy length scale and the Reynolds number based on the turbulence intensity are given below.

Flow Type	R	z'	l [cm]	Re
blade passage	0.891	0.750	0.4767	7.187×10^2
blade passage	0.980	0.979	1.147	1.210×10^3
exit	0.891	0.021	0.5525	1.380×10^3
exit	0.986	0.021	7.642	5.239×10^4

Taylor's microscale (λ_g) is defined as:

$$\lambda_g = \left(\frac{15 \nu}{\epsilon} \right)^{1/2} u'$$

where ϵ is the turbulent dissipation rate. An estimate of ϵ according to Tennekes and Lumley (1972) is given by:

$$\epsilon = \frac{u'^3}{l}$$

The small scale eddies in the dissipation range are represented by the Kolomogorov scale η which is defined as:

$$\eta = (\nu^3/\epsilon)^{1/4}$$

Typical values of the turbulent dissipation rate, Taylor's micro-scale, and the Kolmogorov scale for this investigation are:

Flow Type	R	Z'	$\epsilon[\text{cm}^2 \text{ s}^{-3}]$	$\lambda_g[\text{cm}]$	$\eta[\text{cm}]$
blade passage	0.891	0.750	2.361×10^7	6.887×10^{-2}	3.434×10^{-3}
blade passage	0.980	0.970	3.396×10^6	1.276×10^{-1}	5.588×10^{-3}
exit	0.891	0.021	7.257×10^7	5.761×10^{-2}	2.441×10^{-3}
exit	0.986	0.021	1.385×10^3	1.293×10^{-1}	2.207×10^{-3}

5. The wave number for turbulent flow is defined as:

$$\kappa = \frac{2\pi \omega}{u} \approx \frac{1}{\ell_e}$$

where ω is the frequency at which the contribution due to a correlation between two fluctuating velocity components to the Reynolds stress is being considered. u is the mean flow velocity at which an eddy of length ℓ_e , corresponding to that wave number, is convected. In the spectral representation of the Reynolds stress tensor components, the concept of wave number is very useful in calculating the errors in Reynolds stress correlations. The wave number corresponding to an eddy of sensor length for the blade passage-flow probe and the exit-flow probe is 10.6 cm^{-1} and 10.0 cm^{-1} , respectively. The wave number corresponding to an eddy equal to the distance between the sensors of the blade passage-flow probe and the exit-flow probe is 5.46 cm^{-1} and 6.67 cm^{-1} , respectively.

These wave numbers are required in calculating errors in the Reynolds stress correlations described in Appendix B.

APPENDIX B

ESTIMATION OF THREE-SENSOR HOT-WIRE MEASUREMENT ERRORS

Three-sensor hot-wire probe measurements are prone to various sources of error. These errors can be divided into three categories: probe errors, instrumentation errors, and mechanical errors. Some of these errors are inherent in the measurement technique. However, by employing detailed and careful experimental procedures utilizing precise mechanical apparatus some of these errors can be minimized. Other errors can be compensated for by the inclusion of correction factors. A detailed discussion of a wide range of such errors is given by Anand (1977). Only the errors particular to the investigation are discussed below.

B.1 Three-Sensor Hot-Wire Probe Error

In the case of measurements with a three-sensor hot-wire probe, many sources of error may occur. Some of these sources have been discussed in Chapter 3. This included the error due to the inclination of the wire to the flow streamline (deviation from the cosine law), geometry of the prongs and probe body (inviscid flow and heat transfer effects), and the finite dimensions of individual wire. Additional sources of error specific to the probe are discussed below.

1. Spatial resolution of the probe. The finite distance between the wires or the total sensing area can be a large source of

error for nonuniform three-dimensional flows. This error is most critical in the cross-correlation data. The error is related to the minimum eddy size the probe can correlate because of the separation of the wires. The wave numbers, κ , corresponding to these distances for the blade passage-flow probe and the exit-flow probe are given by,

<u>Probe</u>	<u>κ_{12}</u>	<u>κ_{23}</u>	<u>κ_{31}</u>
blade passage flow	5.46 cm ⁻¹	5.46 cm ⁻¹	5.46 cm ⁻¹
exit flow	6.67	6.67	6.67

as defined and described in Appendix A. The error e in the correction is given by Lumley (1965) as

$$e(\overline{u_1' u_j'}) = \frac{\int_0^\infty \kappa E_{1j}(\kappa) d\kappa}{\int_0^\infty E_{1j}(\kappa) d\kappa} = \frac{\overline{u_1' u_j'} - \overline{u_1' u_1'}(\kappa)}{\overline{u_1' u_j'}}$$

The turbulence of the flow can be considered to be locally isotropic for $km \approx 5 \text{ cm}^{-1}$. An estimate of correlation, and hence the error, may be obtained by assuming that the spectrum of E follows the expressions as described by Wyngaard (1967).

$$\begin{aligned} E_{1j}(K) &= \text{constant } C_1 \quad (0 < K < 0.1) \\ &= \text{constant } C_2/K \quad (0.1 < K < 5.0) \\ &= \text{constant } \epsilon^{2/3} K^{-5/3} \quad (5.0 < K < \infty) \end{aligned}$$

Anand (1977) has shown that the $\overline{u_1' u_j'}$ correlation is directly related to the measured fluctuating voltage correlation

$\overline{e_1 e_j}$. Using these relations the maximum anticipated errors in measured voltage correlations (shear stress) for the blade passage-flow probe and the exit flow probe are 15% and 12%, respectively.

An error is also created in the turbulence measurements. Since the sensor wires are in a non-uniform three-dimensional flow field the effective cooling velocity varies over the entire length due to their finite size. However, the calibration curve is based on a uniform velocity field over the wire. The error in turbulence measurements due to non-uniform flow is given by Hinze (1959) as:

$$e^2 = C \left(\overline{e^2} \right) \text{ measured,}$$

where $\overline{e^2}$ is the corrected voltage and C is the correction factor given by:

$$C = \left(1 - \frac{\ell^2}{6\lambda_g^2} \right)^{-1} \quad (\text{for } \ell/\lambda_g < 1)$$

where ℓ is the sensor length and λ_g is the Taylor's micro-scale of turbulence. For the blade passage-flow measurements $\ell \approx 0.094$ cm and $\lambda_g \approx 0.128$ cm and for the exit-flow measurements $\ell \approx 0.100$ cm and $\lambda_g \approx 1.29 \times 10^{-1}$ cm. These values of ℓ and λ_g are characteristic of the smaller eddies of the flow. The range and distribution for the values of ℓ and λ_g depend upon the nature of the flowfield which varied considerably

from one measurement location to another. This variation is evident from the spectra presented in Chapter 4. The correction factor for the rms voltages is dependent upon the range of values observed for ℓ and λ_g . For the small eddies indicated above the correction factor is 1.10 for the blade passage-flow measurements and 1.11 for the blade exit-flow measurements. This is the maximum value of the correction factor experienced since the turbulence spectra indicate that larger eddies are more apparent which are more accurately measured by the probe.

2. Thermal inertia of the wire. If the fluctuations of the flow-field are very rapid, the hot-wire must be heated and cooled with the same frequency. This is possible only if the thermal inertia of the wire is infinitely small. However, the thermal inertia has a finite value and there is a delay between the rapid fluctuations of the gas velocity and the corresponding temperature fluctuations of the hot-wire.

The sensitivity s of the hot-wire is defined by:

$$\overline{(e^2)}^{1/2} = s \overline{(u^2)}^{1/2}$$

where e is the voltage across the wire and u is the turbulence-velocity change. The sensitivity due to the thermal inertia at any frequency ω is given by Hinze (1959) as:

$$s(\omega) = 1 / (1 + \omega^2 M^2)^{1/2}$$

where M is the time constant of the wire given by:

$$M = \frac{e_c C_w (R_w - R_f)}{b I^2 R_o R_f} = \frac{e_c C_w (\theta_w - \theta_f)}{I^2 R_f}$$

of the hot-wire decreases with increasing values where:

e_c = conversion constant between heat and electrical units.

C_w = specific heat of the wire material.

θ_w = heated hot-wire temperature.

θ_f = working fluid temperature.

I = amperage in the circuit.

R_f = resistance of the wire at fluid temperature.

For the tungsten wires used in the experimental investigation with an over heat ratio of 0.5, the constant M is approximately equal to 1.6×10^{-4} s. The thermal sensitivity of the hot-wire in measured fluctuation levels for 1, 5, and 10 kHz are,

$$s(1 \text{ kHz}) = 0.987$$

$$s(5 \text{ kHz}) = 0.781$$

$$s(10 \text{ kHz}) = 0.530$$

Thus the sensitivity of the hot-wire depends on the frequency of the velocity fluctuation. This is related to the finite thermal inertia of the hot-wire. The sensitivity of the hot-wire decreases with increasing values of the frequency which corresponds to increased error.

3. Aging, oxidation and contamination of the wire. These errors depend upon the total operation time, over-heat ratio, and the flow environment. These errors were minimized by calibrating

the probe before and after the experiment and incorporating the variation in the data reduction process. Also the sensors were cleaned regularly to ensure the validity of the calibration data.

4. Ambient temperature variation. A change in the ambient temperature causes a change in the heat transfer rate of the sensors. This results in a corresponding change in a corresponding change in the measured output voltages from the anemometer. This effect was controlled by maintaining an ambient temperature to within $\pm 2^{\circ}\text{C}$. Also this limited variation in temperature was compensated by correction schemes described by Anand (1977) which were incorporated into the data reduction computer program.

B.2 Instrumentation Errors

The errors arising due to instrumentation may be due to:

1. Improper integration time constant used for the voltmeter and rms meters.
2. Improper balance of the anemometer bridge.
3. Improper gain adjustments in the sum and difference circuits.
4. Improper bandwidth matching of the FM tape recorder.
5. Stray signals from the power line and blade passing frequency.

Most of these sources of error were easily checked. It was assumed that they did not contribute any error to the measurements.

B.3 Mechanical Errors

Various mechanical difficulties were encountered during the rotation of the three-sensor hot-wire probe. Many of these difficulties were overcome through proper modification of the mechanical data acquisition system. Some difficulties could not be eliminated. However they could be minimized to an extent so that they did not actually influence the data. Such sources of error were:

1. Probe body vibrations. The vibration of the probe body due to rotation, flow induced vibration, and transmission of vibration due to other mechanical sources like vibrating belts and pulleys can add a significant amount of spurious signal to the measurements. The natural frequency of the probe and the probe support can be evaluated assuming that the probe acts like a concentrated mass at the end of the support. According to Hortog (1947) the natural frequency in the bending mode is given by:

$$\omega_n^2 = (\omega_n^2)_{\Omega=0} + a \Omega^2$$

where:

$$(\omega_n^2)_{\Omega=0} = 3.03 E I / \ell_o^3 (M + 0.023 m)$$

$$E = \text{elastic modulus} = 30 \times 10^6 \text{ psi}$$

$$m = \text{mass per unit length of the probe} = 0.0018 \text{ lb}_o$$

$$M = \text{mass of the probe} = 0.005 \text{ lbm}$$

$$I = \text{moment of area} = 2.20 \times 10^{-4} \text{ in}^4$$

$$a = \text{constant} = 1.5$$

The natural frequencies at the lower and mid-radial were found to be greater than the cut-off frequency, thus they did not affect the measurements. At higher radial locations the existence of probe body vibration was investigated using a strobe flash. Also an analysis of the hot-wire sensor signal was performed employing a spectrum analyzer. These methods did not indicate the existence of any probe body vibration or spurious signal.

2. Gear slack in the traverse mechanism. Due to an inherent characteristic of the planetary gear system used to traverse the probe in the tangential direction, the probe stem was free to travel 2.49 degrees in the tangential direction. This is a considerable source of tangential location error since the blade passage survey spans 17.14 degrees. To eliminate this source of error the traverse gear shaft was pre-torsioned by a linear spring. This method was observed to be adequate during rotation for accurate tangential location by means of a strobe flash.
3. Improper sensor angle measurement. The three-sensor hot-wire probe requires that the position of all three sensors be measured angularly with respect to the reference coordinate system. Accurate angle measurements are extremely important since a small change in the resulting direction cosines of the sensor results in a substantial change in the resulting velocity measurements. To attain a high degree of accuracy in the angle measurement, the following procedure was employed.

The probe was placed in a fixture with 3-degrees of angular movement on a Bridgeport flatbed mill. This mill was capable of 3-degrees of linear movement. In this arrangement, the three-sensor probe was viewed through a Bausch and Lomb Stereo Zoom Microscope. The projected lengths of the wires were measured in the three orthogonal planes formed by the reference coordinate system. This measurement was performed by two methods. First, the projected lengths were measured using a linear eyepiece of the microscope to an accuracy of ± 0.00127 cm. Second, the scaled movement of the mill bed was used to move the probe with respect to a reference point viewed through the microscope. The mill bed had an accuracy of ± 0.00127 cm in its linear movement. These two methods resulted in reference angles which differed by an average value of 3%. This is the error associated with improper sensor angle measurement.

The various sources of error given above affect the accuracy of the data reported in this thesis. Many of these possible sources of error were eliminated (e.g., traverse gear slack, improperly adjusted instrumentation) and have no consequence upon the accuracy of the reported data. The realization of such possible sources of error permitted corrective measures to be taken. Other sources of error, such as those described in Chapter 3, were compensated for by proper probe alignment and data reduction procedures. In this way some sources of error inherent to the three-sensor probe are not reflected in the reported data. However, some sources of error due to physical limitations of the probe could only be minimized during the experimental investigation. Such sources of error

are due to the spatial resolution of the probe (cross-correlation data) and due to the thermal inertia of the hot-wire (turbulence intensities). These sources of error were minimized by the selection of a probe with small physical dimensions; however, an error of the range indicated above is reflected in the reported data. Through the realization and proper compensation of the above sources of error, the experimental results reported in this thesis accurately describe the characteristics of the flowfield near the annulus-wall region of an axial-flow compressor rotor blade passage.